Porphyrin Molecular Tweezers with Varying Degrees of Rotational Freedom

Rhys Brenton Murphy, B.Sc. (Hons)

Thesis Submitted in Fulfilment of the Requirements for the Degree of

Doctor of Philosophy

School of Chemical and Physical Sciences,

Faculty of Science and Engineering

March, 2016

For Mum, Dad, and Jason. My family, my shining stars. I love you.

Contents

Abstract

Molecular tweezers show significant promise for a variety of applications, from new agents for targeted drug delivery and controlled release, as enzyme mimics, and as components in molecular machines to perform specific functions at the nanoscale. For molecular tweezers with two ligand binding sites, where these are remote but interdependent, the system can benefit from cooperativity during complexation, to positively or negatively influence ligand binding. Recently, cooperativity in supramolecular systems been categorised into several different types depending on the modes of interaction between the architecture and ligands. These include allosteric, chelate, and interannular cooperativity. As such, assessing and quantifying cooperativity between remote ligand binding sites is more complex than previously envisaged. This work investigated cooperativity within tweezer **4**, which has two homotropic ligand binding sites.

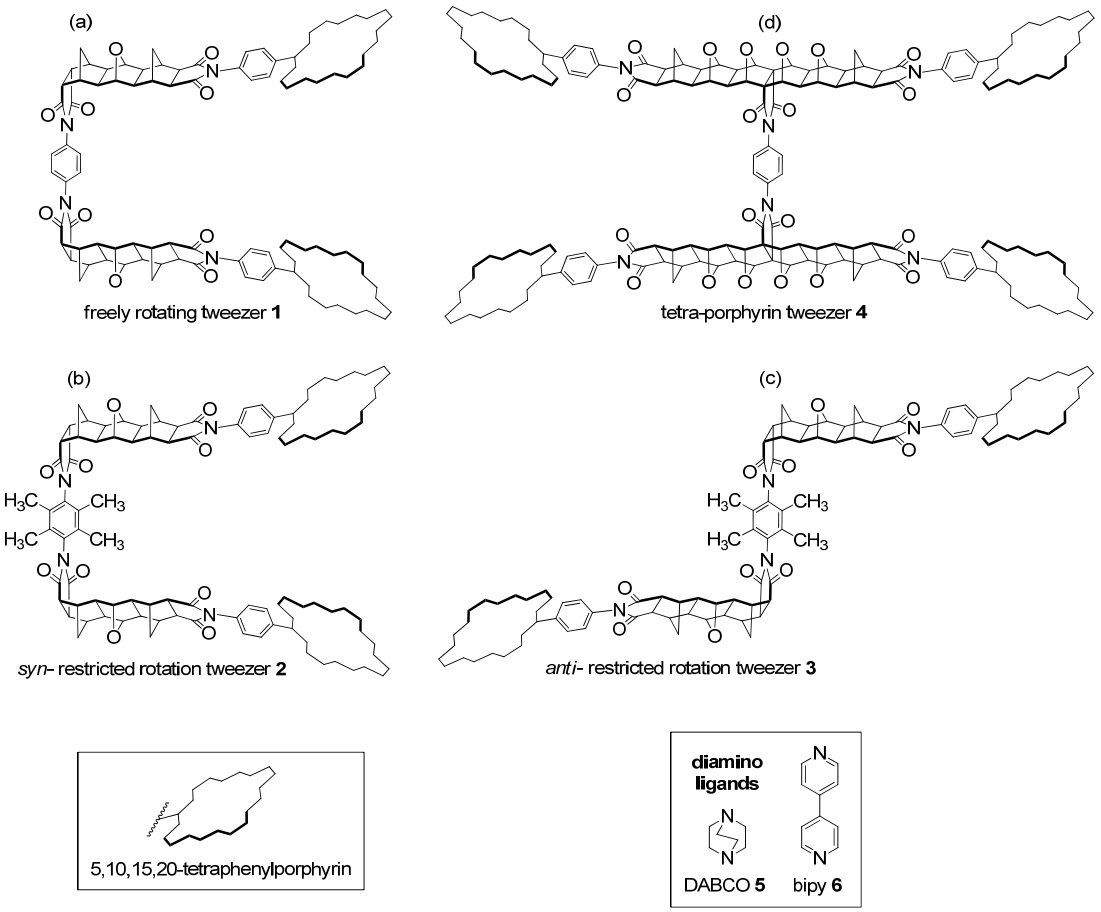

Figure i - Schematic representation of the four molecular tweezers synthesised in this work (a) freely rotating **1**, (b) *syn*- restricted rotation **2**, (c) *anti*- restricted rotation **3**, (d) tetra-porphyrin freely rotating **4**, each studied for complexation with diamino ligands DABCO **5** and bipy **6**.

Using molecular modelling as a guide, a tweezer architecture was designed to complex diamino substrates such as 1,4-diaza[2.2.2]bicyclooctane **5** (DABCO) and 4,4'-bipyridyl **6** (bipy). The modular tweezer design allowed for maximum synthetic variability and resulted in synthesis of three generations of the tweezer (Figure i), each containing rotating bis-porphyrin receptors, linked via a bridged polycyclic backbone, with a central phenyl diimide core of varying rotational freedom. Structural analogues included a freely rotating tweezer **1** with one binding site [1] (a), a rotationally restricted tweezer with non-interconvertible *syn*- **2** and *anti*- **3** conformations (b) and (c), and a freely rotating tetra-porphyrin tweezer **4** with two binding sites (d) [2]. With the exception of the *anti*- restricted system (c), each tweezer formed strong intramolecular sandwich complexes in chloroform with the target diamino substrates, as characterised by UV-Vis and NMR spectroscopy, with the binding model and association constants determined by multivariate global spectral analysis.

The first generation freely rotating single binding site tweezer **1** [1] (Figure i (a)) served as a good model to determine the feasibility of applying the bridged polycyclic scaffold to the tetra-porphyrin system **4**. This probed both the ability of the tweezer to form strong intramolecular sandwich complexes with diamino ligands, as well as the rigidity of the bridged polycyclic scaffold, including free rotation about single bonds at the central phenyl diimide core and porphyrin receptors.

The second generation tweezer (Figure i (b), (c)) was analogous to the first except for the subtle inclusion of sterically bulky methyl substituents about the central phenyl diimide core. In this case, non-interconvertible *syn*- **2** and *anti*- **3** conformations could be physically separated and studied independently of each other. For the *syn*-conformation, this removed the undesired *anti*- conformation only capable of intermolecular complexation with ligands.

After gaining an understanding about the behaviour of the model single binding site systems regarding both substrate complexation and core rotation, the third generation freely rotating tetra-porphyrin tweezer **4** (Figure i (d)) was synthesised [2]. The two bis-porphyrin binding sites are intrinsically linked via the freely rotating phenyl diimide core, which acts as a pivot through which equal and opposite rotation of a largely rigid polycyclic backbone can occur. Statistical evaluation of the interannular cooperativity factor, γ, was undertaken using a method reported in the literature, and

revealed the intramolecular sandwich complex with two molecules of DABCO, tetra-porphyrin:$(DABCO)_2$ was negatively cooperative ($\gamma = 2.41 \times 10^{-3}$), while that with bipy, tetra-porphyrin:$(bipy)_2$, was modestly positively cooperative ($\gamma = 4.65\text{-}5.24$). The negative cooperativity determined for DABCO was unexpected, given the large intramolecular association constants of the model tweezers, and suggests that DABCO could be too small to be bound optimally at both binding sites. The positive cooperativity observed for bipy could be explained by increased optimisation of the interporphyrin distance at the second binding site brought about by binding at the first binding site.

Declaration

I certify that this thesis does not incorporate without acknowledgment any material previously submitted for a degree or diploma in any university; and that to the best of my knowledge and belief it does not contain any material previously published or written by another person except where due reference is made in the text.

.....

Rhys Brenton Murphy,

March, 2016.

Acknowledgements

Firstly, thank you Martin Johnston for the opportunity to undertake this project. It has been a great success and I've very much valued your interest and expertise along the way. I remember being captivated by your seminar on molecular capsules when I was a first year science undergraduate in 2006. Thank you for introducing me to the exciting world of supramolecular chemistry!

A very special thank you to Kevin Wainwright, for your generosity and support, and for your copy of Supramolecular Chemistry by Steed and Atwood. Thanks Mike Perkins for chairing the Organic Seminar series, this is an excellent forum and your comments always encourage good scientific discussion. Malcolm Thompson, I've very much appreciated your support and friendship, and always enjoy our conversations. Thank you to all of my teachers throughout school and university for your enthusiasm and for fostering my interests. I'm very much looking forward to many years ahead as a scientist.

Thank you to our collaborators, Dr Duc-Truc Pham and Prof Stephen Lincoln (The University of Adelaide) for the many conversations shared during the project, in particular your expertise in multivariate global spectral analysis of supramolecular systems. Thanks to Assoc Prof Claire Lenehan (Flinders University) for additional support with multivariate global spectral analysis.

Thanks to the following people for their assistance in instrument access and characterisation of compounds:

- Assoc Prof Christopher Sumby (The University of Adelaide), X-Ray diffraction measurements.
- Dr Rebecca Norman (Flinders University), solving of X-ray crystal structures.
- Prof Jonathan White (The University of Melbourne), X-Ray diffraction measurements and solving of X-ray crystal structures.
- Prof Nico Voelcker (Flinders University 2011), five decimal point balance.
- Assoc Prof Stewart Walker (Flinders University), five decimal point balance.
- Dr Daniel Jardine (Flinders Analytical), mass spectrometry.
- Dr Sally Duck (Monash University), mass spectrometry porphyrin tweezers (special thanks for your tireless efforts, you're an absolute legend!).

Thanks to the following organisations for scholarship and conference travel funding:

- Flinders University (provision of Australian Postgraduate Award, Research Student Conference Travel Grant, Elaine Martin Fund Travel Grant).
- Royal Australian Chemical Institute (provision of Student Bursary).

A warm thank you to the Playford Memorial Trust for a PhD top-up scholarship. I greatly appreciate all the efforts of the Trust and their support of the fantastic research taking place in South Australia. I look forward to supporting the Trust and the vision and legacy of Sir Thomas Playford in the future. Also, thanks to the Australian Federation of University Women - South Australia Inc. Trust Fund, for co-awarding the Doreen McCarthy Bursary to support my professional development as a scientist. You are a very kind group of people.

Thank you to the Onkaparinga City Concert Band and Marion City Band/Warriparinga Brass, for the friendships, laughs, and fun making music together. Band is always my favourite part of the week. And a special thank you to my high school music teachers, Helen Riekie and Gavin Hughes, for the absolute gift of learning the trumpet. Music has changed my life and I honestly don't know what I'd do without it.

On a more personal note, to my dearest friends, Emma Lawrance and Emma White, I love spending time with you both, and moments together have been some of the best times of my life.

And finally, my beautiful family. Mum & Dad, words just cannot describe the many wonderful things I think of you. You have taught me so much about life and to always try my best. You are so wise, giving, caring, and loving. Jason, my brother and best friend, and I'm so glad that we are close. I always look forward to talking with you & sharing those knowing smiles. Thank you to Nanna for always believing in me. You are all such beautiful people; we share a special and unbreakable bond that I deeply cherish. I am so lucky. You mean the world to me, and I love you all very dearly.

1. Literature Review

1.1 Supramolecular Chemistry, Hosts and Guests, and Molecular Tweezers

Supramolecular chemistry refers to the structure and function of molecular assemblies formed when two or more species (typically referred to as the host and guest) interact non-covalently [3, 4]. The host has a degree of organisation and undergoes a recognition event with a complementary guest. This host-guest concept of supramolecular chemistry is summarised in Figure 1.1 (reproduced from [4]).

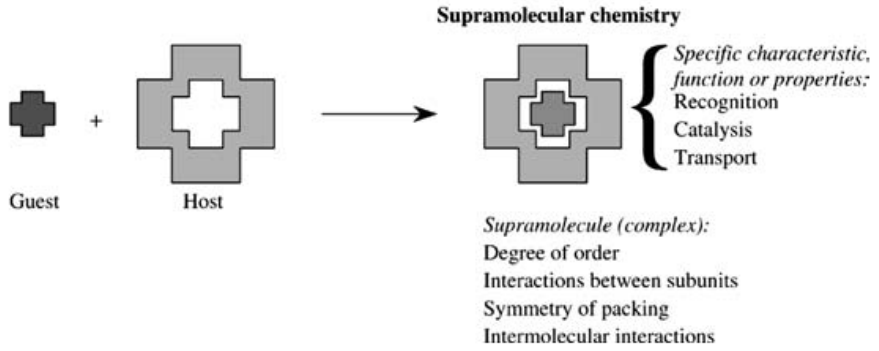

Figure 1.1 - Supramolecular chemistry in terms of hosts and guests (reproduced from [4]).

Nature presents many exquisite and fascinating examples of supramolecular chemistry [4, 5]. However, the remarkable complexity inherent in biological systems requires synthetic analogues to be heavily simplified [5]. Nevertheless, supramolecular systems are excellent candidates for the fabrication of miniaturised molecular devices, as they can be custom assembled from the bottom-up to perform specific functions at the nanoscale [5]. As such, advances in supramolecular chemistry leading to miniaturisation are likely to result in new technologies in the fields of medicine, the environment, energy, and materials [5].

A notable class of supramolecular architectures are molecular tweezers. Molecular tweezers are artificial molecular receptors in which two binding domains are cofacially positioned by means of a linker to define an intramolecular binding site suited to a particular guest [4] (Figure 1.2). The interaction between the host and guest usually arises from hydrogen bonding, metal coordination, π-π interactions, van der Waals forces, or a combination of these [6].

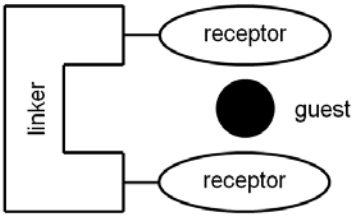

Figure 1.2 - Pictorial representation of molecular tweezers.

Molecular tweezers have been the focus of significant research over the last several decades and continue to be actively pursued today, with several large reviews recently published (including clips and cages) [7-12]. A plethora of architectures have been synthesised which accommodate guests such as aromatic compounds [13-15], anions [6], cations [16-20], fullerenes [21-23] and amines [6, 21, 24-41]. This versatility in design, structure and function makes molecular tweezers excellent candidates for the fabrication of nanoscale molecular devices [7, 9]. Consequently, molecular tweezers are beginning to find applications in targeted drug delivery and controlled release [15], and in the determination of enantiomeric purity or absolute configuration of chiral guest compounds [42-45].

The remainder of this sub-section describes the two defining architectures in the development of the molecular tweezer movement, and culminates in two more recent examples from the literature, demonstrating the advancement of the field.

The earliest example of molecular tweezers are bifunctional derivatives of caffeine [13] (Figure 1.3). In this system, two caffeine receptors are linked by an aliphatic linker, and form intramolecular sandwich complexes with aromatic guests via π-π interactions. The association constant between the bis-caffeine receptor and potassium 1,3-dihydroxy-2-naphthoate guest was approximately 10^4 M^{-1}, and is enhanced in the bifunctional system compared to independently acting caffeine units. The semi-rigid diyne linker, although conformationally mobile (bond rotation of the free host results in *syn*- and *anti*- structures), prevents self-association of the caffeine receptors, and affords larger association constants than using flexible alkyl linkers.

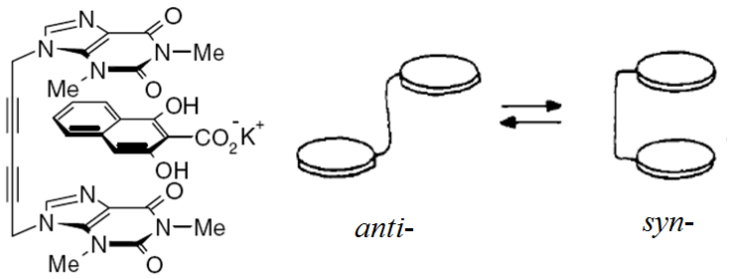

Figure 1.3 - Bifunctional derivatives of caffeine form a π-sandwich complex with aromatic guests. The host is conformationally mobile via linker rotation and can occupy either the *syn*- or *anti*-conformation prior to guest inclusion [13].

The conformational mobility of the linker was later addressed in a bis-acridine system with a rigid dibenz[*c,h*]acridine spacer, which preorganises the receptors in the *syn*- conformation (Figure 1.4) [14]. The association constant for the bis-acridine system with 2,4,7-trinitrofluorenone was approximately 10^2 M^{-1}, calculated by analysis of shifts of the ^{1}H NMR resonances, and is enhanced compared to the mono-acridine [14]. Again, as for [13], introducing flexibility into the linker of [14] resulted in a significant reduction in association constant.

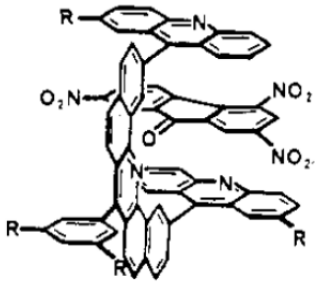

Figure 1.4 - *syn*- bis-acridine molecular tweezers complexed to 2,4,7-trinitrofluorenone [14].

In recent decades, molecular tweezer architectures have evolved to incorporate more dynamic elements. The following example (Figure 1.5) demonstrates fluorescence signal transduction in molecular tweezers via a chelation-induced conformational change [19]. The system is comprised of a tetrasubstituted *cis-anti-cis*-perhydroanthracene core functionalised at opposite ends with bis-2,2'-bipyridyl receptors and bis-pyrene units. Prior to Zn(II) chelation at the bis-2,2'-bipyridyl site, the pyrene groups are equatorial, close in space, and fluoresce as an excimer. Upon Zn(II) chelation, the perhydroanthracene core undergoes a triple ring flip, affording pyrene groups which are axial, far apart in space, and which now fluoresce as monomers. Host-guest complexation was measured by UV-Vis and ^{1}H NMR titrations, while the conformation was determined by NOESY spectroscopy. There

are several variations of this architecture involving different cores, receptors, chelators, and effectors [20, 46].

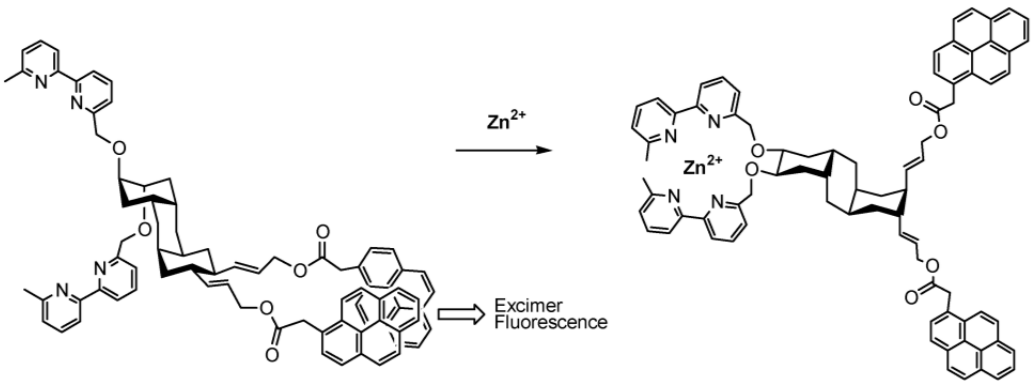

Figure 1.5 - Fluorescence signal transduction by chelation-induced conformational changes to the tweezer architecture [19].

Furthermore, stimuli-responsive molecular tweezers can respond to physical stimuli from their external environment (e.g. light, pH), inducing conformational changes to regulate binding. pH responsive molecular tweezers (Figure 1.6) are being developed for targeted drug delivery and controlled release [15]. In this system, a methoxyphenyl-pyridine-methoxyphenyl triad functionalised with naphthalene receptors was tethered to a water soluble poly(ethylene glycol) polymeric backbone. Under neutral conditions, the naphthalene receptors are arranged cofacially and bind the anticancer drugs quinizarin and mitoxantrone. This quenches the fluorescence of the guest drugs. Following titration with acid, the pyridyl moiety in the triad is protonated, and hydrogen bonds with the oxygen atoms in each of the adjacent methoxy groups. This acts as a switching mechanism in which the conformation of the naphthalene receptors is changed. This decreases the affinity of the receptors to the drug guest, which is released, and can be detected by fluorescence. The change in host conformation was followed using ^{1}H NMR. Although quantification of the dosage and rate of dosage was not established in this communication, the work highlights the emerging potential of intelligently designed molecular tweezers.

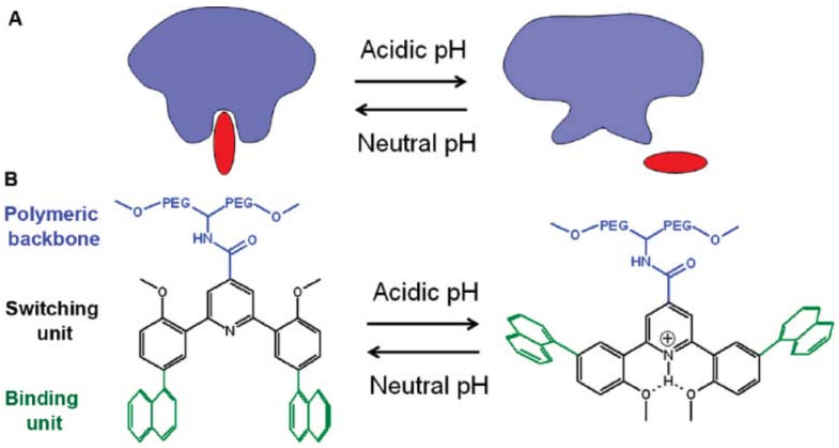

Figure 1.6 - pH responsive molecular tweezers for targeted drug delivery and controlled release of anticancer drugs [15].

1.2 Porphyrin Molecular Tweezers

Metalloporphyrin derivatives play a pivotal role in nature, including photosynthesis in plants and oxygen transport in blood [47]. Porphyrins complex an incredibly wide range of metal ions at their centres through coordination with the four internal nitrogen atoms [47], and depending on the coordination number of the metal centre, can also complex axial ligands [48]. Importantly, porphyrins are synthetically variable and exhibit a remarkable range of chemical and physical properties. This makes them attractive for applications ranging from catalysis [49], to sensors [50], to cancer treatment [51]. Thus, metalloporphyrins are ideal structural motifs as receptors in molecular tweezers.

In particular, early work with Zn(II) porphyrins receptors demonstrated their high affinity for a range of diamino ligands [27, 29, 52-54]. This has resulted in an exponential increase in porphyrin receptors in the literature [24-41, 44, 45, 55-65][1]. Although this list is far from complete, it is representative of the vast number of research groups contributing in this area. A more comprehensive review of these and many more can be found in recent reviews [8, 10-12].

A particularly elegant example in this field is the application of porphyrins to a light operated molecular pedal [24] (Figure 1.7). The host is comprised of a ferrocene

[1] [64, 65] represent outstanding progress in the field of porphyrin receptors. These novel rotaxane-based architectures are threaded with two porphyrin-containing modules, and form strong sandwich complexes with diamino ligands of various lengths. The interporphyrin distance is not only adjusted by the ligand length, but by Cu(I) metallation/demetallation of the 2,2'-bipyridine and phenanthroline coordination sites on the rotaxane thread and porphyrin-containing modules respectively.

pivot, closed on one side with an azobenzene loop, and functionalised on the other side with an open bis-porphyrin cavity. The guest is comprised of two isoquinoline units separated by a single bond, and this was found to form an intramolecular sandwich complex with the bis-porphyrin host. The azobenzene moiety acts as a switch upon irradiation by visible and UV light, undergoing reversible *cis*- *trans*-isomerism respectively. This change in conformation at the azobenzene is transferred through the ferrocene pivot by rotation of its cyclopentadienyl rings, resulting in changes to the interporphyrin spacing at the binding site. In turn, this invokes twisting within the guest by rotation of the single bond linking the two isoquinoline units. The mechanical twisting of the host and the guest are said to be intermolecularly interlocked [24]. Although this system cannot permanently transform the substrate into a product different to its original state, this is a promising step forward in this direction.

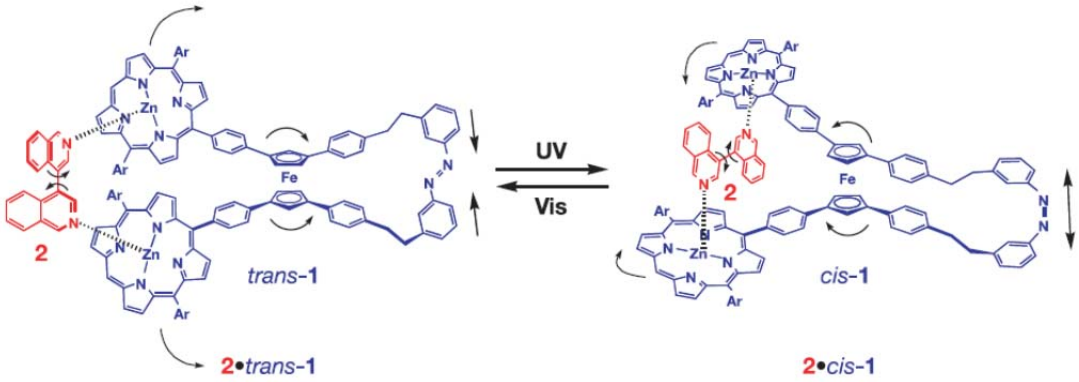

Figure 1.7 - Light-powered azobenzene/ferrocene/porphyrin molecular pedal, capable of inducing changes to guest conformation [24].

In [30] (Figure 1.8), a series of closely related tweezers was designed around an isophthalic acid core, differing only by the connection of the porphyrin *meso*-phenyl with respect to the core. While the *ortho*- and *meta*- dimers form 1:1 intramolecular sandwich complexes with 1,4-diazabicyclo[2.2.2]octane (DABCO), the *para*- dimer forms a 2:2 intermolecular sandwich complex with DABCO. These species are consistent with semi-empirical molecular modelling, in which the amide connectivity adopts a strain free planar geometry.

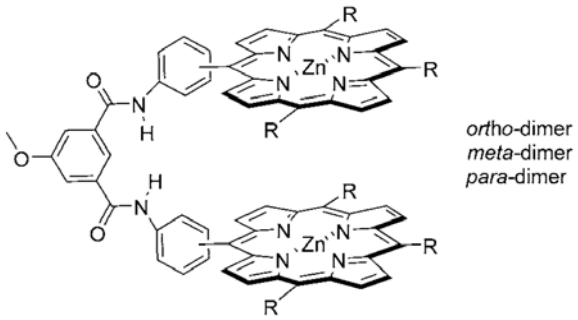

Figure 1.8 - substitution of the bis-porphyrins results in different host-guest behaviour; the *ortho*- and *meta*- porphyrin dimers form 1:1 intramolecular sandwich complexes with the diamino ligand DABCO, while the *para*- dimer forms a 2:2 intermolecular sandwich complex [30].

However, determination of this speciation for the different porphyrin dimers was non-trivial. In particular cases, the data could be fitted to two different binding models, differing only in the stoichiometry of the intermediate sandwich complex (1:1 or 2:2). The authors report that the 1:1 and 2:2 complexes are indistinguishable at a single concentration, and the goodness of the data fitting alone is insufficient to decide the correct binding model [30].

The authors developed a method to determine the correct speciation by using the binding constants determined at UV-Vis concentrations (typically micromolar) to simulate speciation at higher concentrations, such as those used for NMR (typically millimolar). This is based on reasoning that while the stability of a 1:1 intramolecular complex is independent of porphyrin concentration, the stability of a 2:2 intermolecular assembly is dependent on porphyrin concentration, because it requires two hosts [30]. As such, increased stability of the 2:2 species can be expected at higher concentrations, and this different behaviour allows it to be distinguished from the 1:1 species [30]. Comparison of the experimental NMR speciation with the simulated NMR speciation for the different binding models enabled the correct binding model to be assigned. This approach has been adopted in related porphyrin systems with DABCO and other diamino ligands [28, 31, 58]. This work is particularly relevant for this thesis, as this methodology has been undertaken as part of the data analysis of the tweezers synthesised in Chapters 3 to 5.

This method does make the assumption that speciation is the same at UV-Vis and NMR concentrations. However, this is not always the case. Indeed there are circumstances where speciation is concentration dependent, such as the well documented 2:1 bis-(mono-porphyrin):DABCO sandwich complex, which is formed

exclusively at NMR concentrations and not observed at UV-Vis concentrations [27-31, 52, 66]. This was found to be important in some of the work contained in this thesis.

In the following tweezer example (Figure 1.9), a bridged polycyclic scaffold appended with porphyrins and a centrally located internal pendant probe can detect guest via shifts in the probe resonances during ^{1}H NMR [67]. Systems capable of signal transduction are attractive for applications such as switches, relays, diodes, and logic gates [67]. To measure the dimensions of the cavity, complexation was undertaken with diamino ligands of varying lengths and rigidity. Interestingly, the host appears to exhibit a higher degree of flexibility than anticipated from molecular modelling calculations [67], and displays poorer selectivity than anticipated. The authors conclude that small degrees of flexibility in each modular section are amplified across the entire molecule for large, extended backbones.

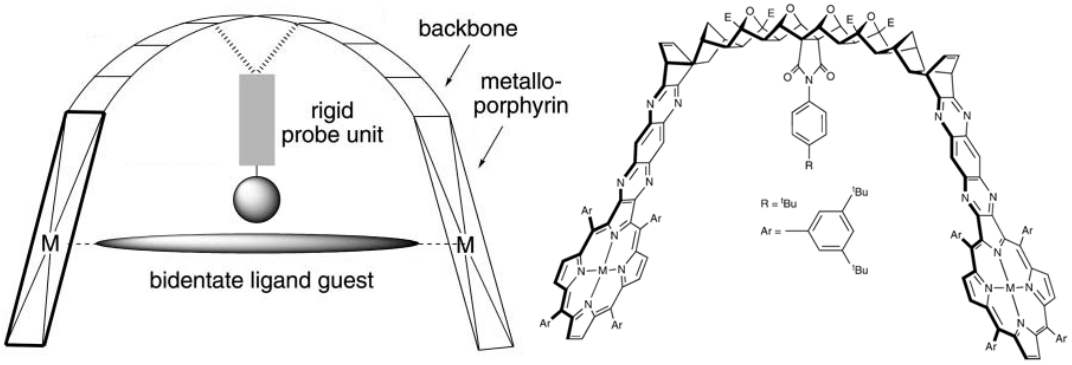

Figure 1.9 - Polycyclic linked bis-porphyrin molecular tweezer with an internal pendant probe capable of guest signal transduction [67].

In addition to the authors' comments on flexibility, there is literature precedent to suggest that fused aromatic linkages can undergo significant out of plane bending [68-70]. As such, the incorporation of 1,4,5,8-tetraazaanthracene units in-line between the bridged polycyclic scaffold and porphyrin receptors could majorly reduce the rigidity and thus selectivity of the host.

Nevertheless, polycyclic scaffolds derived from norbornyl derivatives provide an excellent molecular backbone for positioning receptors, and as such are useful components in a variety of supramolecular architectures (recent examples include anion hosts [71] and coordination cages [72]). In addition, porphyrin-appended polycyclic scaffolds are able to form molecular capsules and tweezers [67, 70, 73-

78]. A more detailed discussion of polycyclic scaffolds is provided in Chapter 2 on molecular design.

1.3 Linkers: Rigidity, Flexibility and Preorganisation

As has been seen throughout this literature review, the design of the linker plays a crucial role in the host-guest behaviour of the tweezer. Another example of this can be observed for a series of bis-porphyrins each sharing a calixarene spacer [38, 40, 41] (structures not shown here), where the calixarene bridging structure (CH_2 or S), conformation (cone or 1,3-alternate), and/or steric bulk of substituents on the calixarene rim alter speciation and guest affinity, arising from changes to cavity size, preorganisation, and interporphyrin distance.

In general terms, it is reported that rigid linkers afford larger association constants than systems with flexible linkers [11, 79], as well as offer substrate selectivity provided the dimensions of the tweezer cavity are suited to the substrate [11]. Conformationally flexible linkers allow complexation of substrates of different sizes and shapes [11, 39], and these systems tend to suffer from poor selectivity. However, it can be advantageous to balance the degree of host preorganisation and rigidity with flexibility [80, 81], as demonstrated by a metalloporphyrin host which catalyses the rate of a hetero-Diels-Alder reaction [80], and disulfide-linked bis(cyclopeptides) which display high affinity and selectivity for the sulfate anion in aqueous solution [81].

In a series of bis-porphyrins each with different linker structures [35, 36, 82] (structures not shown here), it has been observed that large association constants (which are enhanced compared to the reference monomeric complex) can be obtained for architectures containing either conformationally flexible, restricted, or more rigidly constrained linkers, and that the linker need only confer the system with moderate or sufficient preorganisation[2]. Further evidence for this is provided by a variety of porphyrin host-guest systems with varying degrees of preorganisation [6, 32, 34-36, 38-41, 53, 67, 73, 80, 83-86], including those which allow defined changes in interporphyrin distance.

[2] Although there are examples where flexible linkers are insufficiently preorganised and small association constants are obtained [36, 82].

Furthermore, it is known that biological receptors (which are dynamic and far from rigid) appreciate comparatively larger association constants compared to most artificial receptors [79, 81]. This has led to discussion that adopting a rigid-only approach to host design which relies solely on covalent linkages to establish geometry (that is, a host in which no secondary non-covalent interactions or folding contributes to its structure, and which cannot undergo reorganisation when binding guests) could limit the scope of artificial receptors [79, 81].

1.4 Allosteric Receptors and Molecular Tweezers

An allosteric interaction refers to the indirect modification of an active site brought about by conformational changes induced by an effector binding at a remote second site [4, 16, 87]. The effector can either enhance or diminish binding of the primary substrate, referred to as positive or negative cooperativity [87], and are classified as either homotropic or heterotropic depending on whether the effector is the same as or different to the substrate. Cooperativity and allosteric interactions play a key role in biological systems, for example in enzymes, as outlined in Figure 1.10 [87]. Importantly, allosteric interactions offer the ability to control and regulate molecular function, or transduce chemical signals using external stimuli as a feedback mechanism [87].

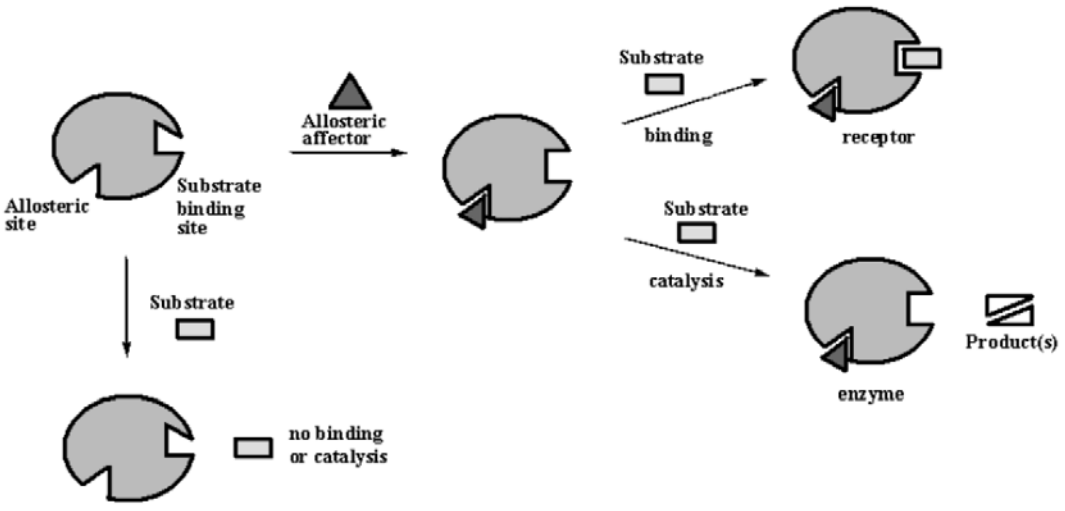

Figure 1.10 - Allosteric effectors can activate substrate binding in enzymes [87].

The following literature examples are of cooperative host-guest systems, and demonstrate the power of cooperativity between two binding sites in influencing the outcomes of host-guest association. In many of these examples, the systems are referred to as allosteric by their authors [6, 17, 21, 84]. However, allosteric

cooperativity has been more strictly defined as the interplay of two or more *intermolecular* binding interactions [88], not involving *intramolecular* interactions. This distinction and precise definition of allosteric cooperativity is further expanded in section 1.4, however, for this current section of the literature review, instances of allosteric behaviour are as envisaged by the authors of these supramolecular systems.

The earliest examples of allosteric hosts are based on a 2,2'-bipyridine 3,3'-crown ether system (Figure 1.11) [16-18]. The binding of transition metal cationic effectors at the bipyridyl moiety forces the aromatic rings to be almost coplanar, directs the benzylic oxygen atoms away from each other, and restricts the conformational flexibility of the crown ether. This diminishes the affinity of the crown ether for alkali metal cations, and is an example of negative cooperativity.

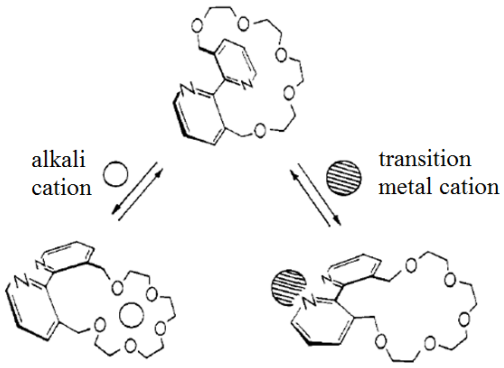

Figure 1.11 - 2,2'-bipyridine 3,3'-crown ether allosteric host. The affinity of the crown ether for alkali metal cations is reduced upon binding transition metal cations at the bipyridyl site [17].

There are several prominent literature examples of porphyrin-based allosteric systems, demonstrating both positive and negative cooperativity. Negative heterotropic cooperativity has been demonstrated for a biphenyl-crown ether linked bis-porphyrin (Figure 1.12) [84]. Without a metal ion effector bound at the crown ether, the bis-porphyrins intramolecularly complex the diamino ligand 1,4-bis(3-aminopropyl)piperazine with an association constant of approximately 10^5 M^{-1}. However, binding a Ba^{2+} effector at the crown ether resulted in dissociation of the diamino ligand, based on UV-Vis and NMR spectral evidence, and is likely to arise from changes to the interporphyrin distance. This architecture was subsequently examined for chirality transfer to the host induced by optically pure guest, and is described in detail in [89].

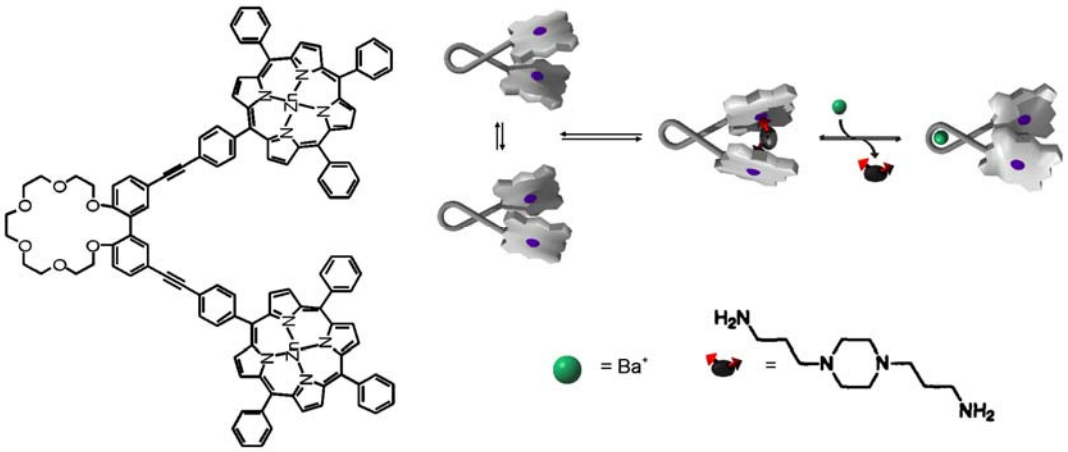

Figure 1.12 - complexed diamino ligand dissociates with Ba^{2+} effector (negative cooperativity) [84] (reproduced from [11]).

The biindole bridged bis-porphyrin (Figure 1.13) [6] is able to complex two heterotropic guests, either singly or simultaneously. The host is conformationally mobile between *syn*- and *anti*-, although molecular modelling suggests free biindoles are more stable in the *anti*- conformation. Titration of the host with either the chloride anion or DABCO affords association constants of 10^4 M^{-1} at the biindole and 10^6 M^{-1} at the bis-porphyrin respectively, with the host now occupying the *syn*-conformation. Subsequent titration of chloride with pre-coordinated DABCO resulted in association constants of 10^5 M^{-1}, while association constants for DABCO with pre-coordinated chloride are 10^7 M^{-1}. The association constants are increased by approximately an order of magnitude when pre-coordinated with the opposite guest, demonstrating positive heterotropic cooperativity.

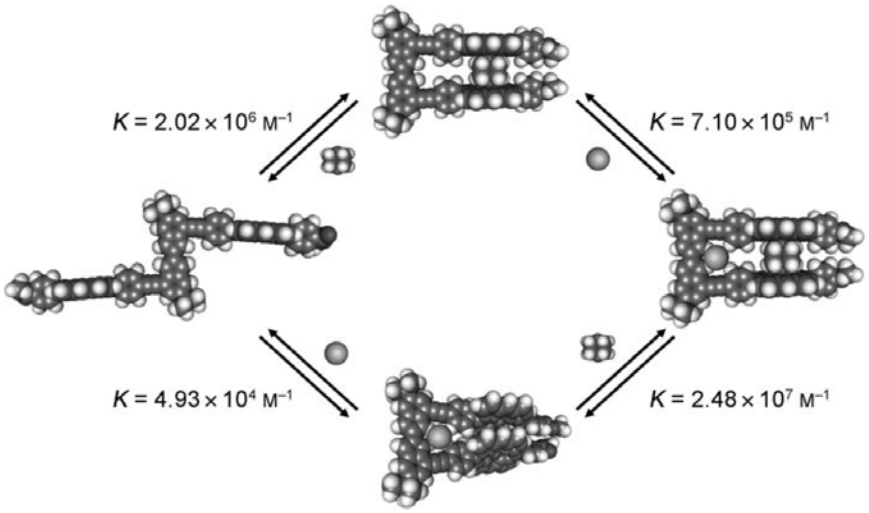

Figure 1.13 - Biindole bridged bis-porphyrin host is positively cooperative for binding of the second guest in the presence of the first guest [6].

Another intriguing example is the pyridyl-zinc porphyrin dimer (Figure 1.14) [21]. The free host is intramolecularly complexed with itself and occupies the *anti*- conformation. The host in this conformation does not undergo competitive complexation with C_{60} fullerene (ordinarily a bis-porphyrin guest). However, addition of a Pd(II) effector results in complexation of the bis-pyridyl moieties, and allows the bis-porphyrins to adopt the *syn*- conformation. The bis-porphyrins are now able to complex C_{60} fullerene.

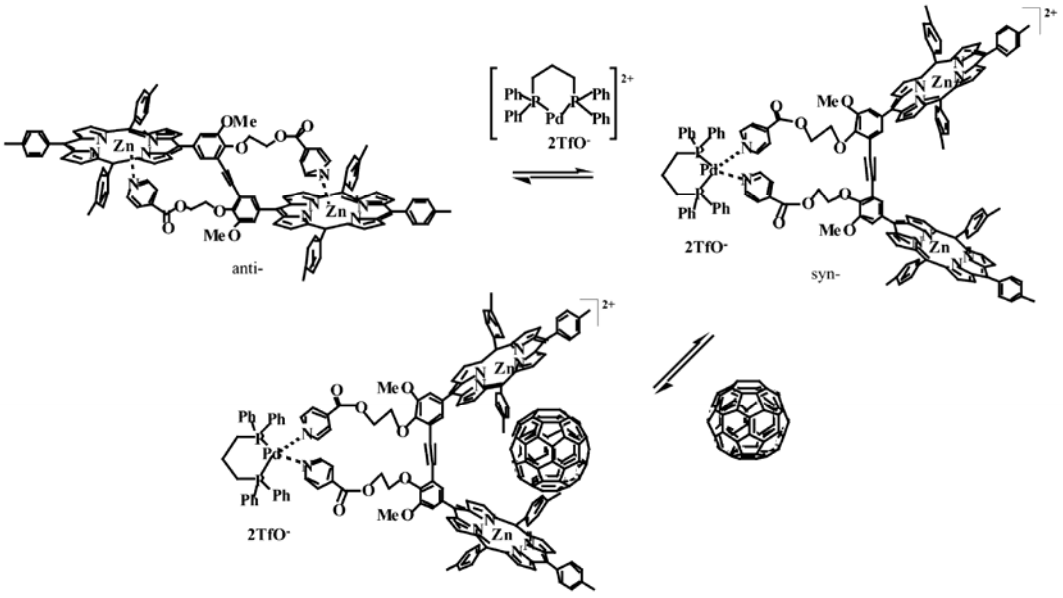

Figure 1.14 - Pd(II) effector changes pyridyl-zinc porphyrin dimer conformation from *anti*- to *syn*-, enabling the complexation of C_{60} [21].

Additionally, while examples in this review have so far focused on cooperativity from steric effects, cooperativity has been shown to arise from electronic effects [90, 91], by using the direction of charge transfer (CT) between the porphyrin host and guest (CT donor or acceptor). Although this is an excellent example of intelligent supramolecular design, the work in this thesis is related to cooperativity under steric control where the two binding sites are electronically isolated, and so [90] will not be reviewed in further detail here.

1.5 Project Rationale

All of the examples presented in the previous section are examples of cooperative systems where an effector at a remote binding site influences the complexation of a substrate at the second binding site. When simplified, each of these architectures can be described by the schematic in Figure 1.15, where receptors are linked through connectors with a rotational element to achieve cooperativity between two binding sites.

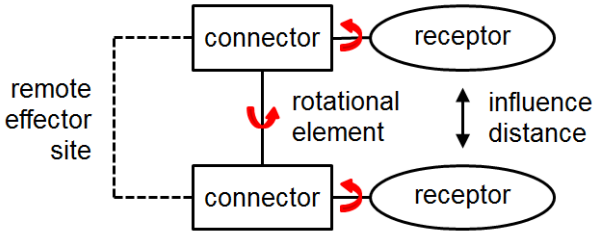

Figure 1.15 - Simplified schematic of cooperative systems in the literature; receptors and are linked through connectors with a rotational element, such that binding at a remote effector site influences the complexation at a second binding site.

Recent reports by Hunter and Anderson [92] and Ercolani [88] delineate cooperativity into three different subsets; allosteric, chelate [88, 92], and interannular [88]. In these reports, allosteric cooperativity is defined as the interplay of two or more *intermolecular* binding interactions [88], not involving *intramolecular* interactions. In explaining this distinction, [88] refers to the reversible oxygen uptake by haemoglobin. This example is widely recognised as a model of allosteric cooperativity [4]. Chelate cooperativity arises from one or more intramolecular binding interactions in cyclic and multicyclic assemblies, driven by the difference in strength between the intermolecular and intramolecular interactions and the chelate effect [88, 92]. Interannular cooperativity is distinct again, in that it arises from the interplay between two or more intramolecular binding interactions

[88]. Distinguishing between these three types of cooperativity enables improved quantitative assessment of cooperativity, as different types can be simultaneously at play within a system [88].

The work contained in this thesis draws on the design features of systems in the literature, selecting the strong intramolecular complexation offered by bis-metalloporphyrins and the excellent synthetic directional control and structural rigidity provided by bridged polycyclic scaffolds, to construct an interannularly cooperative architecture. This thesis contributes to further understanding cooperativity in supramolecular systems, which as exemplified in [88, 93], is not as simple to quantify as previously thought. The following chapter reveals the structure of the interannularly cooperative architecture, along with a detailed discussion of its molecular design.

2. Molecular Design

From the review of the literature in Chapter 1, the design of a cooperative system requires at least two remote binding sites, with the receptors linked by connectors in which a rotational element facilitates changes to the inter-receptor distance upon the binding of an effector. If the remote effector site is defined as homotropic to the second binding site, and the connectors are substituted for rigid rods, the schematic diagram for the system is given by the interannular tetravalent receptor in Figure 2.1 (adapted from [88]).

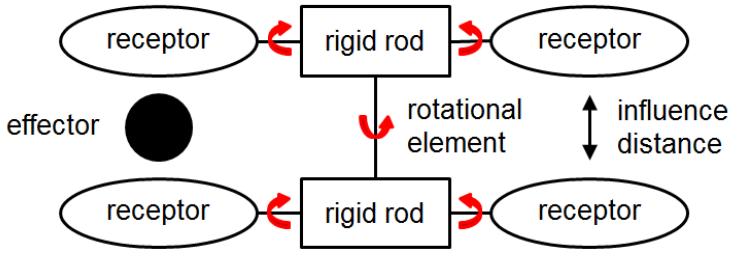

Figure 2.1 - Schematic representation of a tetravalent interannular system (adapted from [88]); receptors are linked via rigid scaffold, in which a rotational element facilitates adjustment of the inter-receptor distance on binding an effector.

This chapter provides an extended explanation of the design features on the interannular tetravalent receptor presented in Chapter 5, including the chemical composition of the linker scaffold, rotational elements, type of receptors, choice of connectivity between modular components, and the target guest substrates.

2.1 Guests and Receptors

The amino functional group is important in a diverse range of biologically relevant molecules [94], from amino acids and DNA bases, to illicit drugs such as amphetamines and pharmaceutical drugs [95]. On route to developing cooperative supramolecular systems to capture such molecules, this work focused on two simple diamino molecules, 1,4-diazabicyclo[2.2.2]octane **5** (DABCO) and 4,4'-bipyridyl **6** (4,4'-bipy, herein referred to as bipy unless otherwise specified) (Figure 2.2).

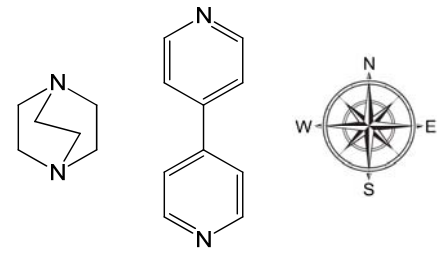

Figure 2.2 - Selected diamino guests; DABCO **5** and bipy **6**.

The diamino functionality for both DABCO and bipy is located at the north and south poles of these molecules. DABCO is an aliphatic and approximately spherical hydrocarbon, with a distance of 2.64 Å between nitrogen atoms (molecular model not shown, semi-empirical AM1), while bipy is aromatic, with a distance of 7.15 Å between nitrogen atoms (molecular model not shown, semi-empirical AM1).

Zinc (II) metalloporphyrins are ideal receptors for diamino ligands, as the metal center coordinates axially with nitrogen, generating sandwich complexes with large association constants [8, 30, 96]. Furthermore, the bis-porphyrin/DABCO/bipy system has been extensively studied by the research groups of Sanders, Hunter, and Anderson [27-31, 37, 52-54, 66, 97] (amongst others), and thus provides an excellent starting point to study new supramolecular architectures.

An advantage of the zinc (II) porphyrin receptor is that it is generally pentacoordinate, leaving only a single position for an axial ligand [98, 99]. This encourages the formation of intramolecular bis-porphyrin diamino ligand sandwich complexes when the inter-porphyrin distance is suited to the bidentate ligand. The inter-porphyrin distance for such complexes is 7.55 Å for DABCO and 11.63 Å for bipy (distance measured between zinc atoms, molecular model not shown, semi-empirical, AM1). These intramolecular sandwich complexes are characterised by enhanced association constants much larger than their mono-porphyrin counterparts [32, 34, 36].

Furthermore, the porphyrin zinc (II) metal centre is acid labile [48]. This could be employed as a stimuli-responsive mechanism for the release of guest in applications such as vehicles for targeted drug delivery and controlled release.

2.2 Linker Scaffold

Polycyclic frameworks, based on norbornyl derivatives, are highly synthetically variable using chemistry developed extensively by the research groups of Warrener and Butler [100-104] and Paddon-Row [68, 69, 105, 106]. The work of Warrener is particularly relevant to this thesis. Polycyclic frameworks provide several distinct advantages, namely providing good control of the direction of extension, including laterally and vertically. Additionally, the chemistry is very much modular, enabling the synthesis of supramolecular architectures with customisable dimensions. Molecular modelling by Warrener [107, 108] and Johnston [109] showed that certain modules result in linearity or curvature to the polycyclic scaffold. Importantly, a number of studies by several research groups has identified that polycyclic backbones are characterised by a higher degree of rigidity when only consisting of fused *bridged* polycyclic rings, with *non-bridged* cyclohexane(ene) rings and fused aromatic rings increasing flexibility [68-70, 110-115]. However, caution must be always be exercised, as small degrees of flexibility within rigid modular sections can be amplified across the complete scaffold [67].

In this project, polycyclic scaffolds are utilised in all host compounds to allow positioning of the porphyrin receptors. An updated schematic of the interannular tetra-porphyrin system is provided in Figure 2.3. The identity of the rotational element is assigned in the following section.

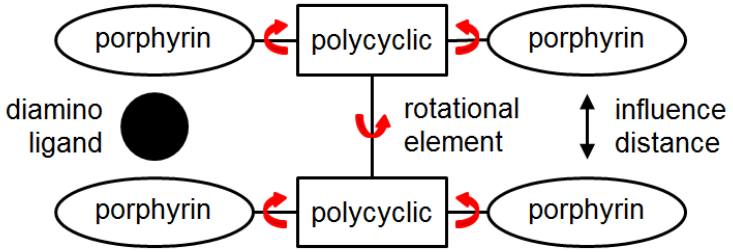

Figure 2.3 – Interannular tetra-porphyrin system; porphyrin receptors linked via a rigid polycyclic scaffold (rotational element currently unassigned).

2.3 Rotational Elements

It was envisaged that an unsubstituted central phenyl core would confer the rotational ability required by the polycyclic scaffold to facilitate cooperativity between the two remote binding sites. Literature precedent suggested phenyl rings can be appended to polycyclic modules by imide functionality [67, 105, 107, 116-118].

Fortunately, there is a substantial body of computational and experimental work exploring rotation in *N*-phenyl imide derivatives [119-135]. In summary, the energy barrier to rotation increases as the size of the *ortho*- R substituent on the phenyl ring increases (Figure 2.4) due to steric repulsion between the R group and the oxygen atom of the imide [119, 123, 124]. Additionally, the angle between the aryl and imide rings increases towards perpendicular with increasing size of the *ortho*- R substituent on the phenyl ring, to minimise steric repulsion between the R group and the oxygen atom of the imide [119-121, 123]. This competes with the resonance delocalisation and conjugation favoured in the planar conformation [136][3].

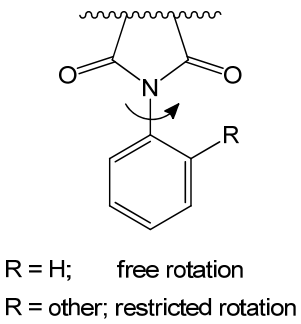

Figure 2.4 - The *N*-aryl angle increases towards perpendicular as the *ortho*- R group increases in size.

Free rotation is observed for unubsituted *N*-phenyl imide derivatives [125, 126], with rotation becoming restricted for *ortho*- substituents other than hydrogen [125-135], while *meta*- and *para*- phenyl substitution does not affect rotation in these systems [126]. Thus an unsubstituted phenyl diimide core was selected as the rotational element between the two polycyclic halves in the tetra-porphyrin system.

In addition, the porphyrin receptors could not be directly fused in a straightforward manner to the polycyclic scaffold without introducing semi-flexible linkages, and so again phenyl imide connectivity was opted for connecting porphyrin receptors to the polycyclic scaffold. Furthermore, rotation of porphyrins about unsubstituted *meso*-

[3] [136] refers to anilide derivatives rather than imides, however, the priciple of balacing steric and electronic factors is the same here.

phenyl rings with respect to the porphyrin β-pyrrole region is well known [137-139]. Thus the freely rotating porphyrin receptors provides the system with the ability to cofacially align the bis-porphyrins after undergoing defined changes to interporphyrin distance upon guest binding as the polycyclic scaffold is rotated through the central core. The final updated schematic of the interannular tetra-porphyrin system is provided in Figure 2.5.

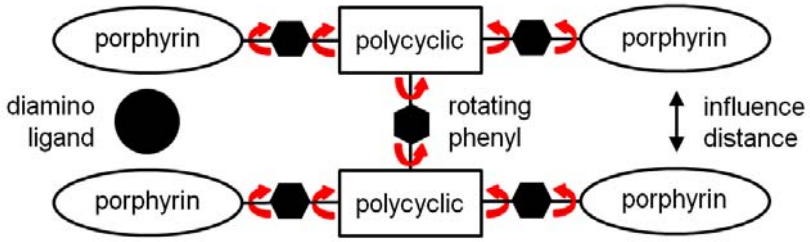

Figure 2.5 - Interannularly cooperative tetra-porphyrin system; porphyrin receptors linked via a rigid polycyclic scaffold with phenyl imide rotational elements.

While it is known that supramolecular effective molarity[4] (EM) is reduced by the introduction of rotors or torsional degrees of freedom [140, 141], the rotating phenyl diimide core in the tetra-porphyrin tweezer is fundamental in achieving interannular cooperativity between the two binding sites, while the rotating porphyrin receptors allow for further cavity adjustment as required by the guest.

2.4 Tetra-porphyrin Tweezer

Considering each of these design features and previous literature reports, the chemical structure and space filling model of the tetra-porphyrin tweezer **4** is shown in Figure 2.6. The molecule is shown in an idealised geometry, where the polycyclic scaffold has been set to parallel about the phenyl diimide core (green). The architecture has four porphyrin receptors (blue), which are arranged in cofacial pairs using the natural curvature of the rigid I-shaped oxa-bridged polycyclic backbone (red and black), giving two remote bis-porphyrin binding sites located on opposite sides of the tweezer. The retrosynthesis of this compound is elaborated on in Chapter 5, considering each colour-coded modular component in Figure 2.6 and their connectivity.

[4] EM is a measure of the stabilisation resulting from the chelate effect for related intermolecular and intramolecular interactions [30, 52, 58], and allows host-guest complementarity to be quantified [53].

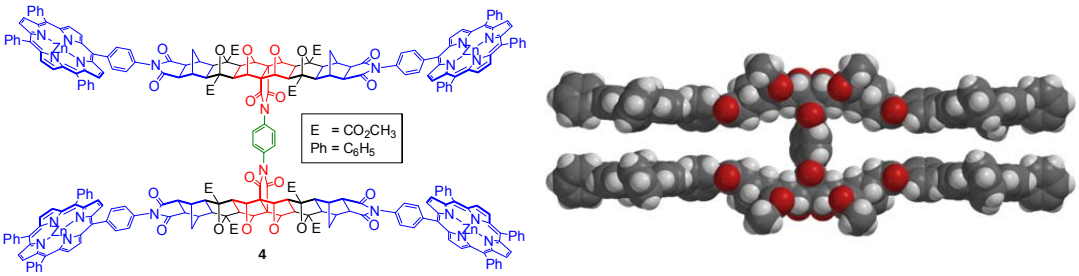

Figure 2.6 - Chemical structure of the tetra-porphyrin **4** system and space filling model, both in an idealised geometry.

It was predicted that the two binding sites should not behave independently, rather that the binding of the first guest would enhance the binding of the second guest via transfer of the required interporphyrin distance through free rotation of the rigid polycyclic scaffold. Thus the system was predicted to be positively interannularly cooperative.

In order to understand the implications of rotation on host-guest behaviour, several model single binding site systems needed to be explored, and are discussed in the following section.

2.5 Model Single Binding Site Tweezers

The model single binding site tweezer **1** is shown in Figure 2.7 and maintains similar structural connectivity and features to the tetra-porphyrin system **4** (half of the structure pertaining to the second binding site has been removed). Again the phenyl diimide core is expected to undergo free rotation (discussed in chapters 3 and 5), which in this case would result in interconverting *syn*- and *anti*- configurations.

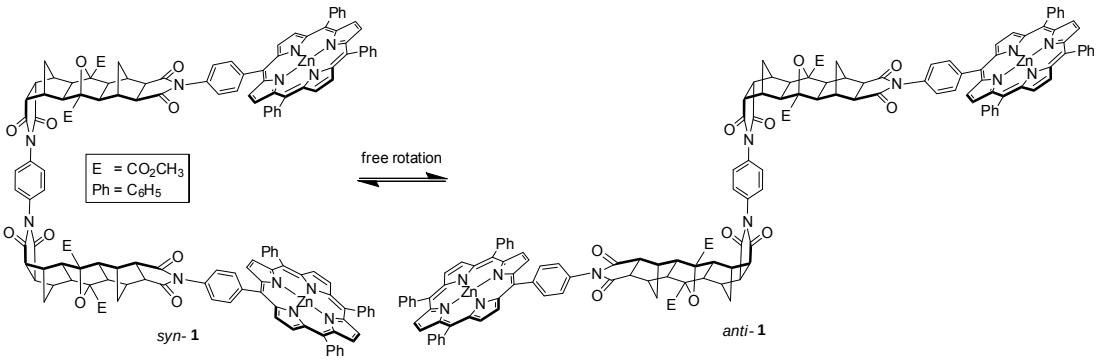

Figure 2.7 - Model single binding site system **1** with interconverting *syn*- and *anti*- conformations via free rotation of the phenyl diimide core.

The *syn*- conformation would be expected to be the most effective intramolecular receptor. The *anti*- conformation detracts from the preorganisation of the system, and

a second model system was designed to constrain the system to the *syn*-conformation. It was speculated that core rotation could be restricted by introducing sterically bulky group to the phenyl diimide core. A literature search indeed showed precedent for this, and is discussed in chapter 4.

A second generation single binding site tweezer with a 2,3,5,6-tetramethylphenyl diimide core was synthesised, and indeed this rotation was found to be sufficiently restricted to allow the isolation of separate *syn*- **2** and *anti*- **3** conformations (Figure 2.8) (non-interconvertible at 95 °C under microwave irradiation). This second generation system, which differs from the first generation system only by the linker core, provides the opportunity to study the complexation of the *syn*- conformation in the absence of the *anti*- conformation.

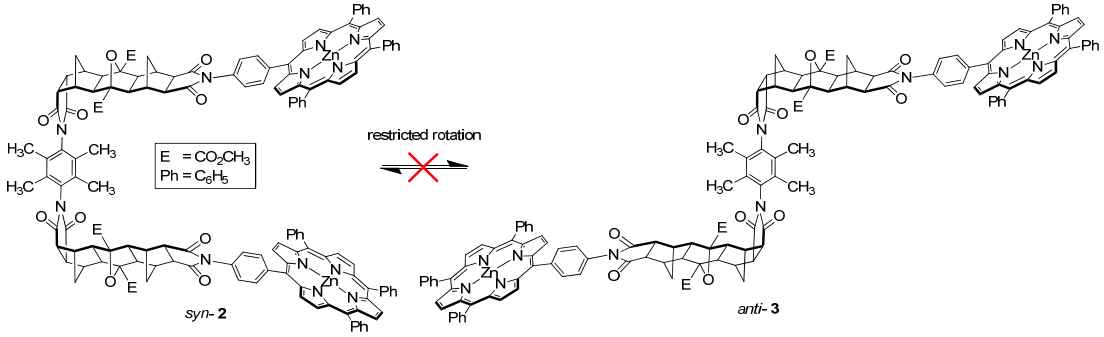

Figure 2.8 - Model single binding site system with restricted rotation; non-interconverting *syn*- **2** and *anti*- **3** conformations due to a sterically bulky 2,3,5,6-tetramethylphenyl diimide core

The synthesis and host-guest behaviour of each of the three generations of tweezer; freely rotating **1**, restricted rotation *syn*- **2** and *anti*- **3**, and tetra-porphyrin **4**; are examined in the following three chapters.

3. Freely Rotating Tweezer

3.1 Declaration

A substantial quantity of this chapter concerning the freely rotating tweezer and its complexation with DABCO has been published [1], and as such these sections of the chapter appear in a similar format and wording to the publication. Curve fitting software was operated by Dr Duc-Truc Pham (Postdoctoral Fellow, The University of Adelaide) to calculate association constants and speciation for different binding models suspected by Rhys Murphy.

Unpublished work includes all data concerning complexation with bipy, and any reference to potential gelation and non-Mitsudo reactivity of particular substrates, and related appendices.

3.2 Introduction and Synthetic Approach

In light of dicussions in Chapters 1 and 2, the molecular tweezer shown in Figure 3.1 was elected as a starting point to understand the behaviour of the architecture, both as the free host and in the presence of guest, before progressing to more complex architectures. Retrosynthesis of this tweezer **1** reveals several basic components; the well known *endo*- **7** [142] and *exo*- **8** [143] Diels-Alder adducts of maleic anhydride and cyclopentadiene (red), *p*-phenylenediamine **9** (green), and amino-tetraphenylporphyrin **10** [144] (blue).

In contrast to other polycyclic porphyrin tweezers reported in the literature, this design opts only for fused bridged polycyclic connecting modules of bicyclo[2.2.1]heptane and 7-oxabicyclo[2.2.1]heptane (fused sequences of norbornane and 7-oxanorbornane), and avoids the incorportation of non-bridged cyclohexane(ene) and fused aromatic linkages. The selected linkages are reported to be characterised by a higher degree of rigidity than their semi-flexible counterparts [68, 70, 110-114].

The most intriguing element of the molecular tweezer design is that the selected linkages allow rotational degrees of freedom about single bonds; about the phenyl diimide core (dotted box, Figure 3.1) to afford *syn*- and *anti*- conformations, and about the porphyrin receptors. These rotations play a key role in mediating host-guest

behaviour (see later in this chapter) by allowing changes to the interporphyrin distance as required for different length guests.

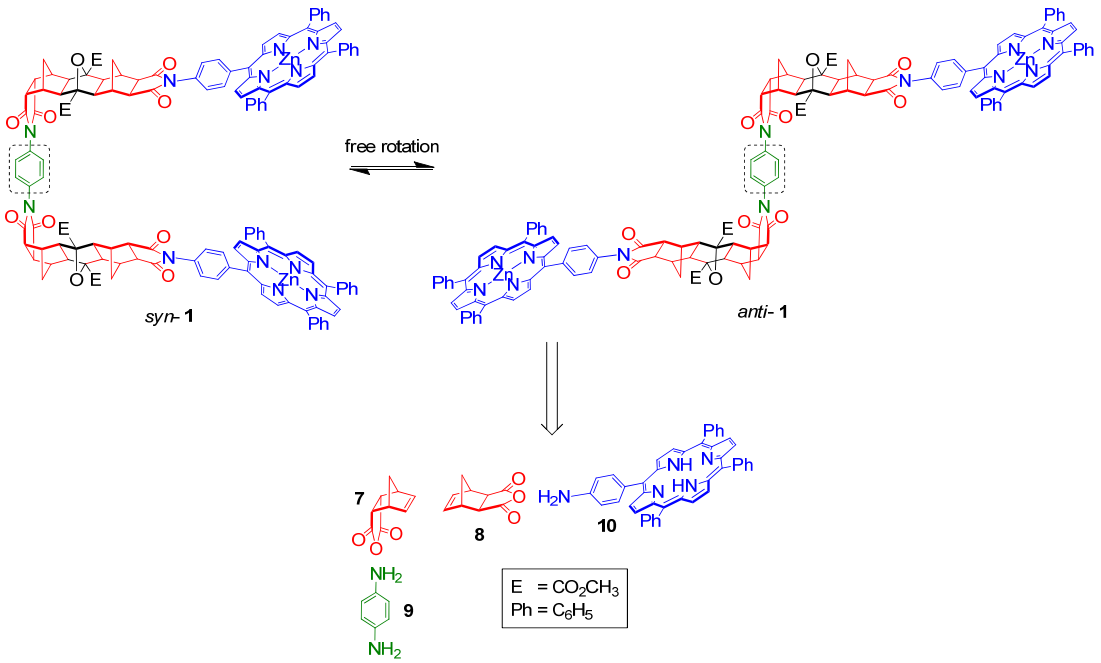

Figure 3.1 - The freely rotating single binding site tweezer **1** (*syn*- and *anti*- conformations) and its retrosynthesis.

3.3 Molecular Modelling

Molecular modelling (Spartan '10, Wavefunction, Inc. [145]) was undertaken to provide information on the equilibrium geometry of tweezer **1** in the absence of guest (semi-empirical, AM1), and is shown in Figure 3.2. Although it would be unwise to assume much structural detail from a semi-empirical level of computational theory, the model shows that the two norbornyl arms of the tweezer can rotate about the central phenyl diimide group, along with the porphyrins about their *meso*-phenyl/phenyl imide connectivity. Thus it is expected that intramolecular complexation of a guest would involve rotation in both of these regions to position the porphyrin units cofacially.

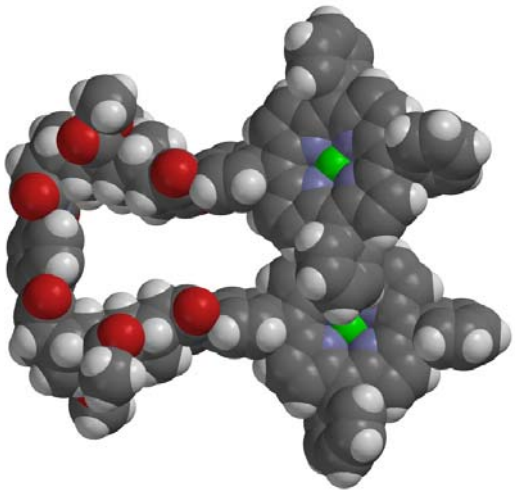

Figure 3.2 - Molecular modelling of the freely rotating tweezer **1** in the absence of guest (semi-empirical, AM1).

3.3.1 Simulating Rotation about the Phenyl Diimide Core

To provide an estimation of whether rotation between the *syn*- and *anti*-conformations could occur at room temperature, a rotational energy profile (Figure 3.3) was calculated to simulate the barrier to rotation about the *N*-aryl bond in the phenyl diimide core (N_2-C_3) using a structurally reduced model **11** to reduce computation time. This was calculated [145], using a Hartree-Fock 6-31G* model for each conformation about the bond specified by the dihedral angle constraint (C_1-N_2-C_3-C_4), with the energy of each conformation (0 to 90 °) recalculated using a B3LYP/6-31G* Density Functional model to improve the fitting function. The model compound for this calculation does not account for π-π interactions between the opposing bis-porphyrins in the *syn*- conformation, changes to bond properties and electronic effects of the second *para*- imide in the linker, or additional steric crowding on the underside of the polycyclic scaffold when additional polycycles are fused to the linker. The angle of rotation at which the energy is the lowest is a competition between relieving steric crowding by rotating away from planar, with the resonance delocalisation and conjugation favoured by the planar conformation [136][5].

[5] [136] refers to anilide derivatives rather than imides, however, the priciple of balancing steric and electronic factors is the same here.

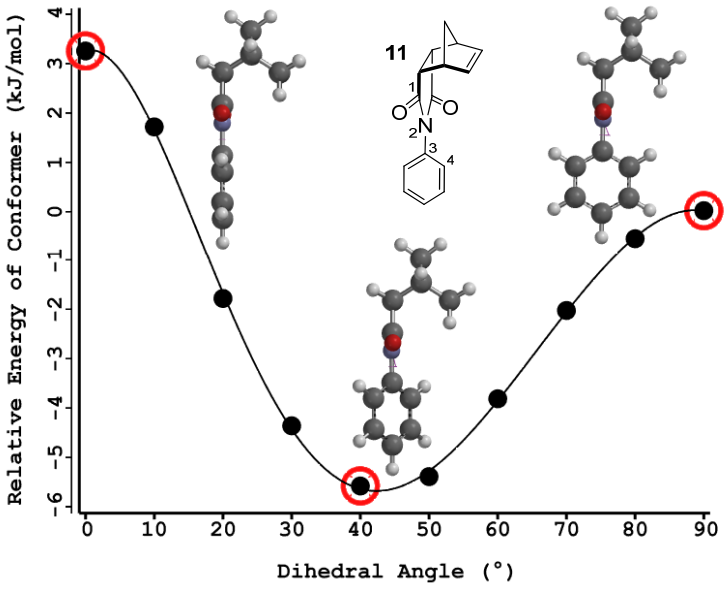

Figure 3.3 - Rotational energy profile and barrier to rotation about the imide-phenyl single bond in the linker (energy profile Hartree-Fock 6-31G*, energy of each conformation recalculated using Density Functional B3LYP/6-31G*).

The relative energy difference between the global maximum and global minimum is approximately 9 $kJmol^{-1}$ (2.15 $kcalmol^{-1}$). Not surprisingly, the highest energy conformer occurs at a dihedral angle of 0 °, when the phenyl ring and imide carbonyl oxygen atoms are planar and interact sterically. The lowest energy conformation occurs at a dihedral angle of approximately 45 °, while a local maximum occurs at 90 °. This calculated barrier suggests that the rotational process is able to occur at room temperature, from thermal energy available from the surroundings [124], and could result in interconversion between the *syn*- and *anti*- conformations, or simply rotation of the phenyl ring while the conformation remains static.

This compares similarly to a literature report for a structurally similar *N*-phenylmaleimide, where the barrier to rotation was calculated to be 12.6 $kJmol^{-1}$ (3 $kcalmol^{-1}$) [124]. In addition, free rotation has been observed in experimental NMR studies on *ortho*- methylphenyl substituted imide derivatives [125, 126].

3.4 Synthesis

The synthesis involved a series of reactions to derivatise the retrosynthetic components shown in Figure 3.1, affording the linker and receptor modules. The coupling between linker and receptor was achieved using chemistry previously developed specifically for fusing polycyclic scaffolds [102, 104].

3.4.1 Freely Rotating Linker

The corner in the linker was established using the *endo*- Diels-Alder anhydride **7** [142] (Figure 3.4). This was appended with a methyl ester substituted cyclobutene ring to afford **12** by the Mitsudo reaction [146, 147], a [2+2] ruthenium-catalysed [148] cycloaddition with dimethyl aceteylenedicaboxylate (DMAD) [149, 150], in good yield with pure product. Compound **12** has previously been reported using a similar procedure [151, 152]. Although the characterisation data was a good match with the literature, [151] reports poor yields, while [152] reports good yields but with impure product.

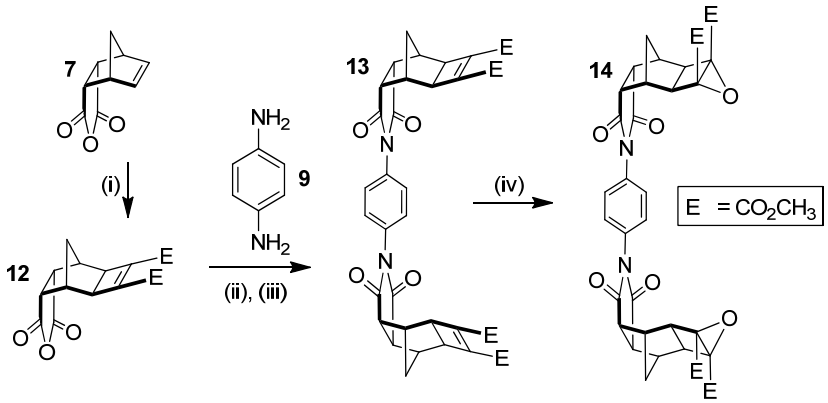

Figure 3.4 - Synthesis of the Linker. (i) 2 eq. DMAD, 5 mol-% $[RuH_2(CO)(PPh_3)_3]$, toluene, 100 °C, 3 days, 77%; (ii) 0.5 eq. *p*-phenylenediamine **9**, Ar deoxygenated, dry DMF, 80 °C, 3 days; (iii) $NaOAc/Ac_2O$, 80 °C, 3 days, 25%; (iv) anhydrous 3.3 M *t*BuOOH in toluene (2.5 eq.), dry CH_2Cl_2, 0 °C, 10 min, *t*BuOK (1 eq.), r.t., 3.5 hrs, 28%.

Synthesis of the linker **13** involved the condensation of two equivalents of *endo*-Mitsudo anhydride **12** with one equivalent of *p*-phenylenediamine **9** (Figure 3.4). This proceeds in two steps; formation of the amic acid, followed by ring closing to the imide. In the ^1H NMR spectrum, the singlet resonance at 7.39 ppm was assigned to the phenyl protons, and not only provided evidence of product formation, but that linker rotation is fast on the NMR timescale. This is in line with other NMR studies reported in the literature for unsubstituted *N*-phenyl imide derivatives [125, 126].

Interestingly, recrystallisation of the linker from chloroform/hexane resulted in the formation of a suspension, which partially resembled a gel. This is discussed in further detail in Chapter 7, Future Directions.

Linker **13** was subsequently epoxidised to afford bis-epoxide **14** (Figure 3.4) via a nucleophilic epoxidation [102, 104] using anhydrous *tert*-butylhydroperoxide in

toluene [153]/potassium *tert*-butoxide, commonly employed for similar norbornene derivatives with electron-deficient methyl ester-substituted alkenes.

3.4.2 Associated Freely Rotating Substrates

Further to the freely rotating *endo*- Mitsudo linker **13**, several additional analogues were synthesised (Figure 3.5). Synthetic detail is provided in Chapter 8. The *endo*-non-Mitsudo linker **15** (Figure 3.5 (a)) was thought to be an alternative pathway to the synthesis of linker **13**, however, poor reactivity of this substrate under standard Mitsudo conditions [146, 147] was encountered which prevented **13** from being obtained. This is the basis of discussions in Appendix 3. The *exo*- non-Mitsudo **16**[6] and *exo*- Mitsudo **17** linker analogues (Figure 3.5 (b) and (c) respectively) supplement the investigation of Mitsudo reactivity in Appendix 3.

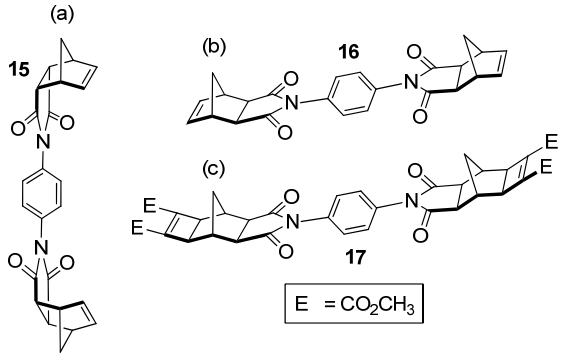

Figure 3.5 - Additional freely rotating *endo*- and *exo*- linker analogues, **15**-**17**.

3.4.3 Porphyrin Receptor (for tweezer synthesis)

To achieve the geometry required for cofacial porphyrin alignment with the *endo*-linker, *exo*- porphyrin receptor **18** [157] was required. This was obtained via condensation of amino-tetraphenylporphyrin **10** [144] with *exo*- Diels-Alder anhydride **8** [143] (Figure 3.6) using method similar to the analogous *endo*-porphyrin receptor reported in [73, 157]. The UV-Vis and ^{1}H NMR appear typical of other single quadrant *para*- functionalised *meso*-phenyl porphyrins in the literature [73, 144, 158]. The ^{1}H NMR shows splitting of the β-pyrrole and *meso*-phenyl resonances as expected for this asymmetry, along with additional resonances for the appended norbornene.

[6] Compound **16** has been previously synthesised using a different method [154-156].

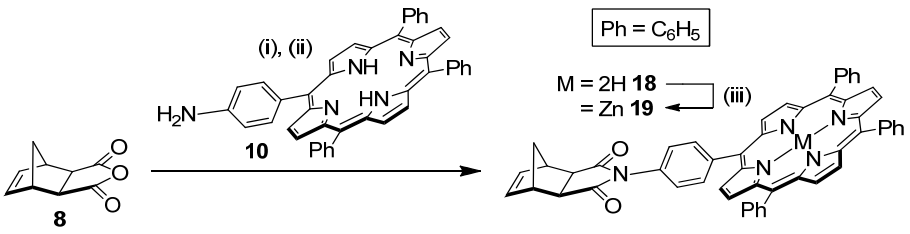

Figure 3.6 - Synthesis of the *exo*- porphyrin receptor. (i) amino-tetraphenylporphyrin **10**, $CHCl_3$, reflux, overnight, Ar deoxygenated; (ii) $NaOAc/Ac_2O$, 80 °C, overnight, 72%; (iii) $Zn(OAc)_2/MeOH/CHCl_3$, reflux, 1 hr.

Interestingly, zinc(II) metallation of the *exo*- porphyrin receptor **18** under standard conditions [159] to give **19** resulted in poor solubility in chloroform. This has also been observed for the *endo*- zinc(II) porphyrin receptor analogue (not shown) [78]. For host-guest studies of mono-porphyrin receptor with ligand, a modified receptor soluble in chloroform was synthesised (compound **22**).

3.4.4 Modified Porphyrin Receptor (soluble for titrations)

Prior to studying the host-guest chemistry of the bis-porphyrin tweezer, the reference microscopic binding constant for a mono-porphyrin receptor with guest was required. A soluble structural analogue of the zinc(II) *exo*- porphyrin receptor **19** was required for the host-guest study, and this was achieved by simple substitution of the *exo*-Diels-Alder anhydride **8** from Figure 3.6 with the Mitsudo variant **20** (Figure 3.7). The Mitsudo *exo*- Diels-Alder anhydride **20** has been previously reported [151, 152] using similar methods, however there is conflicting characterisation data. The ^1H and ^{13}C NMR spectra are an excellent match to that reported in [152], but different to that reported in [151] (although the HRMS of [151] does reflect the molecular mass of the expected product). The melting points reported by [151] (178-184 °C) and [152] (173 °C) are different to each other, and both different again to that found in this work. Although low yields are reported in [151] (14 %), a decent yield was obtained in the work in this thesis and in [152].

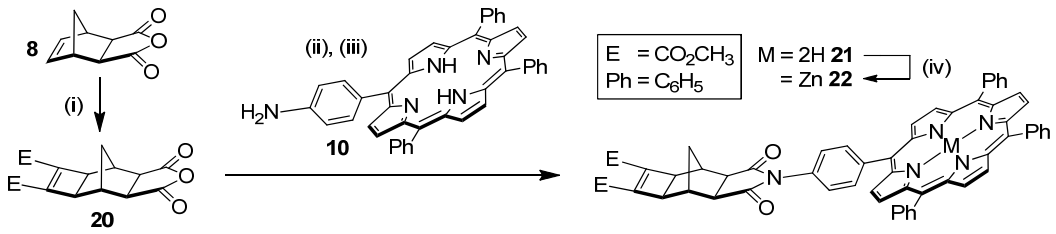

Figure 3.7 - Synthesis of a soluble zinc(II) mono-porphyrin for titration with monodentate ligand. (i) 2 eq. DMAD, 5 mol-% [$RuH_2(CO)(PPh_3)_3$], toluene, 100 °C, 3 days, 67%; (ii) $CHCl_3$, reflux, overnight, Ar deoxygenated; (iii) $NaOAc/Ac_2O$, 80 °C, overnight, 84%; (iv) $Zn(OAc)_2/MeOH/CHCl_3$, reflux, 30 min, 95%.

The remainder of the synthesis in Figure 3.7 remained unchanged to the synthesis used in Figure 3.6 (condensation with amino-tetraphenylporphyrin **10** [144] and zinc(II) metallation [159]). The ^1H NMR spectrum of modified *exo*- zinc(II) porphyrin receptor **22** was observed to be considerably concentration dependent in $CDCl_3$ (dilution from 5 mM to highly dilute, Figure 3.8). Interestingly, large downfield shifts of 0.1-0.25 ppm are experienced for all the polycyclic resonances, accompanied by shifts of 0.05-0.2 ppm for the two *para*- substituted *meso*-phenyl porphyrin resonances. However, unusually, the remaining porphyrin signals (β-pyrrole, unsubstituted *meso*-phenyl) and the ester signal only undergo very small shifts (0.01 ppm). The β-pyrrole porphyrin resonance undergoes changes to its splitting.

The concentration dependence indicates significant intermolecular aggregation of **22**, and two possible orientations are outlined in Figure 3.9. The scenario in Figure 3.9 (b) is unlikely, as two interacting porphyrin ring currents would be expected to result in major shifts for all porphyrin resonances. However, while the head-to-tail scenario in Figure 3.9 (b) would explain the shifts in the polycyclic resonances without significant changes to the porphyrin resonances, it does not account for the very small shift observed for the ester resonance, which in this representation is highly exposed to the porphyrin ring current. Further investigation is necessary to better understand the concentration dependence observed in the ^1H NMR for this compound.

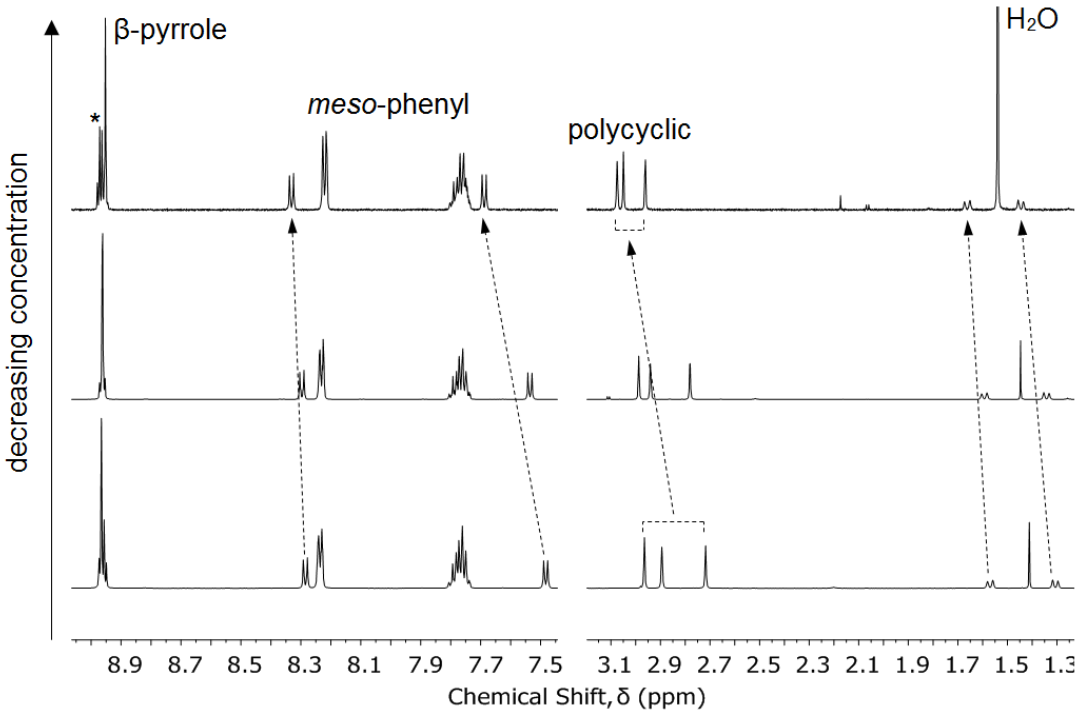

Figure 3.8 - Selected ^{1}H NMR spectral regions showing the concentration dependence of Zn porphyrin receptor **22**, diluted from 5 mM (bottom) to highly dilute (top). The main resonance shifts are annotated by dotted arrows. * indicates changes to splitting of the β-pyrrole porphyrin resonance.

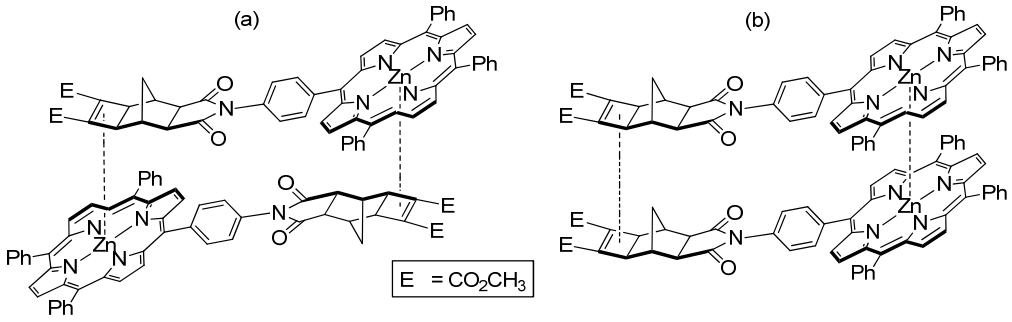

Figure 3.9 - Two possible orientations of the intermolecular aggregate of the modified porphyrin receptor **22**.

3.4.5 Freely Rotating Tweezer

The bis-epoxide **14** was subsequently appended with *exo*-porphyrin receptors **18** via the alkene plus cyclobutane epoxide (ACE) reaction (Figure 3.10). This generates *exo*-fused bridged polycyclic backbones via thermal ring opening of the epoxide to a 1,3-dipole, followed by 1,3-dipolar [3+2] cycloaddition with a norbornene dipolarophile [102, 104]. Conventionally, this reaction takes place in a sealed tube under medium to forcing reaction conditions, at temperatures as high as 170 °C [73] for as long as 90 hrs [67]. However, with the recent development of microwave accelerated ACE reactions [160], reaction times are reported to be much shorter (10

to 60 minutes) with little degradation. The microwave accelerated ACE reaction was found to lend itself to our substrates, giving the freebase freely rotating tweezer **23** in 38 % yield.

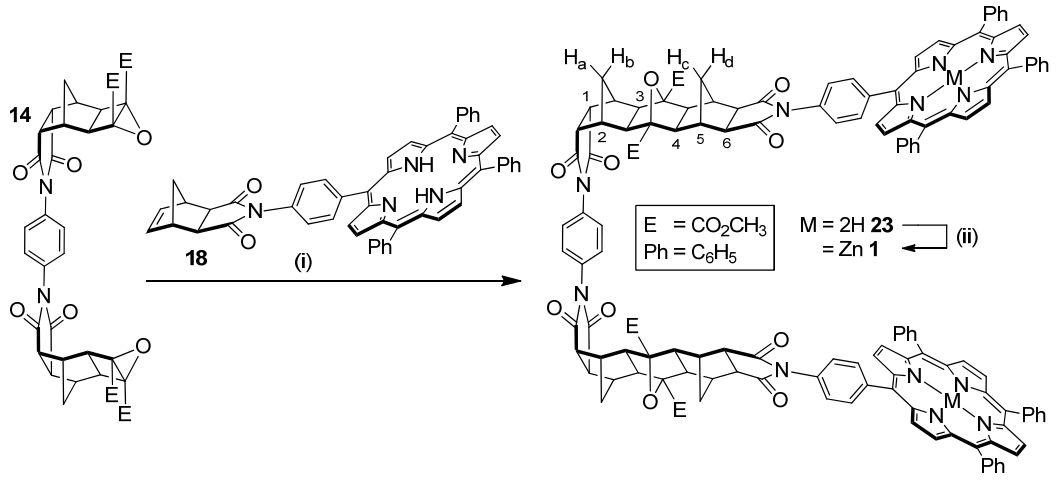

Figure 3.10 - Synthesis of the Freely Rotating Tweezer. (i) dry THF, microwave 80-220 W, 14-20 bar, 180 °C, 2 hrs, 38%; (ii) $Zn(OAc)_2$/MeOH/$CHCl_3$, reflux, 30 min, 95%.

The free base tweezer **23** was identified by several features in the NMR spectra characteristic of ACE reactions. The resonance at 90 ppm in the ^{13}C NMR spectrum is observed in similar polycyclic systems [113] and is assigned to the carbon atoms to which the oxygen bridgeheads are attached in the newly formed methyl ester substituted 7-oxanorbornane [113]. In the ^{1}H NMR spectrum, a small downfield shift was observed for the methyl ester resonance compared to the epoxide [160], along with the disappearance of the norbornene proton resonance from *exo*- porphyrin receptor at 6.45 ppm. Relative integrations correspond with the coupling of two porphyrin receptors to the polycyclic linker.

Within the aromatic region of the ^{1}H NMR spectrum of the tweezer **23** (Figure 3.11), there is some evidence of splitting within the *meso*-phenyl resonances, indicating facial differentiation and interaction between porphyrins at NMR concentrations (millimolar). In considering whether this interaction was intramolecular or the result of intermolecular aggregation, a dilution experiment was undertaken for the zinc(II) tweezer (see later). The singlet resonance at 7.60 ppm was assigned to the phenyl core protons, and provided experimental evidence that phenyl core rotation is rapid on the NMR timescale. Taken together, this could indicate that the phenyl core rotates while the linker arms remain in the s*yn*- conformation. Accurate mass spectrometry further confirmed the identity of the tweezer, $[M+H]^+$ found: 2267.7854, calculated: 2267.7813.

Furthermore, ten polycyclic resonances can be observed as expected (excluding the methyl ester); six singlets and four doublets (Figure 3.11). The doublets arise from two pairs of non-equivalent methylene bridge protons H_a/H_b and H_c/H_d (Figure 3.10). These appear at significantly different chemical shifts, characteristic of steric compression by oxygen in these systems [151], and confirms the formation of a linear ACE product [151]. These resonances occur at chemical shifts of 1.38/2.75 ppm and 1.22/2.55 ppm, however the absence of nOe signals prevented their exact assignment as either H_a/H_b or H_c/H_d. The remaining six singlets correspond with the number of remaining unique proton chemical environments protons along the polycyclic scaffold (1-6, Figure 3.10). The ^{1}H COSY spectrum reveals two separate spin systems for the *endo*- and *exo*- components (1-3 and 4-6 respectively, Figure 3.10) of the polycyclic backbone.

Zinc(II) metallation of **23** under standard conditions [159] afforded freely rotating tweezer **1**. This was characterised by loss of the porphyrin inner pyrrole proton resonance at -2.81 ppm, and further confirmed by accurate mass spectrometry, $[M+H]^+$ found: 2391.6044, calculated: 2391.6094. Again, there is some evidence of splitting within the *meso*-phenyl resonances within the aromatic region of the ^{1}H NMR spectrum of the tweezer, indicating facial differentiation and interaction between porphyrins at NMR concentrations (millimolar). A dilution experiment was undertaken from 18.8 mM to 2.37 mM with only small resonance shifts observed (0.1 ppm). This suggests the porphyrin interaction is intramolecular, and that the system is not significantly intermolecularly aggregated (unless the system remains aggregated at 2.37 mM). The singlet resonance remains at 7.60 ppm for the phenyl core protons. Again, these results could indicate that the porphyrin arms are in the *syn*- conformation, but the phenyl core is undergoing isolated rapid rotation on the NMR timescale about the vertical linker axis.

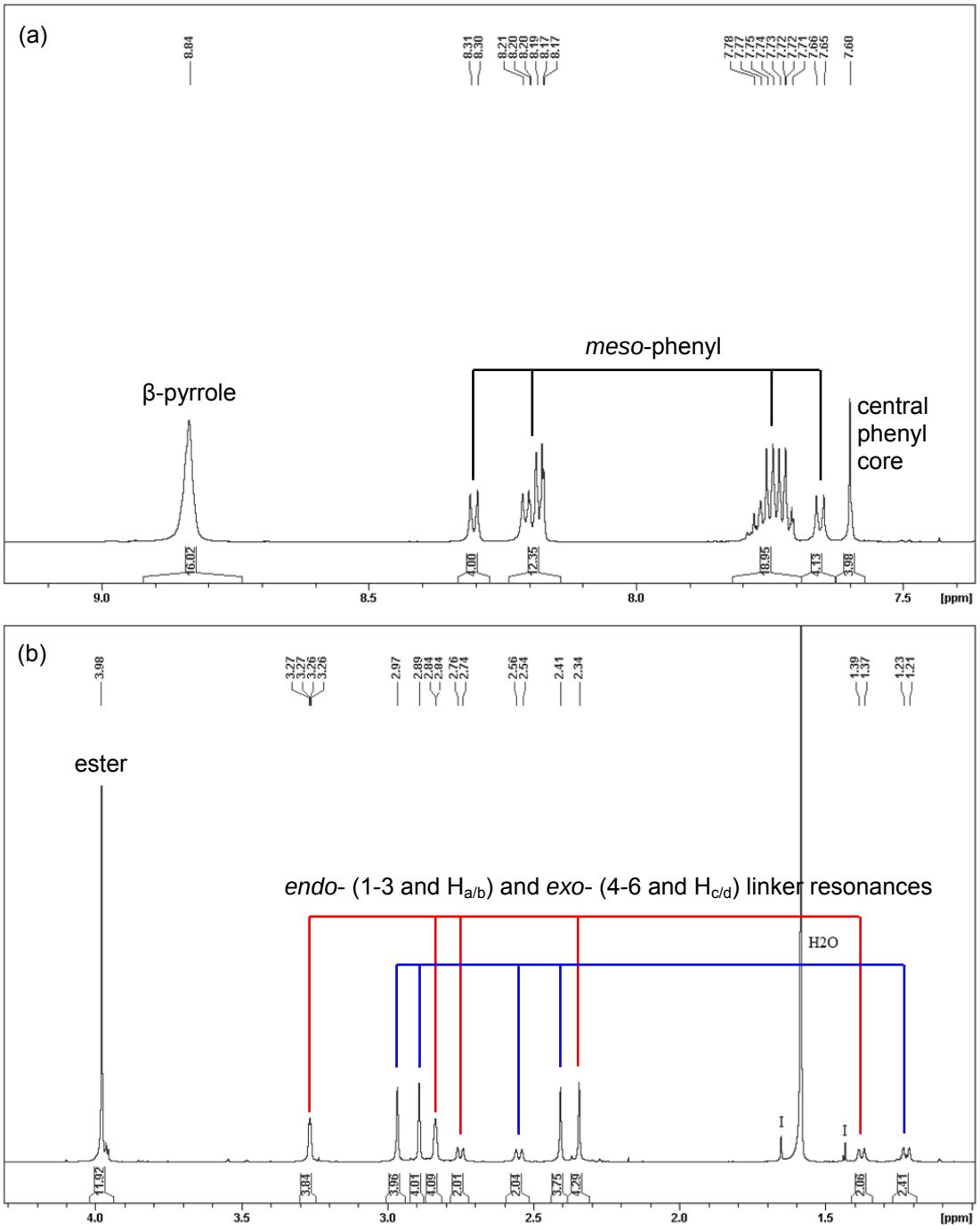

Figure 3.11 - Selected ^{1}H NMR spectral regions of the freebase freely rotating tweezer **23** showing (a) porphyrin β-pyrrole and *meso*-phenyl resonances, (b) polycyclic linker resonances. ^{1}H COSY cross peaks allowed two spin systems to be identified (red and blue) for the *endo*- (1-3 and $H_{a/b}$ [Figure 3.10]) and *exo*- (4-6 and $H_{c/d}$ [Figure 3.10]) linker regions, but not distinguished. I denotes impurity.

The geometry of the freely rotating host **1** was further probed by variable temperature experiments in both $CDCl_3$ and CD_2Cl_2. In $CDCl_3$, there are only minor (< 0.05 ppm) shifts in the spectrum at -40 °C compared to room temperature. In CD_2Cl_2 at +20 °C, splitting of the porphyrin resonances is greater than in $CDCl_3$, indicating increased porphyrin interactions (either intramolecular or intermolecular aggregation) in this solvent compared to $CDCl_3$. Although cooling the sample to -80 °C in CD_2Cl_2 resulted in broadening of the entire spectrum (this could be related to poor shimming at these temperatures[7]), small signal shifts are observed (0.05-0.1 ppm, but a polycyclic signal shifts by 0.2 ppm), and the porphyrin resonances are less split, indicating reduced porphyrin interactions at these temperatures in CD_2Cl_2.

In the UV-Vis spectra, no significant shift in the Soret band was observed from **23** to **1** (the number of Q bands changes due to symmetry factors [47, 58]). Dilution of a chloroform solution of the zinc(II) freely rotating tweezer **1** (10^{-5} to 10^{-7} M) resulted in only minor changes to the peak width, indicating that there was no significant intermolecular aggregation of the tweezer at these concentrations. In fact, the UV-Vis spectra of the Zn(II) freely rotating tweezer **1** and Zn(II) mono-porphyrin receptor **22** display very similar Soret maxima at 419 nm, with peak band widths at half height of 11 and 10 nm respectively. This slight broadening in the freely rotating tweezer could indicate weak exciton coupling interactions between the porphyrins in **1**, although no blue shift of the Soret maxima is observed [37, 58, 73, 85, 161-164]. The weakness of the exciton coupling, if at all, suggests that either the porphyrin units in **1** are able to undergo rotation either about the single bond between the imide and porphyrin moiety, and/or the two porphyrin arms can undergo rotation about the phenyl diimide core. A summary of the UV-Vis data is provided in Table 3.1.

Table 3.1 - Summary of UV-Vis data in chloroform.

Species	**Zn(II) mono-porphyrin, 22**	**Zn(II) freely rotating tweezer, 1**
λ_{max} (nm)	419.3	419.5
Width (nm) [a]	9.9	11
$\varepsilon_{singleporphyrin}$ ($Lmol^{-1}cm^{-1}$) [b]	6.47×10^5	$4.7\text{-}6.9 \times 10^5$ [b]

[a] Peak band width measured at half height.

[b] Quoted as a range to account for possible errors in concentration. $\varepsilon_{singleporphyrin} = \varepsilon_{experimental}/2$ (tweezer has two porphyrins).

[7] Sample was not manually shimmed, shim file was for room temperature.

Prior to host-guest analysis of the freely rotating tweezer **1**, the complexation of mono-porphyrin receptor **22** with monodentate ligands was studied. These association constants are important because they provide the reference intermolecular interaction required to assess interannular cooperativity [88] in Chapter 5.

3.5 Mono-Porphyrin Receptor Host-Guest Study

The complexation of tetraphenylporphyrin and other mono-porphyrins with monodentate ligand 1-azabicyclo[2.2.2]octane (quinuclidine) **24** and bidentate ligand DABCO **5** has been extensively studied by others using UV-Vis and NMR spectroscopy [27-31, 52, 66]. In summary of this work, at micromolar (UV-Vis) concentrations, only the 1:1 mono-porphyrin:DABCO complex is observed, while at millimolar (NMR) concentrations, the 2:1 $(\text{mono-porphyrin})_2$:DABCO sandwich complex is observed up to 0.5 eq. DABCO, opening up to form the 1:1 complex with excess DABCO. This is represented by the equilibria in Figure 3.12. For monodentate ligands such as quinuclidine **24** [28], the equilibrium is between free mono-porphyrin and open 1:1 complex (K_{11} = [mono-porphyrin:ligand]/([mono-porphyrin][ligand]), as outlined by the dotted box in Figure 3.12.

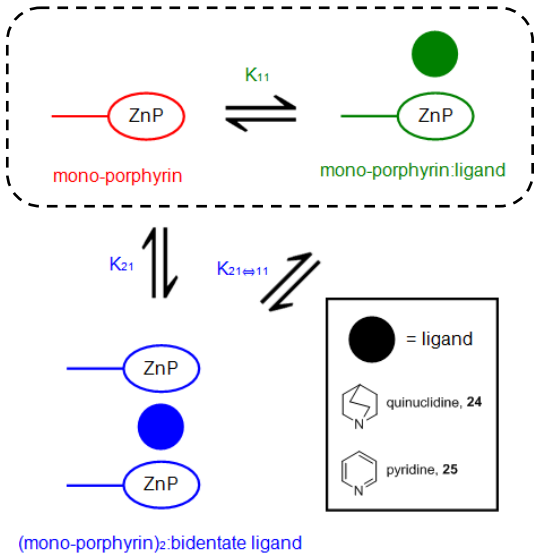

Figure 3.12 - Schematic representation of the various equilibria between mono-porphyrin receptor **22** and ligand (represented by circles). Monodentate ligands operate only in the section marked by the dotted line. Colour coded with red for free host, blue for intramolecular sandwich complex, and green for simple open 1:1 porphyrin:ligand complex.

While the association constant for mono-porphyrin:quinuclidine **22**:**24** was measured in this thesis (and is shown next), unfortunately this was not undertaken for mono-porphyrin:pyridine **22**:**25**. The association constant for pyridine with other mono-

porphyrins in the literature is reported to be of the order of 10^3 M^{-1} [27, 53, 55, 58, 78, 97, 98, 165]. This value has been employed to estimate[8] the association constant for mono-porphyrin:pyridine **22**:**25**.

3.5.1 Mono-Porphyrin Receptor with Quinuclidine (UV-Vis)

Figure 3.13 depicts the complex between mono-porphyrin receptor **22** and the monodentate ligand quinuclidine **24**. In the UV-Vis spectrum, dilution of a chloroform solution of free mono-porphyrin receptor resulted in only minor changes to the peak width, indicating that there was no significant aggregation of the mono-porphyrin.

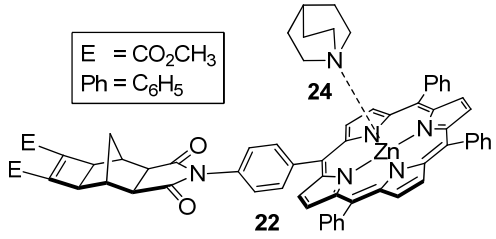

Figure 3.13 - Complex between mono-porphyrin receptor and quinuclidine

Titration of a solution of quinuclidine **24** to a solution of mono-porphyrin receptor **22** resulted in a red shift of the Soret band from 419.3 nm to 430.6 nm, indicating the formation of mono-porphyrin:quinuclidine **22**:**24** (Figure 3.14 (a)). A clear isosbestic point suggests that complexation proceeds between two well defined species in solution without generating an intermediate species [28, 30, 31, 35].

The UV-Vis titration data was analysed using multivariate global spectral analysis (HypSpec, Protonic Software [166]) to determining the binding model. A number of factors must be considered when assigning the binding model, including not only a visual inspection of the fit, but the standard deviation and residuals of the fit, the physical ability of the system to form the species, and whether the calculated spectra are reasonable for the species suggested and resemble the experimental spectra. These criteria and further information on host-guest methodology are provided in Appendix 2.

[8] This is an estimate as different porphyrin substituents can result in small differences in association constants [165]. While the microscopic binding constant of monodentate pyridine to a mono-porphyrin is not the same as half of bidentate bipy (substitution influences basicity) [53], monodentate pyridine enables the reference intermolecular interaction to be determined.

The binding constant K_{11} was determined to be 2.53 x 10^5 M^{-1} in $CHCl_3$ (K_{11} = [mono-porphyrin:quin]/([mono-porphyrin][quin], average of two replicates). The speciation diagram in Figure 3.14 (b) shows the formation of mono-porphyrin:quin at the expense of free mono-porphyrin. The data was an excellent fit to this model as can be seen in Figure 3.14 (c) and (d) at 419 nm. The fitting was equally as good at 430 nm (not shown).

In assessing the suitability of this binding model, the suggested species mono-porphyrin:quin corresponds with the expectation in Figure 3.13, being the only species that this system can physically form (quinuclidine is monodentate). In addition, the standard deviation and residuals of the fit are small (not shown), while the calculated spectra (not shown) for the mono-porphyrin:quin species are consistent with the experimental spectra in Figure 3.14 (a).

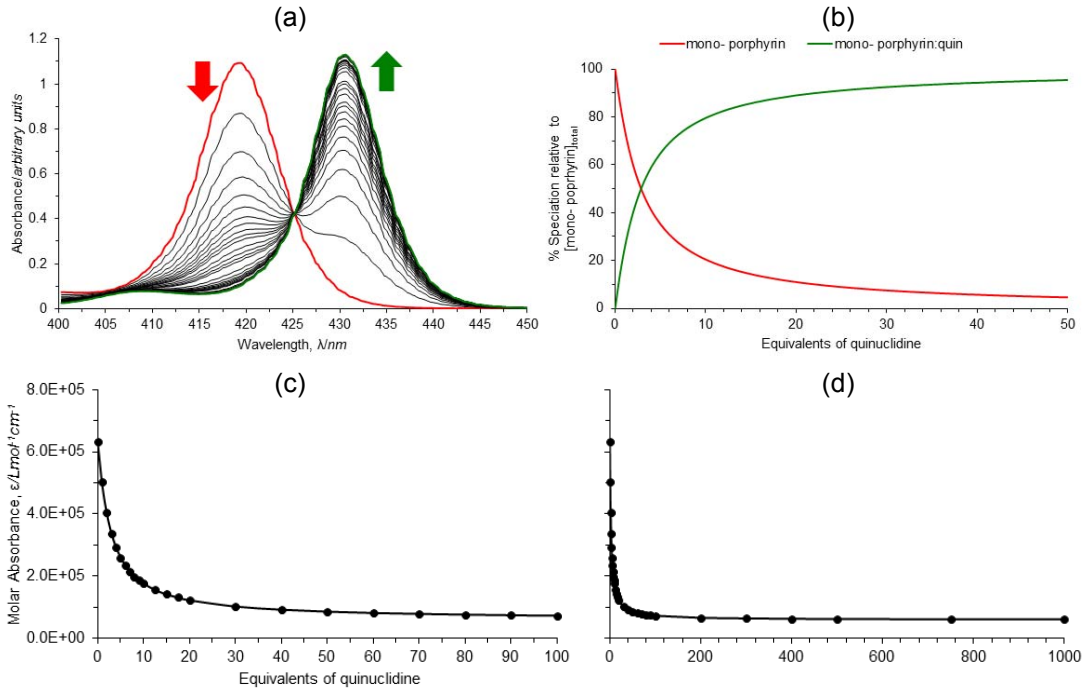

Figure 3.14 – (a) UV-Vis titration of mono-porphyrin with quinuclidine in chloroform; (b) speciation diagram of mono-porphyrin with quinuclidine (1:1, HypSpec, HySS2009); (c) best fit (black line) of the algorithm for equilibria between mono-porphyrin, quinuclidine, and mono-porphyrin:quinuclidine to the titration data (black circles) at 419 nm for 0 - 100 eq. of quinuclidine; (d) 0 - 1000 eq. of quinuclidine.

In comparison to the K_{11} of other mono-porphyrin quinuclidine species reported in the literature (8 x 10^4 M^{-1} [30], 9.8 x 10^4 M^{-1} [78]), the of K_{11} for mono-porphyrin:quin **22**:**24** of 2.53 x 10^5 M^{-1} (1.27 x 10^5 M^{-1} after statistical correction) is similar, but slightly enhanced. This would appear to indicate that the norbornyl

backbone has a positive influence on complex formation, in contrast to our previous statement [1]. Different porphyrin *meso*- substituents have been previously observed to result in small but measurable differences in association constants [165].

The method of continuous variations (Job plot) is a simple technique which allows the determination of the empirical stoichiometry of a host-guest interaction [4, 167, 168], based on the mole fraction at which the concentration of the complex is at a maximum. This was undertaken for mono-porphyrin and quinuclidine using UV-Vis spectroscopy. The Job plot derived from this data is shown in Figure 3.15, and the maxima at a mole fraction of 0.5 confirms the 1:1 stoichiometry.

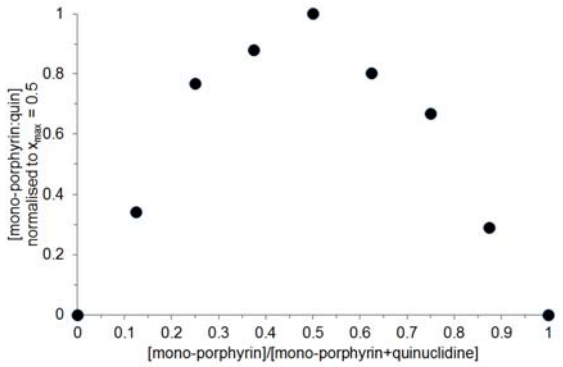

Figure 3.15 - Job Plot for mono-porphyrin and quinuclidine

The host-guest chemistry of the Zn(II) freely rotating molecular tweezer **1** was subsequently studied for the diamino ligands DABCO **5** and bipy **6**. The results of these experiments, including association constants, are discussed in the next section.

3.6 Freely Rotating Tweezer Host-Guest Study

The interaction between the freely rotating Zn(II) tweezer **1** and the diamino ligands DABCO **5** and bipy **6** was examined by UV-Vis and NMR spectroscopy. In line with other bis-porphyrin host systems reported in the literature [28-32, 54, 58, 84-86, 169-171], the tweezer can access a variety of conformations, the extremes of which are *syn*- and *anti*-. These can form various complexes in solution, all of which are in equilibrium. The possibilities are outlined schematically in Figure 3.16, and reveal the possibility of 1:1 (K_{11} = [tweezer:ligand]/([tweezer][ligand]), 1:2 (K_{12} = [tweezer:$(ligand)_2$]/([tweezer][ligand]^2), 2:1 (K_{21} = [$(tweezer)_2$:ligand]/([tweezer]^2[ligand]) and 2:2 (K_{22} = [$(tweezer)_2$:$(ligand)_2$]/([tweezer]^2[ligand]^2) stoichiometries.

With a theoretical understanding of the speciation that can occur in the freely rotating system **1**, a comprehensive experimental host-guest study was undertaken. This is typically achieved by UV-Vis and ^{1}H NMR spectroscopic titrations, which show characteristic spectral features for different species, along with fitting of the titration data to a binding model using multivariate global spectral analysis. These experiments are now described.

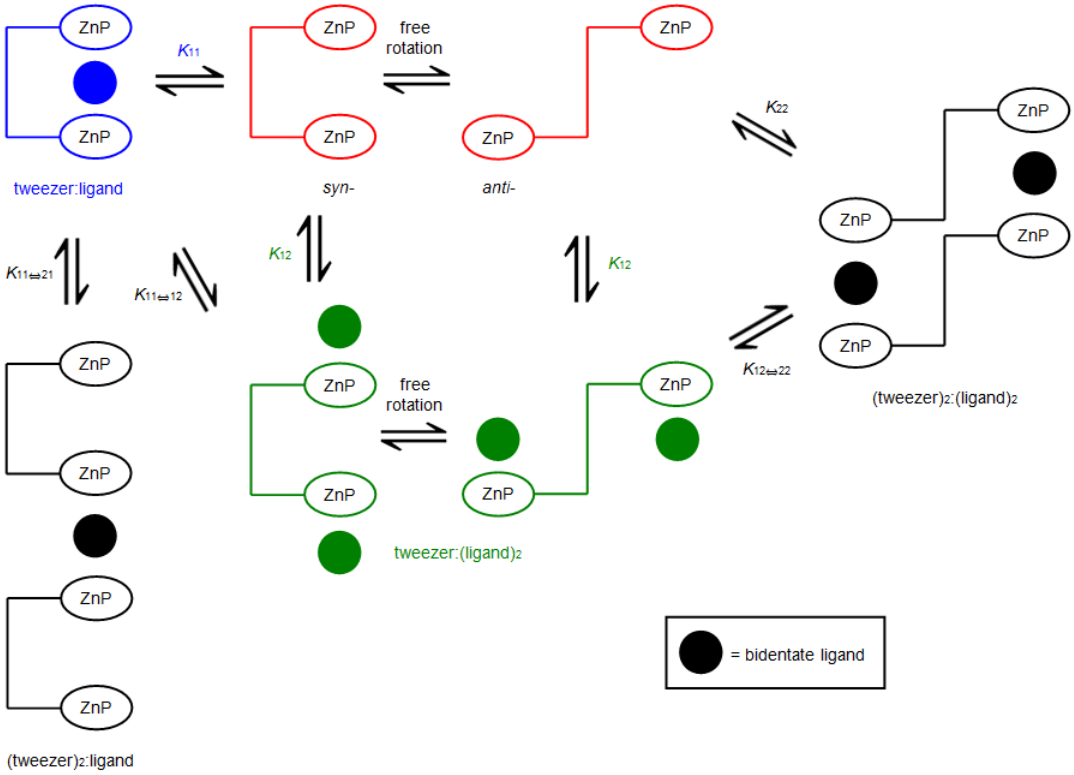

Figure 3.16 - Schematic representation of the various equilibria between freely rotating tweezer **1** and bidentate ligand (represented by circles). Colour coded with red for free host, blue for intramolecular sandwich complex, black for intermolecular sandwich complex, and green for simple open 1:1 porphyrin:ligand complex.

3.6.1 Freely Rotating Tweezer with DABCO (UV-Vis)

Having established the association constant for the mono-porphyrin receptor **22**, the host-guest chemistry of the freely rotating system **1** was explored with the bidentate ligand DABCO **5**. Titration of a solution of DABCO to a solution of freely rotating tweezer resulted in a red shift of the UV-Vis spectrum (Figure 3.17 (a)), with the Soret maximum moving from 419.5 to 423.4 nm, and is characteristic of a bis-porphyrin DABCO sandwich complex [30, 31]. The sandwich complex is stable in the presence of a moderate to large excess of DABCO, after which it is slowly

converted most likely to an open tweezer:$(DABCO)_2$ complex, where DABCO is bound to each porphyrin singly rather than as a sandwich. This transition is only partially complete by the addition of 200 000 equivalents, with a Soret maximum of 429.4 nm. This is characteristic of simple mono-porphyrin DABCO complexes [30, 31], and is similar to that observed for the simple mono-porphyrin quinuclidine complex discussed previously.

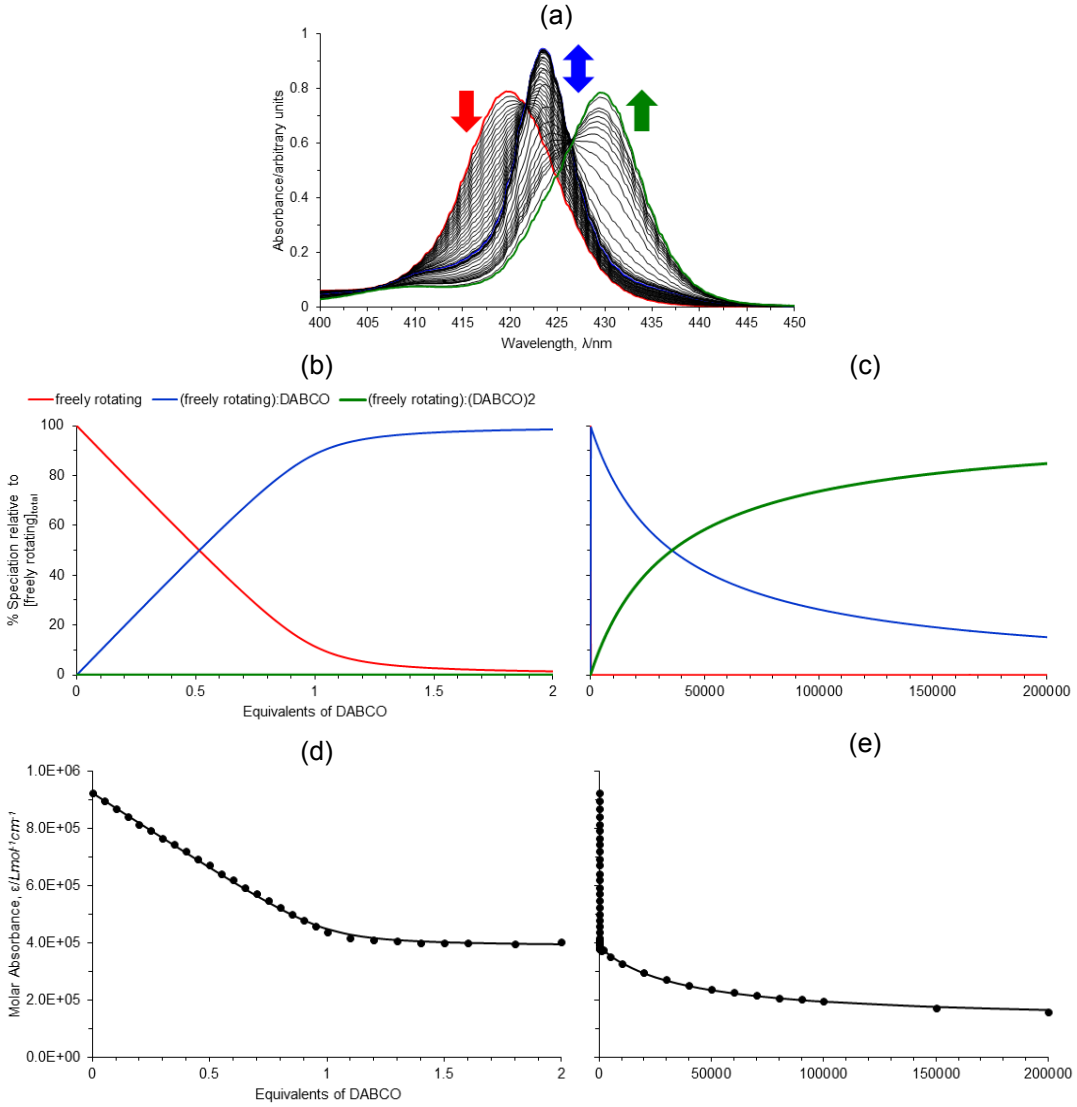

Figure 3.17 - (a) UV-Vis titration of freely rotating tweezer **1** with DABCO **5** in chloroform; (b) speciation diagram of freely rotating tweezer with DABCO (1:1 → 1:2, HypSpec, HySS2009) for 0 - 2 eq. of DABCO; (c) 0 - 200 000 eq. of DABCO; (d) best fit (black line) of the algorithm for equilibria between freely rotating tweezer, DABCO, tweezer:DABCO, and tweezer:$(DABCO)_2$ to the titration data (black circles) at 419 nm for 0 - 2 eq. of DABCO; (e) 0 - 200 000 eq. of DABCO.

The UV-Vis titration data gave excellent fits for a 1:1 plus 1:2 binding model, giving K_{11} = 8.1 x 10^7 M^{-1} and K_{12} = 2.7 x 10^9 M^{-2} in $CHCl_3$ (single replicate). These are assigned to intramolecular tweezer:DABCO **1**:**5** and open tweezer:$(DABCO)_2$ **1**:(**5**)$_2$

respectively (Figure 3.16). Shown in Figure 3.17 (b) and (c) are speciation diagrams for the UV-Vis titration data that have been separated out into 0-2 equivalents DABCO and 0-200 000 equivalents DABCO. Clearly visible is the initial formation of the 1:1 complex between the tweezer and DABCO (tweezer:DABCO, blue line), and its conversion into the 1:2 complex (tweezer:$(DABCO)_2$, green line) as more equivalents of DABCO are added to the solution. The best fit of the algorithm for the formation of tweezer:DABCO and tweezer:$(DABCO)_2$ to the titration data at 419 nm is shown in Figure 3.17 (d) and (e) respectively. The K_{11} obtained for tweezer:DABCO is over two orders of magnitude larger than mono-porphyrin:quinuclidine (Table 3.2), and this enhancement is indicative of a bis-porphyrin DABCO sandwich complex [32, 34, 36].

Table 3.2 - Summary of UV-Vis data in chloroform

Species	**mono-porphyrin, 22**	**mono-por: quin, 22:24**	**freely rotating, 1**	**freely rotating: DABCO, 1:5**	**freely rotating: $(DABCO)_2$, 1:$(5)_2$**
λ_{max} (nm)	419.3	430.6	419.5	423.4	429.4
K_a		2.5×10^5 M^{-1}		8.1×10^7 M^{-1}	2.7×10^9 M^{-2}

Given the other possible complexation geometries shown in Figure 3.16, fitting of the of UV-Vis titration data was attempted in combinations with both the 2:2 and 2:1 complexation stoichiometries, $(tweezer)_2$:$(DABCO)_2$ (K_{22}) and $(tweezer)_2$:DABCO (K_{21}) respectively. However, the data could not be fitted to these species, suggesting that the ternary intermolecular complexes $(tweezer)_2$:$(DABCO)_2$ and $(tweezer)_2$:DABCO are not formed to any appreciable extent at UV-Vis concentrations (10^{-5} to 10^{-7} M).

3.6.2 Freely Rotating Tweezer with DABCO (NMR)

^{1}H NMR spectroscopy has been extensively used to characterise supramolecular complexes in solution, as it is able to provide information on chemical environment, complex geometry, and speciation [28, 30, 31].

With the exception of the ^{1}H NMR titration between freely rotating tweezer and DABCO, all other titrations in this thesis contain consistent errors of 10-15 % (10 % for DABCO, 15 % for bipy) between the number of equivalents of guest titrated with host based on the mass weighed, compared to the number of equivalents suggested by NMR signal integration. Partial investigation was undertaken, including confirming guest purity, and checking for instrumental issues known to affect NMR integration (phasing of spectra, alteration of the D1 parameter in case related to relaxation), but the source of error was frustratingly unable to be determined. The accuracy of the electronic balance was examined, and did display some variation in weighing masses close to its limit, however, further investigation is necessary. Other factors which should be investigated include checking the delivery volume of the microlitre syringes, and filtration of the host in case trace chromatographic silica is present and is contributing to the weighed host mass. If methanol from recrystallisation is present in the sample (coordinated to the zinc(II) porphyrins and/or trapped in the sample), this could be determined by undertaking elemental CHN analysis.

A ^{1}H NMR titration of tweezer with DABCO in $CDCl_3$ enabled the formation of tweezer:DABCO and tweezer:$(DABCO)_2$ to be characterised. These results are shown in Figure 3.18, and the diagnostic porphyrin β-pyrrole and DABCO resonances are now discussed.

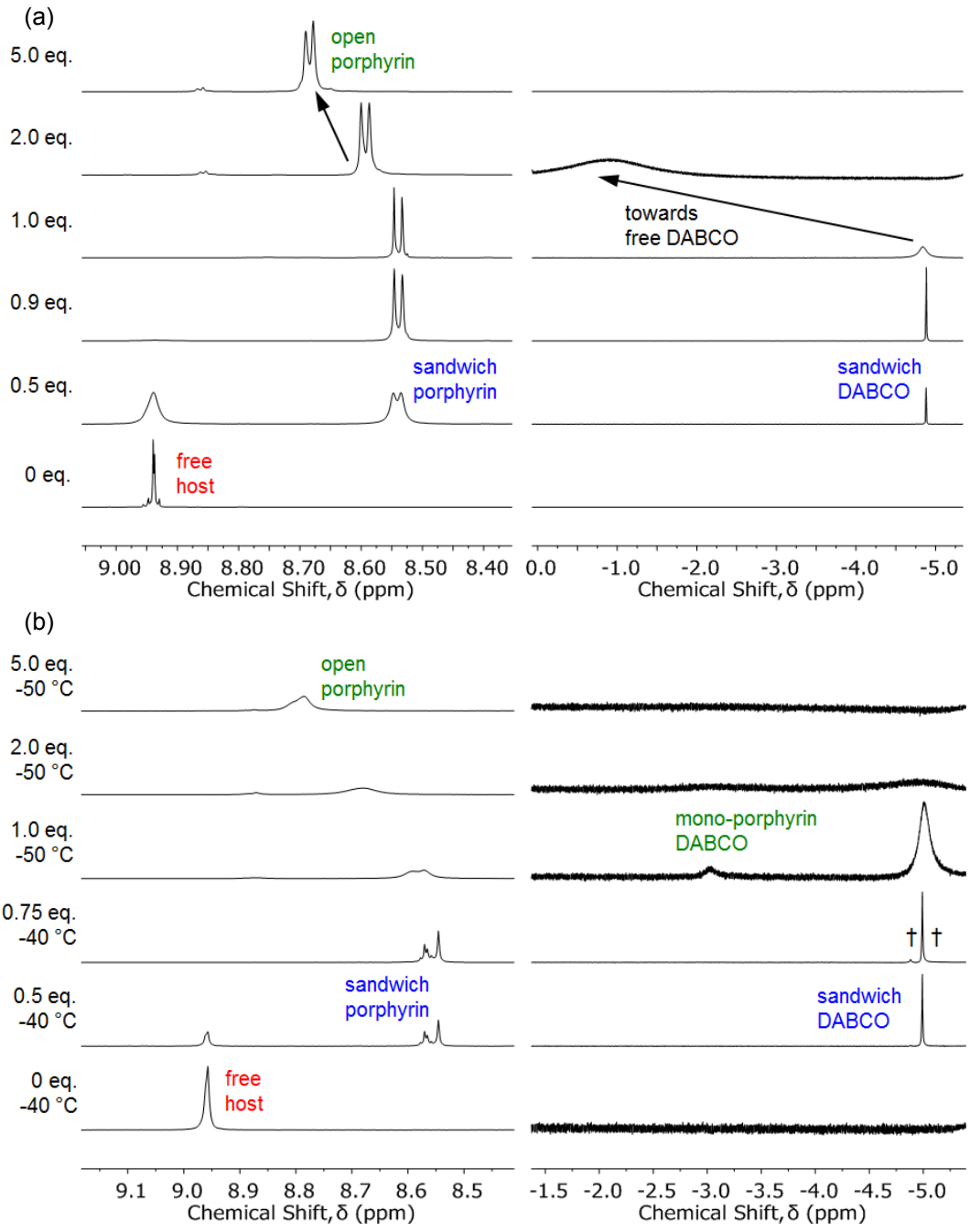

Figure 3.18 – Selected ^{1}H NMR spectral regions with various equivalents of DABCO at (a) 20 °C (top pane) and (b) -40 to -50 °C (bottom pane). † identifies minor amounts of sandwich complexes other than the main complex tweezer:DABCO.

At 20 °C (Figure 3.18 (a)), the β-pyrrole signals for uncomplexed tweezer (free host) are at 8.94 ppm. The addition of 0.5 equivalents of DABCO resulted in a broadening of the porphyrin β-pyrrole resonance and the appearance of a second β-pyrrole signal for the complex at 8.54 ppm. This upfield shift is typical of β-pyrrole protons in a bis-porphyrin DABCO sandwich complex, and results from shielding by opposing ring currents of two porphyrin aromatic systems in close proximity [30, 31, 66]. The species are in slow exchange on the NMR chemical shift timescale at ambient temperature up to 0.9 equivalents of DABCO, with the β-pyrrole sandwich complex signal increasing at the expense of uncomplexed tweezer. The relative integration of the sandwich β-pyrrole resonance to the total β-pyrrole resonance (free plus sandwich) is consistent with the formation of a species with the empirical formula of 1:1, such as tweezer:DABCO or $(\text{tweezer})_2$:$(\text{DABCO})_2$. In the next several paragraphs, the sandwich species is shown to be tweezer:DABCO. Addition of two to five equivalents of DABCO causes the β-pyrrole resonance to shift downfield as increasing proportions of the open porphyrin species, tweezer:$(\text{DABCO})_2$, forms in fast exchange with tweezer:DABCO on the NMR chemical shift timescale.

Further understanding of the complexation of DABCO by the tweezer is gained from the DABCO methylene resonance. For the addition of up to 0.9 equivalents of DABCO, a sharp singlet was observed at -4.89 ppm. This large upfield shift is typical of DABCO methylene protons in a bis-porphyrin DABCO sandwich complex, and again results from shielding by opposing ring currents of two porphyrin aromatic systems in close proximity [27, 29-31, 52, 66, 172]. Again, the relative integration of the DABCO sandwich resonance to the ester signal[9] is consistent with the formation of a species with the empirical formula of 1:1. At one equivalent of DABCO, the sandwich DABCO resonance is broadened, consistent with chemical exchange occurring with another species at a fast exchange rate on the NMR chemical shift timescale at 20 ˚C, most likely a combination of tweezer:$(\text{DABCO})_2$ and free DABCO.

Slowing the exchange rate between the various complexes in solution was achieved by lowering the temperature to between -40 and -50 °C (Figure 3.18 (b)). At -40 °C

[9] The ester signal was selected as a reference because it does not change significantly on complexation and is the sum of free plus sandwiched species. In this case, the number of protons in the host ester resonance is equal to the number of protons in an isolated molecule of DABCO, and so their relative integrations do not require any normalisation.

and less than one equivalent of DABCO, two weak bis-porphyrin DABCO sandwich complex signals are observed in addition to the main signal at -5 ppm (indicated by † in Figure 3.18 (b)). These resonances are most likely to be small amounts of ternary intermolecular complexes such as $(tweezer)_2$:$(DABCO)_2$ and $(tweezer)_2$:DABCO (Figure 3.16), with the main resonance most likely to be intramolecular tweezer:DABCO. At 1 equivalent of DABCO, a broad signal appears at -3.0 ppm in addition to the DABCO sandwich resonance. This is characteristic of the α-methylene protons of DABCO bound to a single porphyrin [28-30] and most likely corresponds to the destruction of the DABCO sandwich complex to the open tweezer:$(DABCO)_2$ complex. When greater than one equivalent of DABCO is added at -50 °C, the broadened open tweezer:$(DABCO)_2$ resonance increases in area while the main DABCO sandwich resonance broadens as its concentration diminishes, and the rate of exchange between the two complexes increases on the NMR chemical shift timescale.

In addition, at -40 ˚C and less than one equivalent of DABCO, differentiation of the *meso*-phenyl proton resonances depending on their facial orientation within the complex was observed (not shown). No further desymmetrisation of the spectrum was observed to -90 ˚C for approximately 0.125 equivalents of DABCO in CD_2Cl_2[10]. This indicated that axial ligand rotation of DABCO about the Zn-Zn axis of the bis-porphyrin sandwich was rapid on the NMR chemical shift timescale at this temperature [173, 174]. NOESY of this same solution at -60 ˚C revealed dipolar connectivity between the DABCO signal and both the β-pyrrole complex signal and several *meso*-phenyl complex signals[11].

To definitively confirm the sandwich species at NMR concentrations (millimolar) was intramolecular tweezer:DABCO and not $(tweezer)_2$:$(DABCO)_2$, a simulated NMR speciation diagram was generated (HySS2009, Protonic Software [166],

[10] Due to the limited solubility of tweezer in CD_2Cl_2, the exact stoichiometry of DABCO was approximate. Spectral analysis was complicated by overlap of the *meso*-phenyl signals from free tweezer and tweezer:DABCO. However, no significant broadening of the DABCO and β-pyrrole complex signals was observed at -90 ˚C.

[11] This NOESY spectrum also revealed a correlation between an aryl and a norbornyl resonance. This was attributed to the linker phenyl diimide protons and their close proximity to protons in the *endo*-region of the linker. However, due to the complexity of the spectra from the mixture of both tweezer and tweezer:DABCO species, no further structural information could be gained.

Figure 3.19), using the association constants K_{11} and K_{12} determined from the UV-Vis titrations, and compared with experimental NMR titration data. This method [28, 30, 31] enables the selected binding model to be verified, and is described Chapter 1 and Appendix 2 (and briefly outlined again now).

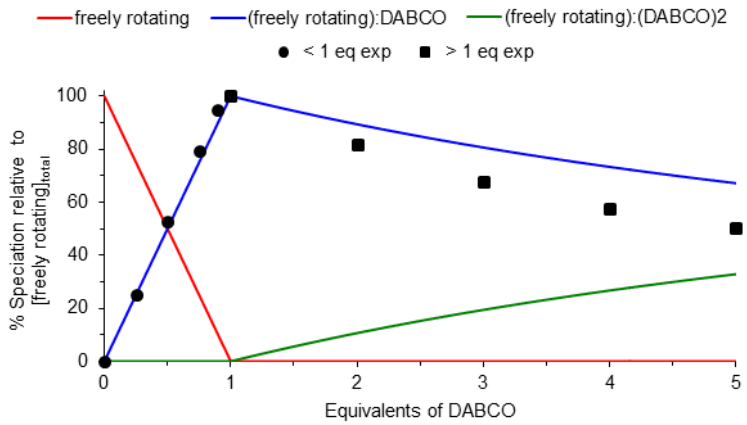

Figure 3.19 - Simulated NMR speciation diagram generated from UV-Vis determined association constants K_{11} and K_{12}. Experimental NMR speciation has been overlayed for both the slow and fast exchange regions of the titration (black circles and squares).

When less than one equivalent of DABCO has been added, the system was in slow exchange on the NMR chemical shift timescale and the relative amounts of free and complexed tweezer can calculated using the integration of the β-pyrrole resonances [28, 30, 31] or the DABCO sandwich resonance, outlined in Appendix 2. When greater than one equivalent of DABCO has been added, the system was in fast exchange on the NMR chemical shift timescale and relative amounts of sandwich and open complexes can be determined from the position of the chemical shift along a number line from known values of fully complexed and fully open[12] [28, 30, 31].

These results are plotted in Figure 3.19, where the blue line represents the simulated NMR speciation for the growth and decay of tweezer:DABCO , and the black circles and squares represent the experimental NMR speciation determined from the titration data (the red and green lines are the free host and open species tweezer:$(DABCO)_2$ respectively). The excellent correlation between the simulated and experimental speciation in the 1:1 region of the plot confirms the formation of intramolecular complex tweezer:DABCO as the dominant species at NMR concentrations. For

[12] A chemical shift of 8.54 ppm (freely rotating + 0.9 eq. DABCO) was selected for the value for fully complexed species. A chemical shift of 8.829 ppm was selected for the value for fully open species, using data obtained in Chapter 4 for the *anti*- restricted rotation tweezer + 5 eq. DABCO.

excess DABCO[13], the experimental decay of the sandwich complex into open species tweezer:$(DABCO)_2$ followed the same trend predicted in the NMR simulation. In this case, the binding model is confirmed to be the same at both UV-Vis and NMR concentrations.

3.6.3 Molecular Modelling of Freely Rotating Tweezer with DABCO

Molecular modelling [145] was undertaken to determine the equilibrium geometry of the tweezer:DABCO complex (semi-empirical, AM1, Figure 3.20). Several interesting geometric features are apparent. Rotation is observed about the porphyrin moieties as well as between the two polycyclic arms of the tweezer about the central phenyl diimide group[14]. Overlay of the polycyclic arms for models with and without DABCO (not shown) revealed only minimal distortion, providing further evidence that the polycyclic arms are largely rigid. The overall complexed structure does not appear to be significantly strained, and this supports the high association constant that has been determined.

[13] Data analysis for 1-5 equivalents of DABCO was acquired 9 months after the original data using the same solution. The spectra indicated the sample had not degraded in this time.

[14] Intriguingly, the molecular model of the *endo*- phenyl diimide core is noticeably curved (bent out of plane) when DABCO is complexed in the tweezer. This deviation from expected planarity of the phenyl diimide could suggest that DABCO is slightly too small for the tweezer cavity, but can be accommodated by a combination of *endo*-phenyl diimide curvature and rotation of the rigid polycyclic arms. However, this curvature is not observed for the analogous *syn*- tweezer with DABCO in chapter 4, and so caution should be taken in the interpretation of geometric features at a semi-empirical level of computational theory.

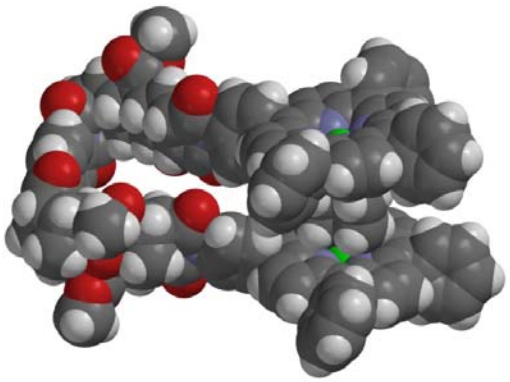

Figure 3.20 - Molecular modelling of the tweezer:DABCO **1**:**5** complex (semi-empirical, AM1).

Having examined the freely rotating tweezer **1** with DABCO **5** by UV-Vis and NMR, attention was turned to the bidentate ligand 4,4'-bipyridyl **6**, to determine if this would be a suitable guest for the freely rotating tweezer **1**. The remainder of this chapter presents a similar analysis and discussion for bipy. A summary of the host-guest behaviour of the freely rotating tweezer is provided at the end of the chapter.

3.6.4 Freely Rotating Tweezer with bipy (UV-Vis)

In a similar manner to the DABCO titration, addition of a solution of bipy **6** to a solution of freely rotating tweezer **1** resulted in a two-stage red shift in the UV-Vis spectrum (Figure 3.21 (a)). Pyridine ligands are widely reported to redshift the UV-Vis spectrum of porphyrins [97, 175]. In this case, the Soret maximum gradually transitions from 419.5 nm to around 426 nm, most likely tweezer:bipy. A similar shift has previously been reported for a bis-porphyrin polycyclic-linked tweezer with bipy [78]. A second gradual redshift occurs to approximately 428.5 nm by 100 000 equivalents of bipy, although this transition appears to only be partially complete. This most likely corresponds to the formation of the open species tweezer:$(bipy)_2$, as it approaches the Soret maxima of 430 nm reported for the reference open species of tetraphenylporphyrin with pyridine [176].

The UV-Vis titration data gave reasonable fits to several different binding models using HypSpec [166], including intermolecular 2:2 plus 1:2, however, the best fit was for intramolecular 1:1 plus 1:2. This model gave K_{11} = 4.97-5.27 x 10^5 M^{-1} and K_{12} = 1.56-1.88 x 10^8 M^{-2} in $CHCl_3$ (single replicate, fitted to 10 000 eq. bipy,

association constant quoted as a range[15]). These are assigned to intramolecular tweezer:bipy **1**:**6** and open tweezer:$(bipy)_2$ **1**:$(\mathbf{6})_2$ respectively (Figure 3.16). The K_{11} obtained for tweezer:bipy is enhanced by approximately two orders of magnitude compared to association constants reported for mono-porphyrin:pyridine [27, 53, 55, 58, 78, 97, 98, 165], and is attributed to the formation of a bis-porphyrin bipy sandwich.

The HypSpec software package output contains calculated UV-Vis spectra based on the fit. Although the calculated maxima for each species are similar to the experimental spectra, the intensity profile is slightly different (not shown); the open 1:2 species is 5 % greater than the intramolecular 1:1 sandwich complex in the calculated spectra, rather than 10 % lower as observed in the experimental spectra.

This difference in intensity profile, coupled with only being able to fit the data to 10 000 equivalents of bipy is of concern, and could indicate a problem with the selected binding model. However, no other binding model could be fitted to the titration data (other than 2:2 plus 1:2, which gave the same issues with respect to intensity profiles and 10 000 eq.), and so the analysis was continued below for the best binding model available of 1:1 plus 1:2.

Shown in Figure 3.21 (b) and (c) are speciation diagrams for the UV-Vis titration data that have been separated out into 0-100 equivalents bipy and 0-10 000 equivalents bipy. Clearly visible is the initial formation of the 1:1 complex between the tweezer and bipy (tweezer:bipy, blue line), and its conversion into the 1:2 complex (tweezer:$(bipy)_2$, green line) as more equivalents of bipy are added to the solution. The best fit of the algorithm for the formation of tweezer:bipy and tweezer:$(bipy)_2$ to the titration data at 419 nm is shown in Figure 3.21 (d) and (e) respectively. An equally good fit was observed at 426.5 and 430 nm.

[15] The data set above was only fitted to 10 000 eq. bipy, as fitting of the full data set to 100 000 eq. bipy resulted in a poor fit. This was also observed for the *syn*- restricted tweezer in Chapter 4.

The association constants are quoted as a range due to uncertainty in the stock tweezer concentration for this titration.

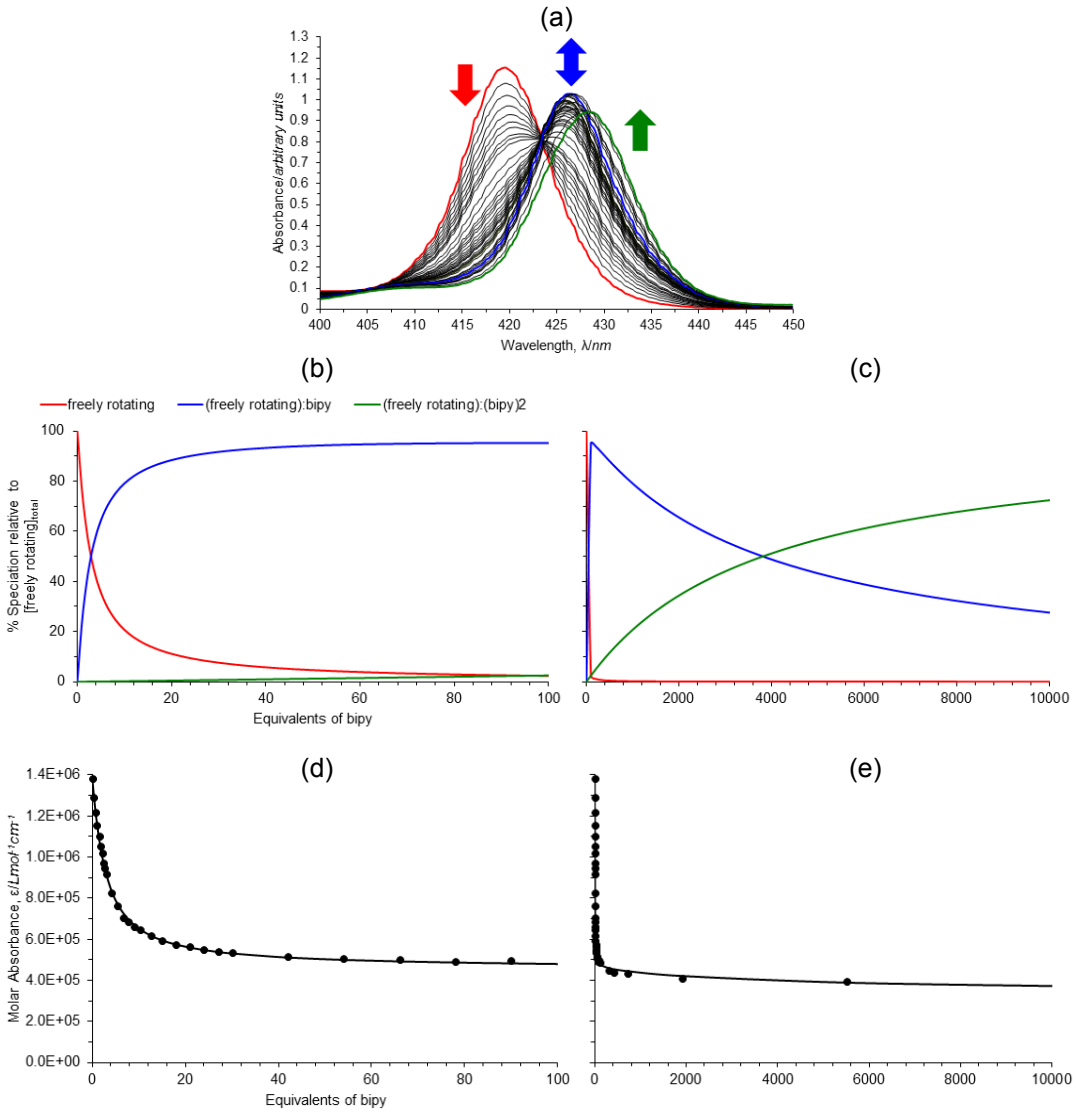

Figure 3.21 - (a) UV-Vis titration of freely rotating tweezer **1** with bipy **6** in chloroform; (b) speciation diagram of freely rotating tweezer with bipy (1:1 → 1:2, HypSpec, HySS2009) for 0 - 100 eq. of bipy; (c) 0 – 10 000 eq. of bipy; (d) best fit (black line) of the algorithm for equilibria between freely rotating tweezer, bipy, tweezer:bipy, and tweezer:$(bipy)_2$ to the titration data (black circles) at 419 nm for 0 - 100 eq. of bipy; (e) 0 - 10 000 eq. of bipy.

3.6.5 Freely Rotating Tweezer with bipy (NMR)

NMR was again employed to examine the suitability of the binding model indicated by UV-Vis experiments. Unfortunately, the information obtained from the NMR titration of bipy with the freely rotating tweezer was limited by the large error (estimated 35-40 %) between the number of equivalents of bipy titrated based on the mass of host and guest weighed out, compared to the number of equivalents experimentally observed by integration. In this case, the large discrepancy is most likely caused by a weighing error in combination with the previously discussed 10-15 % error observed for all titrations. Despite the poor accuracy of this titration, an

adequate understanding of the behaviour of the system was obtained by examining the diagnostic porphyrin β-pyrrole and bipy signals.

The ^{1}H NMR titration of freely rotating tweezer with bipy in $CDCl_3$ at 20 °C is shown in Figure 3.22 (a). For less than 0.5-0.75 titrated equivalents of bipy (integration suggests 1 equivalent), the system was in fast exchange on the NMR chemical shift timescale, indicative of the weaker binding of the less basic bipy when compared to DABCO [52]. The porphyrin β-pyrrole sandwich complex resonance signals are observed as an average between free host at 8.96-8.92 ppm tending towards a value consistent with the formation of a bis-porphyrin bipy sandwich (8.8-8.7 ppm [177]), most likely tweezer:bipy. The β-pyrrole complex resonance is seen to be comprised of two resolved signals; a singlet and a multiplet, each with equal integration. This likely reflects that the non-equivalence of the β-pyrrole resonances from the porphyrin being substituted in a single quadrant (connection to the polycyclic arm), and is better resolved as when the porphyrin is complexed with bipy compared to free host. Addition of greater than 0.75 titrated equivalents of bipy (integration suggests greater than 1 equivalent) resulted in the β-pyrrole resonance shifting downfield, as increasing proportions of open species tweezer:$(bipy)_2$ form in fast exchange on the NMR chemical shift timescale.

While splitting of the *meso*-phenyl resonances is observed in the spectrum of the free host suggesting the porphyrins in the free host are facially differentiated, this desymmetrisation increases during the formation of the sandwich complex, then returns to similar desymmetrisation to the free host, presumably as the sandwich species decays into the open complex (not shown).

Small changes to the chemical shifts for the polycyclic backbone can be observed (0.05 ppm, not shown). Although the linker is somewhat distanced from the porphyrins, these shifts may arise from changes to the tweezer geometry during complexation.

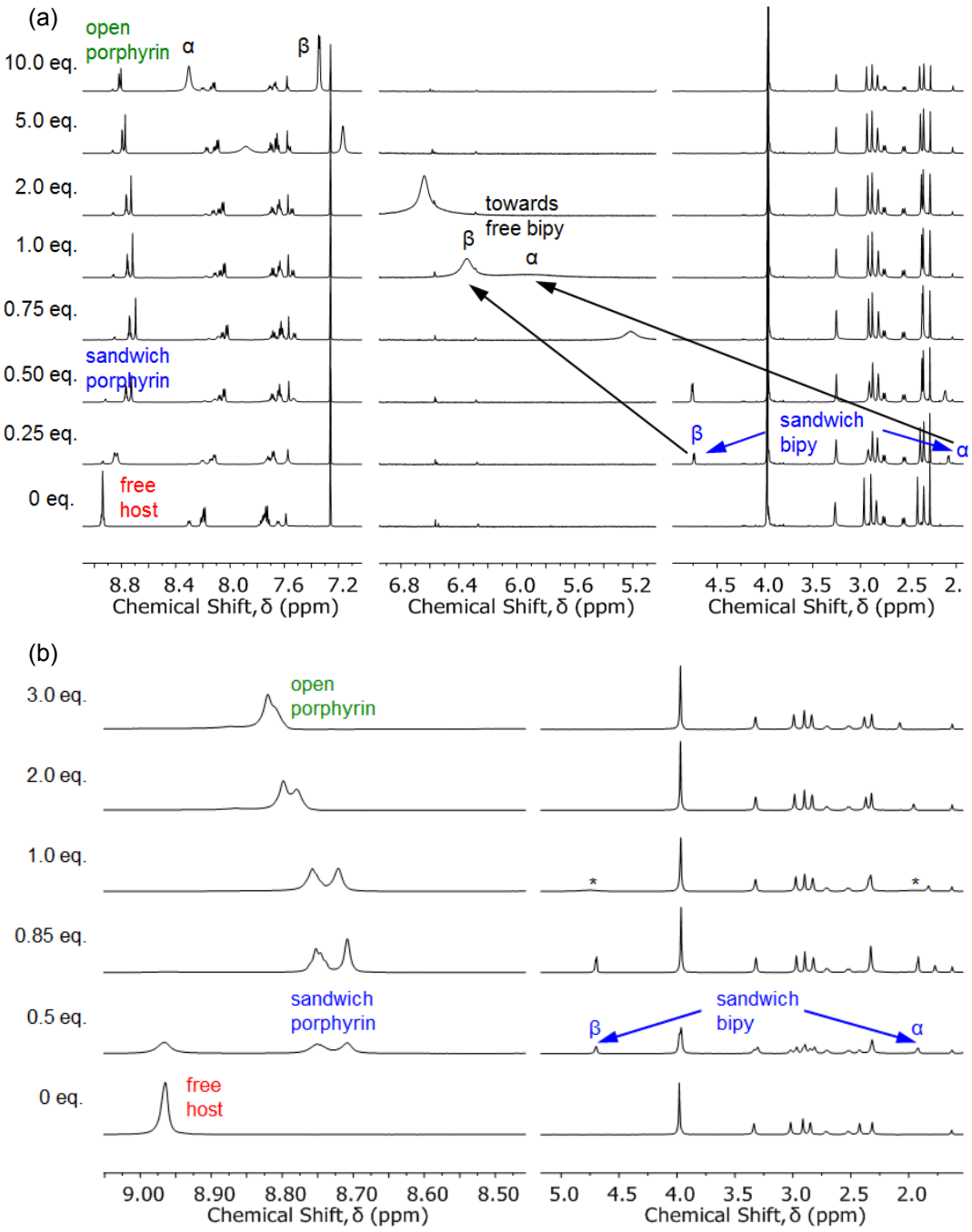

Figure 3.22 - Selected ^{1}H NMR spectral regions with various equivalents of bipy at (a) 20 °C (top pane) and (b) -50 °C (bottom pane). α and β refer to the position of the *ortho*- and *meta*- protons in 4,4'-bipyridyl. * identifies bipy signals broadened into the baseline due to chemical exchange.

Further understanding of the complexation was gained by examination of the bipy resonances. For less than 0.5 titrated equivalents of bipy (integration suggests close to 1 equivalent), two resonances can be observed at 4.74 and 2.08 ppm (Figure 3.22 (a)). This is similar to other bis-porphyrin bipy sandwich complexes reported in the literature [53, 178, 179]. However, the sandwich complex appears to be labile, with fast chemical exchange of the α and β bipy resonances and broadening of the α resonance evident at bipy concentrations of less than 1 equivalent. At greater than

0.75 titrated equivalents of bipy (spectral features suggest greater than 1 equivalent), faster rates of chemical exchange between the sandwich and open species occur on the NMR chemical shift timescale, as a larger proportion of the open species forms in the equilibrium. The bipy resonances shift downfield and approach the value for their free resonances ($\delta_{\alpha(free)}$ = 8.72 ppm, $\delta_{\beta(free)}$ = 7.52 ppm).

Additional information was obtained by conducting the titration at -50 °C (Figure 3.22 (b)). In this titration, the estimated error was 10-15 % between the number of equivalents of guest titrated against host based on mass weighed compared to NMR signal integration. The system was in slow exchange on the NMR chemical shift timescale below 0.85 titrated equivalents of bipy (integration suggests 1 equivalent). The β-pyrrole resonance for free host at 8.97 ppm decreases at the expense of sandwich resonance at 8.78-8.68 ppm, and all free host is converted to sandwich complex by this point. Although the porphyrin *meso*-phenyl protons (not shown) are in slow exchange and are further desymmetrised in the sandwich complex, no further information could be obtained from this spectral data. Additionally below 0.85 titrated equivalents of bipy (integration suggests 1 equivalent), the two bipy resonances are observed at 4.70 and 1.92 ppm, again similar other bis-porphyrin bipy sandwich complexes in the literature [53, 178, 179].

For greater than 0.85 titrated equivalents of bipy (spectral features suggest greater than 1 equivalent), the system moves into fast exchange on the NMR chemical shift timescale. The porphyrin β-pyrrole signals shift downfield, consistent with chemical exchange between sandwich complex and open species. Similarly to observations at 20 °C, the porphyrin *meso*-phenyl protons appear less desymmetrised for excess bipy. The two bipy sandwich resonances broaden into the baseline (indicated by * in Figure 3.22 (b)) and begin to reappear downfield as the sandwich complex and open species exchange, and as these exchange with free bipy.

In a similar manner to the previous DABCO analysis, a simulated NMR speciation diagram was generated for bipy using the association constants determined from the UV-Vis titrations (Figure 3.23). The blue line represents the simulated NMR speciation for the growth and decay of tweezer:bipy (the red and green lines are the free host and open species tweezer:$(bipy)_2$ respectively). Calculation of experimental

speciation for the fast exchange NMR chemical shift timescale was undertaken as described earlier in this chapter and in Appendix 2[16].

The experimental NMR speciation at 20 °C has been overlayed on Figure 3.23 for less than 1 equivalent of bipy only (black circles). Horizontal positive error bars account for the over addition of equivalents of bipy (titrated based on the mass weighed out, compared to experimentally observed by integration). This good correlation between the simulated and experimental speciation in the 1:1 region of the plot confirms the formation of intramolecular complex tweezer:bipy as the dominant species at NMR concentrations. At greater than 1 equivalent of bipy, the cumulative error in the number of equivalents of bipy titrated becomes very large, and so has not been plotted on Figure 3.23. However, the trend in Figure 3.23 showing the decay of tweezer:bipy and the formation of tweezer:$(bipy)_2$ after 1 equivalent is mirrored in the experimental NMR spectra (Figure 3.22 (a)). Although it cannot be confirmed with complete certainty that the binding models for bipy and freely rotating tweezer are the same at UV-Vis and NMR concentrations (because of the inaccuracy of the NMR titration), it can be concluded that at the very least the binding models are very similar.

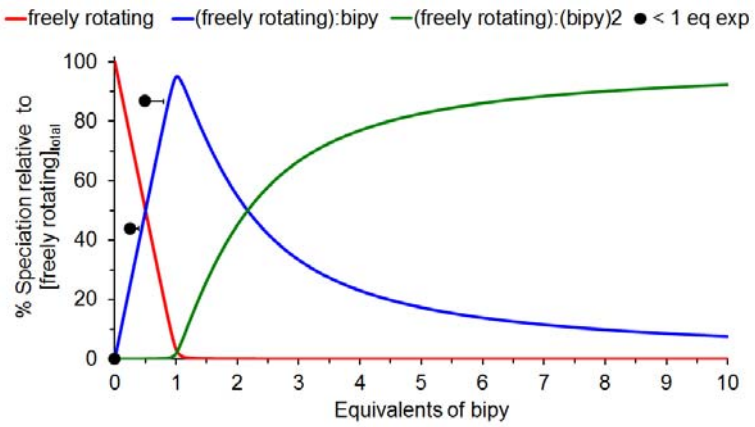

Figure 3.23 - Simulated NMR speciation diagram generated from UV-Vis determined association constants K_{11} and K_{12}. Experimental NMR speciation is overlayed below 1 equivalent of bipy, with horizontal positive error bars to account for the over addition of equivalents of bipy.

[16] A chemical shift of 8.938 ppm was selected for free host. A chemical shift of 8.696 ppm (freely rotating + 0.75 eq. bipy) was selected for the value for fully complexed species.

3.6.6 Molecular Modelling of Freely Rotating Tweezer with bipy

Molecular modelling [145] was undertaken to determine the equilibrium geometry of the tweezer:bipy complex (semi-empirical, AM1, Figure 3.24). As was observed for tweezer:DABCO (Figure 3.20), the porphyrin moieties are rotated somewhat to the idealised representation in Figure 3.10. Again, rotation is also observed between the two polycyclic arms of the tweezer about the central phenyl diimide group, and is very important in the complexation of bipy, as it allows for the required increase in interporphyrin distance for longer guests compared to DABCO. In contrast to DABCO, there was no apparent curvature through the *endo*- phenyl diimide core for the tweezer complex with bipy, indicating bipy is well suited to the size of the expandable cavity. Overlay of the polycyclic arms with and without bipy (not shown) showed minimal distortion to the polycyclic scaffold, again reflecting the rigidity of the polycyclic scaffold. The overall complexed structure does not appear to be significantly strained, and this supports the high association constant that has been determined.

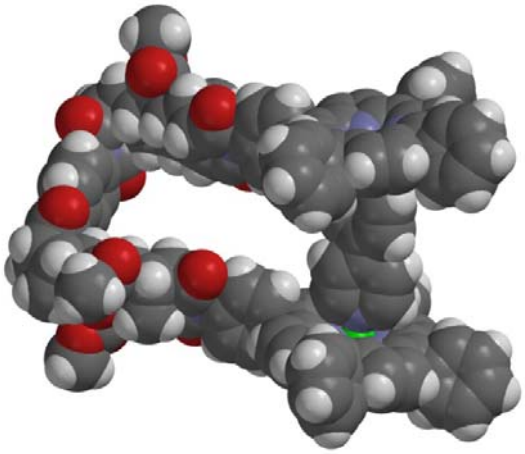

Figure 3.24 - Molecular modelling of the tweezer:bipy **1**:**6** complex (semi-empirical, AM1).

3.7 Summary of the Freely Rotating Tweezer

On route to a more complex tetra-porphyrin molecular tweezer **4**, a model single binding site tweezer **1** was synthesised and the host-guest chemistry explored for diamino ligands DABCO **5** and bipy **6** to probe the behaviour of the system, including the effect of the rotating phenyl diimide core. Additionally, the association constants determined for this model system are important later in Chapter 5 for statistical calculation of interannular cooperativity in the tetra-porphyrin system.

NMR spectral data provided evidence that the phenyl diimide core can freely rotate (a single resonance is observed for the phenyl protons), however, the uncomplexed bis-porphyrins may adopt a *syn*- conformation at millimolar concentrations, even though the *anti*- conformation is energetically accessible (splitting of the *meso*-phenyl resonances is evident in the free host).

From the results of UV-Vis and global spectral analysis of the titration data, the tweezer appears to form strong intramolecular sandwich complex, tweezer:ligand, at low concentrations of guest for both DABCO and bipy, despite the rotational degrees of freedom within the host. Molecular modelling suggests that the polycyclic scaffold regions of the linker remain rigid and that the polycyclic arms rotate about the core to increase the interporphyrin distance when accommodating different sized ligands. The intramolecular sandwich species subsequently decays to the open species, tweezer:$(ligand)_2$, where ligand is bound to each porphyrin singly, in the presence of excess guest. For DABCO, the same binding model was confirmed at higher solution concentrations using NMR, in which experimental speciation was compared with speciation extrapolated from the association constants calculated from the UV-Vis. For bipy, although there was a large inaccuracy in the number of equivalents of bipy titrated compared to the number of equivalents observed by integration, the binding models appear to be similar at both NMR and UV-Vis concentrations.

Synthetic effort was then directed towards a second generation model of the tweezer containing a sterically bulky 2,3,5,6-tetramethyl substituted phenyl linker in order to examine the effect of restricted rotation on the host-guest behaviour of the system. This is presented in Chapter 4 and further probes the importance of rotation on complexation within tweezer systems based on this architecture, prior to pursuing the more complicated tetra-porphyrin tweezer **4** in Chapter 5.

4. Restricted Rotation Tweezer

4.1 Declaration

None of the material in this chapter has been submitted for publication to a journal at the time of thesis submission. The synthesis of the restricted rotation tweezer and its complexation with DABCO has been presented at a conference. X-ray diffraction measurements and solving of X-ray crystal structures were undertaken by Prof Jonathan White (The University of Melbourne). Dr Duc-Truc Pham (The University of Adelaide) provided guidance in the operation of the software package for curve fitting the host-guest data.

4.2 Introduction and Synthetic Approach

Several molecular tweezers published in the literature are able to interchange between *syn*- and *anti*- conformations [6, 58, 180-183]. For molecular tweezer applications, the *anti*- conformation is largely unimportant to tweezer function, and decreases the pre-organisation of the system. To further investigate the role of core rotation on re-organisation of the *syn*- conformation, and to eliminate the undesired *anti*- conformation from the conformations available, the synthesis of a restricted rotation tweezer was undertaken (Figure 4.1).

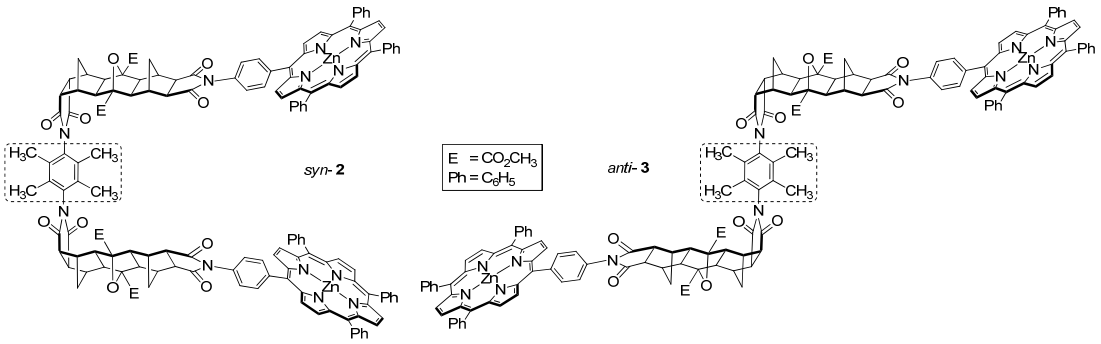

Figure 4.1 - Restricted Rotation Tweezers; *syn*- **2** and *anti*- **3** conformations.

It was hypothesised that the rotational energy barrier about the phenyl diimide could be radically increased by fully substituting the phenyl ring with sterically bulky substituents. Literature precedent for this, both experimental and computational, is discussed in the following section on molecular modelling.

The synthesis from Chapter 3 was repeated, instead with the installation of a 2,3,5,6-tetramethylphenyl diimide core (dotted box in Figure 4.1), and this inclusion was

found to sufficiently restrict rotation to allow isolation of separate *syn*- **2** and *anti*- **3** adducts. This second generation tweezer, which differs from the first generation tweezer only by the linker core, provides the opportunity to study the complexation of the more pre-organised *syn*- conformation[17] independently of the *anti*- conformation.

4.3 Molecular Modelling

Molecular modelling [145] was undertaken to provide information on the equilibrium geometry of the restricted rotation tweezer in the absence of guest (semi-empirical, AM1), and is shown in Figure 4.2. The 2,3,5,6-tetramethyl phenyl core appears to be sufficiently bulky relative to the imide carbonyls so as to prevent rotation between the extreme *syn*- and *anti*- conformations. For the *syn*- **2** conformation, rotation of the polycyclic arms can be observed about the central 2,3,5,6-tetramethyl phenyl diimide group. Although the bis-porphyrins are not arranged in a cofacial orientation, porphyrin *meso*-phenyl rotation is well known [137-139], and so is not expected to hinder guest complexation. For the *anti*- **3** conformation, although an intramolecular sandwich complex is precluded in this geometry, an intermolecular sandwich complex would appear to be a reasonable scenario for this system.

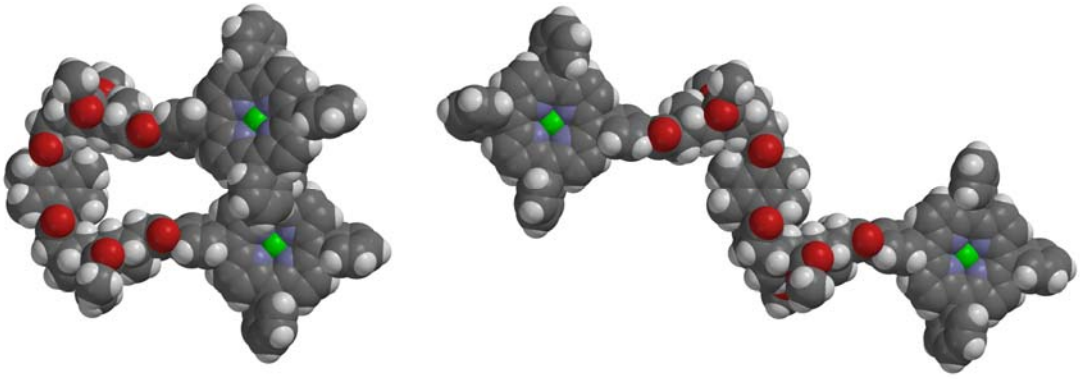

Figure 4.2 - Molecular modelling of the restricted rotation tweezer in the absence of guest; *syn*- **2** and *anti*- **3** conformations (semi-empirical, AM1).

[17] The *syn*- tweezer is not completely pre-organised; both the *syn*- and *anti*- systems can access a range of conformations, however, interconversion between these two extremes was found not to occur under the conditions elaborated later in this chapter.

4.3.1 Simulating Rotation about the 2,3,5,6-Tetramethylphenyl Diimide Core

Next, a rotational energy profile was calculated [145] to simulate the barrier to rotation about the *N*-aryl bond in the 2,3,5,6-tetramethyl phenyl diimide core (N_2-C_3), from *syn*- to *anti*-, using a structurally reduced model to reduce computation time (Figure 4.3). The dihedral angle C_1-N_2-C_3-C_4 was constrained and the energy of ten conformers was calculated from 0 to 90 ° ([145], using the method previously outlined in Chapter 3, and again in Chapter 8). The structurally reduced model compound for this calculation does not account for π-π interactions between the opposing bis-porphyrins in the *syn*- conformation, changes to bond properties and electronic effects of the second *para*- imide in the linker, or additional steric crowding on the underside of the polycyclic scaffold when additional polycycles are fused to the linker.

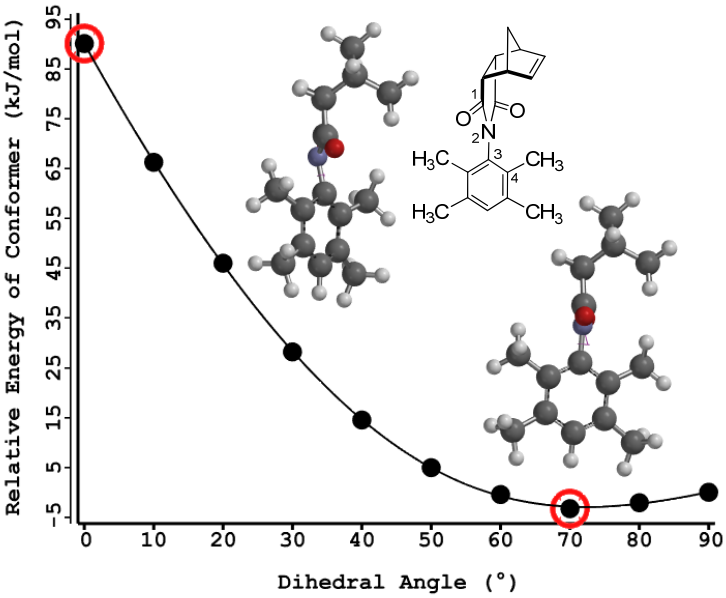

Figure 4.3 - Rotational energy profile and barrier to rotation about the imide-phenyl single bond in the linker (energy profile Hartree-Fock 6-31G*, energy of each conformation recalculated using Density Functional B3LYP/6-31G*).

The relative energy difference between the global maximum and global minimum was calculated to be 93 $kJmol^{-1}$ (22.2 $kcalmol^{-1}$). However, calculations rarely converged without errors; the imide and 2,3,5,6-tetramethylphenyl ring are sterically unable to be in the same plane. When calculations managed to converge (Figure 4.3), the geometry of the 0 ° conformer is clearly highly strained; the imide nitrogen is distorted out of the imide plane. Distortion of the imide from planarity and

pyramidalisation of the imide nitrogen (amongst other distortions within the molecule) has been reported for similar calculations of sterically crowded phenyl imide derivatives as the phenyl ring approaches planarity with the imide, as well as observed in X-ray crystal structures of sterically crowded *ortho*- substituted phenyl imides [119, 121, 122]. The molecular modelling herein indicated an extremely high energy barrier to rotation, and suggested that interconversion between the *syn*- and *anti*- conformations was highly unlikely.

A previous literature report has calculated the barrier to rotation for structurally similar *N*-(2-methylphenyl)maleimide to be 526.7 $kJmol^{-1}$ (125.8 $kcalmol^{-1}$) [124]. Although this energy barrier is substantially higher than that calculated for the more sterically hindered substrate in this thesis, both results suggest the barrier to rotation is significantly greater than for the unhindered substrate in Chapter 3, and greater than that accessible at room temperature. In addition, restricted rotation has been observed in experimental variable temperature NMR studies on *ortho*- methylphenyl substituted imide derivatives [125, 126], however, these systems with a single phenyl substituent do undergo thermal interconversion.

It is important to highlight that for the 2,3,5,6-tetramethylphenyl diimide in this work, partial rotation within each of these conformations without interconversion can reasonably be expected to occur. In Figure 4.3, the lowest energy conformation occurs at a dihedral angle of approximately 75 °, while the 90 ° conformer has a local maximum only slightly higher in energy (3.3 $kJmol^{-1}$/0.79 $kcalmol^{-1}$), and is available from thermal energy from the surroundings [124]. Thus a range of conformers are expected to be energetically accessible, which for the *syn*- adduct provides the tweezer with the capacity to undergo re-organisation upon complexation with guests of different lengths.

4.4 Synthesis

4.4.1 *Syn*- and *Anti*- Linkers

Having identified that incorporation of four methyl groups onto the central phenyl core was able to restrict rotation, attention was focussed on the synthesis. The second generation linker synthesis involved the condensation of one equivalent of *endo*-Mitsudo anhydride **12** with 0.5 equivalents of 1,4-diamino-2,3,5,6-tetramethylbenzene **26**, followed by ring closing to form imides **27** and **28** (Figure 4.4).

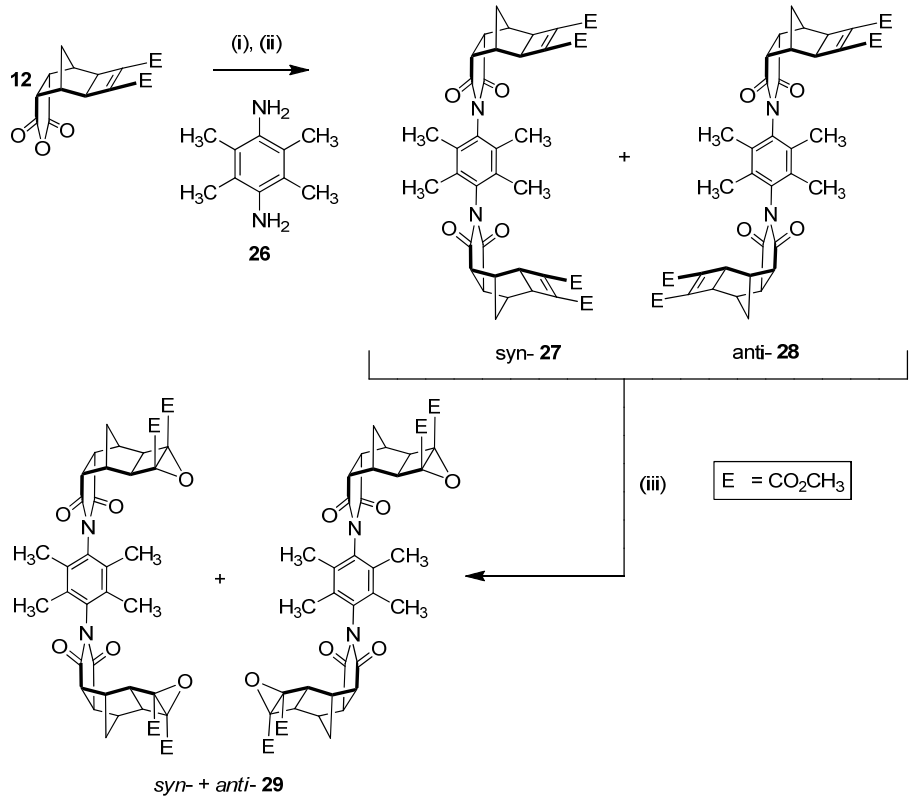

Figure 4.4 - Synthesis of the Restricted Rotation Linker. (i) 2,3,5,6-tetramethyl-*p*-phenylenediamine **26** (0.5 eq.), dry DMSO, Ar deoxygenated, 80 °C, 1 day; (ii) $NaOAc/Ac_2O$, 80 °C, 1 day, 72% (as a mixture of *syn*- **27** + *anti*- **28**); (iii) anhydrous *t*BuOOH in toluene (3.3 M, 2.5-5 eq.), dry CH_2Cl_2, 0 °C, 10 min, *t*BuOK (1-2 eq.), room temp., 3.5 hrs, 51%.

While ^{1}H NMR spectrum of the freely rotating system **13** in Chapter 3 revealed a single proton resonance for the phenyl core, the NMR spectrum of the restricted rotation reaction mixture (not shown) revealed two pairs of signals for the methyl proton resonances. This was suspected to be from the two different linker conformations of *syn*- **27** and *anti*- **28**. The mixture showed a slight deviation from statistical, in an approximately 60:40 ratio based on the relative integration between

the two pairs of signals within the mixture (not shown). However, this requires further investigation; the apparent non-statistical mixture could result from differential solubility of the *syn*- and *anti*- conformations in the precipitate and filtrate during the reaction.

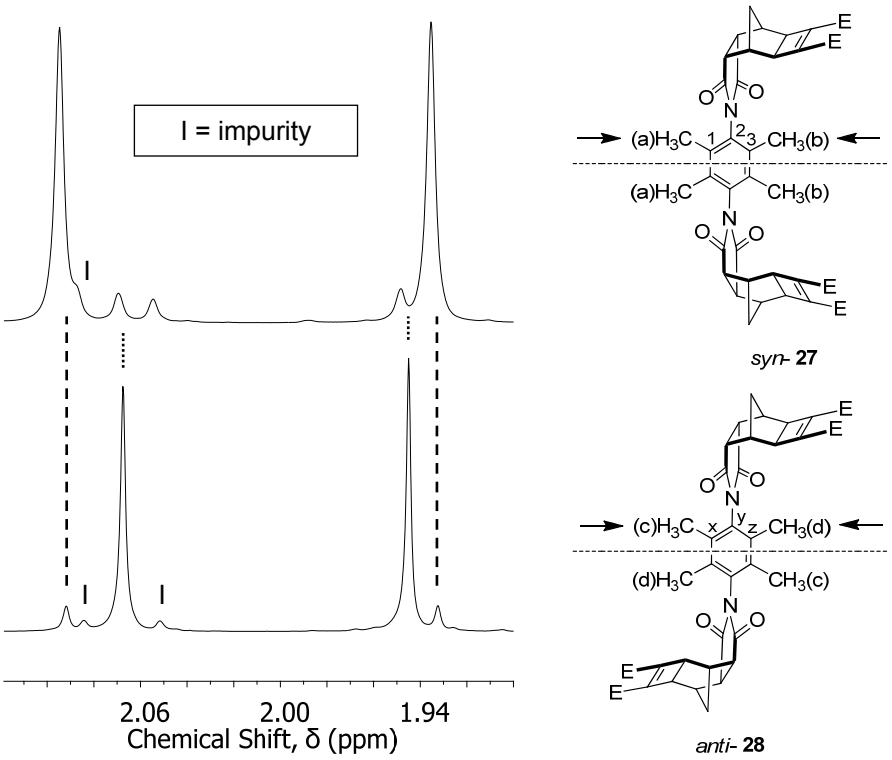

Figure 4.5 - Part of the ^{1}H NMR spectrum of the *syn*- **27** and *anti*- **28** restricted rotation linker (absolute conformation unassigned), showing the different chemical environments of the methyl resonances.

To provide full experimental evidence for separate *syn*- **27** and *anti*- **28** conformers, a small sample was separated by using a combination of column chromatography and selective recrystallisation. The ^{1}H NMR spectrum of the methyl resonances are shown in Figure 4.5[18]. In either conformation, the two phenyl proton resonances are non-equivalent; one of the methyls is positioned underneath the *endo*- polycyclic moiety ((b) in *syn*-, (d) in *anti*-), while the second methyl is positioned on the outside of the polycyclic section ((a) in *syn*-, (c) in *anti*-). Additionally, the *syn*- and *anti*- conformations have different ^{13}C NMR spectra (not shown here); pairs of non-equivalent methyl carbon resonances similar to the ^{1}H NMR spectrum, as well as the

[18] *Syn*- **27** and *anti*- **28** each contained trace of the other conformation from difficulty in separation. These are shown by the dotted lines. Impurity is marked by the letter I.

phenyl carbon resonances themselves (three phenyl signals per conformer, marked 1-3 and x-z on the *syn*- and *anti*- structures respectively in Figure 4.5).

Unfortunately the absolute assignment of each conformer as either *syn*- **27** or *anti*- **28** has not been determined at this stage; ^{1}H NOE spectroscopy was inconclusive, while attempts to grow single crystals suitable for X-Ray crystallographic analysis were unsuccessful. Although assignment of the linker conformation is of interest, it was not critical at this stage of the synthesis. The stability of the *syn*- and *anti*- conformations to interconversion is examined later in this chapter in tweezer form.

The linker mixture was subsequently epoxidised under standard conditions for these substrates (*t*BuOOH/*t*BuOK) [102, 104] as a mixture of *syn*- **27** and *anti*- **28** to afford the bis-epoxide mixture **29** (Figure 4.4). Separation of the *syn*- and *anti*- conformations was undertaken as the tweezer after the addition of the porphyrin receptors to the linker.

4.4.2 Associated Restricted Rotation Substrates

Further to the restricted rotation *endo*- Mitsudo linker **27**/**28**, several additional analogues were synthesised, including the *endo*- non-Mitsudo linker **30 (**Figure 4.6 (a)), and both the *exo*- non-Mitsudo **31**/**32** and *exo*- Mitsudo **33** linker analogues (Figure 4.6 (b), (c), (d) respectively). The reactivity of these restricted rotation *endo*- and *exo*- non-Mitsudo linkers under Mitsudo conditions is discussed in Appendix 3, and synthetic details are provided in Chapter 8.

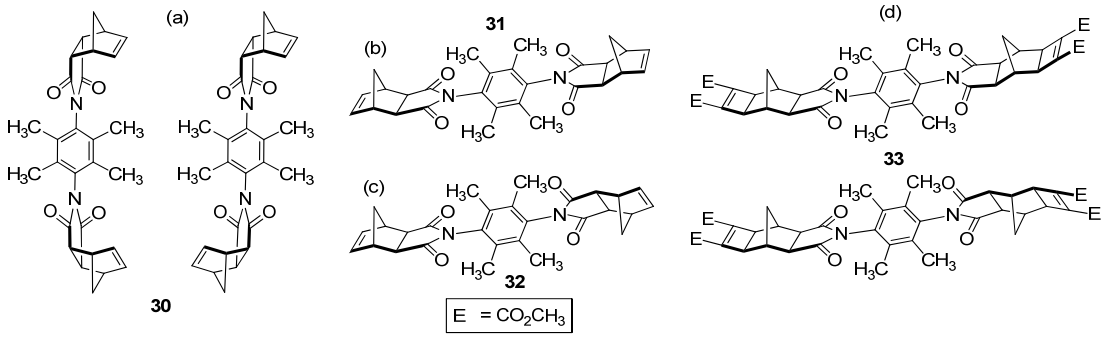

Figure 4.6 - Additional restricted rotation *endo*- and *exo*- analogues **30**-**33**.

During the synthesis of the *exo*- non-Mitsudo restricted rotation linker analogue **31**/**32**, the *syn*- **31** and *anti*- **32** conformations displayed sufficiently different solubilities to be separately expressed in the precipitate and filtrate reasonably purely

of each other, as determined by NMR. For the *exo*- restricted rotation compounds, *syn*- **31** refers to the conformation where both norbornyl bridgeheads are pointing in the same direction, while *anti*- **32** refers to the case where norbornyl bridgeheads are pointing in opposite directions. Conveniently, crystallisation of the compounds contained in both the precipitate and filtrate yielded single crystals suitable for X-ray diffraction measurements (slow evaporation of acetonitrile). The crystal structures (solved by Prof Jonathan White, The University of Melbourne) are shown in Figure 4.7. While crystal packing forces must be considered, these crystal structures provide unequivocal experimental evidence supporting the formation of distinct *syn*- **31** and *anti*- **32** conformations (Figure 4.7 (a) and (b) respectively). Key parameters for the X-Ray crystallographic measurements are provided in Appendix 4.

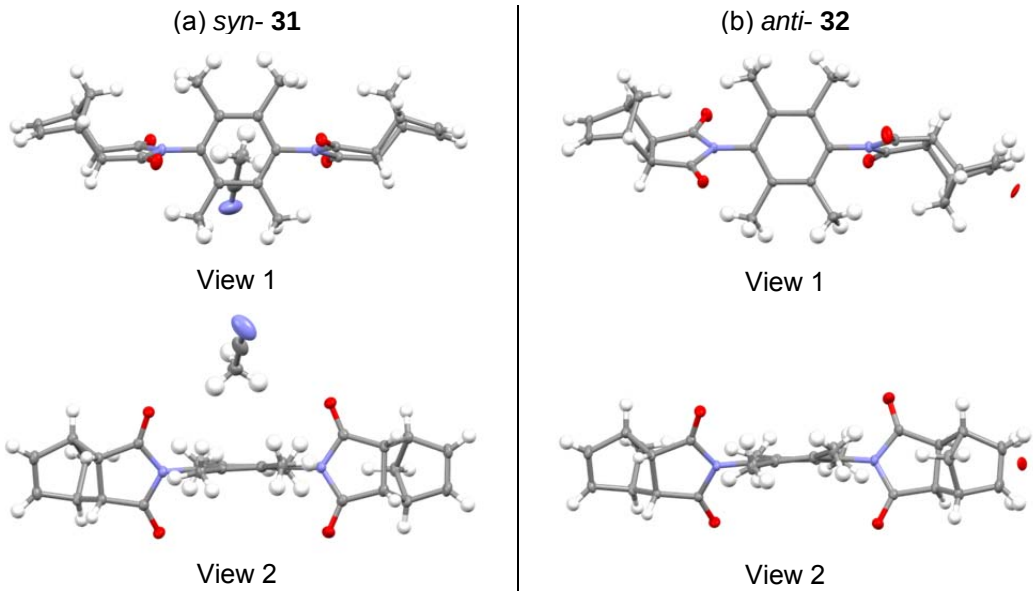

Figure 4.7 - X-ray crystal structures of the *exo*- non-Mitsudo restricted rotation linker; (a) *syn*- **31** (crystallised with a molecule of acetonitrile), (b) *anti*- **32** (co-crystallised with approximately 6 % mono- epoxide).

A particularly interesting structural feature revealed in Figure 4.7 is the noticeable deviation of the 2,3,5,6-tetramethylphenyl core from planar. The *syn*- **31** conformation is co-crystallised with acetonitrile solvent, while the *anti*- **32** conformation is co-crystallised with approximately 6% of a mono-epoxide impurity.

This later co-crystallisation with epoxide impurity was intriguing. Although the HRMS for the *syn*- and *anti*- conformations confirmed the expected molecular formula ($C_{28}H_{28}N_2O_4Na^+$ $[M+Na]^+$), a second signal in the mass spectra of both compounds corresponding to the molecular formula with an additional oxygen atom (epoxide, $C_{28}H_{28}N_2O_5Na^+$), within 37 ppm of the theoretical mass of this ion. There

is a literature report observing partial epoxide conversion on polycyclic derivatives during recrystallisation (structures Figure 4.8) [184]. In this paper, it is discussed that epoxidation of similar structures is known to occur in the presence of molecular oxygen and an initiator, but that perhaps uninitiated epoxidation could occur at a rate too low for convenient measurement [184].

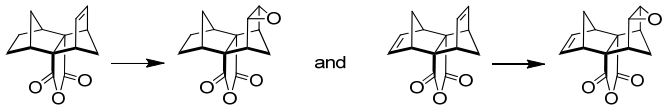

Figure 4.8 - Literature examples of epoxide formation in polycyclic structures during recrystallisation [184].

4.4.3 *Syn*- and *Anti*- Restricted Rotation Tweezers

Returning to the synthesis of the restricted rotation tweezer, the bis-epoxide restricted linker **29** (mixture of *syn*- and *anti*-) was subsequently appended with *exo*-porphyrin receptor **18** [1] via the alkene plus cyclobutane epoxide (ACE) reaction (Figure 4.9). During the period of these reactions, the microwave reactor was offline for maintenance, and the traditional sealed tube method was instead employed [75]. Unfortunately, this appears to have resulted in significantly lower yields than for the freely rotating system, possibly from the extensive purification required to remove a porphyrinic degradation product with a blue/green hue. Overall, the reaction proceeded in a 23% yield, which upon NMR analysis was able to be designated as 10 % *syn*- **34** and 13 % *anti*- **35** conformations.

The ^{1}H NMR spectra of the *syn*- **34** and *anti*- **35** mixture contained several features characteristic of ACE-coupled reactions, including a small downfield shift for the methyl ester resonance compared to the epoxide **29** [160], along with the disappearance of the norbornene proton resonance from the *exo*- porphyrin receptor **18** at 6.45 ppm. The resonance at 90 ppm in the ^{13}C NMR (obtained for the freebase *syn*- **34** and *anti*- **35** mixture) is observed in similar polycyclic systems [113], and is assigned to the carbon atoms to which the oxygen bridgeheads are attached in the newly formed methyl ester substituted 7-oxanorbornane [113].

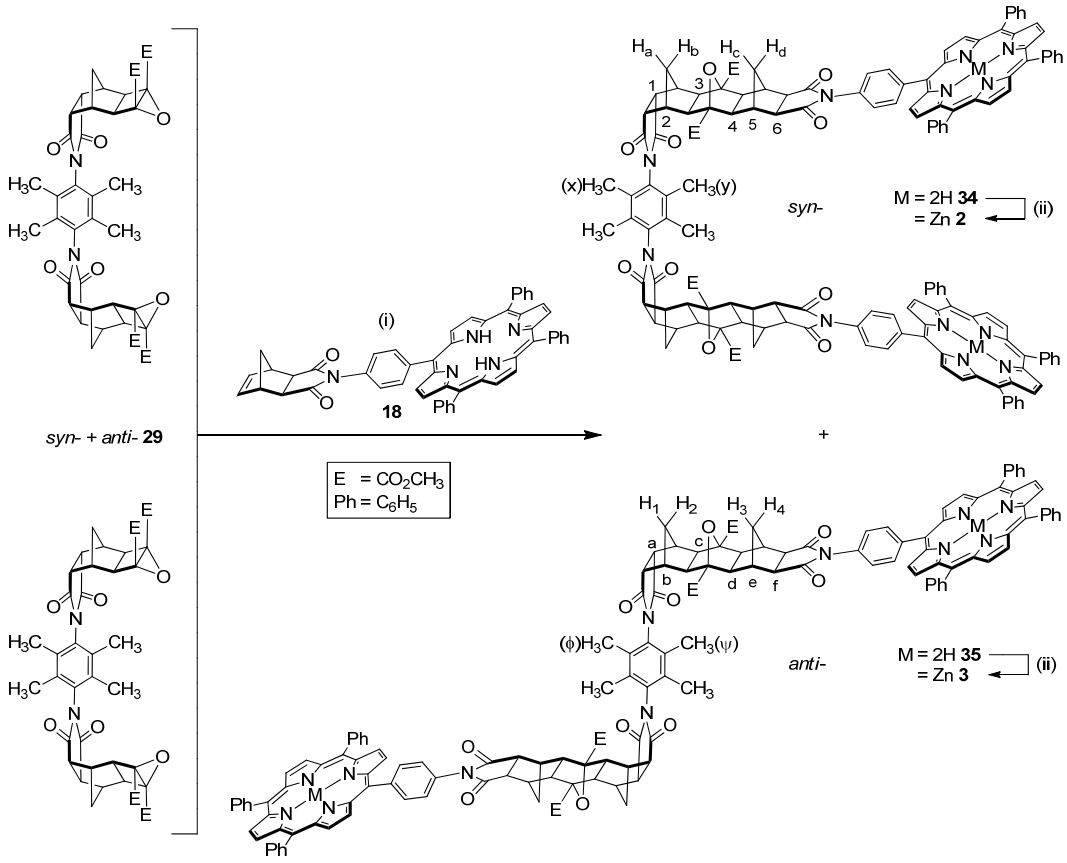

Figure 4.9 - Synthesis of the Restricted Rotation Tweezer, *syn*- **2** and *anti*- **3**. (i) *exo*-porphyrin receptor **18** (2 eq.), dry THF, sealed tube, 160 °C, 24 h, 23% (10 % *syn*- **34** + 13% *anti*- **35**); (ii) $Zn(OAc)_2$/MeOH/$CHCl_3$, reflux, 1 h, > 90%.

In addition, ^{1}H NMR finally enabled the assignment of the *syn*- **34** and *anti*- **35** conformations from the porphyrin resonances (shown later). Relative integration of the two inner pyridyl proton resonances at -2.80 and -2.84 ppm suggested the ratio of *syn*-:*anti*- was approximately 43:57. While separation by column chromatography yielded the *anti*- isomer completely free of *syn*-, the *syn*- conformation contained approximately 25 % residual *anti*-. In an effort to conserve limited product, further purification to remove *anti*- **35** from *syn*- **34** was carried out post- zinc(II) metallation, as *syn*- **2**. The identity of the partially purified freebase *syn*- and *anti*- conformations was confirmed by using accurate MS (ESI-TOF, for two samples containing different ratios of *syn*- **34** and *anti*- **35**: $[M+2H]^{2+}$ found: 1184.4110, calc: 1184.4063, and $[M+2Na]^{2+}$ found: 1162.4267, calc: 1162.4297).

The freebase *syn*- **34** and *anti*- **35** conformations were metallated with zinc(II) under standard conditions [159], giving *syn*- **2** and *anti*- **3** respectively (Figure 4.9). Zinc(II) metallation was characterised by loss of the porphyrin inner pyrrole proton resonance at -2.80 (*anti*-) and -2.84 (*syn*-) in the ^{1}H NMR spectrum. Slow

recrystallisation enabled the zinc(II) *syn*- **2** conformation to be purified completely free of *anti*- **3**.

In the ^{1}H NMR spectrum for each adduct (*syn*- **2** Figure 4.10, *anti*- **3** Figure 4.11), ten polycyclic resonances can be observed as expected (excluding the methyl ester and two methyl core resonances); six singlets and four doublets. The doublets arise from two pairs of non-equivalent methylene bridge protons, H_a/H_b and H_c/H_d in the case of *syn*- **2**, H_1/H_2 and H_3/H_4 in the case of *anti*- **3** (Figure 4.9). These appear at significantly different chemical shifts, characteristic of steric compression by oxygen in these systems [151], and confirms the formation of a linear ACE product [151]. These resonances occur at chemical shifts of 2.77/1.43 ppm and 2.49/1.13 ppm for *syn*- and 2.77/1.42 ppm and 2.54/1.22 ppm for *anti*-. The remaining six singlets correspond with the number of remaining unique proton chemical environments protons along the polycyclic scaffold (marked 1-6 for *syn*- and a-f for *anti*- in Figure 4.9). In addition, a pair of methyl resonances for the substituted linker core can be observed at chemical shifts of 2.31 and 2.00 ppm for *syn*- **2** and 2.28 and 2.04 ppm for *anti*- **3** (x and y for *syn*-, φ and ψ for *anti*-, Figure 4.9, absolute assignment not determined). This is in line with similar observations for the *syn*- **27** and *anti*- **28** linkers described in Figure 4.5.

The difference in the aromatic region between the ^{1}H NMR spectra of the *syn*- **2** and *anti*- **3** adducts is shown in Figure 4.12. Splitting of the porphyrin resonances for the *syn*- conformation, in particular the β-pyrrole resonances, can be observed, indicating facial differentiation and interaction between the bis-porphyrins. For the *anti*- conformation, the porphyrin receptors physically cannot be positioned cofacially (unless intermolecular aggregation occurs), and no major splitting of the porphyrin resonances was observed. Additionally, the *syn*- porphyrin resonances are shielded relative to the *anti*-, further reinforcing the effect of the adjacent π system in the *syn*- conformation. Integration of the ^{1}H NMR resonances corresponded with the coupling of two porphyrin receptors to the polycyclic linker.

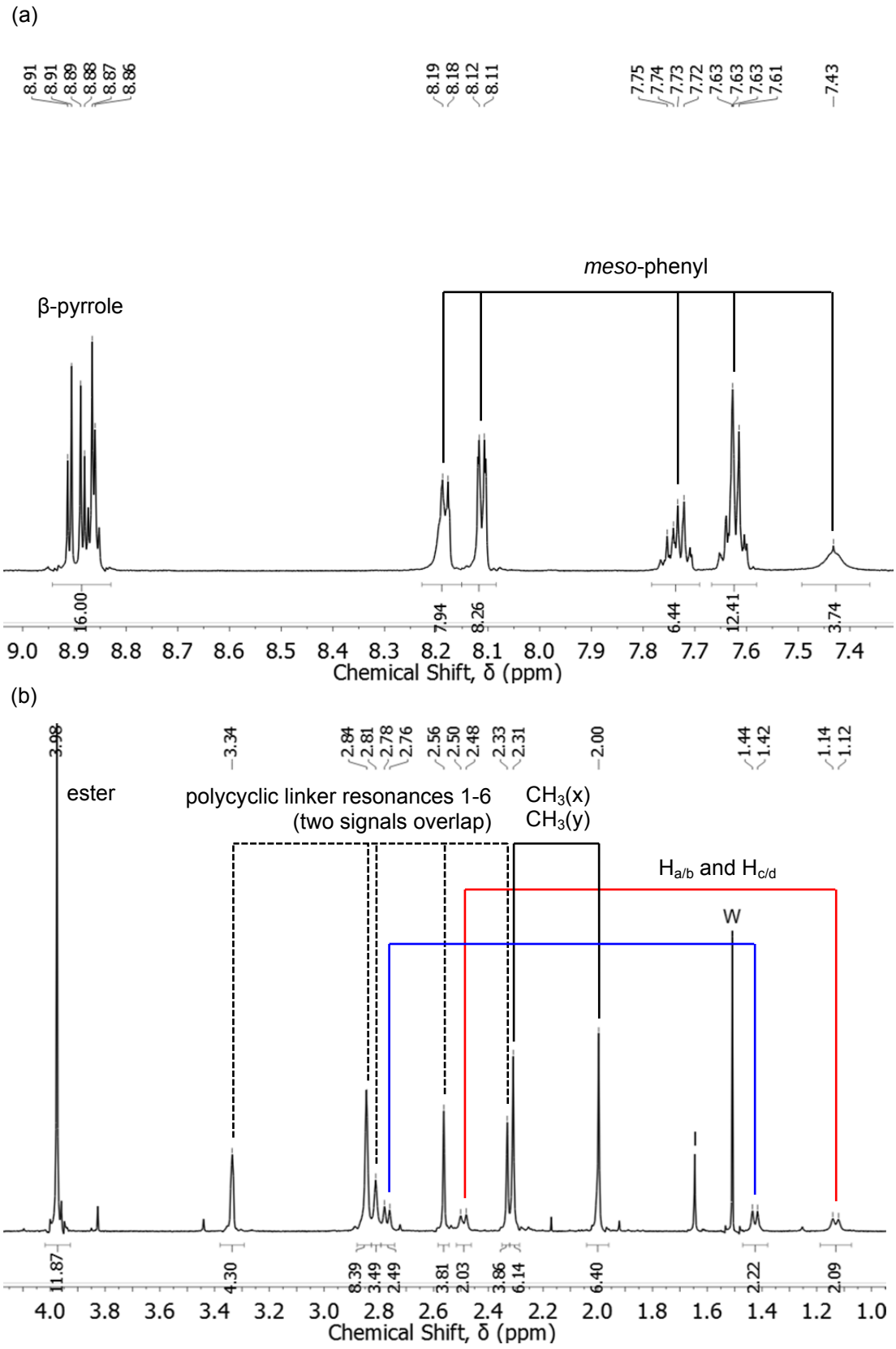

Figure 4.10 - Selected ^{1}H NMR spectral regions of the Zn *syn*- tweezer **2** showing (a) porphyrin β-pyrrole and *meso*-phenyl resonances, (b) polycyclic linker resonances 1-6, H_{a-d}, and CH_3(x/y) [Figure 4.9]. W denotes H_2O, I denotes impurity.

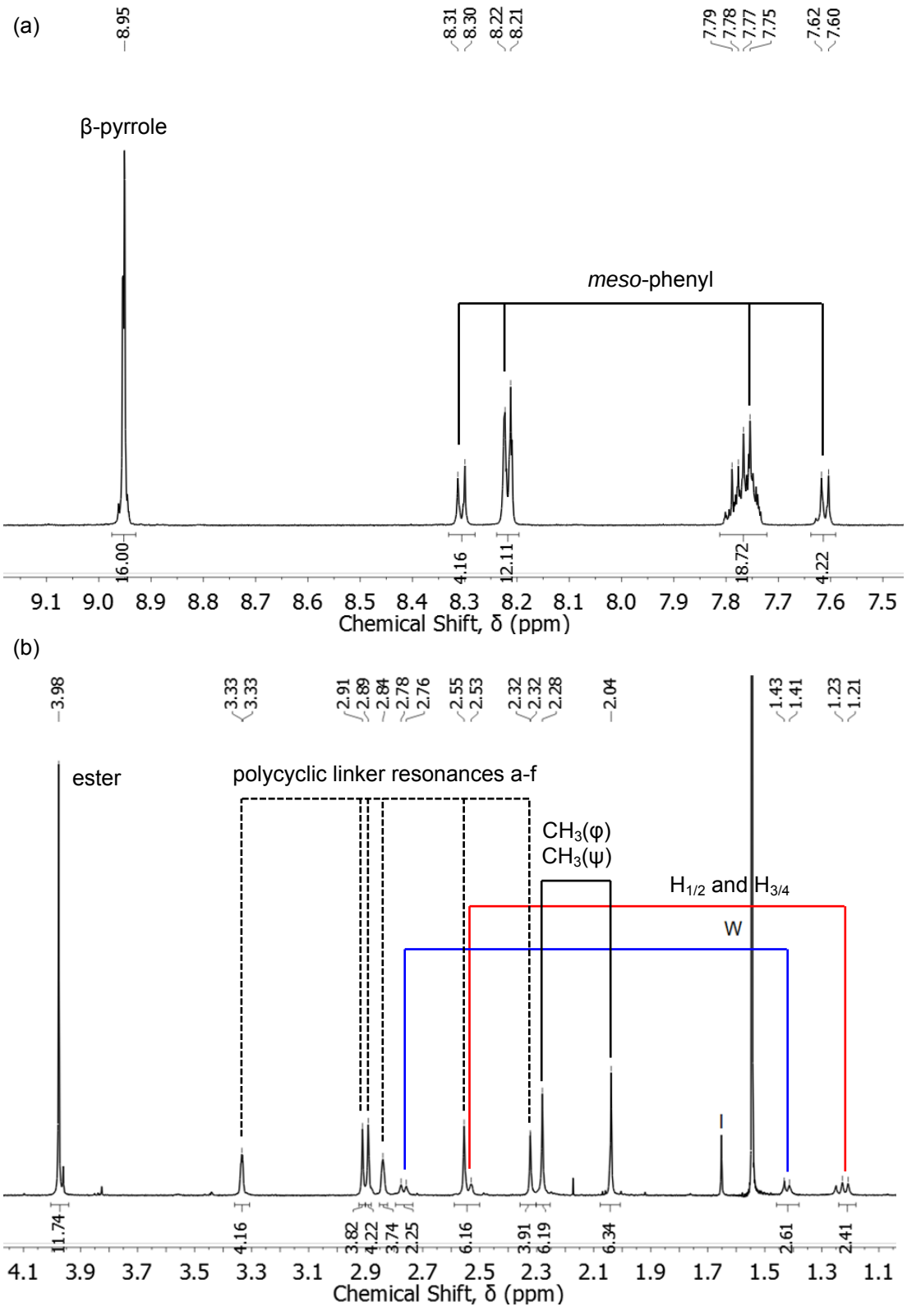

Figure 4.11 - Selected ^{1}H NMR spectral regions of the Zn *anti*- tweezer **3** showing (a) porphyrin β-pyrrole and *meso*-phenyl resonances, (b) polycyclic linker resonances a-f and $H_{1\text{-}4}$, and $CH_3(\varphi/\psi)$ [Figure 4.9]. W denotes H_2O, I denotes impurity.

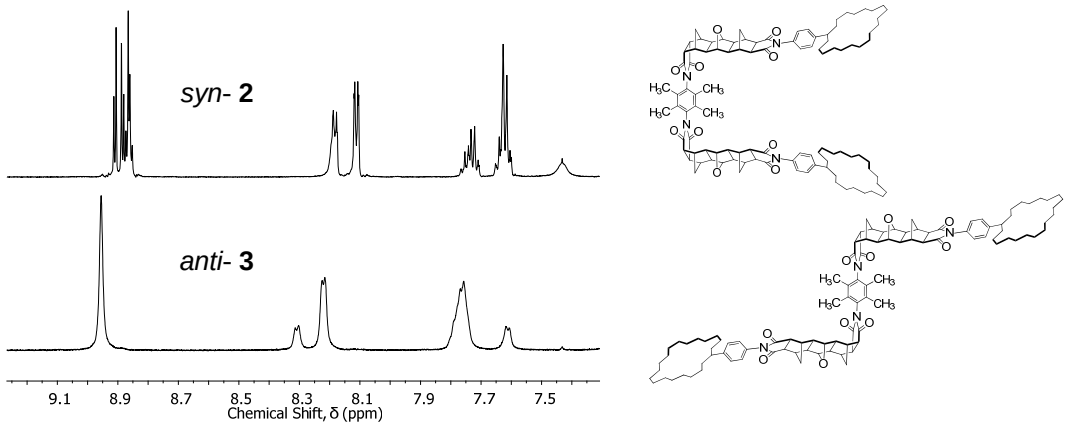

Figure 4.12 - Partial ^{1}H NMR (aromatic region) of the zinc(II) metallated *syn*- **2** and *anti*- **3** restricted rotation tweezer.

For the *syn*- **2** tweezer, several of the porphyrin *meso*-phenyl resonances are very broad while others appear sharp. At very dilute concentrations, these broad signals are slightly sharper. Furthermore, the ^{1}H NMR spectrum was highly concentration dependent (Figure 4.14 (a)), with significant resonance shifts observed for porphyrin and polycyclic resonances upon dilution (0.3-0.7 ppm). Additional resonance shifts are observed between +20 °C and -50 °C (Figure 4.14 (b)). This data suggests that the *syn*- tweezer is undergoing dynamic conformational changes (but not to *anti*-) on the NMR timescale, and/or changes to intermolecular aggregation influenced by concentration and temperature.

Figure 4.13 outlines a possibility of an intermolecular aggregate, an intercalated dimer stabilised by π-π interactions. Future investigation of this hypothesis could be undertaken by conducting a DOSY ^{1}H NMR dilution experiment to examine changes to the hydrodynamic radius with concentration.

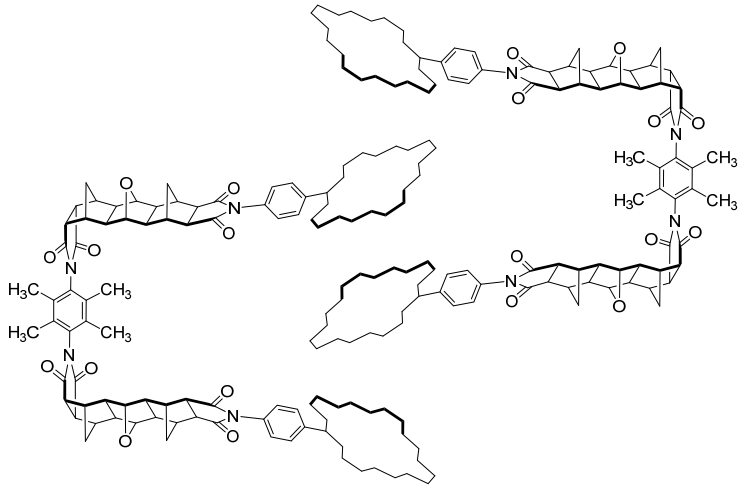

Figure 4.13 - Possible intermolecular aggregation of the *syn*- **2** tweezer (intercalated dimer) which could explain the concentration dependent ^{1}H NMR spectra (structural detail omitted for clarity).

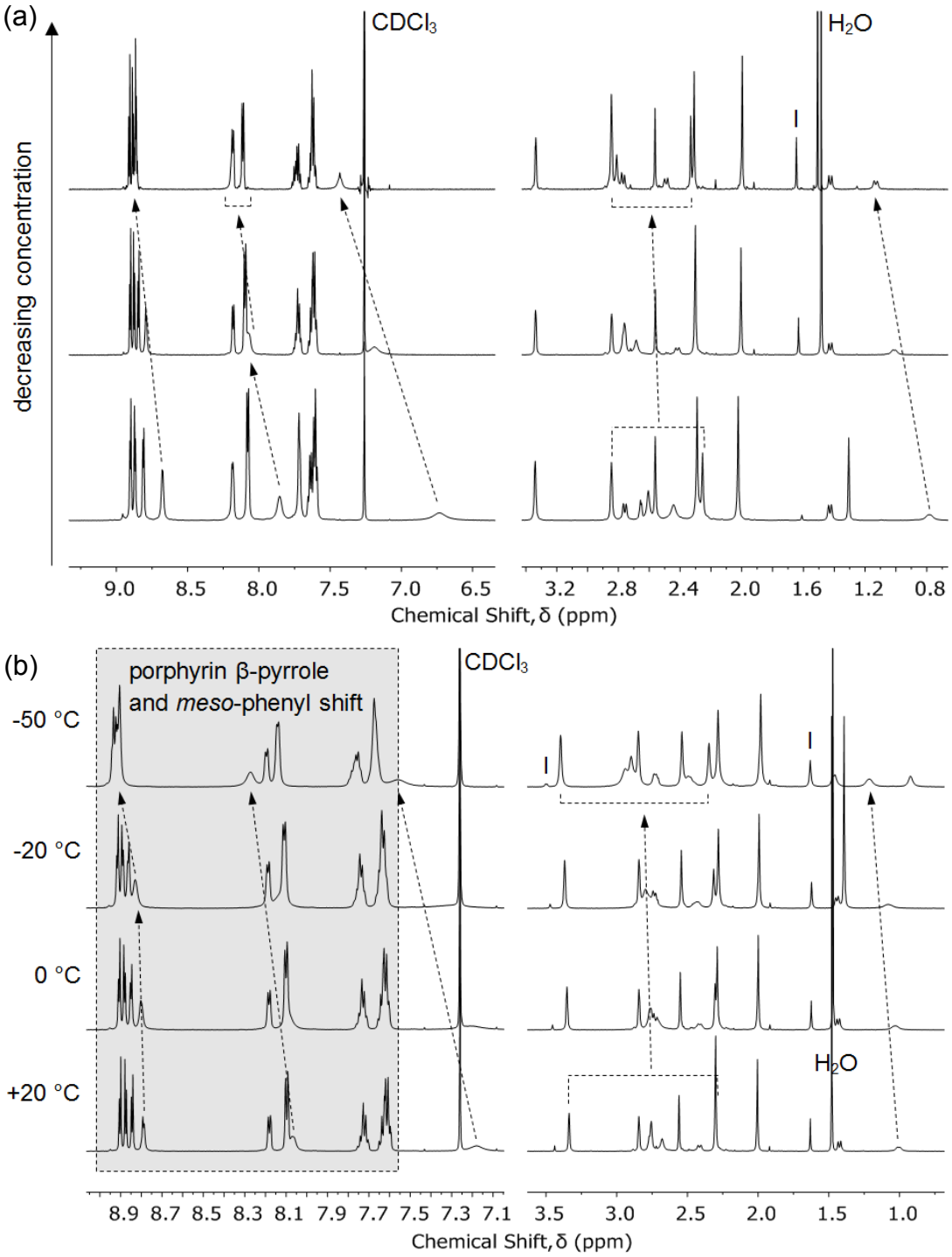

Figure 4.14 - Selected ^{1}H NMR spectral regions of Zn *syn*- **2** showing resonance shifts as (a) the concentration is decreased (bottom to top), and (b) the temperature is decreased (bottom to top). The main resonance shifts are annotated by dotted arrows. I denotes impurity.

For the zinc(II) *anti*- **3** adduct, the ^{1}H NMR spectrum was significantly broadened compared to the freebase adduct. However, this appears to be related to poor solubility in $CDCl_3$, rather than due to an exchange process. There are only minor (< 0.1 ppm) shifts in the spectrum at -50 °C compared to room temperature. Concentration dependence of the ^{1}H NMR could not be established for *anti*- **3** due to poor solubility at concentrations greater than 0.85 mM.

The UV-Vis spectra of the Zn(II) metallated *syn*- **2** and *anti*- **3** adducts revealed further information. The Zn(II) *anti*- tweezer **3** and Zn(II) mono-porphyrin receptor **22** display very similar Soret maxima and peak band widths at half height, 419 nm and 10 nm respectively (Table 4.1). The absence of exciton coupling interactions supports the adoption of the *anti*- conformation [58], where the bis-porphyrins are unable to interact intramolecularly. Conversely, the Soret maxima of the Zn(II) *syn*- **2** tweezer is blue shifted by 1 nm relative to the Zn(II) mono-porphyrin receptor **22**, and has a slightly larger peak band width at half height than the Zn(II) freely rotating tweezer **1** (Table 4.1). Although the blue shift and broadening of the Soret band are both small, this could indicate weak exciton coupling interactions [37, 58, 73, 85, 161-164] between the porphyrins in the *syn*- adduct. The weakness of the exciton coupling in the *syn*- adduct suggests that either the bis-porphyrins are by no means fixed in a cofacial orientation, and that porphyrin units are able to undergo rotation either about the single bond between the imide and porphyrin moiety, and/or the two porphyrin arms can undergo partial but restricted rotation about the phenyl diimide core.

Table 4.1 - Summary of UV-Vis data in chloroform comparing the *syn*- and *anti*- restricted rotation tweezers to other porphyrin adducts in Chapter 3.

Species	**Zn(II) mono-porphyrin, 22**	**Zn(II) freely rotating tweezer, 1**	**Zn(II) *syn*- restricted tweezer, 2**	**Zn(II) *anti*- restricted tweezer, 3**
λ_{max} (nm)	419.3	419.5	418.3-418.5	419.3-419.6
Width (nm) [a]	9.9	11.0	11.5	10.1
$\varepsilon_{singleporphyrin}$ (x 10^5 $Lmol^{-1}cm^{-1}$)	6.47	4.7-6.9 [b] [c]	4.9 [c]	5.8 [c]

[a] Peak band width measured at half height.

[b] Quoted as a range to account for possible errors in concentration.

[c] $\varepsilon_{singleporphyrin} = \varepsilon_{experimental}/2$ (tweezer has two porphyrins).

4.4.4 Stability to Interconversion

The *syn*- **2** and *anti*- **3** restricted rotation tweezers appear to be stable to interconversion at room temperature over the duration of experiments. Additionally, NMR of the pure *anti*- **3** adduct after microwave irradiation at 95 °C for 15 minutes (300 W, 50 psi), and sonication at 30 °C for 15 minutes showed no detectable interconversion from *anti*- **3** to *syn*- **2**. This provides experimental evidence for the high barrier to rotation about the sterically bulky fully substituted 2,3,5,6-tetramethylphenyl diimide core[19], as suggested by molecular modelling. Again, a range of intermediate conformers between the two extremes of *syn*- **2** and *anti*- **3** are expected to be energetically accessible. A schematic representation of restricted rotation is given in Figure 4.15.

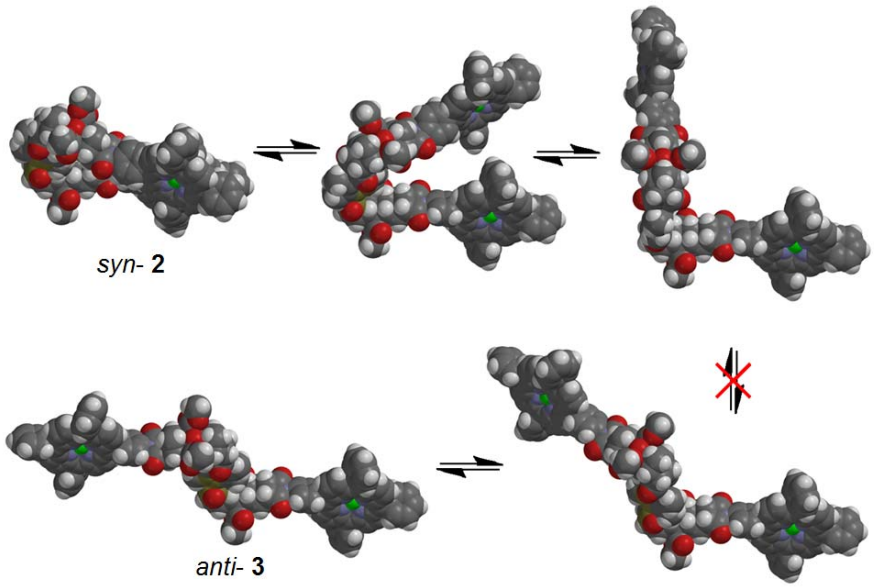

Figure 4.15 - Schematic representation of restricted rotation, but non-interconversion, within *syn*- **2** and *anti*- **3**.

[19] Several NMR studies for 2-methyl substituted *N*-phenyl imide derivatives are reported in the literature [125, 126], and although these system reveals two sets of proton signals for the methyl substituents, pertaining to two different conformations at standard temperatures, these resonances broaden at higher temperatures as the rate of bond rotation increases. Thus, it would appear that although these systems display partially restricted rotation, thermal interconversion does occur when only a single *ortho*- methyl substituent is present.

Further experiments are planned to test the limits of interconversion in this system, including variable temperature NMR, and prolonged heating of the pure *syn*- **2** and *anti*- **3** adducts at ACE coupling temperatures (170 °C), such as occurs during synthesis.

4.5 *Syn*- Host-Guest Study

The *syn*- **2** restricted rotation tweezer was the first to be examined for complexation with the diamino ligands DABCO **5** and bipy **6** using UV-Vis and NMR spectroscopy. The *syn*- host can form various complexes in solution, all of which are in equilibrium. These possibilities are outlined schematically in Figure 4.16, and reveal the possibility of 1:1 (K_{11} = [(*syn*-):ligand]/([*syn*-][ligand]), 1:2 (K_{12} = [(*syn*-):(ligand)$_2$]/([*syn*-][ligand]^2), and 2:1 (K_{21} = [(*syn*-)$_2$:ligand]/([*syn*-]^2[ligand]) stoichiometries.

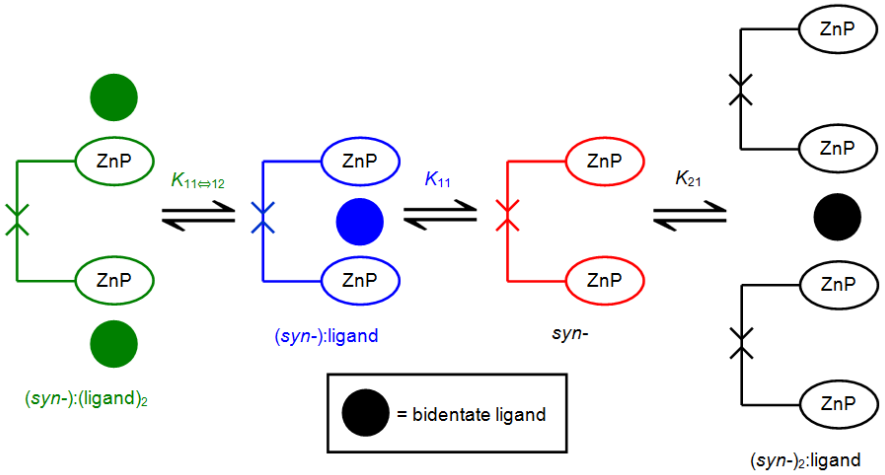

Figure 4.16 - Schematic representation of the various equilibria between *syn*- **2** tweezer and bidentate ligand.

4.5.1 *Syn*- Restricted Rotation Tweezer with DABCO (UV-Vis)

The investigation was commenced with UV-Vis spectroscopy, as this proved extremely informative in Chapter 3. Titration of a solution of DABCO **5** to a solution of *syn*- tweezer **2** resulted in a two-stage red shift of the Soret maximum. The first redshift, from 418.3 nm to 423.4 nm (Figure 4.17 (a)) is characteristic of a bis-porphyrin DABCO sandwich complex [30, 31]. A second gradual redshift occurs to 428.6 nm by 400 000 equivalents of DABCO, although this transition appears to only be partially complete. This is characteristic of simple mono-porphyrin DABCO complexes [30, 31]. Similarly to freely rotating host in Chapter 3, the UV-Vis

titration data was fitted to various binding models using multivariate global spectral analysis (HypSpec [166]). This resulted in equally reasonable fits for two different binding models, including host:guest 1:1 plus 1:2 (shown below) or 2:2 plus 1:2 (not shown).

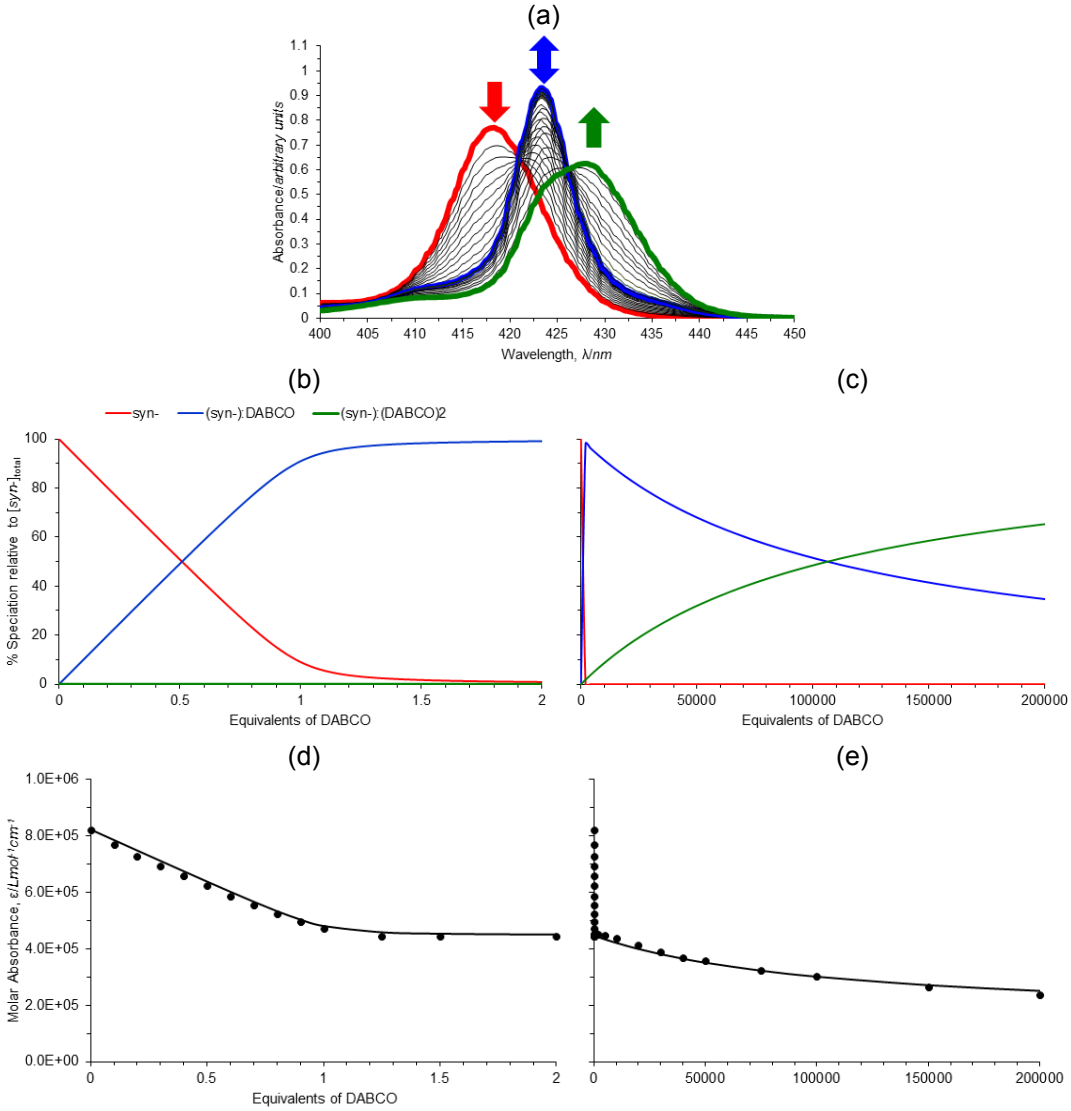

Figure 4.17 - (a) UV-Vis titration of *syn*- tweezer **2** with DABCO **5** in chloroform; (b) speciation diagram of *syn*- tweezer with DABCO (1:1 → 1:2, HypSpec, HySS2009) for 0 - 2 eq. of DABCO; (c) 0 - 200 000 eq. of DABCO; (d) best fit (black line) of the algorithm for equilibria between *syn*-tweezer, DABCO, (*syn*-):DABCO, and (*syn*-):$(DABCO)_2$ to the titration data (black circles) at 419 nm for 0 - 2 eq. of DABCO; (e) 0 - 200 000 eq. of DABCO.

The 1:1 plus 1:2 binding model gave K_{11} = 1.25 x 10^8 M^{-1} and K_{12} = 1.32 x 10^9 M^{-2} (single replicate, fitted to 200 000 eq. DABCO). These are assigned to intramolecular (*syn*-):DABCO **2**:**5** and open (*syn*-):$(DABCO)_2$ **2**:$(\mathbf{5})_2$ respectively (Figure 4.16). Shown in Figure 4.17 (b) and (c) are speciation diagrams for the UV-Vis titration data that have been separated out into 0-2 equivalents DABCO and 0-200 000

equivalents DABCO. Clearly visible is the initial formation of the 1:1 complex between the tweezer and DABCO, (*syn*-):DABCO, blue line), and its conversion into the 1:2 complex, (*syn*-):$(DABCO)_2$, green line) as more equivalents of DABCO are added to the solution.

The best fit of the algorithm for the formation of (*syn*-):DABCO and (*syn*-):$(DABCO)_2$ to the titration data at 419 nm is shown in Figure 4.17 (d) and (e) respectively. The fitting was moderate using the 423 nm and 430 nm data (not shown). The K_{11} obtained for (*syn*-):DABCO is over two orders of magnitude larger than mono-porphyrin:quinuclidine, and this enhancement is indicative of a bis-porphyrin DABCO sandwich complex [32, 34, 36].

The HypSpec software package output contains calculated UV-Vis spectra based on the fit (not shown). For the 1:1 plus 1:2 binding model, the intramolecular 1:1 species is a good match to the experimental spectra. However, the calculated spectral profile for the 1:2 species was slightly inaccurate compared to the experimental data, with the transition to this species being more advanced in the calculated spectrum and of a higher intensity.

Interestingly, the calculated spectra of the alternative binding model of 2:2 plus 1:2 are an excellent match to the experimental data. With equally reasonable fitting to the 1:1 plus 1:2 binding model, this might suggest that the 2:2 plus 1:2 binding model is better suited to the data. However, there are limited scenarios by which the *syn*- restricted system can physically form an intermolecular 2:2 species because of the geometric constraints imposed by restricted core rotation. The molecular modelling of these possible configurations is commented on in section 4.5.3.

In line with observations by others [30, 31], it is not always possible to distinguish between intramolecular 1:1 and intermolecular 2:2 complexes by using UV-Vis alone, and in these cases NMR is crucial in determining the correct binding model. This is examined in the following section.

4.5.2 *Syn*- Restricted Rotation Tweezer with DABCO (NMR)

Additional characterisation of the bis-porphyrin DABCO sandwich complex was provided by ^{1}H NMR titration of *syn*- tweezer with DABCO in $CDCl_3$. As with the freely rotating system, there are two areas of diagnostic signals, namely the

porphyrin β-pyrrole and DABCO complex resonances. As per previous discussion in Chapter 3, there was error between the number of equivalents of guest titrated with host based on mass weighed compared to NMR signal integration, estimated to be 10 % at 20 °C and for 20 % at -50 °C.

At 20 °C, the β-pyrrole signals for uncomplexed *syn*- tweezer occur at 8.92-8.75 ppm (Figure 4.18 (a)). The addition of up to 0.9 titrated equivalents of DABCO (integration suggests 1 equivalent) resulted in the appearance of a second β-pyrrole signal at 8.55 ppm. This upfield shift is typical of β-pyrrole protons in a bis-porphyrin DABCO sandwich complex and results from shielding by opposing ring currents of two porphyrin aromatic systems in close proximity [30, 31, 66]. The species are in slow exchange on the NMR chemical shift timescale, and the β-pyrrole complex signal increases at the expense of uncomplexed *syn*- tweezer. The relative integration of the sandwich β-pyrrole resonance to the total β-pyrrole resonance (free plus sandwich) is consistent with the formation of a species with the empirical formula of 1:1 (within 10 % error), such as intramolecular (*syn*-):DABCO or intermolecular (*syn*-)$_2$:(DABCO)$_2$, and is later shown to be the former. Addition of greater than 1 equivalent of DABCO causes the β-pyrrole resonance to shift downfield as increasing proportions of the open porphyrin species, (*syn*-):(DABCO)$_2$, forms in fast exchange on the NMR chemical shift timescale. However, the shift for the *syn*-tweezer after 5 equivalents of DABCO is comparatively small compared to the freely rotating tweezer ($\Delta\delta$ = 0.033 ppm and 0.082 ppm respectively), indicating the *syn*- DABCO sandwich complex is more resistant to excess DABCO than the freely rotating system at NMR concentrations and on the NMR chemical shift timescale.

The porphyrin *meso*-phenyl protons (not shown) are broadened below 1 equivalent of DABCO in the sandwich complex, but sharpen for greater than 1 equivalent of DABCO and shift downfield, presumably as the sandwich complex fast exchanges with open species on the NMR chemical shift timescale. Little information could be obtained from the polycyclic resonances.

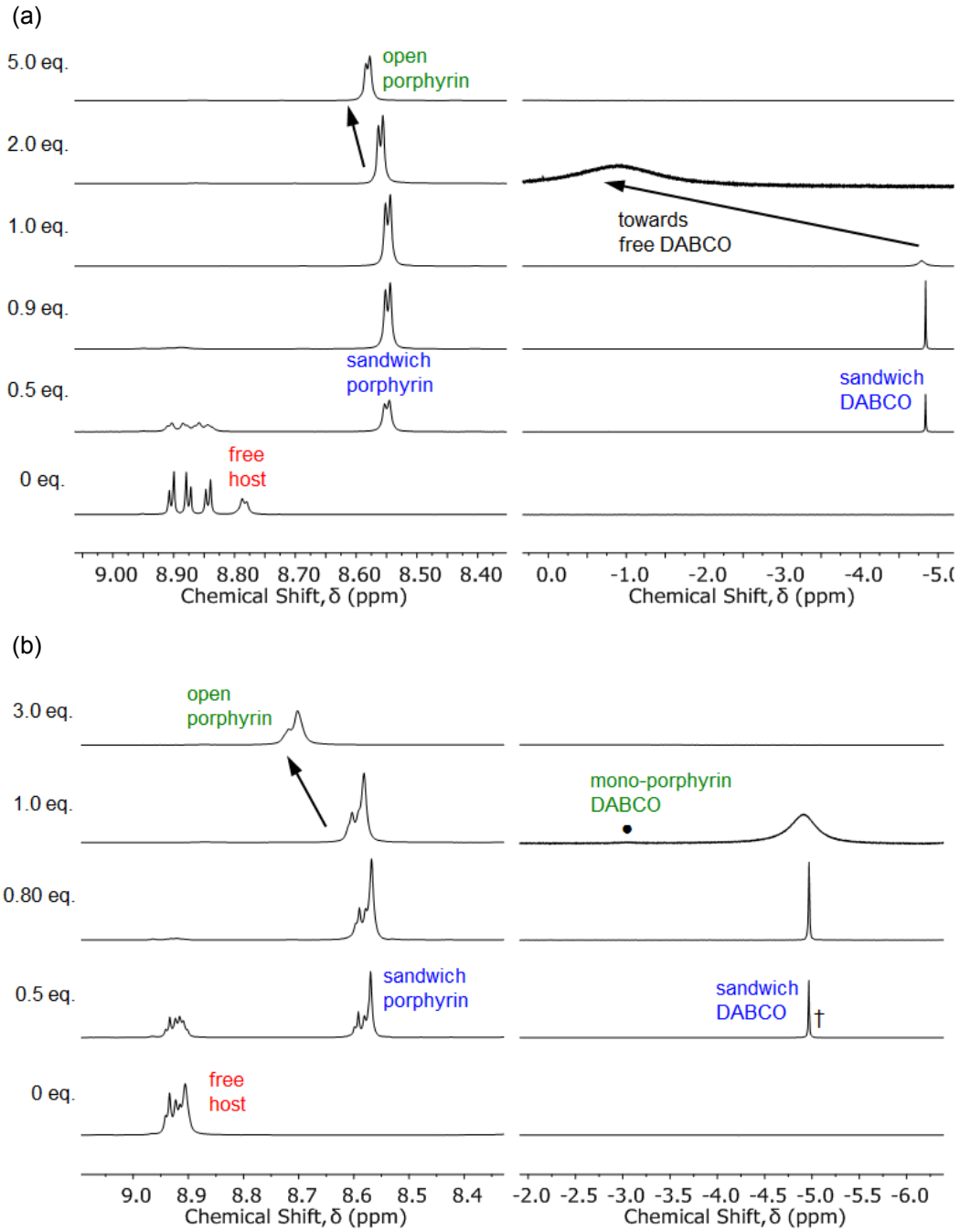

Figure 4.18 - Selected ^{1}H NMR spectra with various equivalents of DABCO at a) 20 °C (top pane) and b) -50 °C (bottom pane). † identifies minor amounts of an additional sandwich complex. ● identifies the mono-porphyrin:DABCO signal broadened into the baseline due to chemical exchange.

Further understanding of the complexation of DABCO by *syn*- is gained from the DABCO methylene resonance (Figure 4.18 (a)). For the addition of up to 0.9 titrated equivalents of DABCO (integration suggests 1 equivalent), a sharp singlet was observed at -4.84 ppm. This large upfield shift is typical of DABCO methylene protons in a bis-porphyrin DABCO sandwich complex, and again results from shielding by opposing ring currents of two porphyrin aromatic systems in close

proximity [27, 29-31, 52, 66, 172]. Again, the relative integration of the DABCO sandwich resonance to the ester signal[20] is consistent with the formation of a species with the empirical formula of 1:1 (within 10 % error). At 1 equivalent and greater of DABCO, the sandwich DABCO resonance broadens, and migrates downfield towards the value for free DABCO. This is consistent with chemical exchange with another species occurring at a fast exchange rate on the NMR chemical shift timescale at 20 ˚C, most likely a combination of (*syn*-):$(DABCO)_2$ and free DABCO.

At less than 1 equivalent of DABCO, all resonances, including the porphyrin and polycyclic resonances, are in slow exchange on the NMR chemical shift timescale, however, several of the free host resonances undergo simultaneous resonance shifts as their signal intensity is depleted and the complex resonance increases (not shown). This was particularly obvious for the methylene bridgehead proton at 1.0-1.3 ppm and the porphyrin β-pyrrole resonance. This phenomena was unusual to observe, and appears to indicate a second process occurring in addition to formation of the sandwich complex. This could be attributed to the concentration dependence of the free host ^{1}H NMR spectrum discussed earlier. In this case, as free host is consumed and complex is formed, the concentration of the free host decreases, which could explain the shifts of the remaining free host resonances.

Slowing the exchange rate between the various complexes in solution was achieved by lowering the sample temperature to -50 °C (Figure 4.18 (b)), and revealed several additional spectral features. Below 0.8 titrated equivalents of DABCO (integration suggests 1 equivalent), a small amount of an additional sandwich complex in addition to the main signal can be observed around -5 ppm (indicated by † in Figure 4.18 (b)). At greater than 0.8 titrated equivalents of DABCO (spectral features suggest greater than 1 equivalent), the system moves into fast exchange on the NMR chemical shift timescale. A small amount of the open complex can be observed at -3.06 ppm (indicated by ● in Figure 4.18 (b)) in addition to the main sandwich complex resonance, now broadened due to chemical exchange. The resonance at -3.06 ppm is characteristic of the α methylene protons of DABCO bound to a single

[20] The ester signal was selected as a reference because it does not change significantly on complexation and is the sum of free plus sandwiched species. In this case, the number of protons in the host ester resonance is equal to the number of protons in an isolated molecule of DABCO, and so their relative integrations do not require any normalisation.

porphyrin [28-30], and most likely corresponds to the destruction of the sandwich complex to open species, in this case (*syn*-):$(DABCO)_2$.

The porphyrin *meso*-phenyl protons (not shown) are sharp and highly desymmetrised below 1 equivalent of DABCO, indicating facial differentiation of the porphyrins within the sandwich complex. For greater than 1 equivalent of DABCO, the porphyrin *meso*-phenyl protons broaden and resymmetrise, suggesting diminishing facial discrimination, then shift downfield, presumably as the sandwich complex fast exchanges with open species on the NMR chemical shift timescale. Little information could be obtained from the polycyclic resonances.

To further investigate the composition of the complex formed between *syn*- tweezer and DABCO at NMR concentrations (millimolar), a simulated NMR speciation diagram (HySS2009, Protonic Software[166]) was generated using the association constants for successfully fitted binding models determined from the UV-Vis titrations, and compared with experimental NMR titration data [28, 30, 31]. Figure 4.19 shows this result for the 1:1 plus 1:2 binding model, where the blue line represents the predicted NMR speciation for the growth and decay of (*syn*-):DABCO, the green line represents the open species (*syn*-):$(DABCO)_2$, and the red line represents free host. The black circles and squares represent the experimental speciation for the slow and fast exchange NMR chemical shift timescale regions respectively, undertaken as described in Chapter 3 and Appendix 2[21].

As can be seen in Figure 4.19, there is excellent agreement between the simulated and experimental speciation across both the slow and fast exchange NMR chemical shift timescale regions. This confirmed that the binding model was the same at both UV-Vis and NMR concentrations for the *syn*-/DABCO system; formation of the intramolecular complex (*syn*-):DABCO and gradual decay of the sandwich complex into open species (*syn*-):$(DABCO)_2$.

This analysis was undertaken for the alternate binding model of 2:2 plus 1:2 (not shown). While the slow exchange NMR chemical shift timescale experimental data also matches the simulated formation of the 2:2 intermolecular complex, (*syn*-

[21] A chemical shift of 8.548 ppm (*syn*- + 0.9 eq. DABCO) was selected for the value for fully complexed species. A chemical shift of 8.829 ppm was selected for the value for fully open species, using data obtained in Chapter 4 for the *anti*- restricted rotation tweezer + 5 eq. DABCO.

)$_2$:(DABCO)$_2$, at NMR concentrations, K_{22} is very large such that minimal decay to the 1:2 open species is predicted by 5 equivalents in the simulation. As such, this does not accurately describe the experimental speciation, and so the 2:2 plus 1:2 binding model can be precluded.

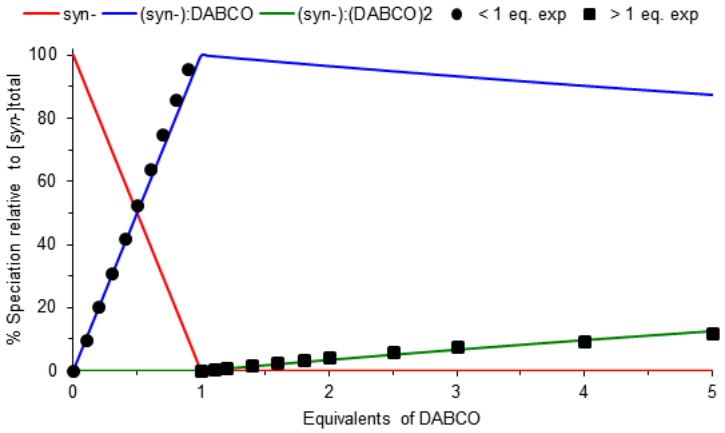

Figure 4.19 - Simulated NMR speciation diagram generated from UV-Vis determined association constants K_{11} and K_{12}. Experimental NMR speciation has been overlayed for both the slow and fast exchange regions of the titration.

4.5.3 Molecular Modelling of *Syn*- Restricted Rotation Tweezer with DABCO

Molecular modelling [145] was undertaken to determine the equilibrium geometry of the (*syn*-):DABCO complex (semi-empirical, AM1, Figure 4.20 (a)). Similarly to the freely rotating tweezer in Chapter 3, rotation is observed about the porphyrin moieties as well as between the two polycyclic arms of the tweezer about the central 2,3,5,6-tetraphenyl diimide group, which is partially distorted from planarity (experimental evidence for this was observed in the XRD crystal structures of a related compound, Figure 4.7)[22]. Again, overlay of the polycyclic arms for models with and without DABCO (not shown) revealed only minimal distortion, providing further evidence that the polycyclic arms are largely rigid. The overall complexed structure does not appear to be significantly strained, and this supports the high association constant that has been determined.

Although not supported by the NMR titration, two possible orientations of the intermolecular (*syn*-)$_2$:(DABCO)$_2$ species are shown in Figure 4.20 (b). These include an intercalated dimer with an internal porphyrin π-π interaction (possible

[22] While the 2,3,5,6-tetraphenyl diimide group is distorted from planarity, no curvature was observed in the molecular modelling for the *syn*- tweezer as was for the freely rotating tweezer in Chapter 3.

bending observed along the imido-porphyrin), and a pseudo-square shaped structure, where each polycyclic arm is rotated with respect to the 2,3,5,6-tetraphenyldiimide core, which when combined with a second host, places the polycyclic arms orthogonal to each other.

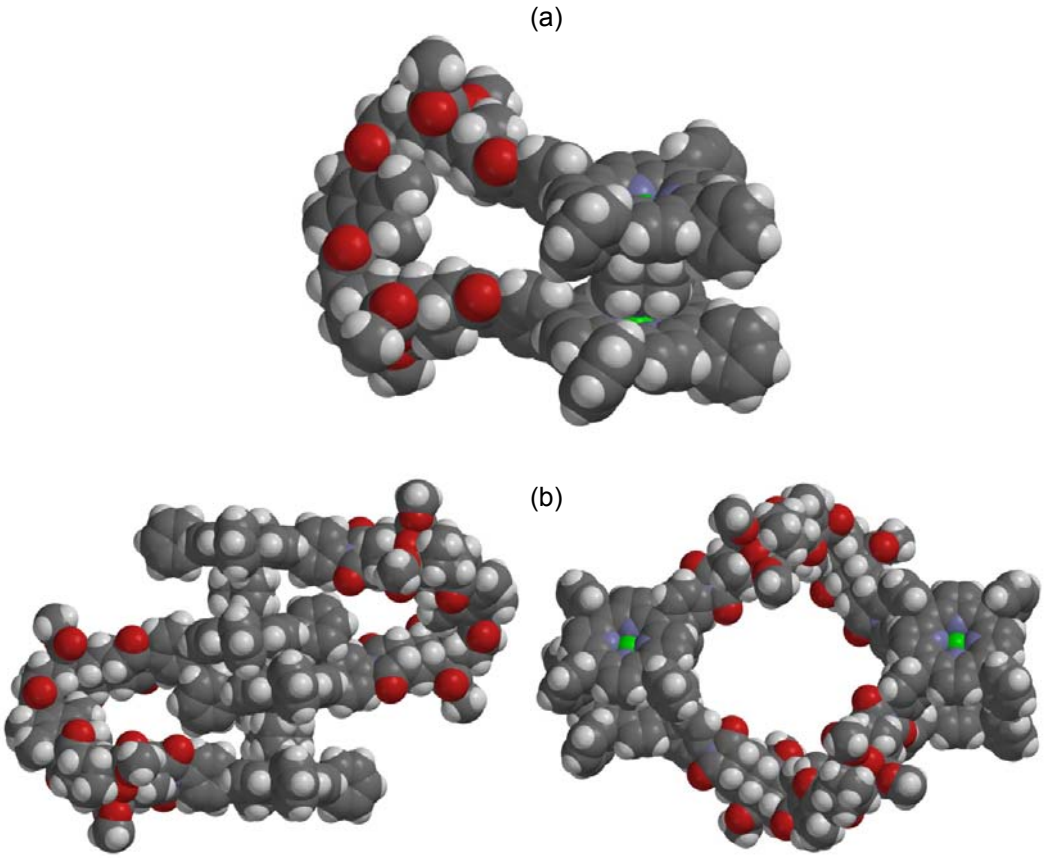

Figure 4.20 - Molecular modelling (semi-empirical, AM1) of the (a) (*syn*-):DABCO **2**:**5** complex; (b) different orientations of (*syn*-)$_2$:(DABCO)$_2$ (**2**)$_2$:(**5**)$_2$.

As undertaken for the freely rotating tweezer, attention was turned to the bidentate ligand 4,4'-bipyridyl **6**, to determine if this would be a suitable guest for the *syn*- **2** tweezer. The next section presents a similar UV-Vis and NMR analysis for *syn*-**2**/bipy **6**.

4.5.4 *Syn*- Restricted Rotation Tweezer with bipy (UV-Vis)

The *syn*- **2**/bipy **6** complexation study was commenced with UV-Vis spectroscopy. Titration of a solution of bipy **6** to a solution of *syn*- **2** restricted tweezer in $CHCl_3$ resulted in a two-stage red shift of the UV-Vis spectrum (Figure 4.21 (a)). The Soret maximum gradually transitions from 418.5 nm to 426.2 nm, and is in line with the value observed in Chapter 3 for a bis-porphyrin bipy sandwich, as well as that reported in [78]. A second gradual redshift occurs, however, although this transition

appears to be only partially complete by 100 000 equivalents of bipy, with a wavelength of 426.5 nm (430 nm is reported for the reference open species of tetraphenylporphyrin with pyridine [176]).

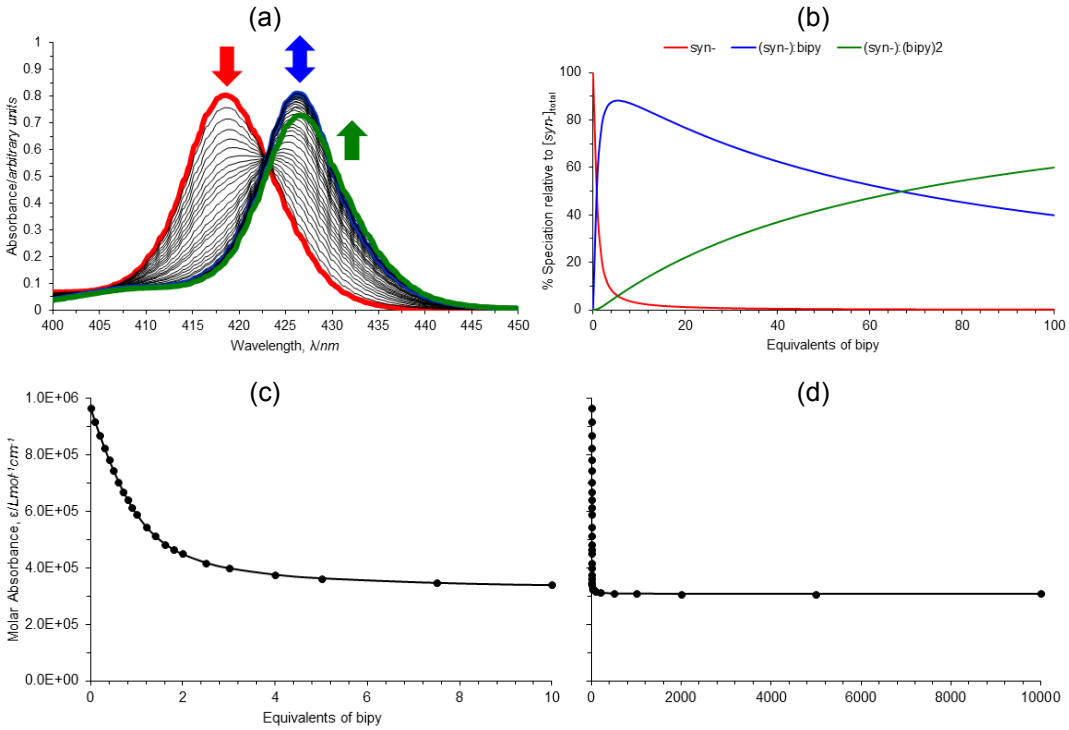

Figure 4.21 - (a) UV-Vis titration of *syn*- **2** tweezer with bipy **6** in chloroform; (b) speciation diagram of *syn*- tweezer with bipy (1:1 → 1:2, HypSpec, HySS2009); (c) best fit (black line) of the algorithm for equilibria between *syn*- tweezer, bipy,(*syn*-):bipy, and (*syn*-):$(bipy)_2$ to the titration data (black circles) at 419 nm for 0 - 10 eq. of bipy; (d) 0 - 10 000 eq. of bipy.

Multivariate global spectral analysis of the UV-Vis data using HypSpec [166] resulting in reasonable fits to several different binding models (two replicates, fitted to 10 000 eq. bipy[23]). Each alternate binding model displayed differences between the intensity profile of the calculated and experimental spectra (not shown) and are briefly discussed below:

- 1:1 plus 1:2. While the intramolecular 1:1 species is a good match between the calculated and experimental spectra, the intensity calculated for the open 1:2 species is 15 % greater than the experimental spectrum.
- 2:1 plus 2:2 plus 1:2. While the intermolecular 2:2 species is a good match between the calculated and experimental spectra, and the spectrum calculated for

[23] The data set was only fitted to 10 000 eq. bipy, as fitting of the full data set to 100 000 eq. bipy resulted in a poor fit. This was also observed for the freely rotating tweezer in Chapter 3.

the 2:1 species appears reasonable on the basis of the ratio of uncomplexed/complexed porphyrins in this species, again the intensity calculated for the open 1:2 species is 15 % greater than the experimental spectrum.

- 2:2 plus 1:2. The fitting and calculated spectra are poorer in the absence of the 2:1 species from the previous fit.
- 2:1 plus 1:1. This binding model can be excluded because it does not account for the experimentally observed open 1:2 complex.

Thus, the two main contenders for the binding model are 1:1 plus 1:2 or 2:1 plus 2:2 plus 1:2. As stated previously, there are limited scenarios by which the *syn*- restricted system can physically form an intermolecular 2:2 species, and the 2:1 species was doubted to be a significant contributor to speciation at UV-Vis concentrations. Therefore, the 1:1 plus 1:2 binding model was selected as the most likely scenario, and has been previously observed for the freely rotating/bipy system in Chapter 3.

A 1:1 plus 1:2 binding model gave K_{11} = 4.3 x 10^6 M^{-1} and K_{12} = 6.1 x 10^{10} M^{-2} in $CHCl_3$ (average two replicates). These are assigned to intramolecular (*syn*-):bipy **2**:**6** and open (*syn*-):$(bipy)_2$ **2**:$(\mathbf{6})_2$ respectively (Figure 4.16). Shown in Figure 4.21 (b) is the speciation diagram for the UV-Vis titration data. Clearly visible is the initial formation of the 1:1 complex between *syn*- and bipy ((*syn*-):bipy, blue line), and its conversion into the 1:2 complex ((*syn*-):$(bipy)_2$, green line) as more equivalents of bipy are added to the solution. The best fit of the algorithm for the formation of (*syn*-):bipy and(*syn*-):$(bipy)_2$ to the titration data at 419 nm is shown in Figure 4.21 (c) and (d) respectively. An equally good fit was observed at 426.5 and 430 nm.

As stated previously, the experimental spectra in Figure 4.21 (a) suggests minimal formation of the open species by 100 000 equivalents of bipy in Figure 4.21 (a). However, this appears to contradict the speciation diagram in Figure 4.21 (b), which indicates that speciation is a 50:50 mix of (*syn*-):bipy and (*syn*-):$(bipy)_2$ at only 70 equivalents of bipy. A similar speciation diagram was observed for the alternate 2:1 plus 2:2 plus 1:2 binding model (not shown), where the 2:2 species rapidly decays into the open 1:2 species at low bipy concentrations.

This apparent mismatch between the experimental spectrum and the speciation diagram raised concern in the validity of the binding models determined from the UV-Vis for the *syn*-/bipy system, and thus an NMR titration was undertaken. NMR

usually assists in the determination of the correct binding model as it allows intramolecular 1:1 and intermolecular 2:2 complexes to be distinguished [30, 31]. Unfortunately however, it was found that the binding models could not be compared across the two different concentration regimes of UV-Vis to NMR (micromolar to millimolar) for the *syn*-/bipy system. This is examined in the next section.

4.5.5 *Syn*- Restricted Rotation Tweezer with bipy (NMR)

Additional characterisation was achieved through a ^{1}H NMR titration of *syn*-restricted tweezer with bipy in $CDCl_3$ and observing the diagnostic porphyrin β-pyrrole and DABCO complex resonances. As per previous titrations, there was error between the number of equivalents of guest titrated against host based on mass weighed compared to NMR signal integration, estimated to be 10-15 % at 20 °C and for 10 % at -50 °C.

At 20 °C for less than 0.8-0.9 titrated equivalents of bipy (integration suggests 1 equivalent), the system was in fast exchange on the NMR chemical shift timescale (Figure 4.22 (a)). The porphyrin β-pyrrole sandwich complex resonance signals are observed as an average between free host at 8.92-8.77 ppm tending towards 8.75-8.68 ppm, consistent with the formation of a bis-porphyrin bipy sandwich [177]. At 0.8-0.9 titrated equivalents of bipy (integration suggests 1 equivalent), the β-pyrrole resonance is much sharper and all free host has been converted into sandwich complex, consistent with the formation of a species with the empirical formula of 1:1 (within 10-15 % error), such as intramolecular (*syn*-):bipy or intermolecular (*syn*-)$_2$:(bipy)$_2$. Addition of greater than 1 equivalent of bipy resulted in a slight downfield shift of the β-pyrrole resonance, as the proportion of open complex (*syn*-):(bipy)$_2$ gradually increases in fast exchange with the sandwich complex on the NMR chemical shift timescale. However, the shift for the *syn*-tweezer after 5 equivalents of bipy is comparatively small compared to the freely rotating tweezer ($\Delta\delta$ = 0.005 ppm and 0.083 ppm respectively), indicating the *syn*- bipy sandwich complex is more resistant to excess bipy than the freely rotating system at NMR concentrations and on the NMR chemical shift timescale.

The porphyrin *meso*-phenyl protons (not shown) are broadened below 1 equivalent of bipy in the sandwich complex, but sharpen for greater than 1 equivalent of bipy. However, the high degree of desymmetrisation, indicative of facial differentiation

and interaction of the porphyrins, and the absence of a downfield shift even for excess bipy provides additional evidence the sandwich species resists decay to the open species. Little information could be obtained from the polycyclic backbone resonances.

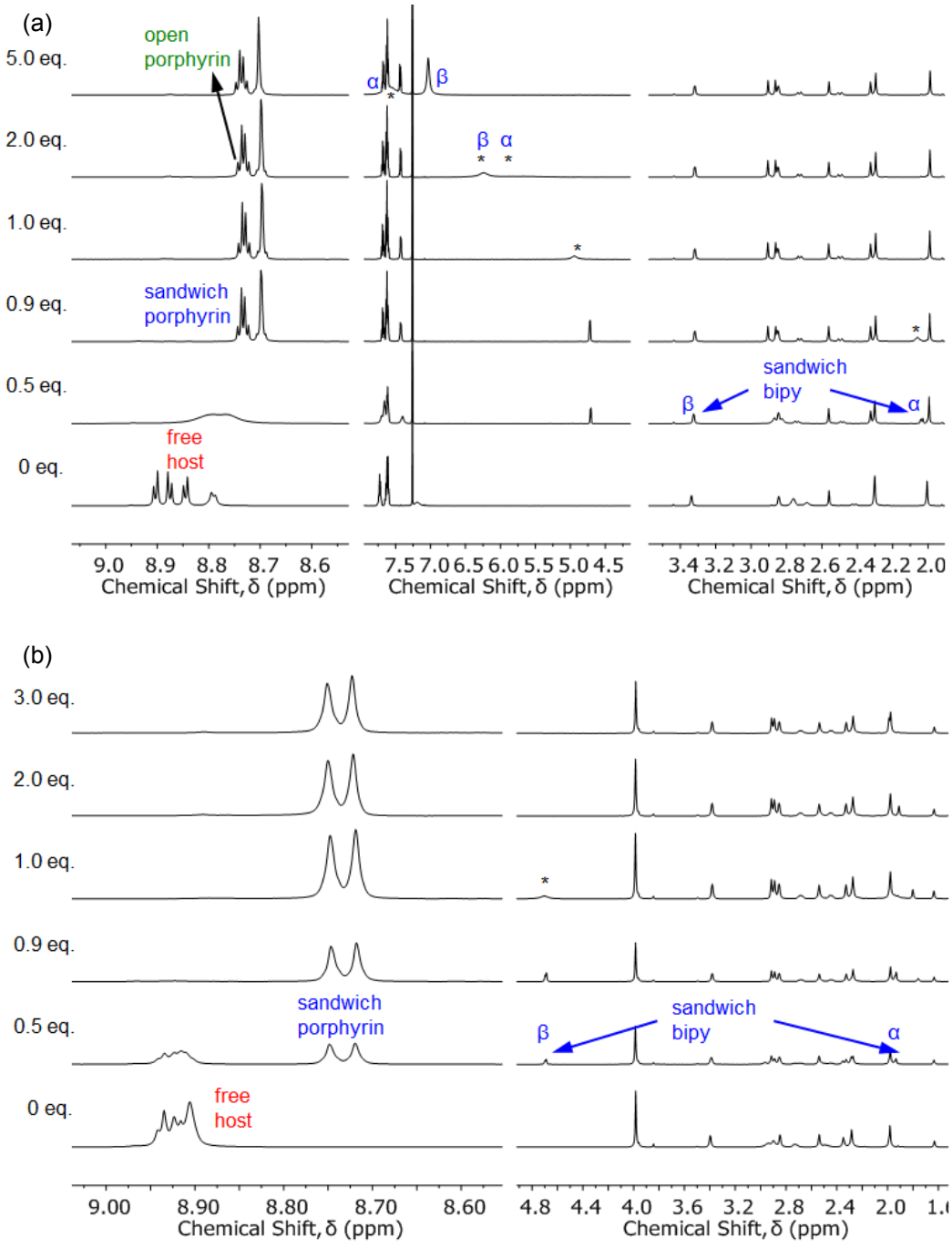

Figure 4.22 - Selected ^{1}H NMR spectra with various equivalents of bipy at (a) 20 °C (top pane) and (b) -50 °C (bottom pane). α and β refer to the position of the *ortho*- and *meta*- protons in 4,4'-bipyridyl. * identifies bipy signals broadened into the baseline due to chemical exchange.

Further understanding of the complexation was gained from the bipy resonances. For less than 0.8-0.9 titrated equivalents of bipy (integration suggests 1 equivalent), two resonances can be observed at 4.71 and 2.04 ppm (Figure 4.22 (a)). This is consistent with the values obtained in Chapter 3 for a bipy bis-porphyrin sandwich, and similar to those reported in the literature [53, 178, 179]. The relative integration of the bipy sandwich resonance to the ester signal is consistent with the formation of a species with the empirical formula of 1:1 (within 10 % error). At 0.9 titrated equivalents of bipy (spectral features suggest greater than 1 equivalent), the two bipy resonances begin to broaden and shift downfield (marked by * in Figure 4.22 (a)), as fast exchange on the NMR chemical shift timescale occurs between sandwich complex, open complex, and free bipy. By 5 eq., the bipy signals approach the value for their free resonances.

Additional information was obtained by conducting the titration at -50 °C (Figure 4.22 (b)), where the system was in slow exchange on the NMR chemical shift timescale below 0.9 titrated equivalents of bipy (integration suggests 1 equivalent). The β-pyrrole resonance for free host at 8.96-8.86 ppm decreases at the expense of sandwich resonance at 8.77-8.68 ppm, and all free host is converted to sandwich complex by this point. Additionally below 0.9 titrated equivalents of bipy (integration suggests 1 equivalent), the two bipy resonances are observed at 4.69 and 1.94 ppm, again typical of bipy in a bis-porphyrin sandwich complex from Chapter 3 and similar to that reported in the literature [53, 178, 179]. For greater than 0.9 equivalents of theoretically added bipy (experimentally 1 equivalent), the system moves into fast exchange on the NMR chemical shift timescale. The two bipy sandwich signals broaden into the baseline (marked by * in Figure 4.22 (b)), as they exchange between sandwich complex and free bipy. No major shift was observed for the porphyrin β-pyrrole sandwich resonances by 3 equivalents of bipy.

The porphyrin *meso*-phenyl porphyrin resonances (not shown) are highly desymmetrised below 1 equivalent of bipy, indicating facial differentiation between the porphyrins in the sandwich complex. While these resonances appear to broaden and resymmetrise for greater than 1 equivalent of bipy, no downfield shift is observed. The broadening could be a result of exchange between the sandwich and open species, however, the absence of a downfield shift for both the porphyrin *meso*-phenyl and β-pyrrole suggests the predominant species is the sandwich complex for

excess bipy. Limited information was provided by the slow exchanging polycyclic resonances (not shown).

In a similar manner to the previous guest analyses, a simulated NMR speciation diagram was generated for bipy using the association constants determined from the UV-Vis titrations. This was undertaken for all four alternate binding models (only 1:1 plus 1:2 is shown in Figure 4.23). Calculation of experimental speciation for the fast exchange NMR chemical shift timescale was undertaken by considering the titration in two separate fast exchange stages, 0 - 1 eq. and 1 - 5 eq. bipy, as described in Appendix 2[24].

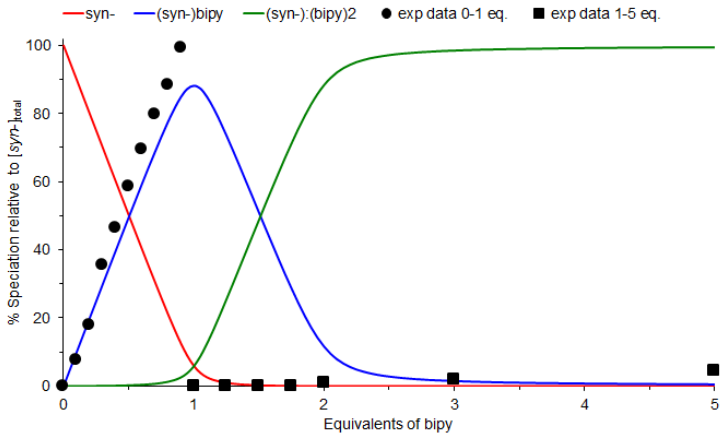

Figure 4.23 - Simulated NMR speciation diagram generated from UV-Vis determined association constants K_{11} and K_{12}. Experimental NMR speciation has been overlayed.

It is clear from Figure 4.23 that the predicted NMR speciation for the 1:1 plus 1:2 binding model does not describe the overlayed experimental speciation. This was found to be the case for all of the alternate UV-Vis determined binding models, where the sandwich complex (in this case 1:1, blue line, Figure 4.23) is converted to the open 1:2 species (green line) at low concentrations of bipy. The experimental NMR data rather suggests the formation of a sandwich complex (black circles), highly resistant to excess bipy, which very gradually decays to an open species (black squares). This is in line with the experimental UV-Vis spectra in Figure 4.21 (a).

[24] A chemical shift of 8.889 ppm was selected for free host. A chemical shift of 8.732 ppm (*syn*- + 0.9 eq. bipy) was selected for the value for fully complexed species. A chemical shift of 8.846 ppm was selected for the value for fully open species, using data obtained in Chapter 4 for the *anti*- restricted rotation tweezer + 5 eq. bipy.

The fitting results of the *syn*-/bipy system are inconclusive. Either, (a) there is a problem with the fitting and/or the binding model, or (b) the fitting and binding model is correct, the speciation is different at UV-Vis and NMR concentrations, and the UV-Vis cannot be visually inspected to gauge stability in this case (perhaps the open species (*syn*-):$(bipy)_2$ has a λ_{max} closer to 426 nm than the 430 nm observed for the reference tetraphenylporphyrin/pyridine system [176]). This will be further investigated in the future.

4.5.6 Molecular Modelling of *Syn*- Restricted Rotation Tweezer with bipy

Similarly to the previous porphyrin tweezers, molecular modelling (Spartan '10, Wavefunction, Inc.[145]) was undertaken to determine the equilibrium geometry of the (*syn*-):bipy complex (semi-empirical, AM1, Figure 4.24).

As was observed for (*syn*-):DABCO (Figure 4.20 (a)), the porphyrin moieties are rotated somewhat to the idealised representation in Figure 4.1. Again, rotation is also observed between the two polycyclic arms of the tweezer about the central 2,3,5,6-tetraphenyl diimide group[25], and is very important in the complexation of bipy, as it allows for the required increase in interporphyrin distance for longer guests compared to DABCO. Overlay of the polycyclic arms with and without bipy (not shown) showed minimal distortion to the polycyclic scaffold, again reflecting the rigidity of the polycyclic scaffold. The overall structure of the 1:1 intramolecular sandwich complex does not appear to be significantly strained, and thus the formation of this species would appear to be reasonable.

[25] Variation in the extent of core rotation was observed depending on the starting geometry prior to optimisation, highlighting the limits of a semi-empirical level of computational theory.

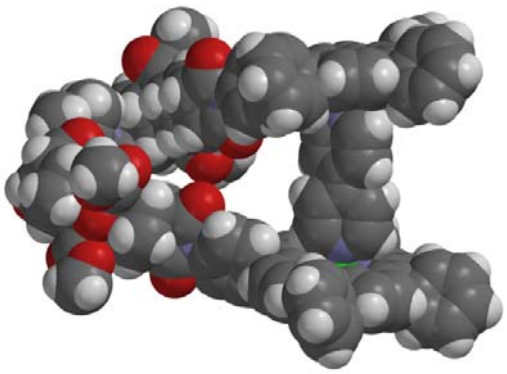

Figure 4.24 - Molecular modelling (semi-empirical, AM1) of the 1:1 intramolecular sandwich species (*syn*-):bipy, **2**:**6**.

4.6 Summary of the *Syn*- Restricted Tweezer and Comparison with the Freely Rotating Tweezer

Using a similar reaction sequence to the freely rotating system in Chapter 3, a second generation system was synthesised with a sterically bulky 2,3,5,6-tetramethylphenyl diimide core. This alteration sufficiently restricted rotation to allow the isolation of non-interconvertible *syn*- and *anti*- adducts, whose host-guest complexation could be studied independently of each other.

Similarly to the freely rotating/DABCO system, the *syn*-/DABCO system supports a 1:1 plus 1:2 binding model at both UV-Vis and NMR concentrations. The K_{11} and K_{12} appear to be similar for both *syn*- **2** and freely rotating **1** (K_{11} = 1.25 x 10^8 M^{-1}/K_{12} = 1.32 x 10^9 M^{-2} and K_{11} = 8.1 x 10^7 M^{-1}/K_{12} = 2.7 x 10^9 M^{-2} respectively), however additional replicates of UV-Vis titrations should be undertaken for both systems to more accurately determine association constants before the systems can be compared in terms of their difference in degree of pre-organisation. Errors in high order binding constants are reported to be large because of their increased sensitivity to inaccuracies in concentration, absorption, and chemical shift [66].

With the guest bipy, multivariate global spectral analysis of the UV-Vis titration data resulted in several alternate binding models, the most likely being 1:1 plus 1:2. If the fitting and binding model is correct (see next paragraph), then K_{11} for *syn*- **2** is an order of magnitude greater that freely rotating **1** (K_{11} = 4.3 x 10^6 M^{-1} and K_{11} = 4.97-5.27 x 10^5 M^{-1} respectively), which suggests that *syn*- **2** forms a stronger intramolecular sandwich complex than freely rotating **1**. However, K_{12} for *syn*- **2** is two orders of magnitude greater than freely rotating **1** (K_{12} = 6.1 x 10^{10} M^{-2} and K_{12} =

1.56-1.88 x 10^8 M^{-2} respectively), which suggests the *syn*- **2** intramolecular sandwich complex is less resistant to excess bipy than freely rotating **1**. However, again additional replicates of the UV-Vis titrations should be undertaken to confirm this result.

Interestingly, both the experimental UV-Vis titration spectra and experimental NMR speciation suggested a bis-porphyrin bipy sandwich complex that is highly resistant to decaying to the open species in excess bipy. However, this is not mirrored by the fitting results for a 1:1 plus 1:2 binding model, or any model, which instead suggests that the sandwich complex decays to the open species at a low excess of bipy. The results are inconclusive and further investigation is required in the future.

In line with the freely rotating system, molecular modelling of the *syn*- system suggests that the polycyclic linker scaffold remains rigid, and that the polycyclic arms rotate about the core to increase the interporphyrin distance when accommodating different sized ligands. It is expected that restricted rotation will be important for the syn- **2** tweezer when complexing longer guests than bipy, in which it would be energetically unfavourable for the polycyclic arms to rotate about the sterically hindered core to achieve the required interporphyrin distance (not undertaken in this thesis).

4.7 *Anti*- Host-Guest Study

Subsequently, the interaction between the *anti*- **3** restricted rotation system and the diamino ligands DABCO **5** and bipy **6** were examined by UV-Vis and NMR spectroscopy. This was undertaken out of interest, as the *anti*- conformation is physically unable to form intramolecular sandwich complexes. However, the *anti*-host can form various intermolecular complexes in solution, all of which are in equilibrium. These possibilities are outlined schematically in Figure 4.25, and reveal the possibility of 2:2 (K_{22} = [(*anti*-)$_2$:(ligand)$_2$]/([*anti*-]^2[ligand]^2), 1:2 (K_{12} = [*anti*-:(ligand)$_2$]/([*anti*-][ligand]^2), 2:1 (K_{21} = [(*anti*-)$_2$:ligand]/([*anti*-]^2[ligand]) stoichiometries, and the step-like polymeric intermolecular assembly n:n (K_{nn} = [(*anti*-)$_n$:(ligand)$_n$]/([*anti*-]^n[ligand]^n).

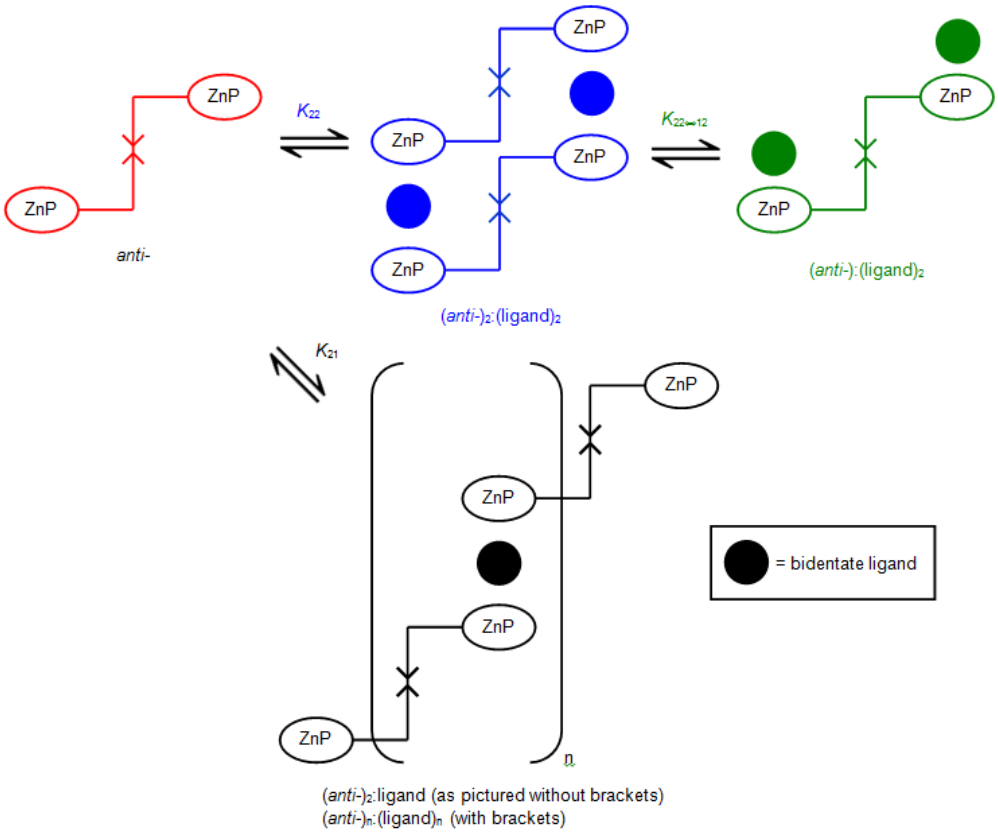

Figure 4.25 - Schematic representation of the various equilibria between *anti*- **3** tweezer and bidentate ligand.

4.7.1 *Anti*- Restricted Rotation Tweezer with DABCO (UV-Vis)

Titration of a solution of DABCO **5** to a solution of *anti*- **3** tweezer resulted in two-stage redshift of the UV-Vis spectrum (Figure 4.26 (a)). The Soret maximum transitions from 419.5 nm to 423.5 nm, and is characteristic of a bis-porphyrin

DABCO sandwich complex [30, 31]. However, this sandwich species is transient, and a second redshift occurs rapidly to 430.0 nm by 10 000 equivalents, after which this transition appears to be complete. This is characteristic of simple mono-porphyrin DABCO complexes [30, 31].

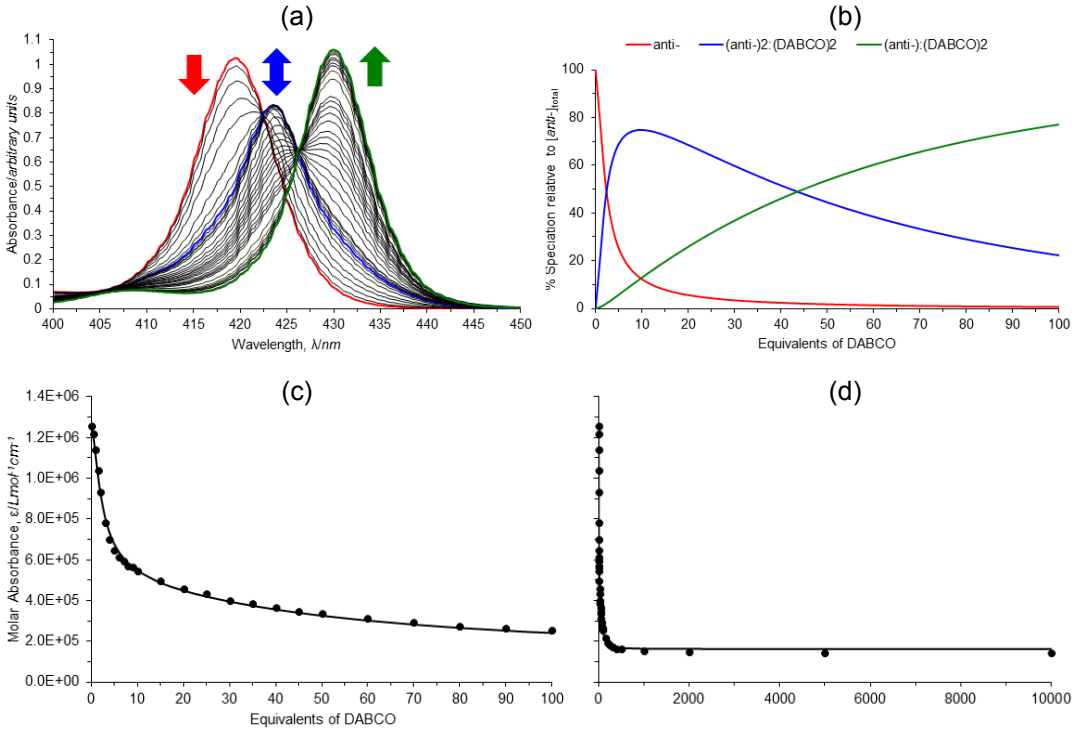

Figure 4.26 - (a) UV-Vis titration of *anti*- **3** tweezer with DABCO **5** in chloroform; (b) speciation diagram of *anti*- tweezer with DABCO (2:2 → 1:2, HypSpec, HySS2009); (c) best fit (black line) of the algorithm for equilibria between *anti*- tweezer, DABCO, (*anti*-):DABCO, and (*anti*-):$(DABCO)_2$ to the titration data (black circles) at 419 nm for 0 - 100 eq. of DABCO; (d) 0 - 10 000 eq. of DABCO.

A reasonable fit was obtained for a 2:2 plus 1:2 binding model, giving K_{22} = 5.57 x 10^{17} M^{-3} and K_{12} = 1.94 x 10^{10} M^{-2} in $CHCl_3$ (average of two replicates, fitted to 10 000 equivalents DABCO). These are assigned to intermolecular (*anti*-)$_2$:$(DABCO)_2$ (**3**)$_2$:(**5**)$_2$ and open (*anti*-):$(DABCO)_2$ **3**:(**5**)$_2$ respectively (Figure 4.25).

Shown in Figure 4.26 (b) is the speciation diagram for the UV-Vis titration data. Clearly visible is the initial formation of the 2:2 complex between the *anti*- tweezer and DABCO, (*anti*-)$_2$:$(DABCO)_2$ (blue line), and its rapid conversion into the 1:2 complex, (*anti*-):$(DABCO)_2$ (green line), as more equivalents of DABCO are added to the solution. The best fit of the algorithm for the formation of (*anti*-)$_2$:$(DABCO)_2$ and (*anti*-):$(DABCO)_2$ to the titration data at 419 nm is shown in Figure 4.17 (c) and (d) respectively. This fit was similar at 423 nm and 430 nm (not shown). The value for K_{22} is similar to other examples of intermolecular porphyrin DABCO sandwich

complexes in the literature (K_{22} = 6.2 x 10^{16} - 6.3 x 10^{22} M^{-3} [28, 30, 31]). The 2:2 plus 1:2 binding model can be physically achieved by the *anti*- system, and the calculated spectra (not shown) compare well with the experimental spectra.

While several other binding models could be fitted to the data (not shown), either the calculated spectra did not match the experimental spectra, or the calculated spectral profile was incorrect for the suggested species (mismatch between ratios of free, sandwich and open porphyrins). A good example of this is the fitting obtained for a 1:1 plus 1:2 binding model for *anti*-/DABCO (not shown). While the fitting for this binding model appears reasonable, the calculated spectra suggests the 1:1 species has a wavelength maxima centred around 423 nm. This wavelength normally suggests an intramolecular bis-porphyrin DABCO sandwich complex, however, the *anti*-conformation cannot physically form such a species, and so this binding model can be rejected. This again highlights that the goodness of the fit alone cannot be used as the criterion to decide the correct binding model [30].

4.7.2 *Anti*- Restricted Rotation Tweezer with DABCO (NMR)

Additional characterisation of the binding model for this system was achieved through a ^{1}H NMR titration of *anti*- restricted tweezer with bipy in $CDCl_3$ (Figure 4.27 (a)), and observing the diagnostic porphyrin β-pyrrole and bipy complex resonances. As per previous titrations, there was error between the number of equivalents of guest titrated against host based on mass weighed compared to NMR signal integration, estimated to be 10 % at 20 °C and for 10-15 % at -50 to -60 °C.

At 20 °C, the β-pyrrole signals for uncomplexed *anti*- tweezer occur at 8.96-8.94 ppm (Figure 4.27 (a)). The addition of up 0.9 titrated equivalents of DABCO (integration suggests 1 equivalent) resulted in the appearance of a second β-pyrrole signal for the complex at 8.55 ppm. This upfield shift is typical of β-pyrrole protons in a bis-porphyrin DABCO sandwich complex and results from shielding by opposing ring currents of two porphyrin aromatic systems in close proximity [30, 31, 66]. The two species are in the slow to medium exchange rate on the NMR chemical shift timescale (resonances are broad but distinct) and the β-pyrrole complex signal increases at the expense of uncomplexed *anti*- tweezer. Limited information could be obtained from the porphyrin *meso*-phenyl or polycyclic backbone resonances (not shown). At 0.9 titrated equivalents of DABCO (integration suggests 1 equivalent), all

free host has been converted to sandwich complex. The relative integration of the sandwich β-pyrrole resonance to the total β-pyrrole resonance (free plus sandwich) is consistent with the formation of a species with the empirical formula of 1:1 (within 10 % error), such as intermolecular (*anti*-)$_2$:(DABCO)$_2$ or the step-like polymeric intermolecular assembly (*anti*-)$_n$:(DABCO)$_n$ (intramolecular (*anti*-):DABCO cannot be formed by the *anti*- conformation).

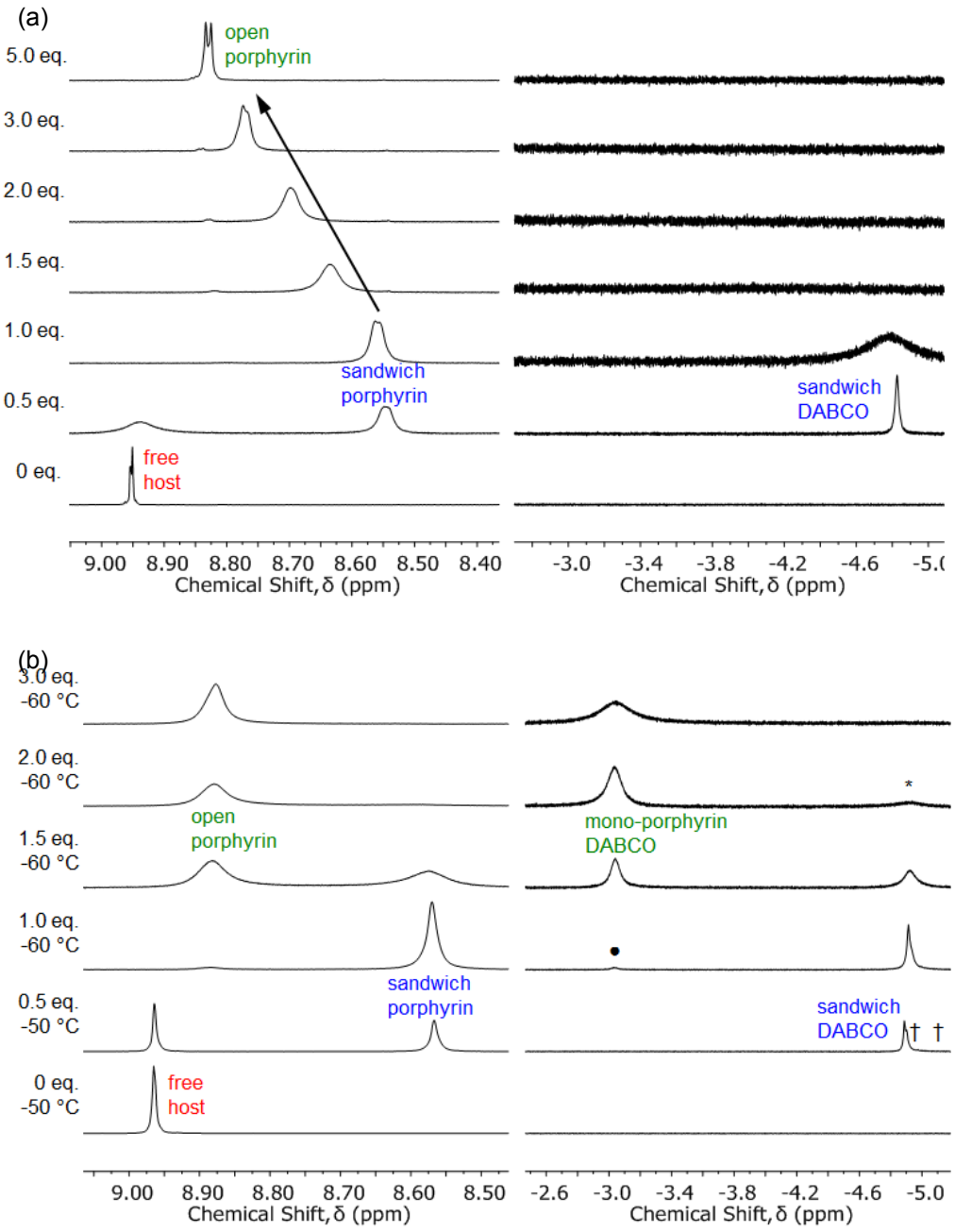

Figure 4.27 - Selected ^{1}H NMR spectra with various equivalents of DABCO at (a) 20 °C (top pane) and (b) -50 to -60 °C (bottom pane). † identifies additional sandwich complexes. * identifies DABCO sandwich signals broadened into the baseline due to chemical exchange. ● identifies the broad mono-porphyrin DABCO resonance.

Further understanding of the complexation of DABCO by *anti*- is gained from the DABCO methylene resonance (Figure 4.27 (a)). At 0.1 equivalents of DABCO (not shown), two sandwich DABCO signals can be observed; major at -4.826 ppm and a minor quantity of a second signal at -4.846 ppm. This large upfield shift is typical of DABCO methylene protons in a bis-porphyrin DABCO sandwich complex, and again results from shielding by opposing ring currents of two porphyrin aromatic systems in close proximity [27, 29-31, 52, 66, 172]. The two signals indicated the formation of two different sandwich complexes. At 0.5 equivalents of DABCO, only the major signal can be observed, and is a sharp singlet up to 0.9 titrated equivalents of DABCO (integration suggests 1 equivalent). Again, the relative integration of the DABCO sandwich resonance to the ester signal is consistent with the formation of a species with the empirical formula of 1:1 (within 10-15 % error), being either (*anti*-)$_2$:(DABCO)$_2$ or (*anti*-)$_n$:(DABCO)$_n$.

Addition of greater than 1 equivalent of DABCO causes the β-pyrrole resonance to rapidly shift downfield as increasing proportions of the open species, (*anti*-):(DABCO)$_2$, forms in fast exchange on the NMR chemical shift timescale (Figure 4.27 (a)). This shift for the *anti*- tweezer after 5 equivalents of DABCO is much larger than for the freely rotating and *syn*- systems ($\Delta\delta$ = 0.282, 0.082, and 0.033 ppm respectively), indicating the *anti*- DABCO sandwich complex is less resistant to excess DABCO than the freely rotating and *syn*- systems at NMR concentrations and on the NMR chemical shift timescale. The porphyrin β-pyrrole and *meso*-phenyl signals are sharper at 5 equivalents of DABCO, presumably as most of the sandwich species has decayed to the open species.

In addition, after 1.5 equivalents of DABCO, the sandwich DABCO resonance is broadened into the baseline by chemical exchange with the open species and free DABCO. After 5 equivalents of DABCO, a large broad signal was observed between 0.8-2.2 ppm under the polycyclic signals (not shown), tending towards the resonance for free DABCO.

Additional spectral features could be observed by conducting the titration at -50 to -60 °C (Figure 4.27 (b)), where the system was in slow exchange on the NMR chemical shift timescale across all concentrations of DABCO. In particular, below 0.9 titrated equivalents of DABCO (integration suggests 1 equivalent), two sandwich DABCO signals can be identified at -4.89 ppm and -4.90 ppm. The species at -4.90

ppm is dominant below 0.3 equivalents of DABCO after which the species at -4.89 ppm becomes dominant. A trace quantity of a third sandwich complex was observed at -4.98 ppm. These sandwich species are marked by † in Figure 4.27 (b). Additional evidence for two major sandwich complexes at low temperature was observed in several of the polycyclic resonances (not shown), several of which are split into three; free host and the two major sandwich complexes. These are most likely to be the discrete intermolecular 2:2 species, (*anti*-)$_2$:(DABCO)$_2$ (several different molecular orientations possible, refer to section on molecular modelling), or the infinite step-like polymeric intermolecular assembly, (*anti*-)$_n$:(DABCO)$_n$. Unfortunately, none of these resonances are sufficiently baseline resolved to be independently integrated. Peak deconvolution was not performed.

After 1 equivalent of DABCO, the system remained in slow to intermediate exchange on the NMR chemical shift timescale, and allowed the resonances for the open complex to be unambiguously assigned. The open species porphyrin β-pyrrole resonance occurs at 8.88 ppm, while the DABCO α-methylene resonance occurs at -3.04 ppm (marked by ● in Figure 4.27 (b)). Both of these chemical shifts are consistent with DABCO interacting with a mono-porphyrin [28-30]. These resonances increase in intensity at the expense of the sandwich complex signals, with the conversion to the open species almost complete by 2 equivalents of DABCO. This again suggests that the *anti*- intermolecular sandwich complex is much less resistant to excess DABCO than the intramolecular sandwich complexes for the freely rotating and *syn*- systems at NMR concentrations and on the NMR chemical shift timescale. After 3 equivalents of DABCO, the mono-porphyrin DABCO resonance broadens, as it likely undergoes exchange with free DABCO.

Interestingly, there is a broad resonance at 0.82 ppm (not shown) at -50 °C which increases in intensity between 1 and 2 equivalents of DABCO. This was tentatively assigned to the β-methylene of DABCO interacting with a mono-porphyrin, in the absence of locating a literature value for this shift. Quinuclidine β-methylene protons are reported to occur at -0.64 ppm for the complex formed with mono-porphyrin [29].

Again, the binding model determined for *anti*- tweezer and DABCO at UV-Vis concentrations (2:2 plus 1:2) was applied to NMR concentrations, and the simulation [166] compared with the experimental NMR speciation [28, 30, 31]. Calculation of

experimental speciation (room temperature) for the slow and fast exchange NMR chemical shift timescale regions was undertaken as described in Chapter 3 and Appendix 2[26]. While the experimental NMR speciation involves a minor second sandwich species, these resonances are not baseline resolved. These resonances are integrated as a single resonance, which makes the assumption that both of the two resonances arise from different configurations of an intermolecular 2:2 sandwich complex.

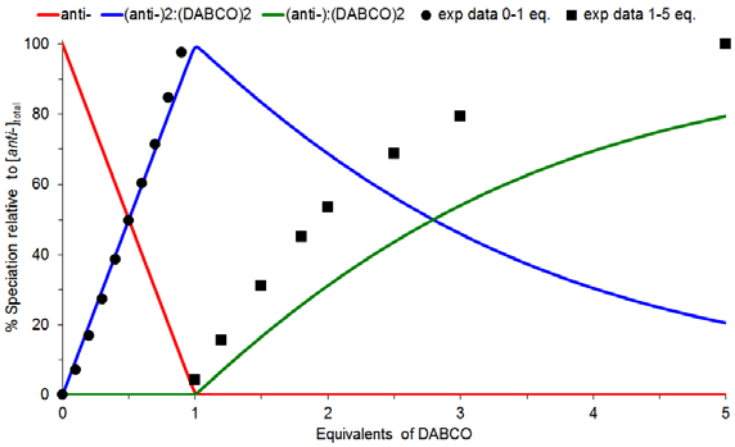

Figure 4.28 - Simulated NMR speciation diagram generated from UV-Vis determined association constants K_{22} and K_{12}. Experimental NMR speciation has been overlayed for both the slow and fast exchange regions of the titration.

Figure 4.28 shows this result for the 2:2 plus 1:2 binding model (blue and green lines respectively, the red line is free host). There was excellent correlation between the simulated and experimental speciation in the slow exchange NMR chemical shift timescale region (black circles), while the experimental data for the fast exchange region (black squares) follows the predicted trend. Thus the NMR and UV-Vis both support the formation of intermolecular (*anti*-)$_2$:(DABCO)$_2$ followed by decay to the open species (*anti*-):(DABCO)$_2$, provided that the two sandwich species observed in the NMR are two different molecular orientations of the intermolecular 2:2 species, and not the infinite step-like polymeric intermolecular assembly (*anti*-)$_n$:(DABCO)$_n$ (see the next section on molecular modelling).

[26] A chemical shift of 8.547 ppm (*anti*- + 0.9 eq. DABCO) was selected for the value for fully complexed species. A chemical shift of 8.829 ppm (*anti*- + 5 eq. DABCO) was selected for the value for fully open species.

4.7.3 Molecular Modelling of *Anti*- Restricted Rotation Tweezer with DABCO

Molecular modelling [145] was undertaken to determine the equilibrium geometry of intermolecular (*anti*-)$_2$:(DABCO)$_2$ complex (semi-empirical, AM1, Figure 4.29). This could exist in several molecular orientations, for example where the polycyclic linkers are stacked horizontally (a) or vertically (b), or the pseudo-square shaped structure (c), where each polycyclic arm is rotated with respect to the 2,3,5,6-tetraphenyldiimide core, which when combined with another host, places the polycyclic arms orthogonal to each other. In addition, the step-like polymeric intermolecular assembly, (*anti*-)$_n$:(DABCO)$_n$, is shown in Figure 4.29 (d), truncated to show a single repeating unit.

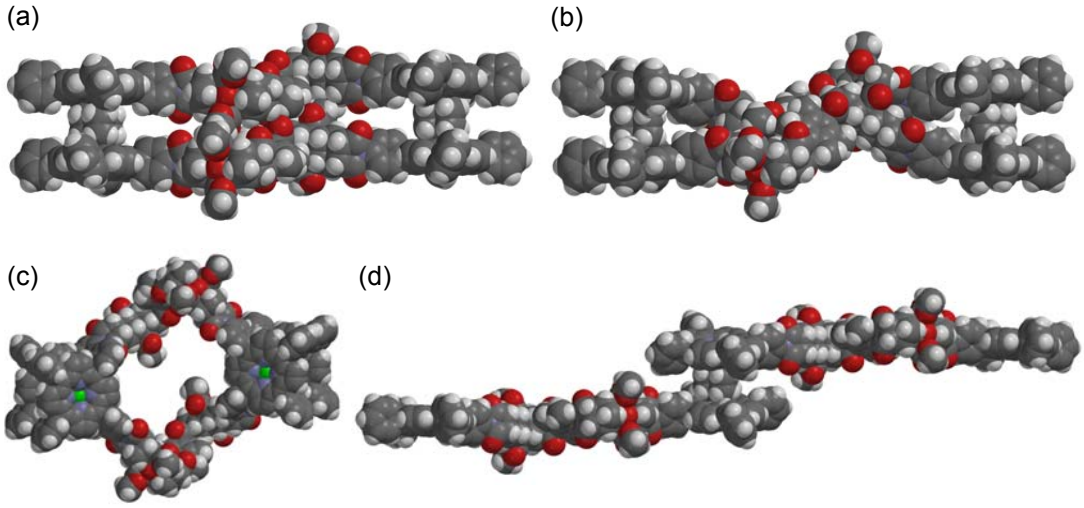

Figure 4.29 - Molecular modelling (semi-empirical, AM1) of the (*anti*-)$_2$:(DABCO)$_2$ (**3**)$_2$:(**5**)$_2$ complex (several possible molecular orientations shown, (a)-(c)); (d) step-like polymeric intermolecular assembly (*anti*-)$_n$:(DABCO)$_n$ (truncated).

As undertaken for all other tweezer systems, the bidentate ligand 4,4'-bipyridyl **6** was subsequently examined with the *anti*- **3** system. A discussion of the results for the UV-Vis and NMR titrations is provided in the next section.

4.7.4 *Anti*- Restricted Rotation Tweezer with bipy (UV-Vis)

With intermolecular complexation observed for *anti*-/DABCO, attention was turned to bipy **6** to determine if similar host-guest behaviour would be observed. Titration of a solution of bipy **6** to a solution of *anti*- **3** tweezer resulted in a red shift of the UV-Vis spectrum (Figure 4.30 (a)). The Soret maximum gradually transitions from 419.6 nm to 429.5 nm. This most likely corresponds to the formation of the open species (*anti*-):(bipy)$_2$, being similar to the Soret maxima of 430 nm reported for the

reference open species of tetraphenylporphyrin with pyridine [176]. The red shift was essentially complete after the addition of 10 000 – 50 000 equivalents of bipy. The absence of peak centred around 426.5 nm, which was observed for other tweezers in this work and in [78], suggested that an intermolecular sandwich complex is not formed at UV-Vis concentrations (micromolar) for the *anti*- system. This was an interesting result, as linear porphyrin dimers are reported to form 2:2 intermolecular sandwich complexes with bipy [52]. This would appear to suggest that the polycyclic scaffold affects the ability of the *anti*- system to intermolecularly complex bipy, and is not simply related to the lower basicity of bipy compared to DABCO.

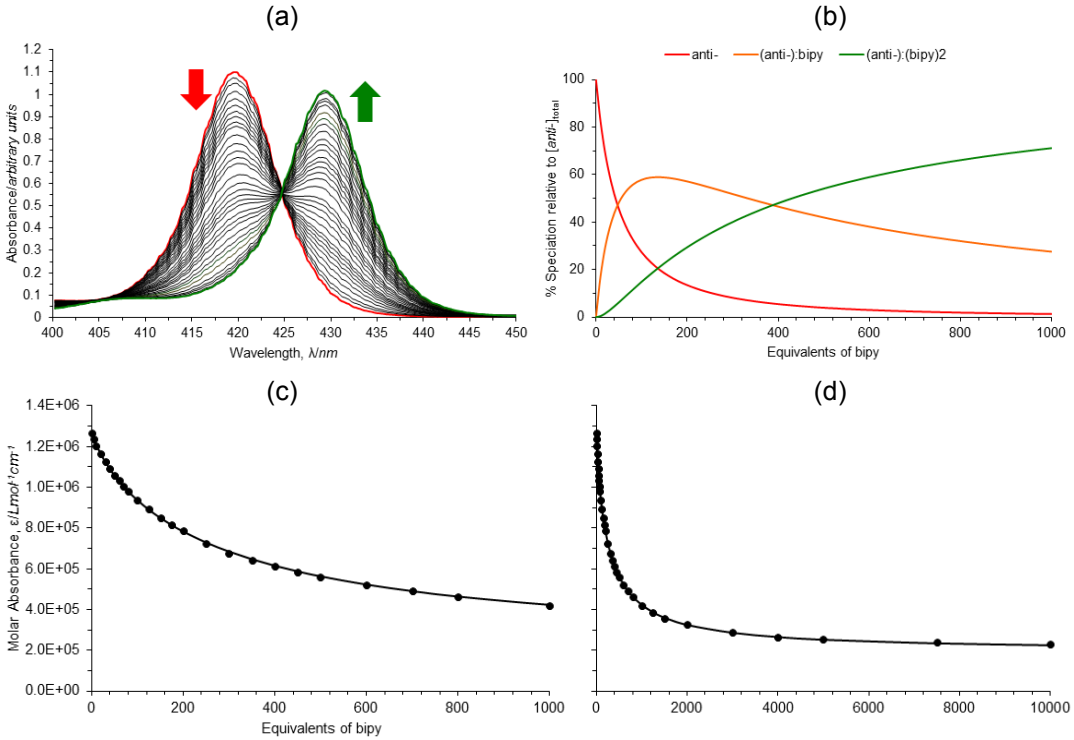

Figure 4.30 - (a) UV-Vis titration of *anti*- **3** tweezer with bipy **6** in chloroform; (b) speciation diagram of *syn*- tweezer with bipy (1:1 → 1:2, HypSpec, HySS2009); (c) best fit (black line) of the algorithm for equilibria between *anti*- tweezer, bipy, (*anti*-):bipy, and (*anti*-):$(bipy)_2$ to the titration data (black circles) at 419 nm for 0 - 1000 eq. of bipy; (d) 0 - 10 000 eq. of bipy.

The UV-Vis titration data was best fitted to a 1:1 plus 1:2 binding model, giving K_{11} = 2.45 x 10^4 M^{-1} and K_{12} = 7.29 x 10^7 M^{-2} in $CHCl_3$ (single replicate fitted to 10 000 eq. bipy). These are assigned to the stepwise formation of open species (*anti*-):bipy and (*anti*-):$(bipy)_2$ respectively. Shown in Figure 4.30 (b) is the speciation diagram for the UV-Vis titration data, and shows the initial formation of (*anti*-):bipy (orange line), which is converted to (*anti*-):$(bipy)_2$ (green line) as more equivalents of bipy are added to the solution. The best fit of the algorithm for the formation of (*anti*-

):bipy **3**:**6** and (*anti*-):(bipy)$_2$ **3**:(**6**)$_2$ to the titration data at 419 nm is shown in Figure 4.30 (c) and (d) respectively. An equally good fit was observed at 426.5 and 430 nm.

However, the calculated spectra from the fitting output are of concern (not shown). While the profile of the calculated spectra for the 1:2 species compares well the experimental spectra, the calculated spectra for the 1:1 species is biased towards 419 nm with a smaller contribution at 430 nm. Experimentally, the 1:1 species should be approximately equally contributed to by 419 and 430 nm, to account for one of the porphyrins being uncomplexed and the other being in an open complex. While several other binding models could be fitted to the data (not shown), each was discounted, as either the calculated spectra are inconsistent with the experimental spectra, or the calculated spectra are inconsistent with the species in the binding model (large mismatch between ratios of free, sandwich and open porphyrins). Thus the 1:1 plus 1:2 binding model remains the best available for the *anti*-/bipy system.

4.7.5 *Anti*- Restricted Rotation Tweezer with bipy (NMR)

With the unusual result of the intermolecular sandwich complex being absent for *anti*-/bipy at UV-Vis concentrations, the system was examined at NMR concentrations. As per previous titrations, there was error between the number of equivalents of guest titrated against host based on mass weighed compared to NMR signal integration, estimated to be 15-20 % at 20 °C and for 10-15 % at -50 °C.

The ^{1}H NMR titration spectra of *anti*- restricted tweezer with bipy in $CDCl_3$ at 20 °C are shown in Figure 4.31 (a), focussing on the diagnostic porphyrin β-pyrrole and bipy complex resonances. At 20 °C, system was in fast exchange on the NMR chemical shift timescale across all concentrations of bipy, between free host, a sandwich species, open species, and free bipy.

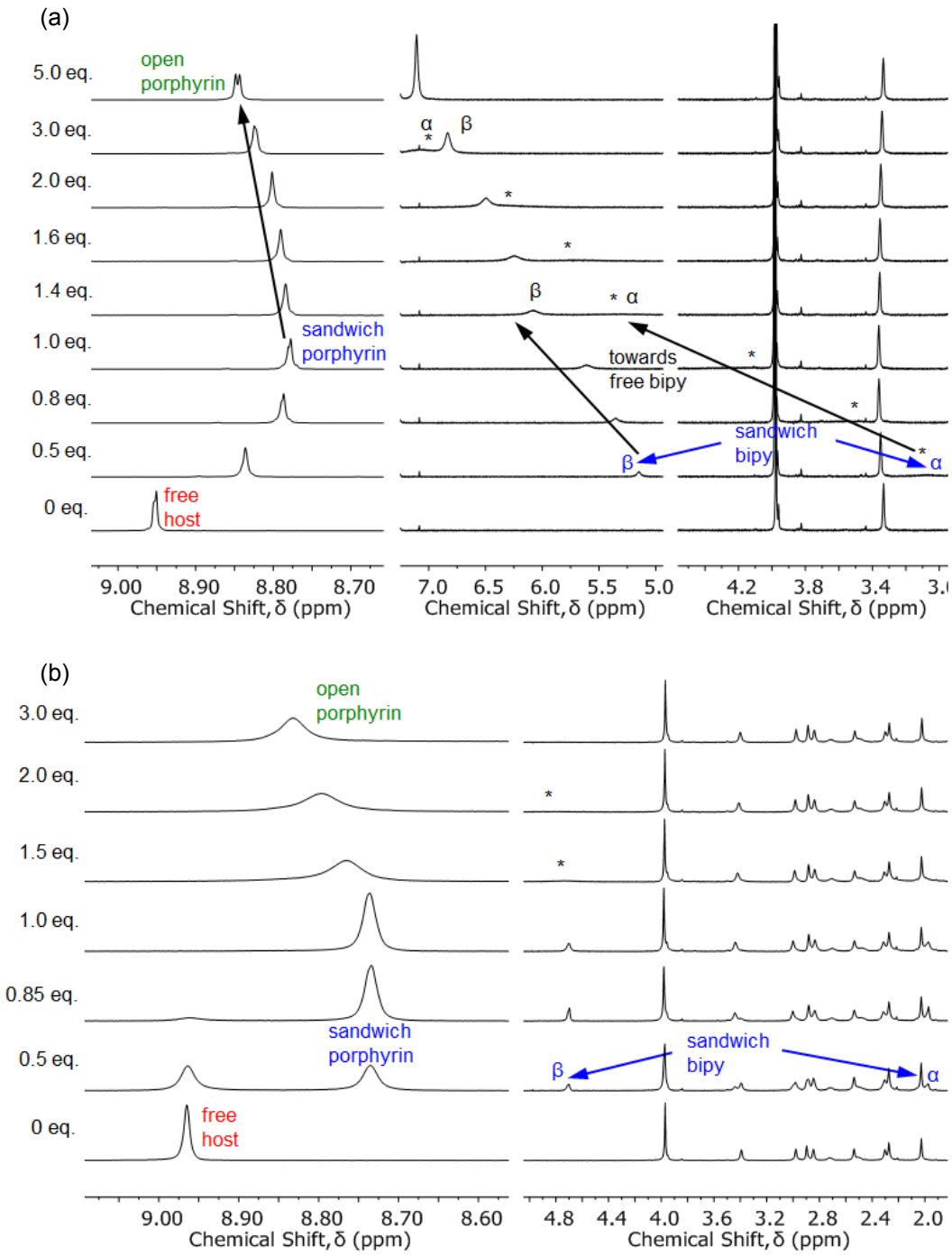

Figure 4.31 - Selected ^{1}H NMR spectra with various equivalents of bipy at (a) 20 °C (top pane) and (b) -50 °C (bottom pane). α and β refer to the position of the *ortho*- and *meta*- protons in 4,4'-bipyridyl. * identifies signals broadened into the baseline due to chemical exchange.

Below 1 equivalent of bipy, the porphyrin β-pyrrole sandwich complex resonance signals are observed as an average between free host at 8.96-8.94 ppm and 8.79-8.77 ppm (Figure 4.31 (a)). This later chemical shift is consistent with the formation of a bis-porphyrin bipy sandwich [177]. At 0.8-1.0 titrated equivalents of bipy (integration suggests 1 equivalent), the β-pyrrole resonance is fully converted into sandwich complex, consistent with the formation of a species with the empirical

formula of 1:1 (within 15-20 % error), such as intermolecular (*anti*-)$_2$:(bipy)$_2$ or the step-like polymeric intermolecular assembly (*anti*-)$_n$:(bipy)$_n$[27]. This indicated immediately that speciation was different at NMR concentrations (millimolar) compared to UV-Vis concentrations (micromolar), where the sandwich complex was absent. This can be rationalised by the increased stability of intermolecular 2:2 species at higher concentrations of host [30]. Addition of greater than 1 equivalent of bipy resulted in a downfield shift of the β-pyrrole resonance, as increasing proportions of open species (*anti*-):(bipy)$_2$ form. Limited information could be obtained from the porphyrin *meso*-phenyl and polycyclic linker resonances.

Further understanding of complexation was gained from the bipy resonances in Figure 4.31 (a). Below 1 equivalent of bipy, two broad bipy signals can be observed downfield at 5.17-5.12 and 3.08-3.01 ppm for the α- and β- bipyridyl protons respectively (the α- bipyridyl protons are particularly broadened by chemical exchange and are marked with * as necessary in Figure 4.31 (a)). These sandwich chemical shifts are already exchanging between open species and free bipy below 1 equivalent (the α- bipyridyl protons are usually closer to 2 ppm for the other bis-porphyrin sandwich complexes in this thesis), suggesting the sandwich complex is labile. As further bipy is added up to 5 equivalents, these signals shift downfield and begin to sharpen as they approach the value for their free resonances.

Additional information was obtained by conducting the titration at -50 °C (Figure 4.31 (b)), where the system was in slow exchange on the NMR chemical shift timescale below 0.85 to 1 titrated equivalents of bipy (integration suggests 1 equivalent). The porphyrin β-pyrrole resonance for free host at 8.97 ppm decreases at the expense of sandwich resonance at 8.74 ppm, and all free host is converted to sandwich complex by 0.85 titrated equivalents of bipy (integration suggests 1 equivalent). Furthermore below 0.85 to 1 titrated equivalents of bipy (integration suggests 1 equivalent), two sharp bipy resonances are observed at 4.70 and 1.98 ppm, again typical of bipy in a bis-porphyrin sandwich complex from Chapter 3 and similar to that reported in the literature [53, 178, 179]. At this point, the relative integration of the bipy sandwich resonances to the ester signal was consistent with the formation of a species with the empirical formula of 1:1 (within 10-15 % error).

[27] DOSY ^{1}H NMR at different concentrations could assist in the identification of this sandwich species.

For greater than 1 equivalent of bipy, the system moves into fast exchange on the NMR chemical shift timescale (Figure 4.31 (b)). The two bipy sandwich signals broaden into the baseline (marked * in Figure 4.31 (b)), as they exchange with open species and free bipy. The β-pyrrole resonance experiences a downfield shift, as increasing proportions of open species (*anti*-):$(bipy)_2$ form. Limited additional information could be obtained from the porphyrin *meso*-phenyl and polycyclic linker resonances.

The plot comparing predicted and experimental NMR speciation generated for other systems in this thesis is not applicable to the *anti*-/bipy system, as the binding model and speciation are obviously very different between UV-Vis and NMR concentrations, namely the presence of the intermolecular 2:2 sandwich complex at NMR concentrations only.

4.7.6 Molecular Modelling of *Anti*- Restricted Rotation Tweezer with bipy

Molecular modelling [145] was undertaken to determine the equilibrium geometry of the (*anti*-)$_2$:$(bipy)_2$ complex (semi-empirical, AM1, Figure 4.32), assuming this is the sandwich species observed in the NMR. Similarly to (*anti*-)$_2$:$(DABCO)_2$, this could exist in several molecular orientations, for example where the polycyclic linkers are stacked horizontally (a) or vertically (b). The interporphyrin distance is of course larger for bipy than for the DABCO analogues of these intermolecular 2:2 sandwich species. Although not shown here, the step-like polymeric intermolecular assembly, (*anti*-)$_n$:$(bipy)_n$ is another a possibility for the sandwich species observed in the NMR for *anti*-/bipy.

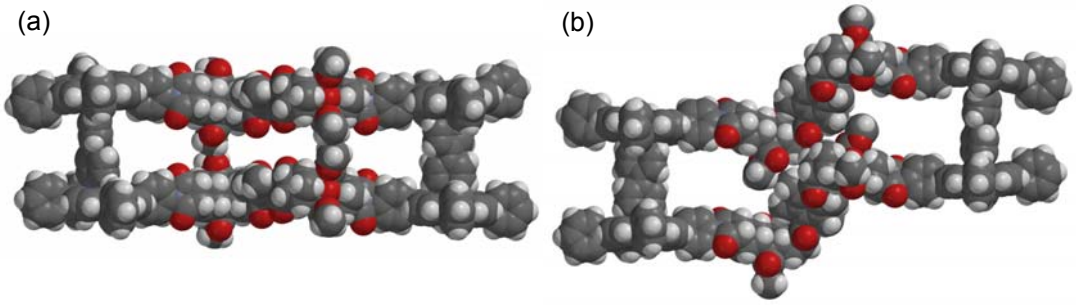

Figure 4.32 - Molecular modelling (semi-empirical, AM1) of the (*anti*-)$_2$:$(bipy)_2$ (**3**)$_2$:(**6**)$_2$ complex, two molecular orientations (a) and (b).

4.8 Summary of the *Anti*- Restricted Rotation Tweezer

The *anti*- **3** conformation of the restricted rotation tweezer has very different host-guest behaviour to the *syn*- **2** conformation and the freely rotating tweezer **1**, as it is physically unable to form intramolecular sandwich complexes with bidentate ligands and can only form intermolecular sandwich complexes.

With the best available information from host-guest experiments and data fitting, the *anti*- restricted tweezer supported a 2:2 plus 1:2 binding model for DABCO at both UV-Vis and NMR concentrations. The UV-Vis and NMR spectra suggest that the *anti*- intermolecular 2:2 sandwich complex with DABCO is labile compared to the intramolecular 1:1 sandwich complexes observed for freely rotating and *syn*-restricted with DABCO. The NMR of *anti*-/DABCO indicated the formation of a major and minor sandwich species, most likely to be two different orientations of the intermolecular 2:2 species, $(anti\text{-})_2$:$(DABCO)_2$.

For *anti*-/bipy, no sandwich complex was observed at UV-Vis concentrations. The UV-Vis data was best described by a 1:1 plus 1:2 binding model, where bipy complexes to each mono-porphyrin in a stepwise progression. Although there was some uncertainty in this binding model, no other sensible or realistic binding model could be determined. Speciation was found to be different at NMR concentrations, with the observation of a sandwich complex, likely to be either a discrete intermolecular 2:2 species, $(anti\text{-})_2$:$(bipy)_2$, or a step-like polymeric intermolecular assembly, $(anti\text{-})_n$:$(bipy)_n$.

With an increased understanding of core rotation and host-guest behaviour of the architecture, synthetic effort was then directed towards a third generation tetra-porphyrin tweezer **4** containing two bis-porphyrin binding sites linked via a rotating phenyl core. This is presented in Chapter 5, along with a statistical analysis of the association constants to assess interannular cooperativity.

5. Tetra-porphyrin Tweezer

5.1 Declaration

A substantial quantity of this chapter concerning the synthesis of the tetra-porphyrin tweezer is likely to be submitted for publication during the thesis examination. Results have been partially presented at conferences. X-ray diffraction measurements and the solving of X-ray crystal structures were undertaken by Assoc Prof Christopher Sumby (The University of Adelaide), Dr Rebecca Norman (Flinders University), and Prof Jonathan White (The University of Melbourne). Dr Duc-Truc Pham (The University of Adelaide) provided guidance in the operation of the software package for curve fitting the host-guest data.

5.2 Introduction

The model single binding site tweezers in both Chapter 3 (freely rotating **1**) and Chapter 4 (*syn*- restricted **2**) provided key information about the host-guest behaviour of the system; namely that these architectures enable diamino ligands to be complexed with large association constants, and that the phenyl diimide core and rotating porphyrins provides the tweezer with the ability to re-organise the interporphyrin distance depending on the dimensions of the guest.

Equipped with an improved understanding of the behaviour of the tweezer scaffold, the synthesis of a two binding site tetra-porphyrin tweezer **4** was undertaken. This structure is shown in Figure 5.1, and is comprised of porphyrin receptors (blue), a freely rotating phenyl diimide core (green), and a rigid polycyclic backbone (parallel rods, combination of red/black/blue). As previously discussed in the literature examples in Chapter 1 and the molecular design in Chapter 2, the combination of the rigid polycyclic scaffold with the rotating core connects the two bis-porphyrin binding sites, with the interporphyrin distance at both binding sites moderated by the length of the guest intramolecularly complexed. In addition, the porphyrin receptors are free to rotate about the *meso*-phenyl-imide bond, ensuring that the porphyrins can always align cofacially to complex guest irrespective of the degree of core rotation. Thus it was hypothesised that the binding of two molecules of the same guest would be positively cooperative, given that the second binding site should be more optimised for guest following complexation at the first binding site.

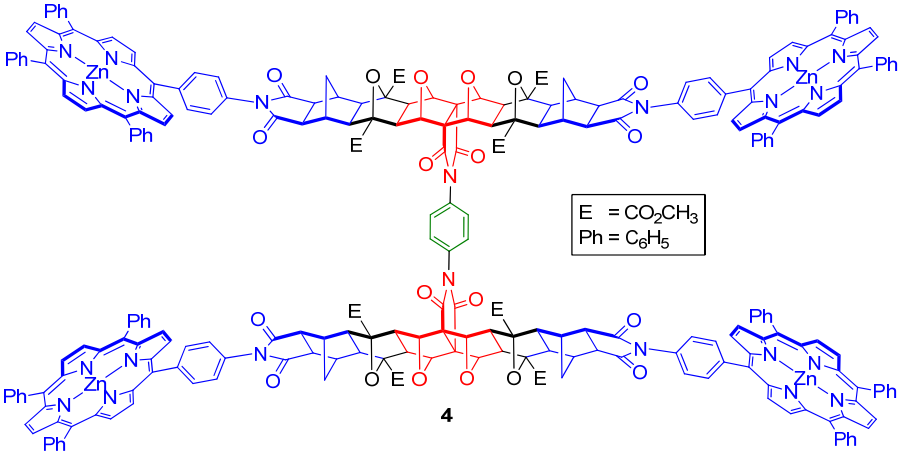

Figure 5.1 - Chemical Structure of the tetra-porphyrin tweezer **4**

The tetra-porphyrin tweezer **4** is an example of an interannular system [88], which has recently been defined as a system in which there is interplay between two or more intramolecular binding interactions [88]. The two binding sites are unable to be distinguished spectroscopically, and so a statistical analysis of the association constants was undertaken to calculate the interannular cooperativity factor, γ [88], with interesting results.

5.3 Molecular Modelling

Similarly to the tweezers from the two preceding chapters in this thesis, the equilibrium geometry of the tetra-porphyrin tweezer **4** in the absence of guest was examined by molecular modelling (semi-empirical, AM1 [145]), and is shown in Figure 5.2. Again, rotation is observed about the porphyrin moieties as well as between the two polycyclic halves of the tweezer about the central phenyl diimide core. This indicates that the polycyclic scaffold does not necessarily adopt a parallel alignment, as per the idealised reaction scheme structures such as Figure 5.1. Also not accounted for by the idealised reaction scheme structures is the naturally curved topology of polycyclic scaffold with fused norbornyl and 7-oxanorbornane modules [107, 108] (which in this case is largely rigid), a crucial design feature in this system which enables the bis-porphyrin binding sites to be coplanar in each half [109] and cofacial between the two halves, if an idealised conformation is adopted when complexed with guest.

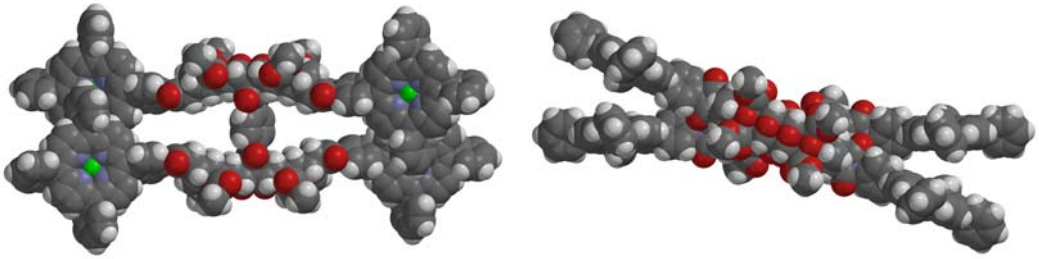

Figure 5.2 - Molecular modelling of the tetra-porphyrin tweezer **4** in the absence of guest (side on, top down) (semi-empirical, AM1).

5.3.1 Simulating Rotation about the Phenyl Diimide Core

Also in a similar manner to the previous tweezer systems, the rotational energy profile of a structurally reduced version of the linker was calculated [145], and is shown in Figure 5.3. This simulates the barrier to rotation about the *N*-aryl bond in the phenyl diimide core (N_2-C_3) by examining the energy of each conformation specified by the dihedral angle constraint C_1-N_2-C_3-C_4 from 0 to 90 °. The model compound for this calculation does not account for π-π interactions between the opposing bis-porphyrins in the tetra-porphyrin tweezer, changes to bond properties and electronic effects of the second *para*- imide in the linker, or additional steric crowding on the underside of the polycyclic scaffold when additional polycycles are fused to the linker.

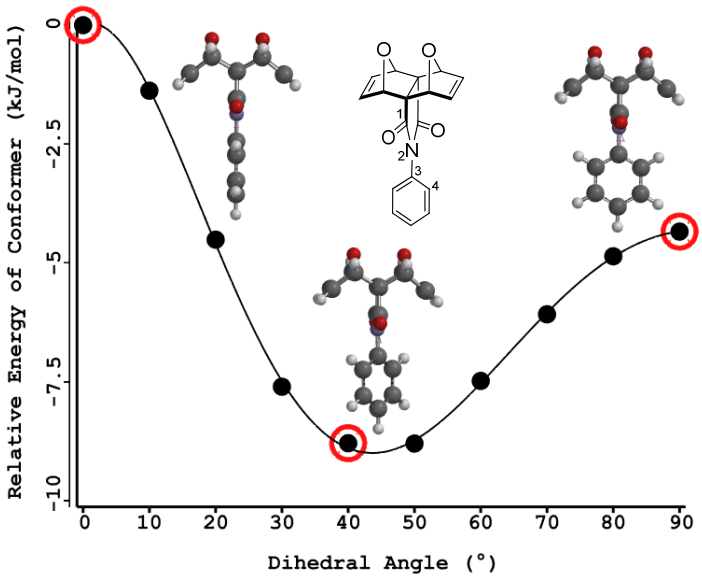

Figure 5.3 - Rotational energy profile and barrier to rotation about the imide-phenyl single bond in the linker (energy profile Hartree-Fock 6-31G*, energy of each conformation recalculated using Density Functional B3LYP/6-31G*).

Not surprisingly, the energy profile closely resembles the calculation for the freely rotating linker in Chapter 3, owing to the structural similarity in the region of rotation. The relative energy difference between the global maximum and minimum is approximately 9 $kJmol^{-1}$ (2.15 $kcalmol^{-1}$) and supports free rotation in this system at room temperature, from thermal energy available from the surroundings [124]. Not surprisingly, the highest energy conformer occurs at a dihedral angle of 0 °, when the phenyl ring proton atoms and imide carbonyl oxygen atoms are in the same plane and are interacting sterically. The lowest energy conformation occurs at a dihedral angle of approximately 45 °, while a local maximum occurs at 90 °.

Molecular modelling has previously been employed to calculate the ground state optimised geometry of a similar *N*-phenyl imide system [105, 116]. In this study, the angle of the phenyl with respect to the imide was determined to be 70-71 ° (RHF/3-21G [116], HF3-21G [105]), and 5.65 kJ (1.35 kcal) more stable than the case where the phenyl is constrained to the plane of the imide [116]. While the two different computational methods (geometry optimisation [105, 116] and the rotational energy profile from this thesis) afford different phenyl imide angles for the global energy minimum, both computations suggest that the highest energy state is where the phenyl is in the plane of the imide, where the hydrogen and oxygen atoms are sterically interacting.

5.3.2 Simulating Guest Inclusion

As with previous tweezer systems, molecular modelling [145] was undertaken to determine the equilibrium geometry of the tetra-porphyrin:$(guest)_2$ complexes (semi-empirical, AM1, Figure 5.4). Again, the key point is that the system is able to accommodate both small (DABCO **5** (a)) and larger (bipy **6** (b)) guests by rotating the rigid polycyclic rails via the phenyl diimide core, as well as the porphyrin receptors. In this way, the interporphyrin distance can be adjusted for different guest lengths. For example, the polycyclic rails can be seen to be rotated further with respect to each other for bipy than for DABCO in Figure 5.4. With respect to each guest, approximately equal interporphyrin distance was observed at the two binding sites. Neither the DABCO nor bipy complexed structures appear to be significantly strained. As was the case with previous tweezer systems, overlay of the polycyclic rails for models with and without guest (not shown) revealed only minimal distortion, providing further evidence that the polycyclic rails are largely rigid.

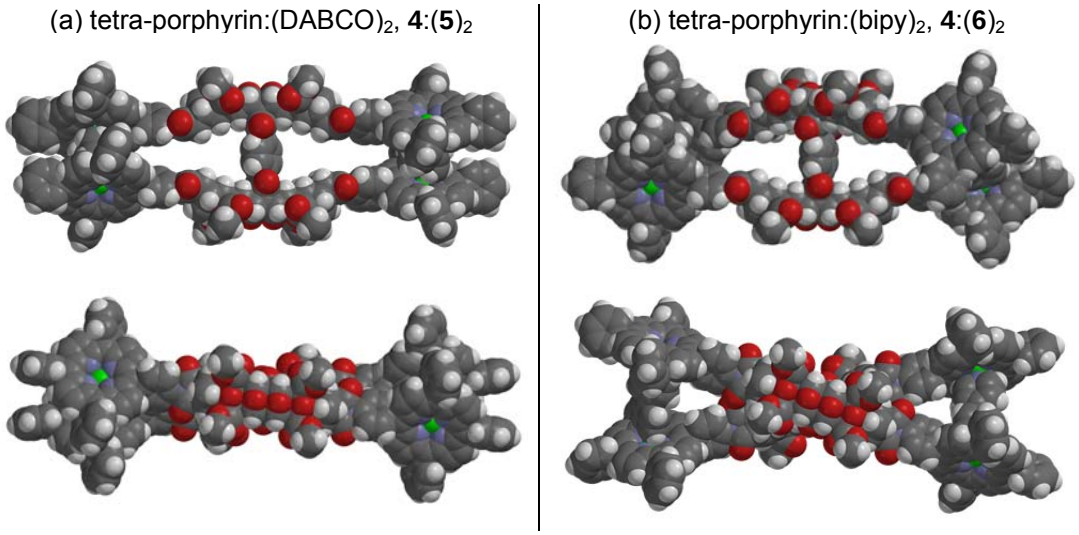

Figure 5.4 - Molecular modelling (semi-empirical, AM1) of tetra-porphyrin:(ligand)$_2$ (a) ligand = DABCO **5** (two different views), (b) ligand = bipy **6** (two different views).

5.4 Synthesis

Retrosynthetic analysis of the tetra-porphyrin tweezer (Figure 5.5) highlighted three key modules; porphyrin receptor **18** (blue), phenyl core (green), and the linking polycyclic T-piece (red). The southern functionality of the T-piece module (R^1 or R^2) can be modified to give either the dicarboxylic acid **36** [185, 186], diacid chloride **42** [67, 187], anhydride **37** [188], or imide **51** [106, 189-192] derivatives (these compounds are referred to later in this chapter). The 1,4-substituted phenyl core (R^3) can be can modified to almost any functional group, to enable compatibility for coupling with the T-piece.

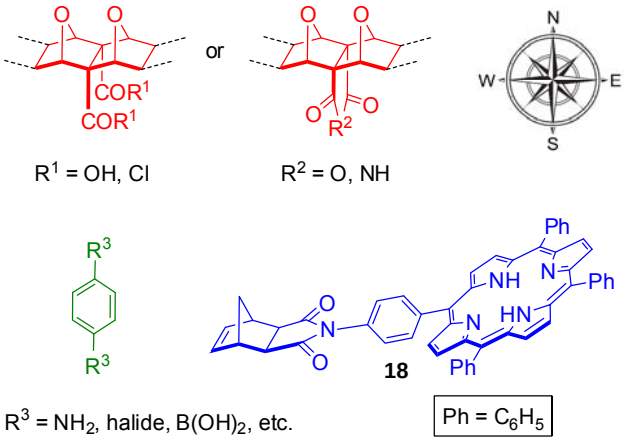

Figure 5.5 - Retrosynthesis of tetra-porphyrin tweezer **4** to several key building blocks; porphyrin receptor **18** (blue), phenyl core (green), linking polycyclic T-piece (red).

In principle, these modules can be joined in different combinations and orders, and led to two main approaches; convergent and divergent (Figure 5.6). The convergent approach involves joining two complete halves to generate the core in the final step, whereas in the divergent approach, the core is generated early, and the structure is built out towards the periphery. The convergent approach is synthetically preferable, as it provides increased structural control when functionalising with receptors; there are two points of reactivity per half. For example, a convergent approach would enable asymmetric tweezers with different receptors to be accessed. On the contrary, a divergent approach provides less structural control, as the core has four simultaneous points of reactivity for receptor functionalisation. For these reasons, initial attempts targeted a convergent approach, and are now summarised.

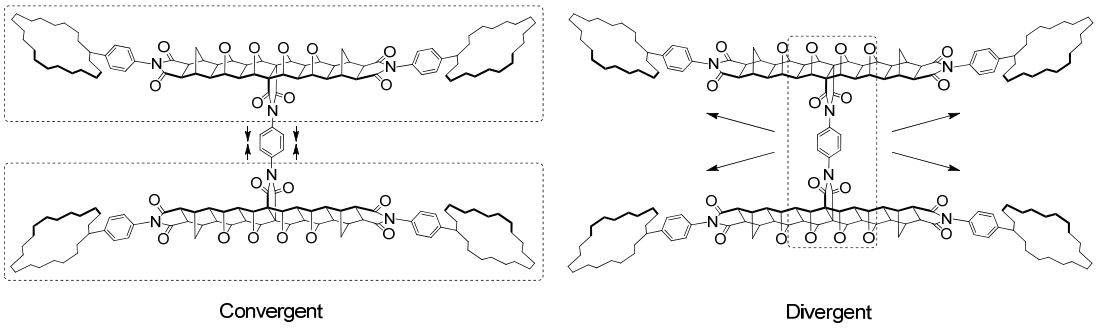

Figure 5.6 - Convergent and divergent synthetic approaches to tetra-porphyrin tweezer **4** synthesis. (porphyrin and polycyclic structural detail omitted for clarity).

5.4.1 Synthetic Problems Encountered with the Convergent Approach

The most suitable starting material was the anhydride derivative **37** of the bis-(7-oxanorbornane) T-piece (Figure 5.7). This compound can be accessed in large quantities in a single step from the bis-carboxylic acid **36** [185, 186] (square box, Figure 5.7) under ring closing conditions prescribed in [188]. The anhydride **37** displayed good solubility in organic solvents, while the bis-carboxylic acid **36** is soluble in more polar solvents and is reported to be less thermally stable than the anhydride **37** [103]. While the bis-acid chloride derivative **42** is also known [67, 187], it would difficult to carry this moisture sensitive functional group through the entire synthetic sequence.

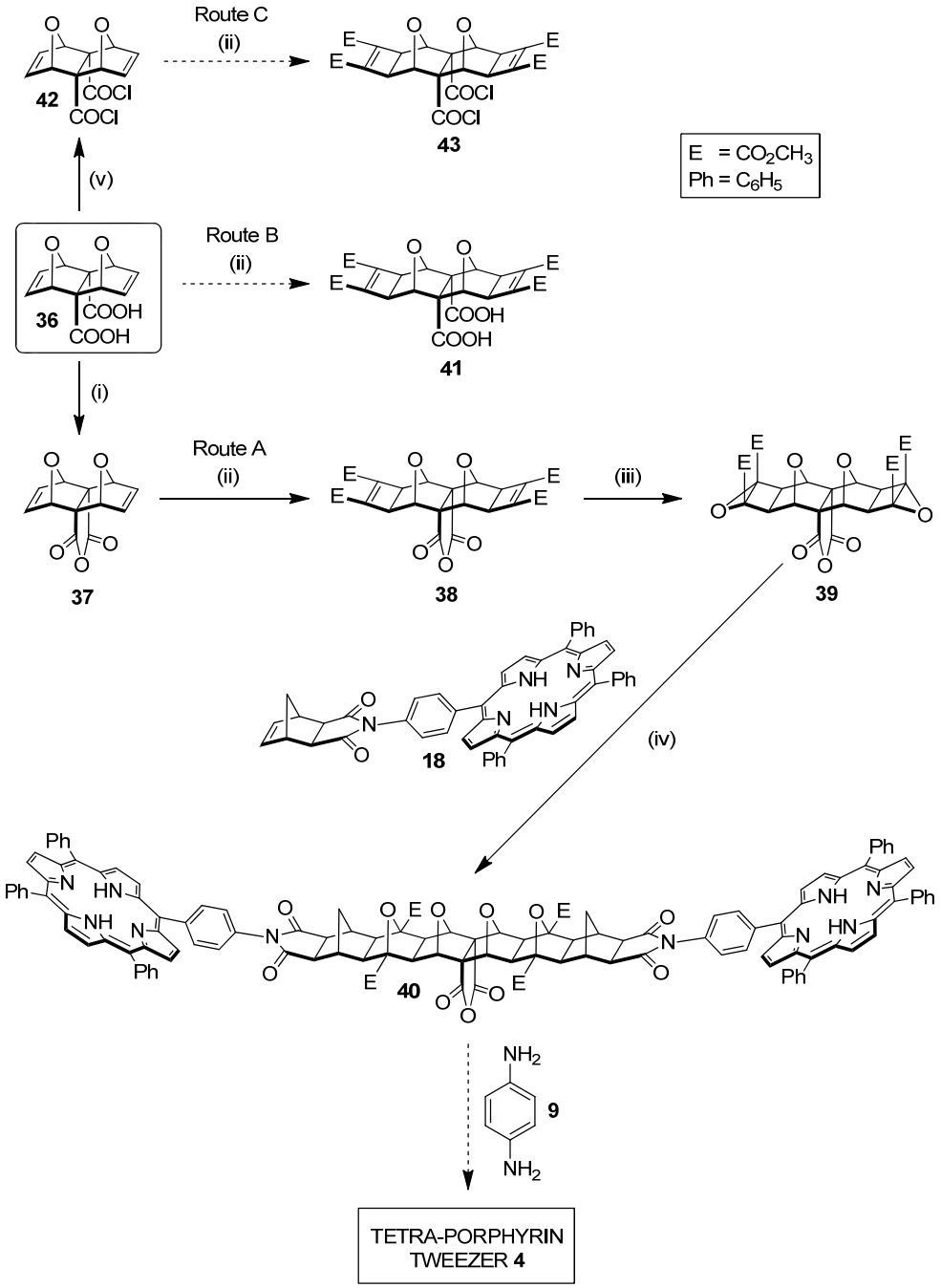

Figure 5.7 - Convergent approaches to tetra-porphyrin tweezer synthesis. Route A through anhydride **37**. Route B through bis-carboxylic acid **36**. Route C through bis-acid chloride **42**. (i) Et_3N, Ac_2O, 60 °C, nitrogen, overnight [188]; (ii) DMAD (2-4 eq.), 5-20 mol-% [$Ru[H_2CO(PPh_3)_3]$, toluene, 80 °C (Route A) or 20-60 °C (Routes B and C), nitrogen, 4 days, 86 % **38**; (iii) anhydrous 3.3 M *t*BuOOH in toluene (2.5 eq.), dry CH_2Cl_2, 0 °C, 10 min, *t*BuOK (1 eq.), r.t., 3.5 hrs, 49 %; (iv) *exo*-porphyrin receptor **18** (2 eq.), dry THF, microwave 80-220 W, 14-20 bar, 170 °C, 2 hrs; (v) PCl_5, $CHCl_3$, argon bubbling through mixture, room temperature, 24 hrs, 54 % (modified [67]).

Pursuing Route A from the anhydride **37** in Figure 5.7, this compound was subjected to standard Mitsudo conditions [146, 147] to afford the bis-(cyclobutene methyl ester) adduct **38** [157] in excellent yield, which was subsequently epoxidised in the

normal manner [102, 104], giving the bis-epoxide **39** in good yields for this type of reaction. Microwave accelerated ACE reaction [160] with mono-porphyrin receptor **18** successfully generated the bis-porphyrin half **40**. This was confirmed by HRMS (calcd $[M+2H]^{2+}$ 1050.3421, found 1050.3432), as this compound was insoluble in a wide range of common organic solvents (DMSO, CH_3CN, DMF, toluene, $CHCl_3$, THF, EtOAc), prohibiting characterisation by NMR. Unfortunately, poor solubility limits further reaction of the bis-porphyrin half **40**. The poor solubility of **40** could be attributed to the formation of an intermolecular π-π aggregate (Figure 5.8), although this has not been investigated. Compound **40** was soluble in sulfuric acid and trifluoroacetic acid, giving the characteristic emerald green colour associated with the protonation of the pyrrolic nitrogens and the formation of the porphyrin dication. Zinc(II) metalation was not attempted for compound **40**.

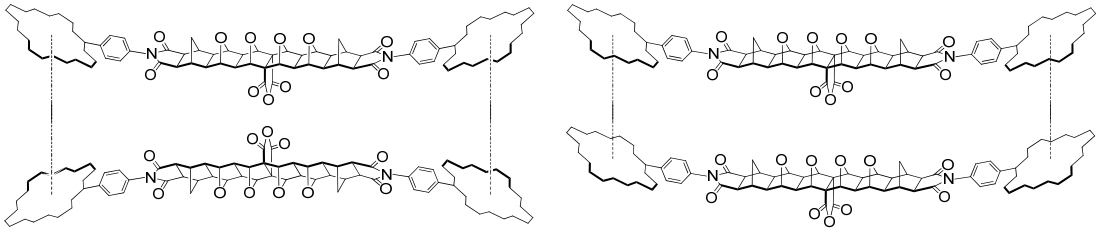

Figure 5.8 - Two possible molecular orientations of a π-π intermolecular aggregate of the bis-porphyrin half **40**. Another orientation is possible, where the anhydrides are both directed away from each other (porphyrin and polycyclic structural detail omitted for clarity).

The analogous bis-phenyl half **45** (Figure 5.9) was synthesised from the *exo*-phenyl receptor **44** for the purposes of examining the ^1H NMR spectra. This showed the formation of two products **45** and **46**, the product ratio of which could be altered by varying the reaction time and temperature (**45** was favoured for longer reaction times and at higher temperatures). Following purification, the symmetrical bis-phenyl 2:1 adduct **45** (soluble in DMSO-d_6, insoluble $CDCl_3$) was identified from the ^1H NMR spectrum by five polycyclic resonances (labelled 1-5, Figure 5.9), a single ester resonance, and two doublets for protons attached to the bridgehead carbon (H_a and H_b), each with expected relative integrations to the phenyl resonances. The ^1H NMR of the second product was consistent with the asymmetric mono-phenyl 1:1 adduct **46** (soluble $CDCl_3$), with seven polycyclic resonances (labelled a-g, Figure 5.9), two ester resonances of equal integration (E_x and E_y) at 3.87 and 3.72 ppm, and two doublets for protons attached to the bridgehead carbon (H_1 and H_2), all with expected relative integrations to the phenyl resonances.

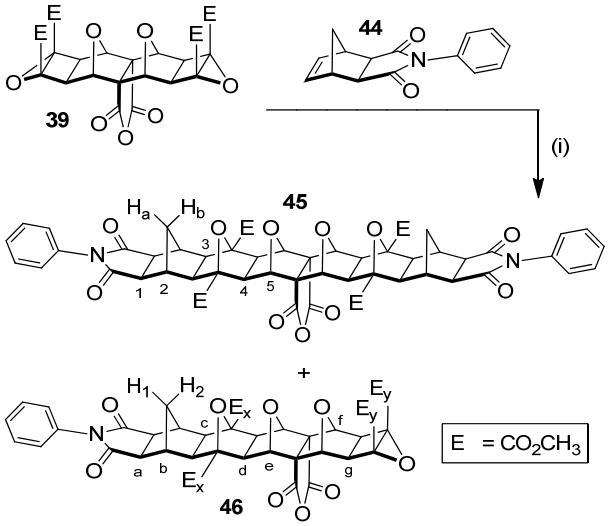

Figure 5.9 - Bis-phenyl **45** and mono-phenyl **46** adducts of the ACE reaction of diepoxide **39**; (i) dry THF, microwave 80-220 W, 14-20 bar; 170 °C, 2 hrs (favours **45**), or 140 °C, 50 minutes (**46** can be isolated).

Asymmetric adducts such as compound **46** are of particular interest as it would allow for the synthesis of asymmetric mixed receptor systems [78]. Although the identity of the terminal epoxide on the mono-phenyl adduct **46** was not confirmed by accurate mass spectrometry in this work, previous work [78] has shown by mass that the epoxide is indeed conserved in reactions of similar substrates [78].

As the bis-porphyrin half **40** displayed poor solubility, the Mitsudo anhydride **38** was employed as a soluble model compound in an attempt to ascertain whether the convergent synthesis could be completed as represented in Figure 5.6. However, the Mitsudo anhydride **38** was found to be unreactive to conventional condensation with aromatic amines. Furthermore, there is literature precedent which reports that lateral functionalisation of this substrate renders the anhydride terminus impervious to reaction with aromatic amines even under forcing conditions [117]. The authors suggest that the anhydride is shielded in such derivatives, by the hydrogen atoms at the ring junctions [117]. This is supported by X-ray crystal structures of similar compounds later in this chapter. Thus even if the bis-porphyrin half **40** was soluble, condensation with *p*-phenylenediamine **9** as depicted in Figure 5.7 would not be a viable convergent pathway to the tetra-porphyrin tweezer **4**.

Nonetheless, the poor solubility of the bis-porphyrin half **40** was unfortunate, as it is an excellent model compound for studying the formation of intermolecular 2:2 sandwich complexes with guest, likely to occur for tetra-porphyrin tweezer **4** in

addition to the intramolecular complex. An example of a possible orientation of the intermolecular 2:2 sandwich formed between bis-porphyrin half **40** and bidentate ligand is shown in Figure 5.10, where the anhydrides are directed away from each other as would occur for tetra-porphyrin tweezer **4**. Future derivatives of compound **40** to investigate intermolecular complexation could involve variation of the methyl ester substitution to increase solubility, or pendant groups in place of the anhydride, which would likely both assist in solubility and discourage formation of the remaining two orientations of the bis-porphyrin half not accessible by the tetra-porphyrin tweezer **4**, where the anhydrides are both directed inwards, or both in the same direction (not depicted in Figure 5.10).

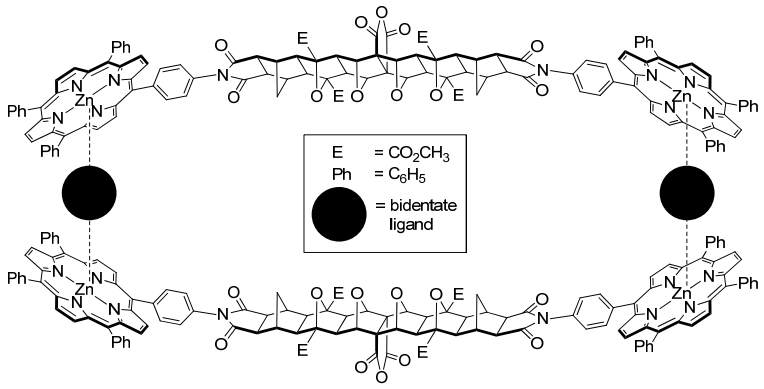

Figure 5.10 - Bis-porphyrin half **40** as a reference compound for the analysis of 2:2 intermolecular sandwich complexes likely to be encountered for the tetra-porphyrin tweezer **4** (one of three orientations of **40** depicted).

Attention was then briefly focussed on Routes B and C (Figure 5.7), which are the Mitsudo reaction of the bis-carboxylic acid **36** and bis-acid chloride **42** derivatives respectively. As discussed earlier, this 7-oxanorbornene are known to be thermally unstable prior to lateral functionalisation, being prone to loss of furan via a retro-Diels-Alder reaction (Alder-Rickert fragmentation) [67, 100, 103, 117, 118, 188]. Routes B and C resulted in complex reaction mixtures for conditions ranging from room temperature to 60 °C, however, further optimisation of the reaction conditions are necessary to determine if the desired Mitsudo adducts **41** and **43** can be isolated by these routes. Literature regarding the analogous bis-methyl ester of **36** (not shown) has demonstrated that degradation can be minimised and the desired Mitsudo adduct favoured by undertaking the reaction at room temperature with high catalyst loadings [100]. This was not investigated because of positive progress with a different reaction pathway explored in section 5.4.3 and 5.4.4.

In summary, various attempts towards a convergent approach were unsuccessful. These problems stem from the bis-(7-oxanorbornane) T-piece module, which unfortunately exhibits a combination of thermal instability (retro-Diels-Alder) for analogues prior to lateral functionalisation [67, 100, 103, 117, 118], and poor anhydride reactivity (when R^2 = O in Figure 5.5) via conventional condensation with aromatic amines (R^3 = NH_2 in Figure 5.5) [67, 118], particularly following lateral functionalisation [117]. Although other similar T-piece modules exist [107], the 7-oxanorbornane version is critical to providing the curvature to the scaffold [107, 108] to facilitate coplanar alignment of the porphyrin receptors in each half [109], and cofacial alignment between the porphyrins in opposing halves, as per the idealised conformation.

Synthetic efforts towards a divergent approach are discussed in the next section, and eventually proved successful.

5.4.2 Synthetic Problems Encountered with the Divergent Approach

In parallel to the convergent approach, a divergent approach was explored, again from the more thermally stable anhydride derivative **37** [103]. While the anhydride moiety of the non-laterally functionalised substrate displays excellent reactivity with aliphatic amines, including both linear [103] and cyclic (not shown) derivatives, it was found that conventional condensation of this anhydride with aromatic amines (such as *p*-phenylenediamine **9**) does not occur (Route D, Figure 5.11), in line with reports by others [67, 118].

While there are earlier reports of *N*-aryl imides accessed from the anhydride [105, 116], a literature search located synthetic procedures for the N-aliphatic species only. Additional reports suggest that high pressure reaction conditions can aid condensation of polycyclic anhydride derivatives with aromatic amine derivatives [67, 107]. However, this method has been reported to favour side products when applied to anhydride **37** [67], while the polycyclic anhydride in [107] is condensed with derivatives of amino pyridine rather than derivatives of aniline, and is undertaken on a different polycyclic substrate to **37**. Thus high pressure was not explored as a pathway, particularly the given literature precedent that this is largely unsuccessful for **37**.

Interestingly, condensation of the anhydride **37** with aromatic amines deprotonated by strong base (*n*-BuLi) has been reported [117] (not shown). This suggests that poor reactivity for the non-laterally functionalised anhydride is related to the nucleophilicity of the incoming amine. This method [117] was not applied to Route D, as a successful alternate pathway, Route E, Figure 5.11, was determined prior to uncovering method [117].

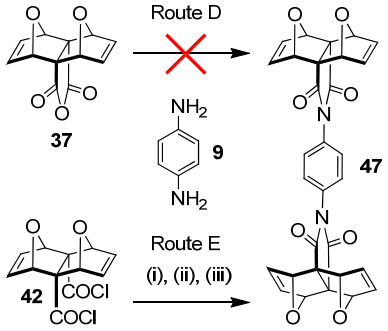

Figure 5.11 - Divergent approaches to tetra-porphyrin tweezer synthesis. Route D: *p*-phenylenediamine **9** (0.5 eq.), solvent, Ar, 60-80 °C, 3-5 days. Route E: (i) *p*-phenylenediamine **9** (0.5 eq.), dry THF, Ar, room temperature, dropwise addition of LiHMDS (0.5 eq., 10-15 seconds), 30 minutes; (ii) bis-acid chloride **42** (2 eq., as solid), 1 hour; (iii) dry THF, HOBt (~3 eq.), 5 mins, DCC (~ 3 eq.), Et3N (~ 10 eq.), room temperature, 4 days, then 50 °C, 2 days.

Literature precedent suggested the bis-acid chloride **42** derivative could be condensed with aniline derivatives [67]. Initial attempts with *p*-phenylenediamine **9** and bis-acid chloride **42** to generate the precursor phenyl diimide core **47** using method [67] were unsuccessful. Later however, it was found that this same structure **47** had previously been synthesised in a related work [118] using method [67], over a period of days. The order of addition of reactants prescribed in [67] is likely to be important; in particular the presence of pyridine to remove any residual HCl from the bis-acid chloride prior to the addition of *p*-phenylenediamine **9**.

Meanwhile, the synthesis was modified by using a strong non-nucleophilic base (LiHMDS) to deprotonate *p*-phenylenediamine **9** to increase the its nucleophilicity (Route E, Figure 5.11) [193]. Slow addition of less than 1 equivalent of LiHMDS was important; greater than 1 equivalent of LiHMDS formed an intensely coloured insoluble mixture, presumably the dianion. The mono-anion of *p*-phenylenediamine most certainly encouraged formation of the intermediate amic acid, which precipitated instantly on addition of the bis-acid chloride **42**. This is a substantial improvement in reaction time compared to similarly deprotonated amines with the

anhydride **37** (hours) [117], or for non-deprotonated *p*-phenylenediamine **9** with the bis-acid chloride **42** (days) [118]. Carbodiimide-mediated ring closing of the amic acid to the imide [67, 118] afforded a product with identical NMR spectra to that prescribed in [118], confirming the product as the non-Mitsudo I-piece **47** (HRMS calcd $[M+Na]^+$ 559.1117, found 559.1123).

Conveniently, crystals of **47** suitable for X-ray analysis could be grown from DMSO, and a crystal structure for the precursor phenyl diimide core **47** was obtained (Prof Jonathan White, The University of Melbourne). This is shown in Figure 5.12 (two different views), co-crystallised with a molecule of DMSO, and demonstrates successful formation of the diimide. Most notably, the polycyclic regions adopt a parallel orientation in the solid state, with the phenyl ring rotated out of the plane of the imides. However no further comments nor comparisons to values obtained from molecular modelling can be made, due to crystal packing forces in the solid state. Key parameters for the X-Ray crystallographic measurements are provided in Appendix 4.

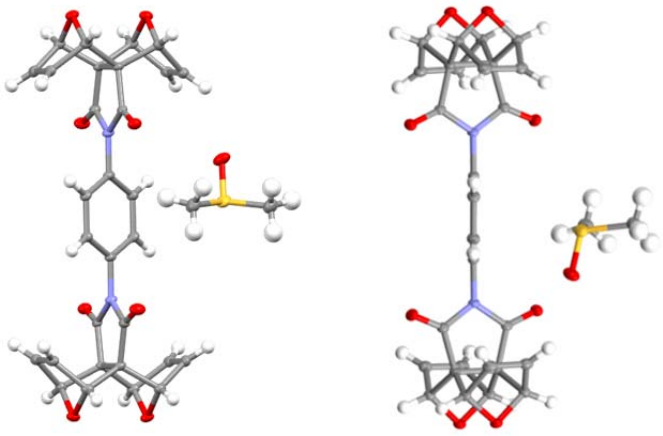

Figure 5.12 - X-ray crystal structure of the precursor phenyl diimide core (two different views).

Unfortunately, this I-shaped linker **47** was found to be unreactive to standard Mitsudo conditions (Figure 5.13) [146, 147], as previously encountered during the synthesis of the freely rotating linker **13** in Chapter 3. Appendix 3 provides further commentary on this matter, as examples of unreactive substrates are rarely reported in the literature.

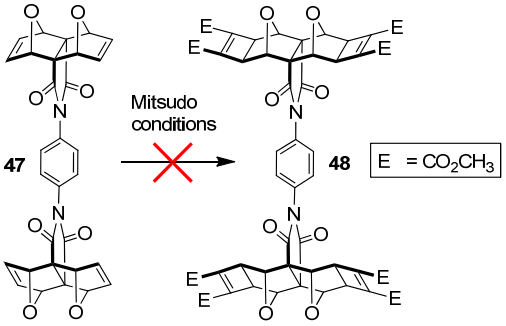

Figure 5.13 - Attempted Mitsudo reaction conditions on the I-piece **47**: 8 eq. DMAD, 20 mol-% $[RuH_2(CO)(PPh_3)_3]$, toluene, 50 °C, 3 days.

5.4.3 The Mitsudo T-piece Imide

Faced with the competing triad of thermal instability, poor anhydride reactivity of the T-piece module **37** to aromatic amines, and the inability of the I-piece linker **47** to undergo the Mitsudo reaction, a new substrate was required to circumvent each of these complications. The Mitsudo T-piece imide **49** (Figure 5.14) was identified as a target compound which could address all of these problems; reactivity in the southern direction is moved off the carbonyl and one atom down to the imide nitrogen to alleviate any steric issues, whilst the pre-installed Mitsudo cyclobutene rings both prevent thermal degradation and commence lateral functionalisation.

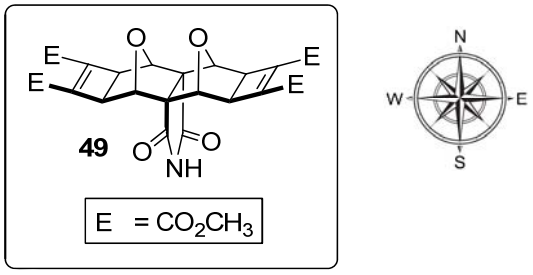

Figure 5.14 - The Mitsudo T-piece imide **49** was identified as a target addressing all of the complications encountered in the previous synthetic strategies in this chapter.

Fortunately, there was literature precedent for the non-Mitsudo T-piece imide **51** [106, 189], in two steps from the anhydride **37** (Figure 5.15). This method uses *p*-methoxybenzylamine (PMB) as a nitrogen source, with the intermediate PMB-protected T-piece **50** cleaved using ammonium cerium(IV) nitrate to afford the T-piece imide **51** [106, 189]. Reaction conditions and workup procedures in this thesis are only partially optimised[28], and further optimisation could improve yields. The literature imide derivative **51** was subjected to Mitsudo conditions [146, 147] to

[28] Limited experimental and characterisation data was provided in [106, 189].

afford the crucial Mitsudo T-piece imide **49** as a new compound. The NMR shows the expected number of resonances in both the ^{1}H and ^{13}C spectra, and the molecular mass was confirmed by HRMS (calcd $[M-H]^-$ 514.0986, found 514.0982).

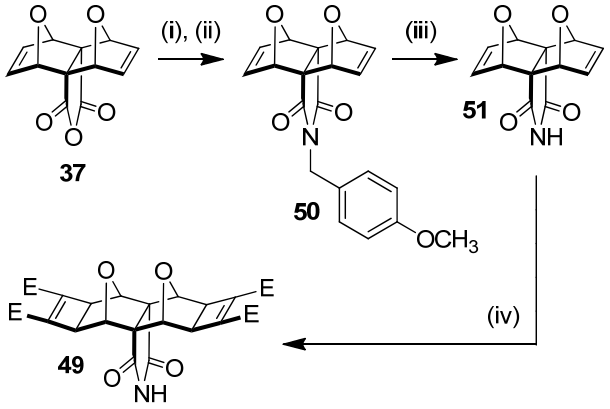

Figure 5.15 - Synthesis of the Mitsudo T-piece Imide **49**. (i) *p*-methoxybenzylamine (2 eq.), deacidified $CHCl_3$, nitrogen, 50 °C, overnight; (ii) $NaOAc/Ac_2O$, nitrogen, 50 °C, overnight, 52 %; (iii) 9:1 CH_3CN/H_20, 40 °C, ammonium cerium(IV) nitrate (3 eq., 2 hrs; 2.3 eq. 90 mins + 0.3 eq. 30 mins), 73 %; (iv) 4eq. DMAD (4 eq.), 20 mol-% $[Ru[H_2CO(PPh_3)_3]$, dry DMF, 60 °C, nitrogen, 24 hrs, 34 %.

Conveniently, crystals suitable for X-ray analysis could be grown for all three compounds in the 7-oxanorbornane imide synthetic series in Figure 5.15 (slow evaporation, CH_3CN for PMB protected T-piece **50**, CH_3CN/DMSO for T-piece imide **51**, CH_3CN for Mitsudo T-piece imide **49**). X-ray crystallographic data was collected by Prof Chris Sumby (The University of Adelaide), with crystal structures solved by Dr Rebecca Norman (Flinders University). These are shown in Figure 5.16, in which (b) **51** solves as an asymmetric unit (full structure shown), and (c) **49** is co-crystallised with CH_3CN and H_2O (not shown). Notably, these two structures clearly show changes to the spatial orientation of the hydrogen atoms with respect to the imide after lateral functionalisation going from (b) **51** to (c) **49** (refer to arrows Figure 5.16). This supports the comment by [117] that the anhydride (or in this case the carbonyl of the imide) is more shielded by the hydrogen atoms at the ring junctions following lateral functionalisation. Key parameters for the X-Ray crystallographic measurements are provided in Appendix 4.

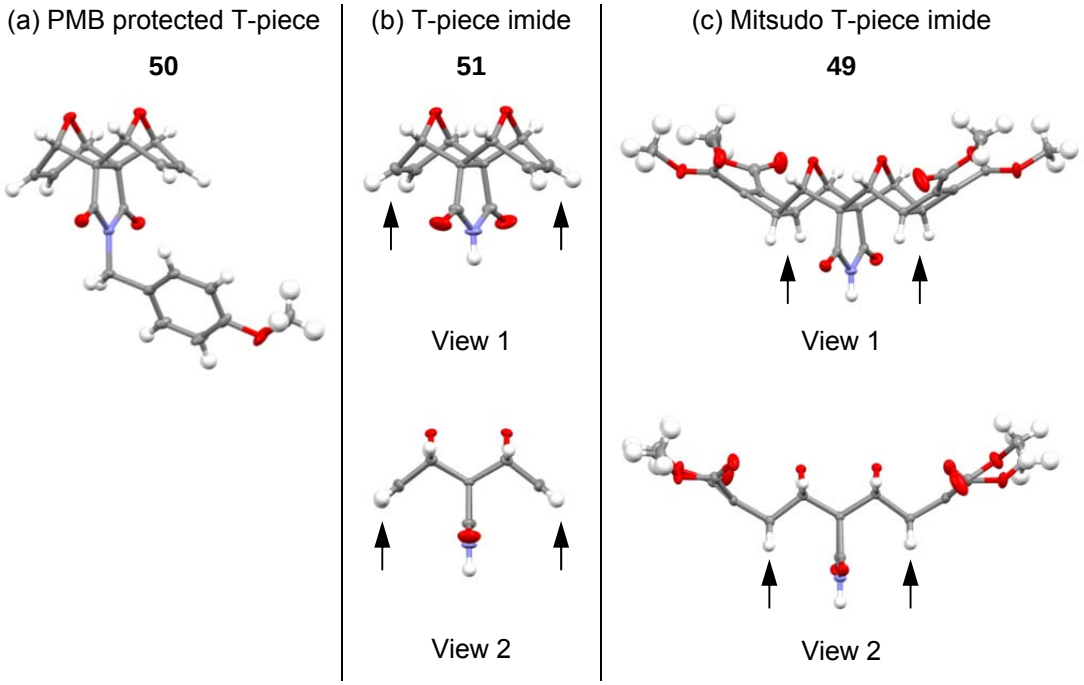

Figure 5.16 - X-ray crystal structures of the 7-oxanorbornane imide series; (a) PMB protected T-piece **50**, (b) T-piece imide **51** (two different views), (c) Mitsudo T-piece imide **49** (two different views)

The Mitsudo T-piece imide **49** briefly renewed efforts towards a divergent synthesis. Unfortunately however, the formation of the diepoxide imide **52** could not be achieved (Figure 5.17). The strong base (*t*-BuOK) required for nucleophilic epoxidation abstracts the proton from the free imide, precipitating the imide salt even in polar solvents. Epoxidation of the protected Mitsudo T-piece imides **53** (Troc [106] and Boc), also failed to afford the desired diepoxide imide **54**. An alternative epoxidation using dimethyldioxirane [194, 195] (undertaken in conjunction with Emma Muehlberg, Flinders University) was unsuccessful, although perhaps not surprising given that dimethyldioxirane is reported to behave as an electrophilic epoxidising agent [194, 195] and alkenes with strong electron withdrawing substituents are reported to react slowly [194, 195].

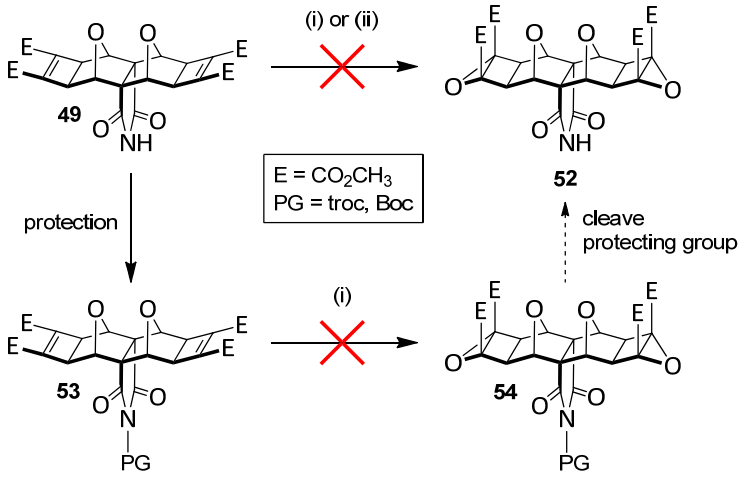

Figure 5.17 - Attempted formation of the Mitsudo imide diepoxide **52**. (i) standard nucleophilic epoxidation conditions (anhydrous *t*BuOOH in toluene (3.3 M)/dry CH_2Cl_2/*t*-BuOK); (ii) dimethyldioxirane, acetone, room temperature, overnight.

5.4.4 Imide Coupling Chemistry

It was evident by this stage that reactions commonly employed for polynorbornyl substrates would be unsuitable for the synthesis of the tetra-porphyrin tweezer **4**. Again returning to a divergent approach, it was necessary to determine a method to form the tetra-functional phenyl diimide core **48** depicted in Figure 5.18. On review of the literature, two candidates for coupling nitrogen-containing molecules with aryl species were identified, neither of which appeared to have been demonstrated on norbornyl molecules. These are described below.

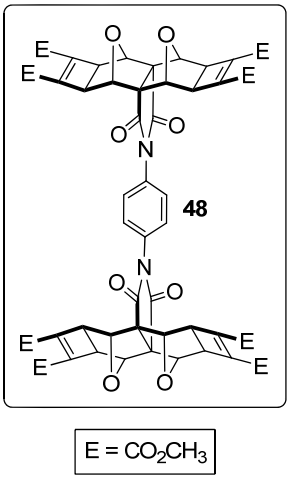

Figure 5.18 - The tetra-functional phenyl diimide core **48** required for divergent synthesis of the tetra-porphyrin tweezer **4**.

Imide-Aryl Halide/Cu(0) Microwave Coupling

Literature precedent existed for the microwave-assisted coupling of imides such as phthalimide with mono-aryl halides in the presence of activated elemental copper (0) [196]. Modification of this procedure was found to successfully lend itself to the Mitsudo imide **49**. Phenyl imide **56** was afforded by using excess iodobenzene **55** (as the solvent) relative to imide **49** at 150 °C for several cycles in the microwave (Figure 5.19). The addition of an organic solvent such as ethyl acetate resulted in a large reduction in product, even for excess iodobenzene **55** relative to imide **49**, while an equimolar mixture of iodobenzene **55** and imide **49** in ethyl acetate failed to yield any coupled adduct. Additionally, the glass reaction vessels for the microwave are susceptible to fracture from the spot heating of elemental copper by the focussed microwave reactor, further complicating this technique.

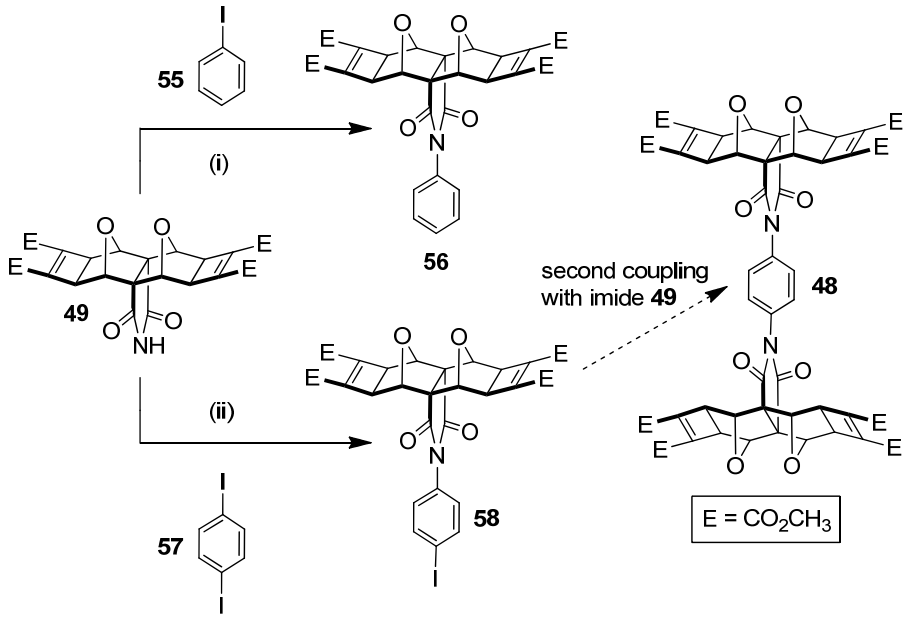

Figure 5.19 - Imide-Aryl Halide/Cu(0) Microwave Coupling. (i) 1-iodobenzene **55** (excess, as solvent), freshly precipitated Cu(0) (5 eq.), 4x 10 minute microwave cycles (300 W, high stirring, air cooling, 150 °C); (ii) 1,4-diodobenzene **57** (8 eq.), freshly precipitated Cu(0) (8 eq.), EtOAc (1 mL), microwave cycles at 300 W, high stirring, and air cooling as follows: (a) 1 hr, 120-150 °C; (b) additional Cu(0) (8 eq.), 1.5 hrs, 120-150 °C; (c) toluene (1 mL), 1 hr, 150 °C; (d) 8.5 hrs, 150 °C.

Unfortunately, the synthesis of the tetra-functional phenyl diimide core **48** was found to be much more challenging than the phenyl imide **56** described in the previous paragraph. 1,4-diiodobenzene **57** is a solid and only 0.5 eq. is required to generate the diimide core. Solvation was necessary to ensure adequate mixing of the otherwise solid reaction mixture, however this results in dilute solutions, and no product (**48** or

58) was detected. A solventless melt of excess 1,4-diodobenzene **57** relative to imide **49** resulted in rapid temperature fluctuations and pressurisation of the vessel, and so was not investigated further. Although the original publication recommends water as a solvent [196], this was not investigated, as an alternate coupling proved to be successful during this time.

A small quantity of the asymmetric phenyl 1-imide-4-iodo adduct **58** was generated (Figure 5.19), by using excess 1,4-diiodobenzene **57** in solvent and subjecting to microwave irradiation over an extended period (12 hrs total). However, the inefficiency associated with forming precursor **58**, along with the second coupling with additional imide **49** required to generate the diimide **48** (not attempted) resulted in the exploration of an alternative imide coupling procedure which proved to be successful and is discussed now.

Imide-Phenyl Boronic Acid/Cu(II)/Air Coupling

Further literature precedent suggested that imidazole can be coupled with aryl boronic acid in the presence of a simple Cu(II) salt, without complex bases, ligands, or other additives [197]. Compressed air is bubbled through the reaction mixture to regenerate spent catalyst. This reaction was found to lend itself to the Mitsudo imide **49**, which in the first instance was reacted with phenyl boronic acid using the conditions in [197], giving identical ^{1}H NMR spectra to the phenyl imide **56** generated via the former method [196].

Fortunately, by using a 1:2 stoichiometric quantity of benzene-1,4-diboronic acid **59** to imide **49**, phenyl diimide **48** was obtained (Figure 5.20). The optimum Cu(II) catalyst loading was found to be < 5%, at which the reaction only yielded about a third of the desired product; another third was starting material imide **49**, while the remaining third was an unexpected side product. This side product was identified as the phenyl 1-imide-4-solvent adduct (**60** and **61**), and indicated a competitive reaction between boronic acid, imide, and solvent (MeOH gave methoxy substitution **60**). At > 5% catalyst loadings, the side product was the major product. This side product was not reported in [197], which only uses mono-aryl boronic acids. This led to a brief exploration of the involvement of solvent in the reaction.

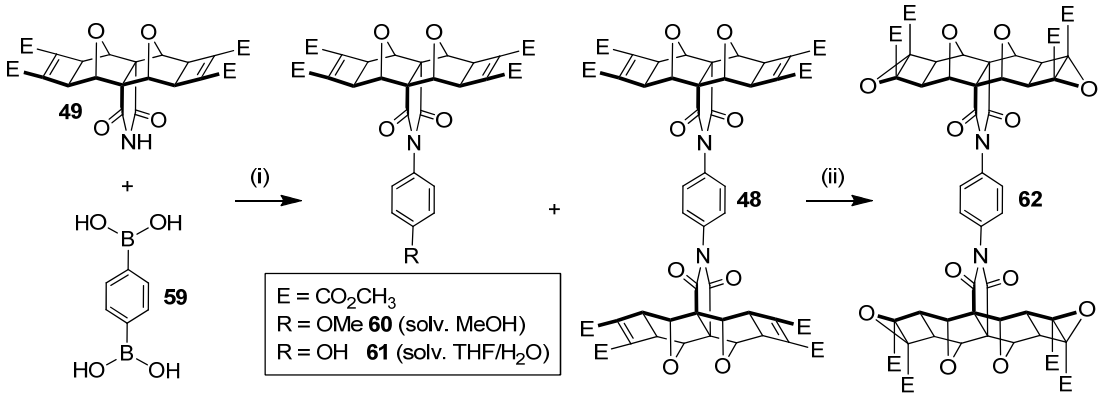

Figure 5.20 - Imide-Phenyl Boronic Acid/Cu(II)/Air Coupling. (i) Mitsudo T-piece imide block **49**, benzene-1,4-diboronic acid **59**, copper (II) acetate (5 mol-%), MeOH or THF/H_2O, reflux, air bubbler, 18 hrs, ~30 % phenyl 1-imide-4-solvent adduct **60** or **61** + 30 % phenyl diimide adduct **48**; (ii) anhydrous 3.3 M *t*BuOOH in toluene (5 eq.), dry CH_2Cl_2, 0 °C, 10 min, *t*BuOK (2 eq.), r.t., 3.5 hrs, ~50%.

As reported in [197], no coupling was found to occur in aprotic solvents such as THF. However, coupling was successful in 9:1 THF/H_2O, and again, this afforded not only the phenyl diimide, but side product with hydroxyl substitution **61** (Figure 5.20). Further optimisation of the reaction conditions is required to minimise competitive reaction with solvent, including investigation of less nucleophilic protic solvents such as isopropanol [198]. Additionally, it is speculated the side reaction could be related to oxidation of an intermediate product by the Cu(II) salt, however, this requires further investigation.

Nevertheless, a sufficient quantity of the tetra-functional phenyl diimide core **48** (Mitsudo I-piece) was obtained. This was an excellent outcome since this is a key compound in the divergent synthetic strategy. The mass was confirmed by HRMS (calcd $[M+Na]^+$ 1127.2182, found 1127.2166), while the ^1H and ^{13}C NMR both show the expected number of resonances. The singlet in the ^1H NMR at 7.38 ppm is assigned to the phenyl core and demonstrates that rotation is rapid on the NMR timescale.

Compound **48** was subsequently subjected to a four-fold nucleophilic epoxidation at the electron deficient alkene [102, 104] and afforded the tetra-epoxide **62** (Figure 5.20). The epoxidation was evidenced by shifts to most of the ^1H NMR resonances, and was confirmed by HRMS (calcd $[M+Na]^+$ 1191.1978, found 1191.1984). The yield of 50 % was very good for this type of reaction, particularly given there are

four epoxides. The isolation of compound **62** was very exciting, being a single step from the synthesis of the tetra-porphyrin tweezer **4**.

5.4.5 Tetra-porphyrin Tweezer Synthesis

Thus the tetra-epoxide **62** was subsequently appended with *exo*-porphyrin receptor **18** [1] via the alkene plus cyclobutane epoxide (ACE) reaction (Figure 5.21) using microwave irradiation [160]. Although ACE chemistry has been well established for polycyclic scaffolds for some time, there appear to be no examples of tetra-functional substrates undergoing four simultaneous ACE reactions. ^{1}H NMR of the crude reaction mixture indicated that the tetra-porphyrin adduct **63** was the major product of the reaction, however, the high degree of purity required for host-guest titrations resulted in significant loss of product during purification, affording only 16 % after repeated recrystallisations. The identity of the freebase tetra-porphyrin tweezer **63** was confirmed by HRMS (calcd $[M+4H]^{4+}$ 1068.3540, found 1068.3566). Due to the significance of the tetra-porphyrin tweezer **63** (**4** when metallated with zinc(II)), the NMR spectra will now be discussed in some detail.

The ^{1}H NMR spectra reflected the symmetry of the tetra-porphyrin tweezer **63**, arising from free rotation about the phenyl diimide core and porphyrin receptors. Several features characteristic of ACE-coupled reaction products could be observed, including a small downfield shift for the methyl ester resonance [160], along with the disappearance of the norbornene proton resonance from the *exo*-receptor **18** at 6.45 ppm. The resonance at 90 ppm in the ^{13}C NMR is observed in similar polycyclic systems [113], and is assigned to the carbon atoms to which the oxygen bridgeheads are attached in the newly formed methyl ester substituted 7-oxanorbornane [113].

In the ^{1}H NMR spectrum (Figure 5.22), seven polycyclic resonances can be observed as expected (excluding the methyl ester); five singlets and two doublets (a doublet of doublets). Of the five singlets, two arise from the central 7-oxanorbornane component, labelled 1-2, Figure 5.21), while the remaining three signals arise from the *exo*- component (labelled 3-5, Figure 5.21). The doublets, which occur at chemical shifts of 1.27 and 2.62 ppm, correspond to the methylene bridge protons H_a/H_b (Figure 5.21), which appear at different chemical shifts due to the influence of the 7-oxanorbornane in these linear systems [109, 151].

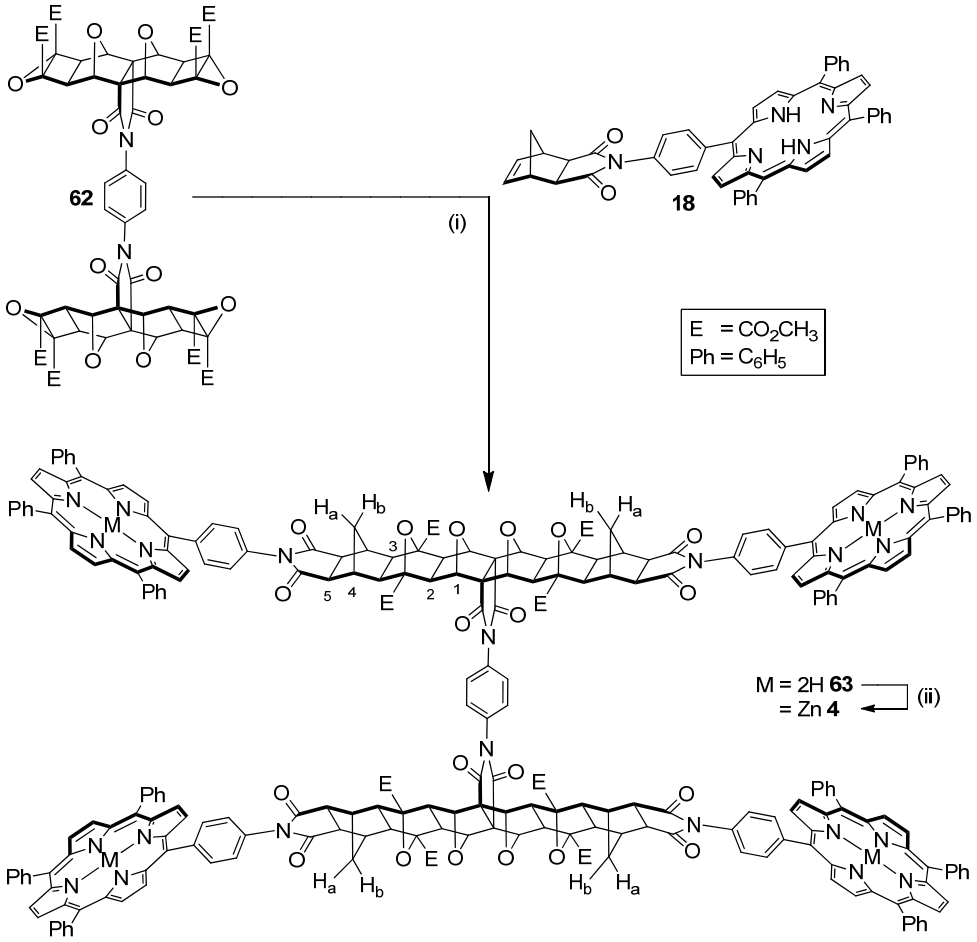

Figure 5.21 – Tetra-porphyrin Tweezer Synthesis **4** (i) *exo*-porphyrin receptor 4 (4 eq.), dry THF, microwave 80-220 W, 14-20 bar, 170 °C, 2 hrs, 16 % (after purification); (ii) $Zn(OAc)_2$/MeOH/$CHCl_3$, reflux, 2 hrs, 70 % (after purification).

There is some evidence of minor desymmetrisation within the porphyrin aromatic region of the ^{1}H NMR spectrum of the freebase tetra-porphyrin tweezer **63** (Figure 5.22). While the β-pyrrole resonance appears as a singlet, there is slight splitting within some of the *meso*-phenyl resonances, and the linking *meso*-phenyl resonances are somewhat broad. This facial differentiation indicates there is some interaction of opposing porphyrins or intermolecular aggregation at NMR concentrations (10^{-3} - 10^{-4} M).

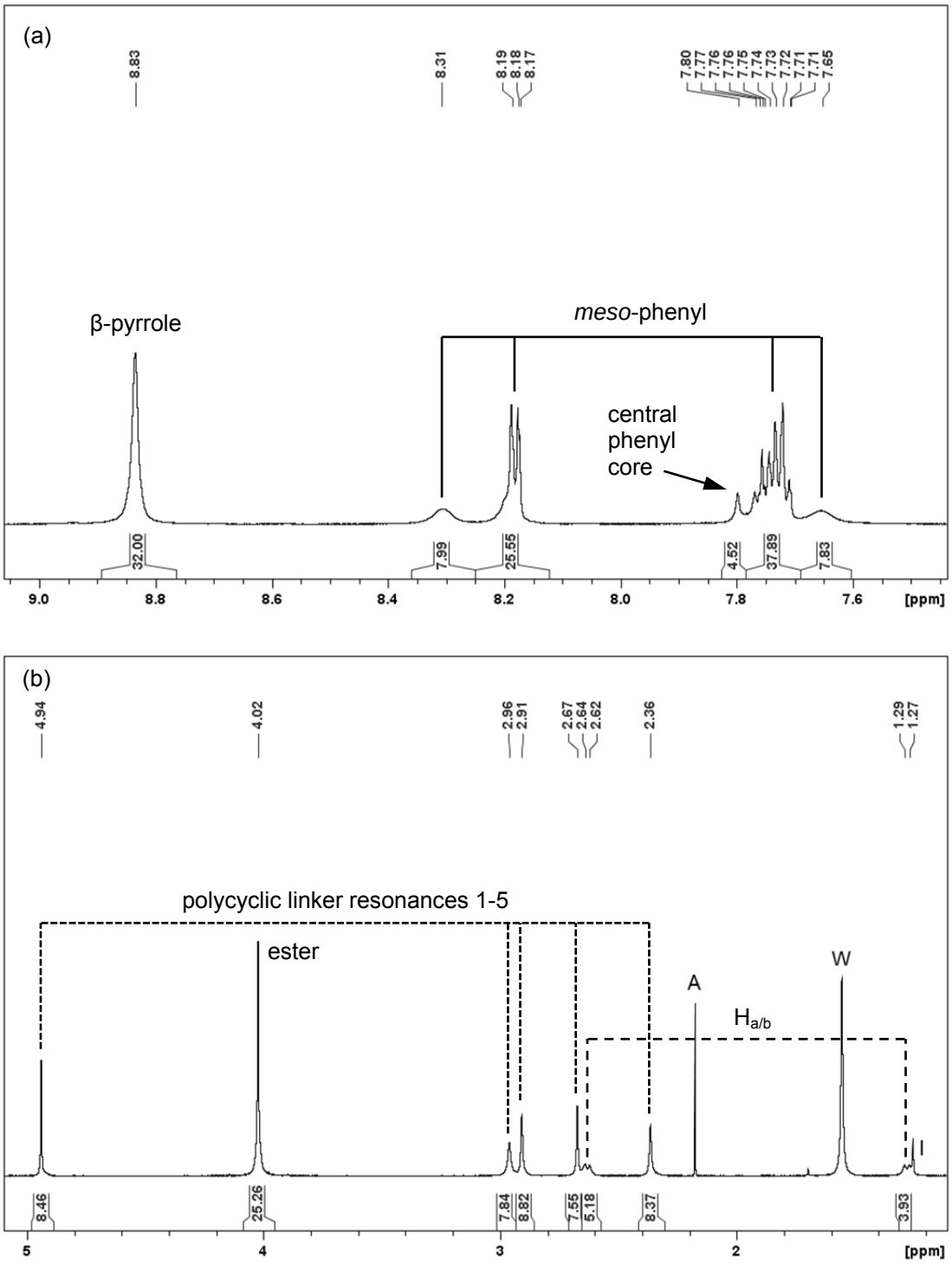

Figure 5.22 - Selected ^{1}H NMR spectral regions of the freebase tetra-porphyrin tweezer **63** showing (a) porphyrin β-pyrrole and *meso*-phenyl resonances, (b) polycyclic linker resonances 1-5 and $H_{a/b}$ [Figure 5.21]. A denotes acetone, W denotes H_2O, and I denotes impurity.

The freebase tetra-porphyrin tweezer **63** was metallated with zinc(II) under standard conditions [159] to afford final compound **4** (Figure 5.21), and was characterised by loss of the porphyrin inner pyrrole proton resonance at -2.81 ppm in the ^{1}H NMR spectrum. The linking *meso*-phenyl resonances remain broad in the metallated adduct

at 20 °C, however upon cooling to -50 °C, sharpen into doublets (Figure 5.23 (a)). This suggests that the tetra-porphyrin tweezer **4** is undergoing conformational changes on the NMR timescale influenced by the temperature. The ^{1}H NMR spectrum was only slightly concentration dependent in $CDCl_3$; dilution from 1.8 mM to highly dilute resulted in resonance shifts of 0.02-0.05 ppm for several resonances. This suggests that the porphyrin interaction in tetra-porphyrin **4** is intramolecular, and that the system is not significantly intermolecularly aggregated (unless the system remains aggregated at the lowest concentration). At highly dilute concentrations, the linking *meso*-phenyl resonances appeared sharper and splitting could be observed (Figure 5.23 (b)).

Table 5.1 summarises the main UV-Vis spectral features for all tweezer analogues **1**-**4** in this thesis. In line with other tweezers seen in previous chapters, no significant shift was observed for the Soret band of the tetra-porphyrin tweezer **63** upon zinc(II) metalation to **4**, with only changes to the Q-bands being observed (related to symmetry factors [47, 58]). The Soret peak band width of 10.6 nm for the tetra-porphyrin tweezer **4** is barely broadened compared to the values for mono-porphyrin receptor **22** and *anti*- restricted tweezer **3** (Table 5.1), indicating that exciton coupling interactions between the porphyrins in the tetra-porphyrin tweezer **4** are largely absent at UV-Vis concentrations (10^{-6} - 10^{-7} M). This suggests either the porphyrin units are able to undergo rotation either about the single bond between the imide and porphyrin moiety, and/or the two porphyrin arms can undergo rotation about the phenyl diimide core.

Table 5.1 - Summary of UV-Vis data in chloroform comparing all tweezer analogues **1**-**4**.

Species	**Zn(II) mono-porphyrin, 22**	**Zn(II) freely rotating tweezer, 1**	**Zn(II) *syn*-restricted tweezer, 2**	**Zn(II) *anti*-restricted tweezer, 3**	**Zn(II) Tetra-porphyrin Tweezer, 4**
λ_{max} (nm)	419.3	419.5	418.3-418.5	419.3-419.6	419.6
Width (nm) [a]	9.9	11	11.5	10.1	10.6
$\varepsilon_{singleporphyrin}$ (x 10^5 $Lmol^{-1}cm^{-1}$)	6.47	4.7-6.9 [b] [c]	4.9 [c]	5.8 [c]	5.65 [d]

[a] Peak band width measured at half height.

[b] Quoted as a range to account for possible errors in concentration.

[c] $\varepsilon_{singleporphyrin} = \varepsilon_{experimental}/2$ (tweezer has two porphyrins).

[d] $\varepsilon_{singleporphyrin} = \varepsilon_{experimental}/4$ (tweezer has four porphyrins).

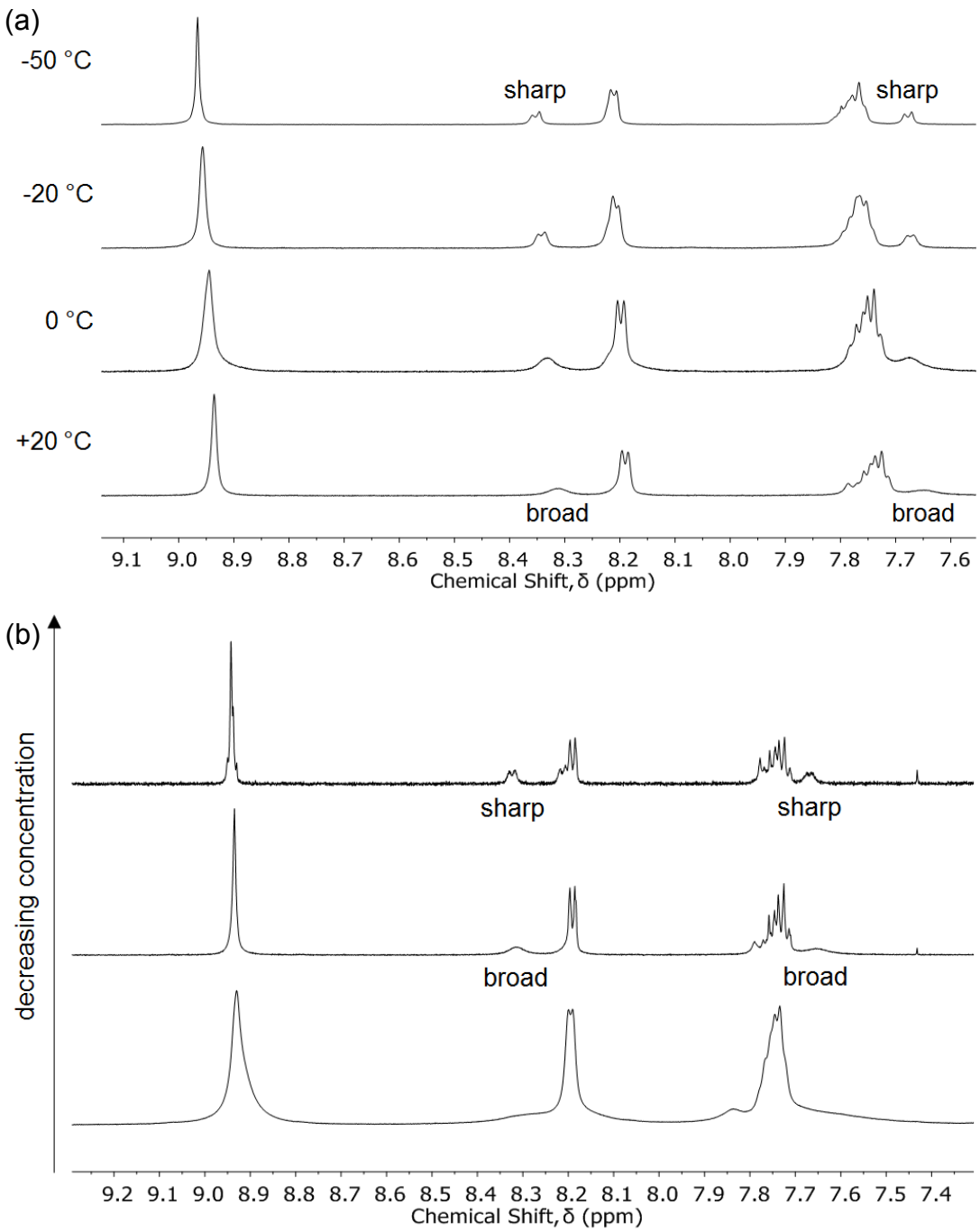

Figure 5.23 - Selected ^{1}H NMR spectral regions of Zn tetra-porphyrin tweezer **4** showing sharpening of the linking porphyrin *meso*-phenyl resonances as (a) the temperature is decreased (from bottom to top), and (b) the concentration is decreased from 5 mM (bottom) to highly dilute (top).

5.5 Tetra-porphyrin Host-Guest Study

Having completed the synthesis and characterisation of the Zn(II) tetra-porphyrin tweezer **4**, the host-guest behaviour of this fascinating system could now be examined. In line with the host-guest studies from previous chapters, the interaction between Zn(II) tetra-porphyrin tweezer **4** and the diamino ligands DABCO **5** and bipy **6** was examined by UV-Vis and NMR spectroscopy. The tetra-porphyrin host can form various complexes in solution, all of which are in equilibrium. These possibilities are outlined schematically in Figure 5.24 and reveal the possibility of 1:1 (K_{11} = [tetra-porphyrin:ligand]/([tetra-porphyrin][ligand]), 1:2 (K_{12} = [tetra-porphyrin:(ligand)$_2$]/([tetra-porphyrin][ligand]^2), 2:2 (K_{22} = [(tetra-porphyrin)$_2$:(ligand)$_2$]/([tetra-porphyrin]^2[ligand]^2), 1:3 (K_{13} = [tetra-porphyrin:(ligand)$_3$]/([tetra-porphyrin][ligand]^3), and 1:4 (K_{14} = [tetra-porphyrin:(ligand)$_4$]/([tetra-porphyrin][ligand]^4) stoichiometries.

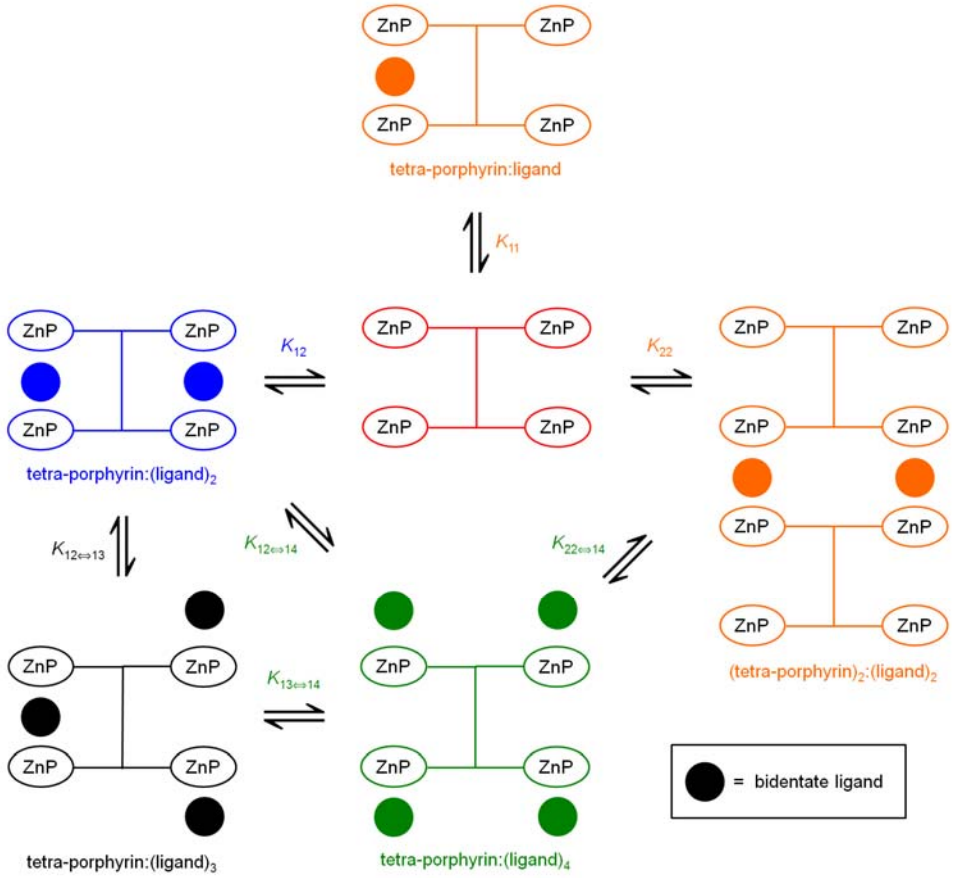

Figure 5.24 - Schematic representation of the various equilibria between tetra-porphyrin tweezer **4** and bidentate ligand (represented by circles). Colour coded with red for free host, blue for intramolecular sandwich complex, orange for species containing both free and sandwich complex porphyrins (intra- or inter- molecular), and green for simple open 1:1 porphyrin:ligand complex. The 1:3 species is shown in black.

5.5.1 Tetra-porphyrin Tweezer with DABCO (UV-Vis)

The first guest examined with the tetra-porphyrin system **4** was DABCO **5**. Titration of a solution of DABCO to a solution of tetra-porphyrin tweezer resulted in a two-stage red shift of the UV-Vis spectrum (Figure 5.25 (a)), in line with results from previous chapters. The Soret maximum transitions from 419.6 nm to 423.6 nm, and is characteristic of a bis-porphyrin DABCO sandwich complex [30, 31]. A second gradual redshift occurs to 429.5 nm by 500 000 equivalents of DABCO, although this transition appears to be only be partially complete by this number of equivalents. This spectral transition is characteristic of simple mono-porphyrin DABCO complexes [30, 31].

The UV-Vis titration data gave reasonable fits for two different binding models, namely 1:2 plus 1:4, and 2:2 plus 1:2 plus 1:4. However, the binding model with three coloured species (2:2 plus 1:2 plus 1:4) had a slightly better fit and so was selected for further analysis, even though the formation of the intermolecular 2:2 species in competition with the intramolecular 1:2 species at UV-Vis concentrations could be seen as unusual. At no stage was a 1:1 or 1:3 species found to be suitable to aid fitting in the various binding models examined.

The 1:2 plus 2:2 plus 1:4 binding model gave K_{12} = 6.32x 10^{13} M^{-2} and K_{22} = 3.04 x 10^{20} M^{-3}, and K_{14} of = 1.92 x 10^{16} M^{-4} in $CHCl_3$ (average of two replicates, fitted to 200 000 equivalents of DABCO). These are assigned to intramolecular tetra-porphyrin:$(DABCO)_2$ **4**:$(\mathbf{5})_2$, intermolecular (tetra-porphyrin)$_2$:$(DABCO)_2$ $(\mathbf{4})_2$:$(\mathbf{5})_2$, and open tetra-porphyrin:$(DABCO)_4$ **4**:$(\mathbf{5})_4$ respectively (Figure 5.24). The value for K_{22} is consistent with other examples of intermolecular porphyrin DABCO sandwich complexes in the literature (K_{22} = 6.2 x 10^{16} - 6.3 x 10^{22} M^{-3} [28, 30, 31]).

Shown in Figure 5.25 (b) and (c) are speciation diagrams for the UV-Vis titration data that have been separated out into 0-10 equivalents DABCO and 0-200 000 equivalents DABCO. Clearly visible is the initial formation of both the 2:2 and 1:2 complexes between the tweezer and DABCO, (tetra-porphyrin)$_2$:$(DABCO)_2$ (orange line) and tetra-porphyrin:$(DABCO)_2$ (blue line), followed by their conversion into the 1:4 complex, tetra-porphyrin:$(DABCO)_4$ (green line), as more equivalents of DABCO are added to the solution. The best fit of the algorithm for the formation of tetra-porphyrin:$(DABCO)_2$, (tetra-porphyrin)$_2$:$(DABCO)_2$, and tetra-

porphyrin:$(DABCO)_4$ to the titration data at 419 nm is shown in Figure 5.25 (c) and (d) respectively. A similar fit was observed using the 423 nm data (not shown), however, the fit at 430 nm was only moderate (not shown).

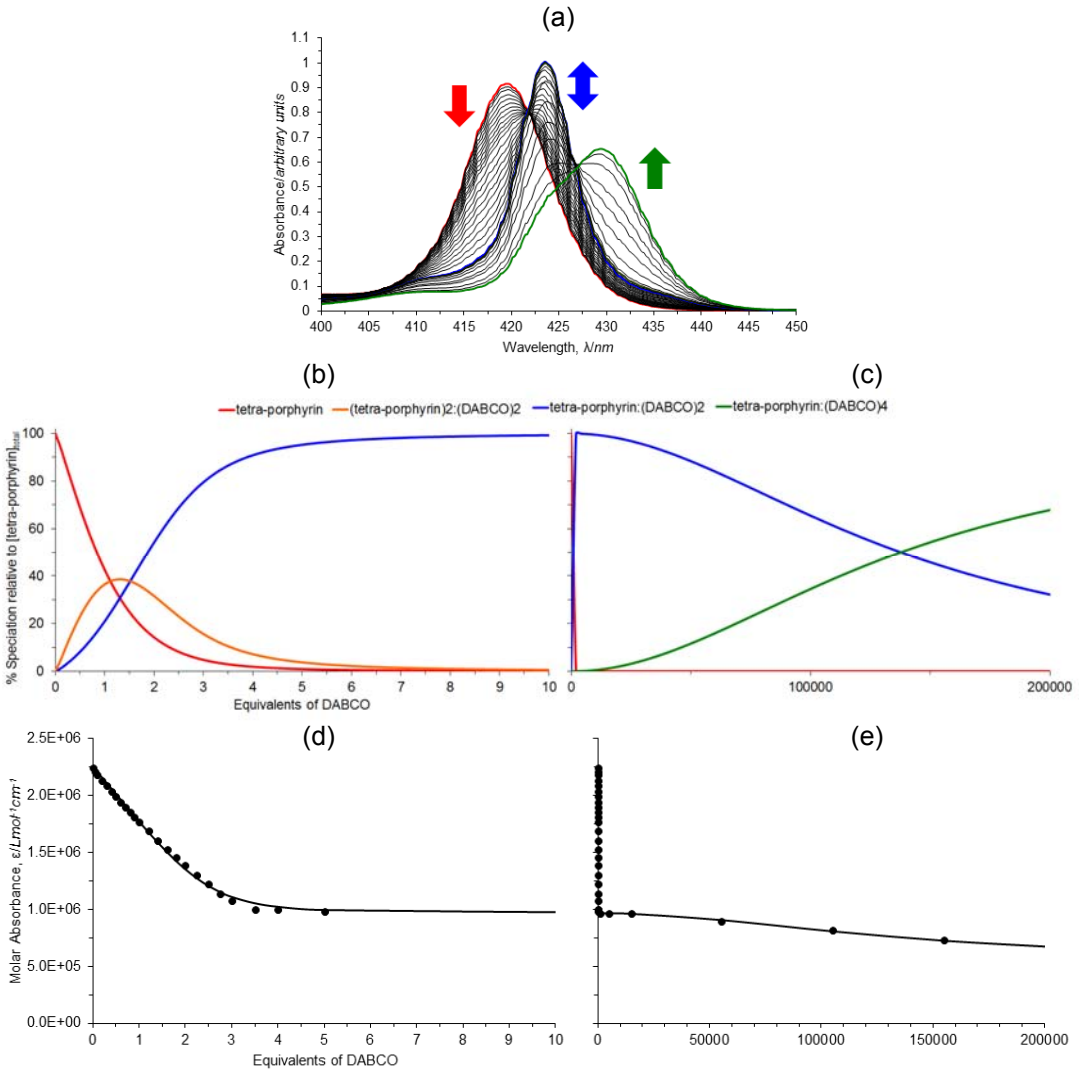

Figure 5.25 – (a) UV-Vis titration of tetra-porphyrin tweezer **4** with DABCO **5** in chloroform; (b) speciation diagram of tetra-porphyrin tweezer with DABCO (2:2 + 1:2 → 1:4) for 0 - 10 eq. of DABCO; (c) 0 - 200 000 eq. of DABCO; (d) best fit (black line) of the algorithm for equilibria between tetra-porphyrin tweezer, DABCO, tetra-porphyrin:$(DABCO)_2$, and tetra-porphyrin:$(DABCO)_4$ to the titration data (black circles) at 419 nm for 0 - 10 eq. of DABCO; (e) 0 - 200 000 eq. of DABCO.

The HypSpec software package output contains calculated UV-Vis spectra based on the fit (not shown), and these are a reasonable match to the experimental spectra. The calculated profile for intermolecular 2:2 complex reflects the correct ratio of free and sandwich complexed porphyrins. However, the profile for the 1:4 species was slightly inaccurate compared to the experimental data, with the transition to this species being more advanced in the calculated spectrum than occurs experimentally.

Nevertheless, the 2:2 plus 1:2 plus 1:4 binding model was the most suited to the data, and so the analysis was continued.

5.5.2 Tetra-porphyrin Tweezer with DABCO (NMR)

Additional characterisation of the bis-porphyrin DABCO sandwich complex was provided by ^{1}H NMR titration of tetra-porphyrin tweezer with DABCO in $CDCl_3$, again focussing on the diagnostic porphyrin β-pyrrole and DABCO resonances. As per previous titrations, there was error between the number of equivalents of guest titrated against host based on mass weighed compared to NMR signal integration, estimated to be 5-10 % at 20 °C and for 5-15 % at -50 °C.

At 20 °C, the β-pyrrole signals for the uncomplexed tetra-porphyrin host are at 8.94 ppm (Figure 5.26 (a)). The addition of up to 1.9 titrated equivalents of DABCO (integration suggests 2 equivalents) resulted in the appearance of a second β-pyrrole signal at 8.57-8.51 ppm. This upfield shift is typical of β-pyrrole protons in a bis-porphyrin DABCO sandwich complex and results from shielding by opposing ring currents of two porphyrin aromatic systems in close proximity [30, 31, 66]. Interestingly, a very small amount of a third broader porphyrin β-pyrrole signal was observed between 8.90-8.73 ppm (dotted box, inset Figure 5.26 (a)), similar in chemical shift to the free host porphyrin resonances. This was not observed for any of the other tweezers in this thesis, and conjecture is given to the identity of this species later in this chapter. All three species are in slow exchange rate on the NMR chemical shift timescale below 1.7-1.9 titrated equivalents of DABCO (integration suggests 2 equivalents). The main β-pyrrole sandwich complex signal at 8.57-8.51 ppm increases at the expense of the main uncomplexed tetra-porphyrin tweezer at 8.94 ppm, with this transition complete by approximately 1.9 titrated equivalents of DABCO (integration suggests 2 equivalents). Limited information could be obtained from the porphyrin *meso*-phenyl resonances (broad but desymmetrised, not shown) and polycyclic backbone resonances (not shown).

Between 2 and 10 equivalents of DABCO, no changes are observed in the chemical shift of the porphyrin β-pyrrole sandwich resonance at 8.57-8.51 ppm, suggesting the complex resists decay to the open species in excess DABCO. While the porphyrin *meso*-phenyl protons resymmetrise then sharpen (not shown), no downfield shift is observed. The broadening could be a result of exchange between the sandwich and

open species, however, the absence of a downfield shift for both the porphyrin *meso*-phenyl and β-pyrrole suggests the predominant species is the sandwich complex for excess bipy.

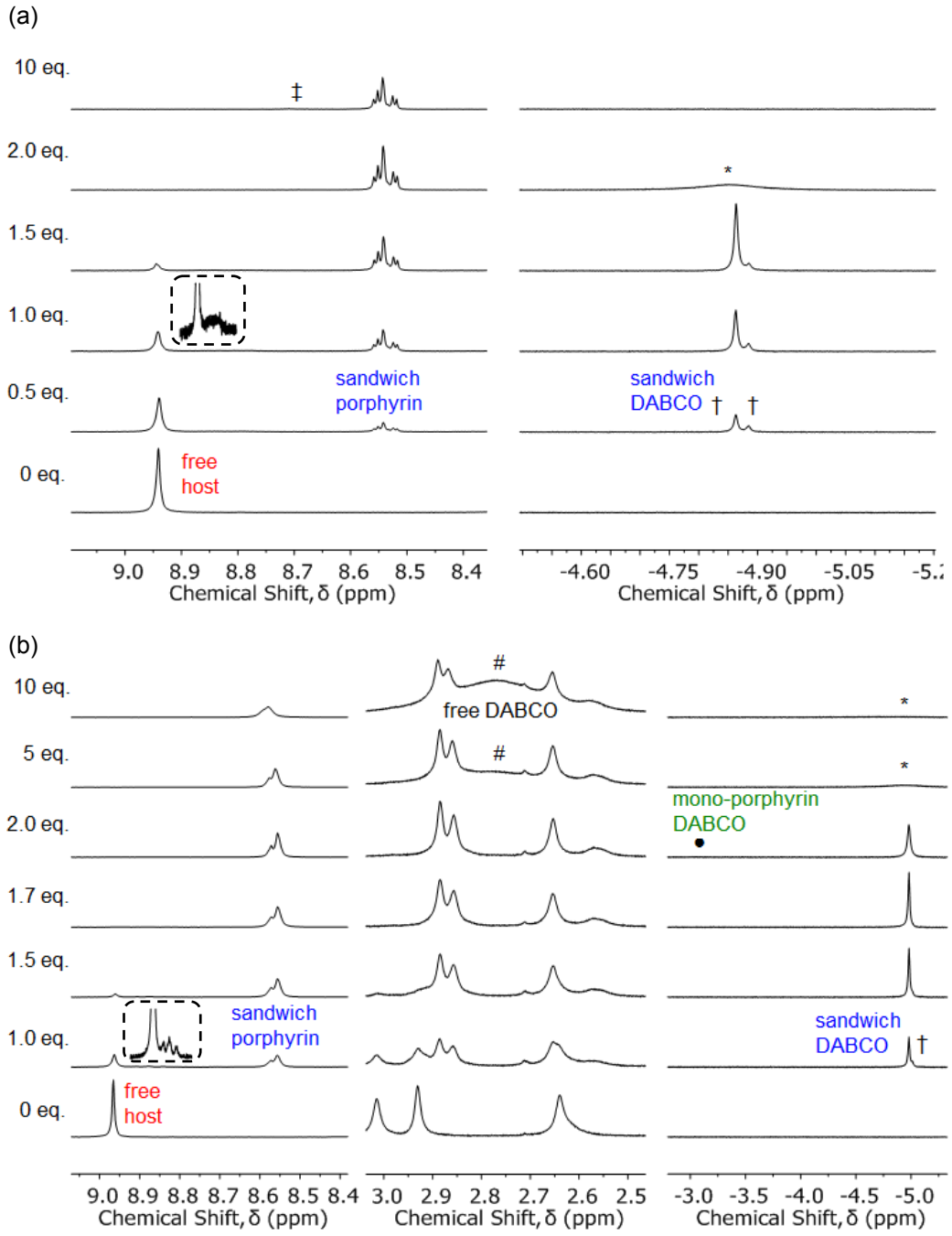

Figure 5.26 - Selected ^{1}H NMR with various equivalents of DABCO at (a) 20 °C (top pane) and (b) -50 °C (bottom pane). † identifies additional sandwich complexes. * identifies sandwich signals broadened into the baseline due to chemical exchange. ‡ indicates an unidentified weak porphyrin resonance observed at 10 equivalents of DABCO. ● identifies the broad mono-porphyrin DABCO resonance. # identifies the broad free DABCO resonance.

Additionally, a weak porphyrin resonance is appears to be increasing at 8.7 ppm (marked with ‡ in Figure 5.26 (a)), however, this species has not yet been identified. Although purely speculative at this stage, these spectral changes might arise from a 1:3 species (Figure 5.24), but requires further investigation.

Further understanding of the complexation of DABCO by the tetra-porphyrin tweezer was gained from the DABCO methylene resonance (Figure 5.26 (a)). At 0.1 equivalents of DABCO, two sharp DABCO signals can be observed at -4.87 ppm and -4.88 ppm (indicated by †). This large upfield shift is typical of DABCO methylene protons in a bis-porphyrin DABCO sandwich complex, and again results from shielding by opposing ring currents of two porphyrin aromatic systems in close proximity[27, 29-31, 52, 66, 172]. The signal at -4.88 ppm is slightly favoured at very low concentrations of DABCO. At higher concentrations of DABCO, but below 1.7-1.9 titrated equivalents of DABCO (integration suggests 2 equivalents), the resonance at -4.87ppm becomes the major sandwich species. An extremely low intensity third DABCO sandwich signal can be observed at -4.82 ppm (again indicated by †).

At greater than 1.9 titrated equivalents of DABCO (spectral features suggest greater than 2 equivalents), the sandwich DABCO resonance broadens into the baseline and cannot be observed by 5 equivalents of DABCO (indicated by * in Figure 5.26 (a)). This is consistent with chemical exchange occurring with another species at a fast exchange rate on the NMR chemical shift timescale at 20 ˚C. After 10 equivalents of DABCO, a large broad peak can be observed between 2.9-1.6 ppm underneath the polycyclic resonances, as the concentration of free DABCO increases (not shown).

Slowing the exchange rate by lowering the temperature to -50 °C (Figure 5.26 (b)) revealed several finer spectral details. Below 1.7-1.9 titrated equivalents of DABCO (integration suggests 2 equivalents), the resonance for the third porphyrin β-pyrrole signal is much sharper (dotted box, inset Figure 5.26 (b)). Again, this is evidence of different speciation in the tetra-porphyrin system compared to the other tweezer examples presented in this thesis. A major and minor DABCO sandwich signal can again be observed (indicated by † in Figure 5.26 (b)).

At greater than 1.7-1.9 titrated equivalents of DABCO (spectral features suggest greater than 2 equivalents), the system moves into intermediate to fast exchange on

the NMR chemical shift timescale. The major DABCO sandwich resonance at -4.98 ppm is broadened due to chemical exchange (marked with * in Figure 5.26 (b)), while an extremely small resonance can be observed at -3.06 ppm (marked with ●). This chemical shift is characteristic of the α methylene protons of DABCO bound to a single porphyrin [28-30], such as would occur for open species tetra-porphyrin:$(DABCO)_4$. Importantly however, between 3 and 10 equivalents, the DABCO sandwich resonance appears to mainly exchange with a broad signal at 2.77 ppm (marked with #), close to the value for free DABCO. The porphyrin β-pyrrole sandwich resonance only undergoes small changes in chemical shift at these temperatures (0.02 ppm), indicating that the sandwich complex is resistant to excess DABCO, but that decay to the open species is starting to occur.

The porphyrin *meso*-phenyl porphyrin resonances (not shown) are highly desymmetrised below 2 equivalents of DABCO, indicating facial differentiation between the porphyrins in the sandwich complex. While these resonances broaden and resymmetrise for greater than 2 equivalents of DABCO, only a small downfield shift is observed, in line with the porphyrin β-pyrrole sandwich resonance and conclusions about the onset of decay of the sandwich species to the open species.

The major speciation supported by the NMR is the formation of a 1:2 intramolecular sandwich complex, tetra-porphyrin:$(DABCO)_2$, based on the relative integration of the DABCO sandwich resonance to the ester signal at 1.9 titrated equivalents of DABCO at 20 °C. The speciation of the second sandwich species evidenced by the additional DABCO sandwich resonance could not be identified by NMR, while the species evidenced by the third β-pyrrole resonance (marked by the dotted box inset into Figure 5.26) must contain uncomplexed porphyrins based on its chemical shift. If these uncomplexed porphyrin β-pyrrole and DABCO sandwich complex resonances belong to the same species, these signals could describe either intramolecular 1:1 species, tetra-porphyrin:DABCO, or the intermolecular 2:2 species, $(\text{tetra-porphyrin})_2$:$(DABCO)_2$ (Figure 5.24), which both contain equal numbers of free and sandwich complexed porphyrins (Figure 5.27).

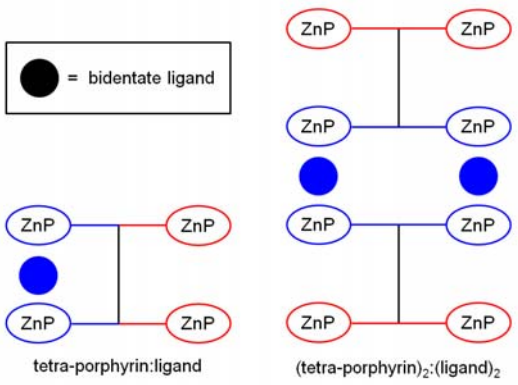

Figure 5.27 – Both tetra-porphyrin:ligand and $(\text{tetra-porphyrin})_2$:$(\text{ligand})_2$ contain equal ratios of free and uncomplexed porphyrins, and could explain unassigned resonances in the NMR.

To further investigate the composition of the complex formed between tetra-porphyrin tweezer and DABCO at NMR concentrations (millimolar), a simulated NMR speciation diagram (HySS2009, Protonic Software[166]) was generated using the association constants for successfully fitted binding models determined from the UV-Vis titrations [28, 30, 31]. Figure 5.28 shows this result for the 2:2 plus 1:2 plus 1:4 binding model.

The experimental NMR speciation is not plotted on Figure 5.28 as has been done in previous chapters, as the ratio of the two sandwich species cannot be determined by integration of the free and sandwich porphyrin β-pyrrole resonances. The main difficulty is that the sandwich porphyrin β-pyrrole resonances appear at the same chemical shift for both the major intramolecular 1:2 sandwich species and the minor sandwich species (which could be either intramolecular 1:1 or intermolecular 2:2 as outlined in Figure 5.27). Nor can speciation be estimated by integration of the two DABCO sandwich resonances, as these are not baseline resolved after 1 equivalent of DABCO (peak deconvolution was not performed).

However, it is immediately apparent from the NMR spectra that the experimental speciation involves the simultaneous co-existence of two sandwich species at concentrations below 1 equivalent of DABCO (Figure 5.26 (a)). This is in stark contrast to the simulated speciation in Figure 5.28, where the 2:2 species is exclusively formed up to 1 equivalent, only after which the 1:2 species is formed at the expense of the 2:2 species. Thus, it is clearly evident that the binding model is different between UV-Vis and NMR concentrations for the tetra-porphyrin system with DABCO.

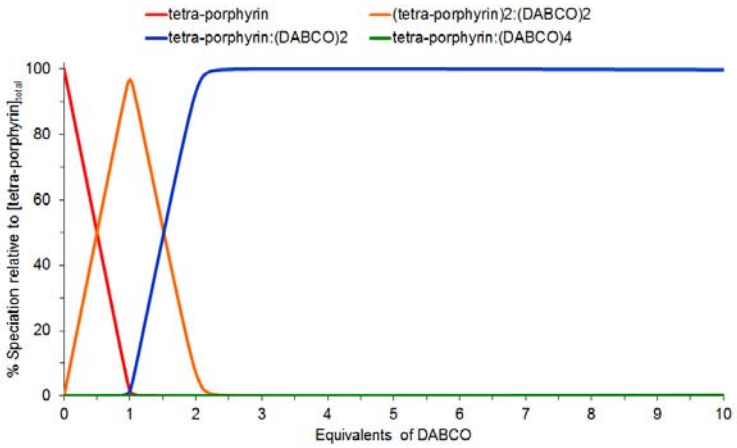

Figure 5.28 - Simulated NMR speciation diagram generated from UV-Vis determined association constants K_{22}, K_{12}, and K_{14}.

5.5.3 Tetra-porphyrin Tweezer with bipy (UV-Vis)

The second guest examined with the tetra-porphyrin tweezer **4** was bipy **6**. This was undertaken to compare the behaviour of the system with different guests. In a similar manner to previous bipy titrations, addition of a solution of bipy to a solution of tetra-porphyrin tweezer resulted in a two-stage red shift of the UV-Vis spectrum (Figure 5.29 (a)). The Soret maximum gradually transitions from 419.5 nm to 426.5 nm, and is in line with the value observed for previous bis-porphyrin bipy sandwich complexes in this work, as well as that reported in [78]. A second gradual redshift occurs from 426.5 nm to 428 nm, suggesting the sandwich species is decaying to an open species, however this transition appears to be only partially complete by 400 000 equivalents of bipy (430 nm is reported for the reference open species of tetraphenylporphyrin with pyridine [176]).

Although the UV-Vis titration data fitted similarly to two different binding models, (1:1 plus 1:2 plus 1:4, and 2:2 plus 1:2 plus 1:4), the calculated molar absorbance spectra for the 2:2 species (not shown) does not account for the equal ratio of free and sandwich complexed porphyrins in this species (Figure 5.24). This is different to the results for DABCO earlier in this chapter, where the 2:2 species was supported by the data. Instead for bipy, the calculated molar absorbance spectra was a good match for the 1:1 species (which interestingly was not supported for DABCO), thus the 1:1 plus 1:2 plus 1:4 binding model was selected for bipy.

A 1:1 plus 1:2 plus 1:4 binding model gave K_{11} = 2.14 x 10^6 M^{-1}, K_{12} = 5.17 x 10^{12} M^{-2}, and K_{14} = 1.94 x 10^{15} M^{-4} in $CHCl_3$ (average of two replicates, fitted to 200 000 equivalents of bipy). These species are assigned to intramolecular tetra-porphyrin:bipy **4**:**6**, tetra-porphyrin:$(bipy)_2$ **4**:$(\mathbf{6})_2$, and open tetra-porphyrin:$(bipy)_4$ **4**:$(\mathbf{6})_4$ respectively (Figure 5.24).

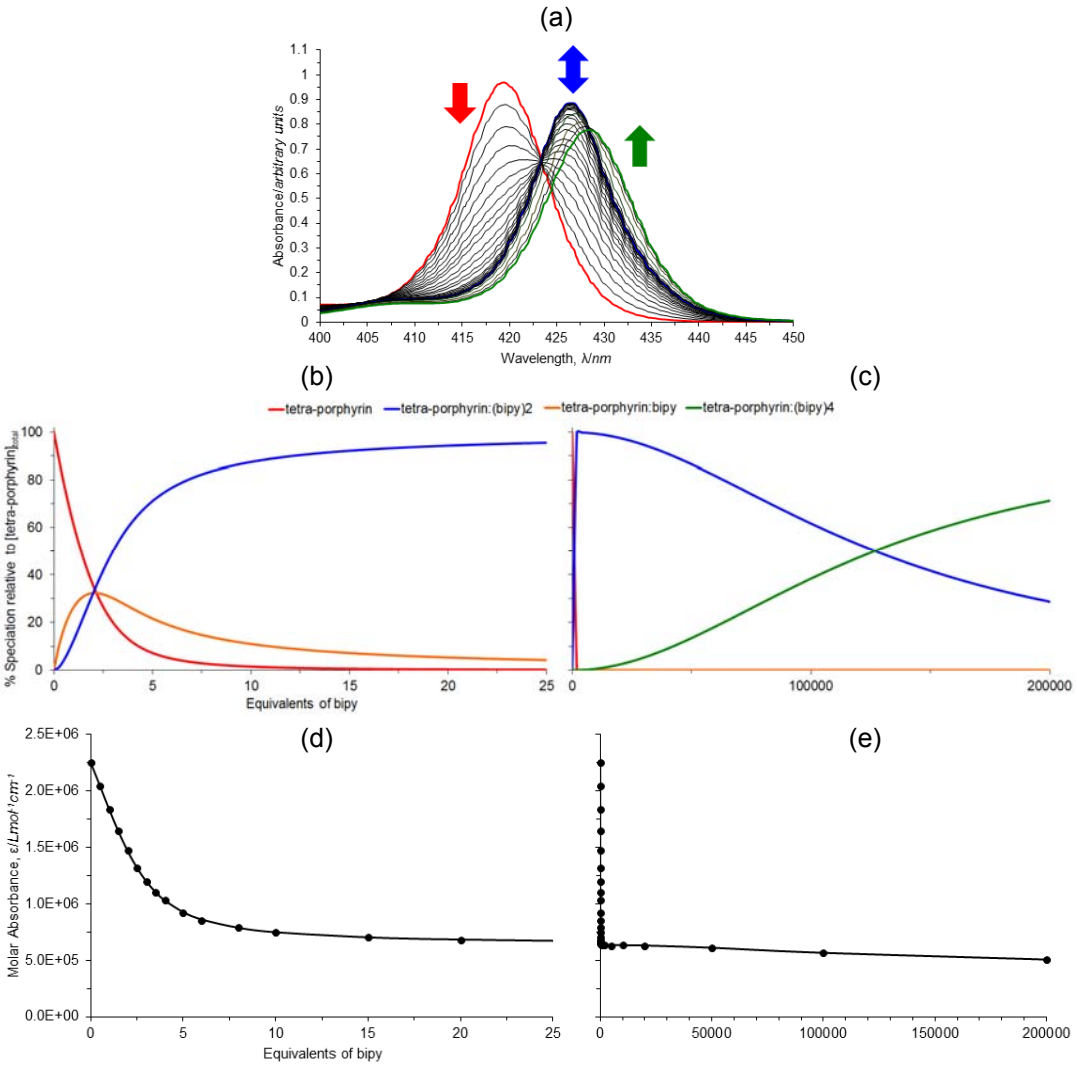

Figure 5.29 - (a) UV-Vis titration of tetra-porphyrin tweezer **4** with bipy **6** in chloroform; (b) speciation diagram of tetra-porphyrin tweezer with bipy (1:1 + 1:2 → 1:4, HypSpec, HySS2009) for 0 - 25 eq. of bipy; (c) 0 - 200 000 eq. of bipy; (d) best fit (black line) of the algorithm for equilibria between tetra-porphyrin tweezer, bipy, tetra-porphyrin:bipy, tetra-porphyrin:$(bipy)_2$, and tetra-porphyrin:$(bipy)_4$ to the titration data (black circles) at 419 nm for 0 - 25 eq. of bipy; (e) 0 - 200 000 eq. of bipy.

Shown in Figure 5.29 (b) and (c) are speciation diagrams for the UV-Vis titration data that have been separated out into 0-25 equivalents of bipy and 0-200 000 equivalents of bipy. This shows the initial formation of both the 1:1 and 1:2 complexes from tetra-porphyrin host and bipy, tetra-porphyrin:bipy (orange line) and

tetra-porphyrin:$(bipy)_2$ (blue line). The subsequent conversion of 1:1 into 1:2, and the conversion of 1:2 into the 1:4 complex, tetra-porphyrin:$(bipy)_4$ (green line), is evident as more equivalents of bipy are added to the solution. The best fit of the algorithm for the formation of tetra-porphyrin:bipy, tetra-porphyrin:$(bipy)_2$ and tetra-porphyrin:$(bipy)_4$ to the titration data at 419 nm is shown in Figure 5.29 (d) and (e) respectively. This fit was similar at 426.5 nm and 430 nm (not shown).

5.5.4 Tetra-porphyrin Tweezer with bipy (NMR)

After the tetra-porphyrin host and bipy had been examined by UV-Vis, complexation was studied by NMR. The ^{1}H NMR spectra for the addition of bipy to tetra-porphyrin host in $CDCl_3$ at 20 °C is shown in Figure 5.30 (a). In this titration, the estimated error was approximately 25 % between the number of equivalents titrated based on the mass weighed, compared to the number of equivalents integrated by NMR. In this case, the large discrepancy is most likely caused by a weighing error in combination with the previously discussed 10-15 % error for all titrations. Nevertheless, the accuracy of the titration was adequate to understand the behaviour of the system through examination of the diagnostic porphyrin β-pyrrole and bipy signals.

For less than 1.5-1.7 titrated equivalents of bipy (integration suggests 2 equivalents), the system was in fast exchange on the NMR chemical shift timescale. The porphyrin β-pyrrole sandwich complex resonance signals are observed as an average between free host at 8.94 ppm, tending towards 8.77-8.64 ppm, consistent with the formation of a bis-porphyrin bipy sandwich [177]. By 1.7 titrated equivalents of bipy (spectral features suggest 2 equivalents) this transition was complete. Between 2 and 10 equivalents of bipy, no changes are observed in the chemical shift of the porphyrin β-pyrrole sandwich resonances, indicating the sandwich complex is resistant to excess bipy.

Additionally, the porphyrin *meso*-phenyl protons (not shown, broadened below 2 equivalents of bipy), sharpen for greater than 2 equivalents of bipy. The high degree of desymmetrisation is indicative of facial differentiation and interaction of the porphyrins, which coupled with the absence of a downfield shift even for excess bipy provides additional evidence the sandwich species resists decay to the open species.

Only small shifts to polycyclic backbone resonances can be observed for the duration of the titration (not shown).

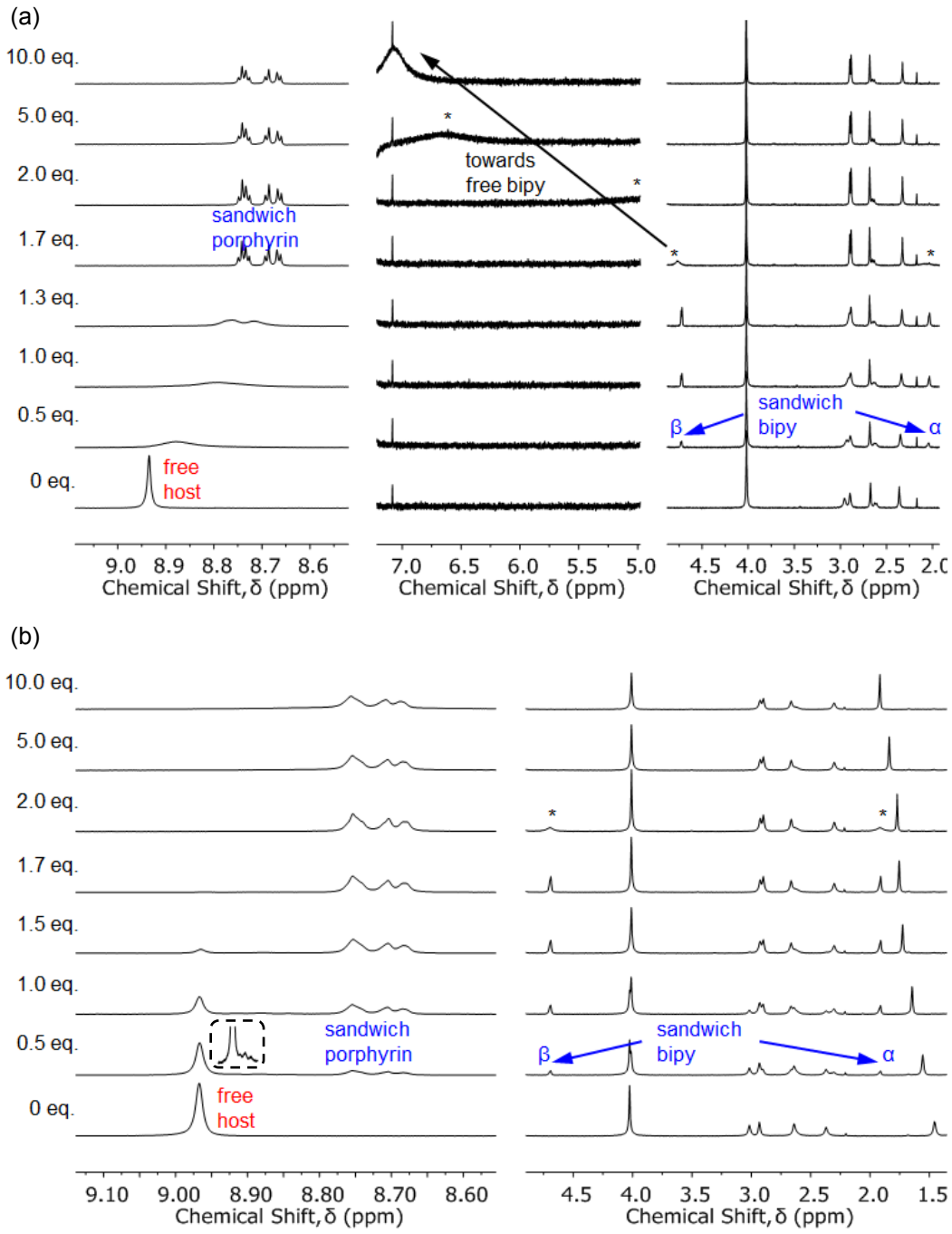

Figure 5.30 - Selected ^{1}H NMR with various equivalents of bipy at (a) 20 °C (top pane) and (b) -50 °C (bottom pane). α and β refer to the position of the *ortho*- and *meta*- protons in 4,4'-bipyridyl. * identifies bipy signals broadened into the baseline due to chemical exchange.

Further understanding of the complexation was gained from the bipy resonances (Figure 5.30 (a)). For less than 1.5-1.7 titrated equivalents of bipy (integration suggests 2 equivalents), two sharp bipy signals can be observed at 4.72 and 2.04 ppm, consistent with bipy in a bis-porphyrin sandwich complex from Chapters 3 and

4, and similar to that reported in the literature [53, 178, 179]. By 1.7 titrated equivalents of bipy (spectral features suggest 2 equivalents), the two bipy sandwich signals broaden into the baseline (marked by * in Figure 5.30 (a)), and further additions of bipy result in a downfield shift, consistent with fast exchange between sandwich complex and free bipy.

Additional information was obtained by conducting the titration at -50 °C (Figure 5.30 (b)). In this titration, the estimated error was 15 % between the number of equivalents of guest titrated with host based on mass weighed compared to NMR signal integration, and is consistent with the error observed for all NMR titrations as discussed previously.

The system was in slow exchange on the NMR chemical shift timescale below 1.7 titrated equivalents of bipy (integration suggests 2 equivalents). The β-pyrrole resonance for free host at 8.97 ppm decreases at the expense of sandwich resonances at 8.78-8.65 ppm, and all free host is converted to sandwich complex by this point. A small amount of a third porphyrin β-pyrrole signal was observed between 8.93-8.82 ppm (dotted box, inset Figure 5.30 (b)) which was not observable when the system was in fast exchange at 20 °C (Figure 5.30 (a)). This unusual porphyrin β-pyrrole resonance is similar in chemical shift to the free host porphyrin resonances, and was observed for the tetra-porphyrin host with DABCO, again providing evidence for different speciation in the tetra-porphyrin system compared to the other tweezer examples presented in this thesis. Although the porphyrin *meso*-phenyl porphyrin resonances (not shown) are observed to be desymmetrised below 2 equivalents of bipy, little additional information could be obtained from this spectral data. Little information was provided by the slow exchanging polycyclic resonances (not shown). Additionally below 1.7 titrated equivalents of bipy (integration suggests 2 equivalents), the two bipy resonances are observed at 4.69 and 1.92 ppm, again typical of bipy in a bis-porphyrin sandwich complex from Chapters 3 and 4 and similar to that reported in the literature [53, 178, 179].

For greater than 1.7 titrated equivalents of bipy (spectral features suggest 2 equivalents), the system moves into fast exchange on the NMR chemical shift timescale. The two bipy sandwich signals broaden into the baseline (marked by * in Figure 5.30 (b)), as they exchange between sandwich complex and free bipy. No major shift was observed for the porphyrin β-pyrrole sandwich resonances by 10

equivalents of bipy, however the porphyrin *meso*-phenyl signals broaden and appear less desymmetrised (not shown). The broadening could be a result of exchange between the sandwich and open species, however, the absence of a downfield shift for both the porphyrin *meso*- phenyl and β-pyrrole suggests the predominant species is the sandwich complex for excess bipy. No major shift was observed for the polycyclic resonances for excess bipy (not shown).

The major speciation supported by the NMR at 20 °C is the formation of a 1:2 intramolecular sandwich complex, tetra-porphyrin:$(bipy)_2$. This is based on spectral changes at 2 equivalents of bipy (1.7 titrated equivalents), namely the broadening of the bipy sandwich resonances due to exchange with free bipy, and the stabilising of the porphyrin β-pyrrole resonance at the known value for a sandwich complex (Figure 5.30 (a)). The presence of a second species such as intramolecular 1:1, tetra-porphyrin:bipy, or intermolecular 2:2, $(\text{tetra-porphyrin})_2$:$(bipy)_2$, could not be detected in the NMR at 20 °C. Evidence of a species different to free host but containing uncomplexed porphyrins was observed at -50 °C (marked by the dotted box inset into Figure 5.30 (b)), and could describe either the 1:1 or 2:2 species. This species could be concealed at 20 °C by the fast exchanging β-pyrrole resonances. No additional bipy sandwich species can be detected, although these could overlap with the resonances for the 1:2 species.

In a similar manner to the previous DABCO analysis, a simulated NMR speciation diagram was generated for bipy using the association constants determined from the UV-Vis titrations (Figure 5.31). However, because only tetra-porphyrin:$(bipy)_2$ can be observed experimentally at 20 °C (other complexes, if present, go undetected at 20 °C), the stepwise binding model determined at UV-Vis concentrations cannot be proved or disproved at NMR concentrations.

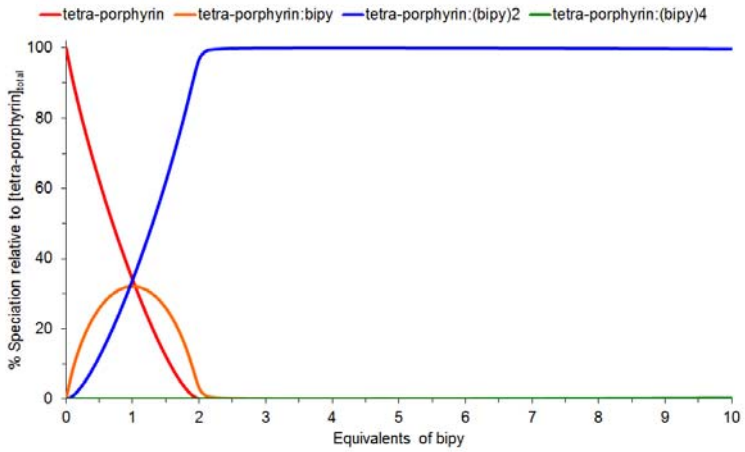

Figure 5.31 - Simulated NMR speciation diagram generated from UV-Vis determined association constants K_{11}, K_{22} and K_{14}.

5.6 Statistical Analysis of Association Constants and Cooperativity Calculations

After determining K_{12} of the tetra-porphyrin tweezer **4** with both DABCO **5** and bipy **6**, a method was required to determine the cooperativity between the two binding sites. A statistical analysis of association constants is extensively reported in the literature [28, 30, 31, 58, 88, 93, 199], albeit with variations to the method employed. The tetra-porphyrin system in this work is most accurately described as interannular, where there is interplay between two intramolecular binding interactions [88]. Cooperativity in interannular systems can be assessed using the statistical analysis of Ercolani [88].

The method of Ercolani for interannular systems [88] is explained in Appendix 2, but in summary:

(a) A number of symmetry-related parameters (σ_{ext}, σ_{int}, $\sigma_{species}$, K_σ) are derived for the free host, free ligand, and combined host/ligand for the mono-porphyrin/monodentate ligand system, the bis-porphyrin/bidentate ligand system, and the interannular/bidentate ligand system. These account for degenerate complexes [93, 199].

(b) The reference intermolecular association constant, K_{inter}, is derived from the experimental association constant for the reference mono-porphyrin/monodentate ligand system and symmetry-related parameters.

(c) The reference microscopic effective molarity, EM,[29] is derived from K_{inter} and the experimental association constant for the reference ring closing bis-porphyrin/bidentate ligand system and symmetry-related parameters.

(d) The product of the effective molarity for the tetra-porphyrin/bidentate ligand system, EM_1EM_2 (two binding sites), is derived from K_{inter} and the experimental association constant for the tetra-porphyrin/bidentate ligand system.

(e) The interannular cooperativity factor, γ, can then be calculated by taking the ratio of EM_1EM_2 to EM^2. If EM is equal to EM_1 and equal to EM_2, the system is non-cooperative ($\gamma = 1$). If EM_1EM_2 is greater than EM^2, the system is positively interannularly cooperative ($\gamma > 1$). If EM_1EM_2 is less than EM^2, the system is negatively interannularly cooperative ($\gamma < 1$).

Usually, it is important to ascertain that allosteric cooperativity (which arises from the interplay of two or more intermolecular interactions) is not present for the system, otherwise this can result in the incorrect determination of the reference EM value, leading to allosteric cooperativity being misinterpreted as interannular cooperativity [88]. This can be achieved by studying association of the bis-porphyrin/monodentate ligand system to determine the allosteric cooperativity factor, α [88]. However, unfortunately this data has not been collected for the reference freely rotating system **1** with quinuclidine **24** or pyridine **25**. In the calculations below, the absence of allosteric cooperativity has been assumed ($\alpha = 1$).

A statistical analysis of interannular cooperativity was subsequently undertaken for the tetra-porphyrin tweezer **4** with DABCO **5** and bipy **6**, and these intriguing results are now described.

5.6.1 Interannular Cooperativity for Tetra-porphyrin Tweezer with DABCO

Using Ercolani's method [88], interannular cooperativity was first assessed for the tetra-porphyrin/DABCO system, with the key parameters summarised in Table 5.2. An expanded version of this table with additional symmetry-related parameters is provided in Appendix 5, along with a worked example.

[29] Microscopic EM is defined as the ratio K_{intra}/K_{inter} (units $molL^{-1}$) [93]. The non-microscopic EM is the product of microscopic EM and the cyclisation statistical factor [88, 92]. EM is a measure of the stabilisation resulting from the chelate effect for related intermolecular and intramolecular interactions [30, 52, 58], and has been used extensively by both Hunter and Anderson [30, 31, 52, 53] to quantify host-guest complementarity [53].

Table 5.2 - Summary of statistical parameters, experimental association constants and derived parameters, and the interannular cooperativity factor, γ, for tetra-porphyrin with DABCO.

Species	K_σ	K_{exp}	K_{inter}	**EM**[#]	**EM$_1$EM$_2$**	$\gamma^{\#}$
mono-por:quin, **22**:**24**	2	2.53×10^5 M^{-1}	1.265×10^5 M^{-1}	-	-	-
freely rotating: DABCO, **1**:**5**	8	8.1×10^7 M^{-1}	-	6.28×10^{-4} M	-	-
tetra-porphyrin: $(DABCO)_2$, **4**:(**5**)$_2$	256	6.32×10^{13} M^{-2}	-	-	9.5×10^{-10} M^2	2.41×10^{-3}

[#] assuming the absence of allosteric cooperativity (α = 1).

Importantly, the interannular cooperativity factor, γ, is significantly less than 1 for tetra-porphyrin:$(DABCO)_2$ (Table 5.2), suggesting the binding of two molecules of DABCO occurs with negative cooperativity ($\gamma = 2.41 \times 10^{-3}$). This was an unexpected result, as binding was predicted to be positively cooperative; binding of the first molecule of DABCO was expected to optimise of the interporphyrin distance at the second binding site for a second molecule of identical guest, via rotation of the rigid polycyclic scaffold about the phenyl diimide core. Negative cooperativity for DABCO could be explained by the scenario where DABCO is too small to be optimally bound at both binding sites. This could lead to optimised and non-optimised binding sites within the same tetra-porphyrin tweezer, or a situation where both binding sites dynamically compete for optimal complexation which is achieved by neither binding site. The behaviour of the system is difficult to predict with the many degrees of rotational freedom.

While distortion of the imide nitrogen atom from trigonal planar was considered as a mechanism for the optimisation of one binding site to the detriment of the other, it is doubted that the strength of association of DABCO in a bis-porphyrin sandwich is sufficient for this to occur. While the distortion of imides from planarity and pyramidalisation of imide nitrogen atoms is documented in the literature [119, 121, 122], these cases specifically refer to X-ray crystal structures of sterically crowded *ortho*- substituted phenyl imides and molecular modelling calculations as the phenyl and imide rings approach planarity for sterically crowded ortho- substituted phenyl imides.

5.6.2 Interannular Cooperativity for Tetra-porphyrin Tweezer with Bipy

Interannular cooperativity was then assessed for the tetra-porphyrin/bipy system using the same method [88], and these key parameters are summarised in Table 5.3. An expanded version of this table with additional symmetry-related parameters is provided in Appendix 5. Bipy was treated as a rigid guest with no internal rotation of the biphenyl bond.

Table 5.3 - Summary of statistical parameters, experimental association constants and derived parameters, and the interannular cooperativity factor, γ, for tetra-porphyrin with bipy.

Species	K_σ	K_{exp}	K_{inter}	**EM**[#]	**EM$_1$EM$_2$**	$\gamma^{\#}$
mono-por: pyridine, **22**:**25**	2	2 x 10^3 M^{-1} *	1 x 10^3 M^{-1}	-	-	-
freely rotating: bipy, **1**:**6**	8	4.97-5.27 x 10^5 M^{-1} †	-	6.21-6.59 x 10^{-2} M †	-	-
tetra-porphyrin: $(bipy)_2$, **4**:$(\mathbf{6})_2$	256	5.17 x 10^{12} M^{-2}	-	-	2.02 x 10^{-2} M^2	4.65-5.24 †

* literature reports association constants of the order of 10^3 M^{-1} [27, 53, 55, 58, 78, 97, 98, 165]. † quoted as a range due to uncertainty in the stock tweezer concentration for this titration, affecting the association constant, EM, and γ. [#] assuming the absence of allosteric cooperativity (α = 1).

In this case, the interannular cooperativity factor, γ, is greater than 1 for tetra-porphyrin:$(bipy)_2$ (Table A5.3). This suggested that the binding of two molecules of bipy to tetra-porphyrin is a positively cooperative process, albeit only modestly (γ = 4.65-5.24).

Positive cooperativity could be explained by the binding of the first molecule of bipy resulting in an optimisation of the interporphyrin distance at the second binding site for a second molecule of bipy, via rotation of the rigid polycyclic scaffold about the phenyl diimide core. In addition, although the interporphyrin distance at the second binding site is optimised by the binding of bipy at the first binding site, the porphyrin receptors at the second binding site can still freely rotate prior to complexing bipy, and as such the receptor positioning, although improved, is still not absolutely preorganised for bipy.

5.7 Summary of the Tetra-porphyrin System

After extensive attempts to synthesise the tetra-porphyrin tweezer via a convergent approach, successful synthesis was instead achieved using a divergent approach. The Mitsudo T-piece imide was established as the key synthon for a novel coupling with benzene-1,4-diboronic acid under simple Cu(II) salt catalysis. This afforded the tetra-functional core, which following epoxidation, was subjected to a four-fold ACE reaction with porphyrin receptor to give the tetra-porphyrin tweezer, which was characterised by NMR and HRMS.

For DABCO, the UV-Vis titration data best supported a 1:2 plus 2:2 plus 1:4 binding model, giving K_{12} = 6.32x 10^{13} M^{-2} and K_{22} = 3.04 x 10^{20} M^{-3}, and K_{14} of = 1.92 x 10^{16} M^{-4} in $CHCl_3$. The NMR titration data supported the formation of two sandwich species, including intramolecular 1:2 as the major species. Additional spectral evidence suggested a minor species containing free porphyrins. The minor species was likely to be either intramolecular 1:1 or intermolecular 2:2, both which contain a combination of free and sandwiched porphyrins. Speciation was found to be different between UV-Vis and NMR concentrations, particularly with regard to the co-existence of two sandwich species below 1 equivalent of DABCO in the NMR spectra, in contrast to the UV-Vis-derived simulated NMR speciation, where only a single sandwich species is predicted below 1 equivalent of DABCO.

For bipy, the UV-Vis titration data best supported a 1:1 plus 1:2 plus 1:4 binding model (different to DABCO), giving K_{11} = 2.14 x 10^{6} M^{-1}, K_{12} = 5.17 x 10^{12} M^{-2}, and K_{14} = 1.94 x 10^{15} M^{-4} in $CHCl_3$. The NMR titration data supported the formation of intramolecular 1:2 as the major species. At low temperature, spectral evidence suggested a minor species containing free porphyrins. This was not observed at 20 °C, but could be concealed by the fast exchanging porphyrin β-pyrrole resonances. Although a second sandwich species was not observed, this could be obscured by similar spectral features to the major 1:2 sandwich species. Thus it remains unknown if the stepwise intramolecular binding model determined at UV-Vis concentrations is mirrored at NMR concentrations.

A statistical analysis of interannular cooperativity for the tetra-porphyrin/diamino ligand was undertaken, using the reference values of K_{inter} and EM obtained from the reference compounds presented earlier in this thesis (mono-porphyrin receptor, freely

rotating tweezer, Chapter 3). Unexpectedly, tetra-porphyrin:$(DABCO)_2$ was found to be negatively cooperative ($\gamma = 2.41 \times 10^{-3}$). This could be explained by DABCO being too small to be optimally bound at both binding sites. The intramolecular sandwich species tetra-porphyrin:$(bipy)_2$ was found to be modestly positively cooperative ($\gamma = 4.65\text{-}5.24$). This is in line with the hypothesis that the interporphyrin distance at the second binding site is more optimised upon guest complexation at the first binding site, via rotation of the rigid polycyclic scaffold about the phenyl diimide core, yet is not completely preorganised because the porphyrin receptors can rotate prior to complexation.

Additional investigations are planned for the tetra-porphyrin system, and these future directions are discussed in Chapter 7.

6. Conclusions

A small library of molecular tweezers (compounds **1**-**4**) was synthesised to intramolecularly complex diamino ligands DABCO **5** and bipy **6**. The tweezer analogues all contained freely rotating bis-porphyrin receptors linked via a rigid bridged polycyclic backbone with a central phenyl diimide core of varying degrees of rotational freedom. The combined techniques of UV-Vis spectroscopic titration, multivariate global spectral analysis of the data, and NMR spectroscopic titration provided insight into the host-guest behaviour of the systems and the most likely binding model, although speciation was clearly concentration dependent in several circumstances.

The degree of rotation about the phenyl diimide core can be restricted from freely rotating **1** by the subtle incorporation of sterically bulky substituents such as methyl groups (Figure 6.1 (a) and (b)). Evidence from NMR spectra, X-ray crystal structures, and host-guest titrations demonstrated the 2,3,5,6-tetramethylphenyl diimide core results in non-interconvertible *syn*- **2** and *anti*- **3** conformations, which can be physically separated and studied independently of each other. The conformations are stable and non-interconvertible during experiments under ambient conditions, as well as non-interconvertible upon heating and external agitation such as a microwaves and sonication. This however does not suggest that the *syn*- and *anti*- systems cannot undergo partial rotation within their respective conformations.

The large association constants obtained for the two model single binding site systems (freely rotating **1** [1], *syn*- restricted **2**) clarified that each of these systems are sufficiently preorganised to intramolecularly complex both DABCO **5** and bipy **6**. Molecular modelling suggests that the interporphyrin distance in both systems is modulated by partial rotation of the polycyclic scaffold about the phenyl diimide core, rather than flexibility in the polycyclic scaffold itself, explaining the ability of the system to complex substrates of different lengths. Additional replicates of UV-Vis titrations should be undertaken for each of these systems to more accurately determine association constants before the association constants can be compared on the basis of differing preorganisation, as errors in high order binding constants are highly sensitive to inaccuracies in concentration, absorption, and chemical shift [66].

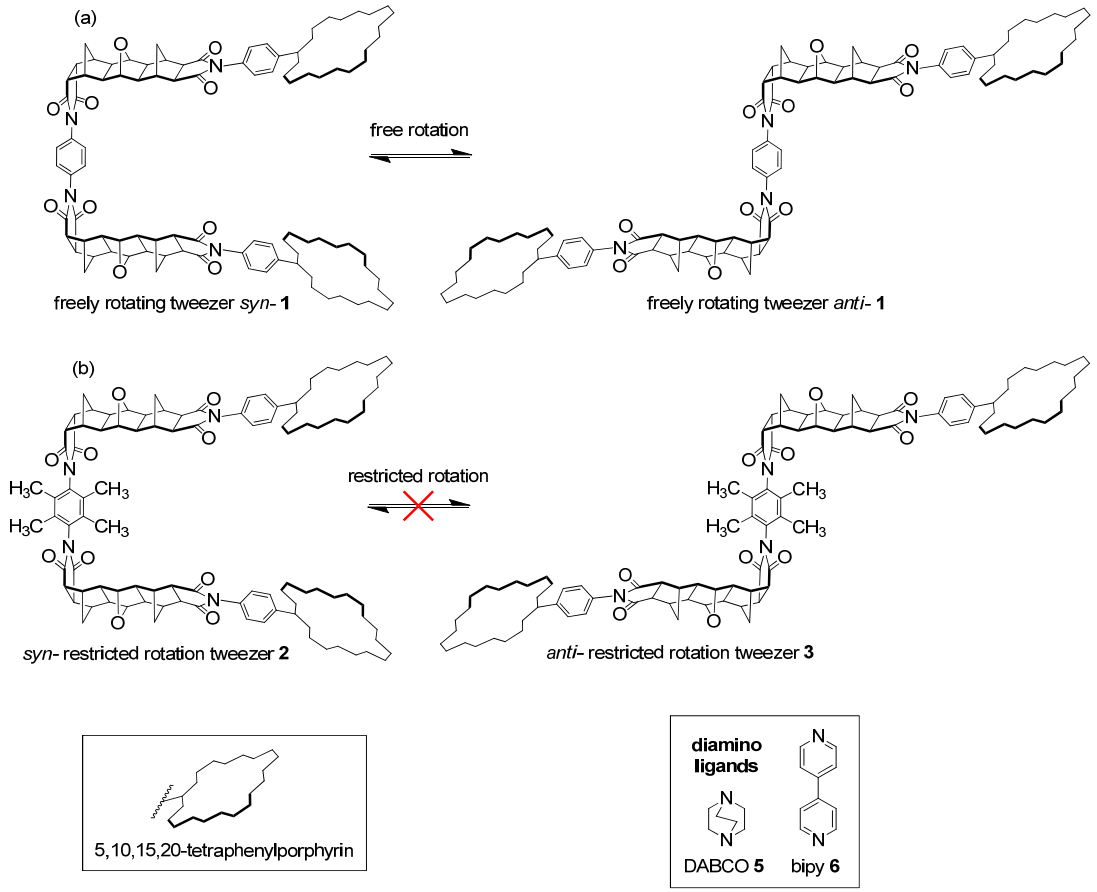

Figure 6.1 - (a) The freely rotating tweezer **1** can occupy a *syn*- or *anti*- conformation; (b) The restricted rotation system has non-interconvertible *syn*- **2** and *anti*- **3** conformations (structural detail omitted for clarity).

At NMR concentrations (millimolar) there was evidence of more complex speciation for the freely rotating **1** and *syn*- **2** systems than at UV-Vis concentrations (micromolar), such as minor intermolecular sandwich complexes. The *anti*- restricted rotation system **3** generated intermolecular sandwich complexes with DABCO **5** at both UV-Vis and NMR concentrations, while the intermolecular sandwich complex with bipy **6** was only detected at NMR concentrations, preferring to complex to each mono-porphyrin in a stepwise progression at UV-Vis concentrations.

The information from these model systems enabled the study of the more complex tetra-porphyrin tweezer **4**. This was synthesised via a divergent approach, with the core established using a key coupling reaction between a polycyclic imide **49** and benzene-1,4-diboronic acid **59**. The four porphyrin receptors can be arranged in cofacial pairs, giving two bis-porphyrin binding sites located on opposite sides of the tweezer (Figure 6.2). The two binding sites are intrinsically linked via the freely rotating phenyl diimide core, which acts as a pivot through which equal and opposite rotation of the otherwise rigid bridged polycyclic backbone occurs.

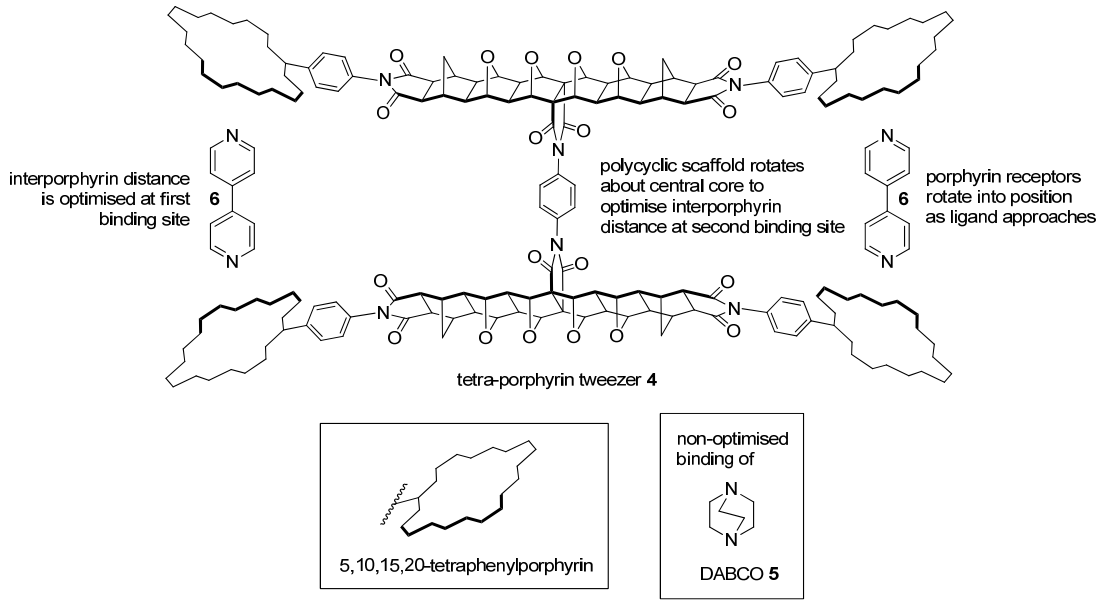

Figure 6.2 - explanation of positive homotropic interannular cooperativity of tetra-porphyrin tweezer **4** with bipy **6**.

Using a statistical analysis to assess interannular cooperativity of tetra-porphyrin tweezer **4** [88], the homotropic intramolecular sandwich complex tetra-porphyrin:$(DABCO)_2$ was determined to be negatively cooperative, while tetra-porphyrin:$(bipy)_2$ was determined to be modestly positively cooperative. Negative interannular cooperativity for DABCO **5** ($\gamma = 2.41 \times 10^{-3}$) could be explained by DABCO being too small to be optimally bound at both binding sites. Positive interannular cooperativity for bipy **6** ($\gamma = 4.65\text{-}5.24$) could be explained by increased optimisation of the interporphyrin distance at the second binding site upon guest complexation at the first binding site, via rotation of the rigid polycyclic scaffold about the phenyl diimide core.

Additional work is planned for the tetra-porphyrin system **4**, and these future directions are discussed in the next chapter.

7. Future Directions

This chapter addresses several of the synthetic challenges encountered in this work, and recommends new strategies to combat these difficulties. In addition, several further host-guest experiments with different ligands are scheduled, and intend to provide a better understanding of tweezer behaviour, particularly in regard to rotational degrees of freedom. Finally, plans for the exciting next generation of cooperative tweezer analogues will be presented, along with the wider applications of the work.

7.1 Synthetic Optimisations

7.1.1 Convergent Synthesis

The main difficulty encountered during tweezer synthesis was determining an appropriate synthetic route to pursue a convergent synthesis. Achieving this approach will be key to providing a more versatile synthesis of future tweezer analogues with interesting structural features such as mixed receptors.

The Mitsudo imide **49** (Figure 7.1) synthesised in this work is extremely close to a achieving the convergent approach. This all but requires a suitable protecting group to be introduced to the imide **54**, to prevent deprotonation and precipitation of the salt during epoxidation. The protecting group must be a) resistant to the strong base required during nucleophilic epoxidation, and b) able to be easily cleaved following epoxidation to afford compound **52**. ACE reaction of imide bis-epoxide **52** with porphyrin receptor **18** would subsequently yield the imide bis-porphyrin half **64**, as summarised in Figure 7.1. The imide bis-porphyrin half **64** however does raise the question of solubility issues; the anhydride analogue **40** synthesised in chapter 5 was found to be highly insoluble in a range of solvents. In this case, solubilising groups may need to be introduced to either the porphyrins or polycyclic scaffold earlier in the synthesis.

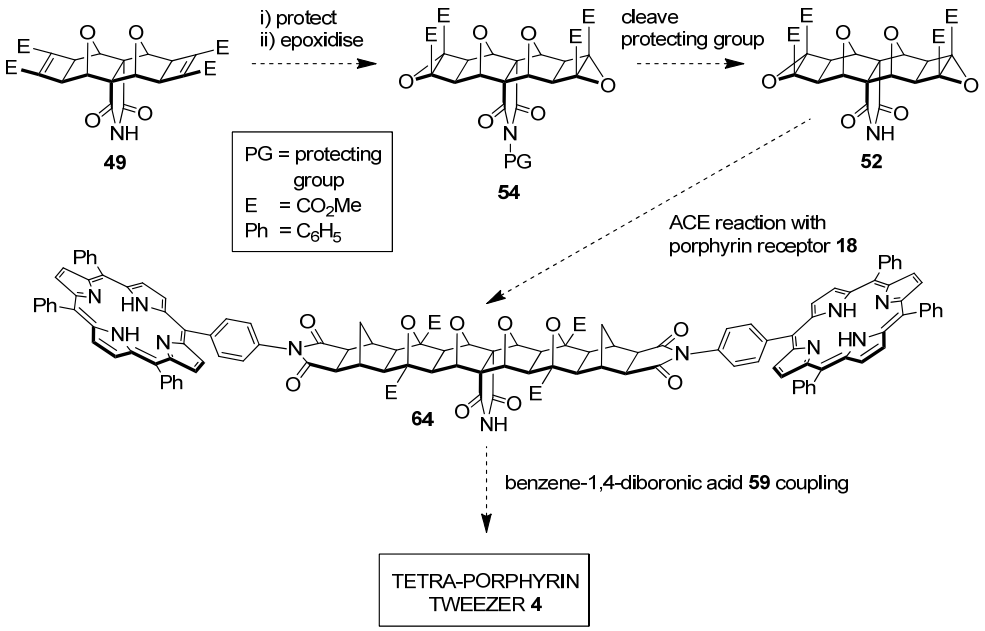

Figure 7.1 - Proposed convergent synthesis of the tetra-porphyrin tweezer via the imide bis-porphyrin half **64**.

It is reasonable to expect that coupling of the imide bis-porphyrin half **64** with benzene-1,4-diboronic acid **59** (as established for the divergent synthesis to afford the tetra-functional phenyl diimide core **48**) would afford the tetra-porphyrin tweezer **4**. Optimisation of the conditions for this coupling reaction (solvent, type of catalyst, catalyst loading) to minimise side reactions encountered with **48** will now be discussed.

7.1.2 Imide-Phenylboronic Acid Coupling

In summary of the findings in chapter 5 and shown again for convenience in Figure 7.2, only a 30 % yield of the desired diimide **48** was obtained for a 1:2 stoichiometric quantity of benzene-1,4-diboronic acid **59** to imide **49**, for reflux in methanol with a Cu(II) catalyst loading of < 5%. Approximately 30 % was imide starting material **49**, while the remaining 30 % was an unexpected side product identified as the phenyl 1-imide-4-solvent adduct **60** or **61**.

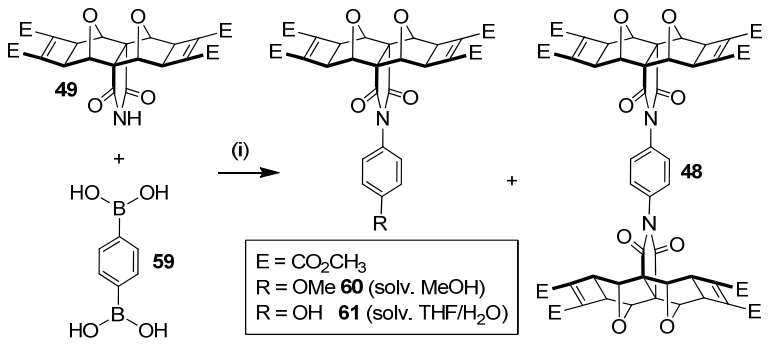

Figure 7.2 - Imide-Phenyl Boronic Acid/Cu(II)/Air Coupling. (i) Mitsudo T-piece imide block **49**, benzene-1,4-diboronic acid **59**, copper (II) acetate (5 mol-%), MeOH or THF/H_2O, reflux, air bubbler, 18 hrs, ~30 % phenyl 1-imide-4-solvent adduct + 30 % phenyl diimide adduct

Several variables should be considered in the optimisation of this reaction. At > 5% catalyst loadings, the side product **60** or **61** was the major product. It is speculated the side reaction could be related to oxidation of an intermediate product by the Cu(II) salt, followed by reaction with solvent. Catalyst loadings of << 5 mol- % should be investigated, although [197] report that yields for their substrates sharply decreases below 3 mol- %. Additionally, [197] reports reaction rates are greater for copper (I) salts than copper (II) salts. As such, copper (I) salts should be investigated for coupling compounds **49** and **59**. This will of course depend on the relative rates of the imide coupling and side reaction with solvent. However, it should be noted that complications may arise in using copper (I) salts if longer reaction times are necessary, as copper (I) salts are well known to be unstable and easily oxidised in air, which is continuously bubbled through the reaction mixture in this method [197].

In conjunction with the catalyst, the solvent is likely to be critical in reducing the competitive side reaction observed in this work. While it was found that the solvent must be protic for coupling to occur (originally reported in [197]), investigation of less nucleophilic protic solvents such as isopropanol (personal communication [198]), or mixtures of less nucleophilic protic solvents with aprotic solvents should be investigated. Furthermore, reaction temperature is expected to be important; [197] reports excellent yields in refluxing methanol for 3 hours, compared to only trace product at room temperature over 5 days.

Additionally, [197] reports increased yields for an excess of the nitrogen-containing species relative to the phenyl boronic acid. Unfortunately, the stoichiometry of the desired diimide **48** in this work prevents the imide **49** from being present in excess with respect to the benzene-1,4-diboronic acid **59**. A two-step synthesis could be

undertaken to isolate the 1:1 adduct, but unnecessarily lengthens the synthetic protocol if the single-step synthesis can be optimised.

7.1.3 T-piece Imide Synthesis

Furthermore, the literature preparation of the T-piece imide **51** [106, 189] is highly inefficient. Currently, substitution of the anhydride oxygen in **37** for the imide nitrogen in **51** requires a PMB protection/deprotection step (compound **50**, Figure 7.3). The atom economy of this step (compound **37** to **51**) is very poor, and generates a vast amount of chemical waste.

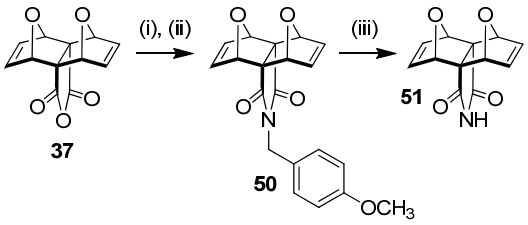

Figure 7.3 - Synthesis of the T-piece Imide **51**. (i) *p*-methoxybenzylamine (2 eq.), deacidified $CHCl_3$, nitrogen, 50 °C, overnight; (ii) NaOAc/Ac_2O, nitrogen, 50 °C, overnight, 52 %; (iii) 9:1 CH_3CN/H_2O, 40 °C, ammonium cerium (IV) nitrate (3 eq., 2 hrs; 2.3 eq. 90 mins + 0.3 eq. 30 mins), 73 %.

Several methods exist for the conversion of *endo*- **7** and *exo*- **8** anhydrides to their respective free imides, including heating with NH_4OAc/AcOH [200], reflux with aqueous ammonia [201], and urea melt [202, 203]. Unfortunately, the thermal requirement of these methods is likely to limit their application to the thermally unstable anhydride **37**[30].

A promising method is the literature precedent for the synthesis of cyclic imides from the corresponding diacid using trifluoroacetamide and EDCCl/HOBt [204], which proceeds in a single step under mild conditions (Figure 7.4). This should be immediately investigated for the synthesis of the T-piece imide **51** from the bis-carboxylic acid **36**, as it could potentially remove three steps from the current synthesis described in this thesis.

[30] Thermally stable Mitsudo anhydride **38** was subjected to these imide conditions in [200] (NH_4OAc/AcOH, 140 °C, 1 week), however none of the Mitsudo imide **49** was detected. While the laterally functionalised Mitsudo anhydride **38** is thermally stable compared to **37**, the anhydride reactivity in **38** is reduced as previously discussed in Chapter 5.

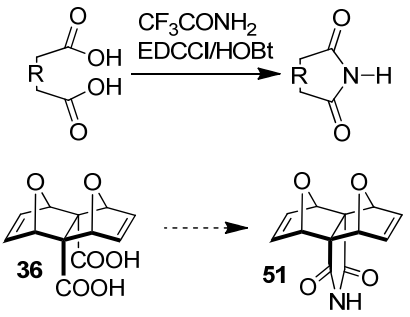

Figure 7.4 – Synthesis of cyclic imides in a single step, reproduced from [204] to be explored for the conversion of bis-carboxylic acid **36** to T-piece imide **51**.

7.2 Host-Guest Experiments: Ligand Length, Rotational Degrees of Freedom, and pK_a

The work in this thesis was limited to two different length guests, DABCO **5** (2.64 Å) and 4,4'-bipy **6** (7.15 Å). Rotation of the phenyl diimide and tetramethylphenyl diimide cores has not been explored beyond these guests, in terms of maximum inter-porphyrin distance in freely rotating **1** and *syn*- restricted **2**. This could be probed with rigid north-south diamino ligands of different lengths, including Figure 7.5 (b) (11.47 Å [semi-empirical, AM1], commercially available) and Figure 7.5 (c) (15.79 Å [semi-empirical, AM1], recently reported in the literature [64, 65, 205]).

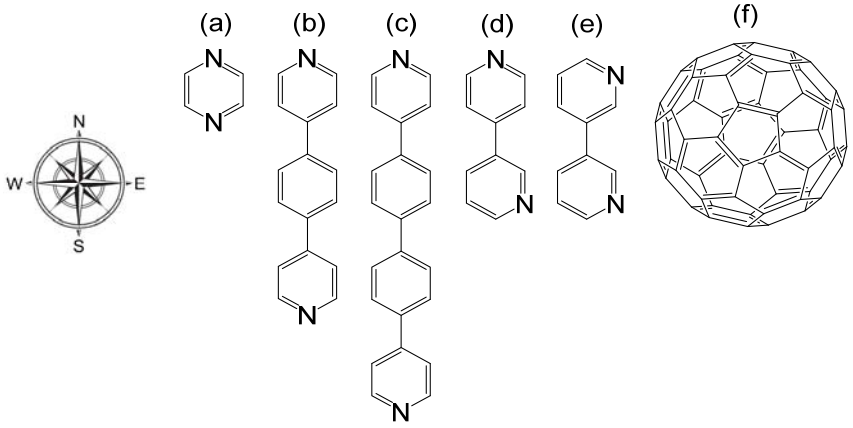

Figure 7.5 - Examples of diamino ligands for future host-guest experiments, (a) pyrazine; (b) and (c) different lengths; (d) and (e) 3,4'- and 3,3'- regioisomers of bipy; (f) C_{60} fullerene.

For the freely rotating tweezer **1**, as the length of the diamino ligand increases, there is likely to be a crossover from *syn*- intramolecular complexation to *anti*- intermolecular complexation, as the energy barrier to rotation is low. For the *syn*-restricted rotation system **2**, the maximum ligand length for intramolecular complexation will be controlled by the higher barrier to rotation about the 2,3,5,6-tetramethylphenyl diimide core, with intramolecular complexation expected to

become increasingly energetically unfavourable as the inter-porphyrin distance is increased.

Additionally, complexation of tweezers **1**-**4** should be explored for non-north-south ligands such as the 3,4'- and 3,3'- bipy regioisomers (Figure 7.5 (d), (e)). The porphyrin receptors are able to rotate and are could conform around these guests (internal bipy rotation could also play a role during complexation). Other known guests for bis-porphyrins receptors, such as C_{60} fullerene (Figure 7.5 (f)), should be investigated.

Finally, it is well known that association constants increase with increasing ligand pK_a (increasing ligand basicity) [206, 207]. As such, in hosts with bis-porphyrin binding sites (e.g. tweezers **1**-**4**), it would be important to explore the effects of pK_a, which along with ligand length and geometry constraints of the host collectively affect the association constant. For example, there is a significant difference in pK_a (Table 7.1) between DABCO and pyrazine (Figure 7.5 (a)), yet these are similar in length (difference of only 0.2 Å).

Table 7.1 - pK_a of the diamino ligands DABCO **5**, bipy **6**, and pyrazine [208-210].

Diamino Ligand	**pK_a [a]**
DABCO **5**	8.47-8.7
pyrazine (Figure 7.5 (a))	0.65
4,4'-bipy **6**	4.82

[a] pK_a of the conjugate acid/protonated form of the ligand in H_2O.

7.2.1 Competitive Ligand Binding Experiments

It would be particularly interesting to conduct competitive ligand binding experiments for the tetra-porphyrin system **4** with two different types of guests (e.g. DABCO **5** and bipy **6**). This would provide direct experimental insight into cooperativity in this system, and the ability of tetra-porphyrin host **4** to reorganise on guest complexation, which so far has been examined using a statistical analysis from experimental data for a single type of guest. If a mixed complex such as tetra-porphyrin:DABCO:bipy (**4**:**5**:**6**, [Figure 7.6]) was observed, this would challenge our field's current understanding of the rigidity of these fused bridged polycyclic architectures. Furthermore, competitive guest binding would assist in better understanding complexation with single types of guests, for example the detection of 1:1 complexes enroute to 1:2 complexes. This was observed for tetra-porphyrin **4**

with bipy **6** in Chapter 5, but not detected for DABCO **5** (from fitting of the UV-Vis titration data to a binding model).

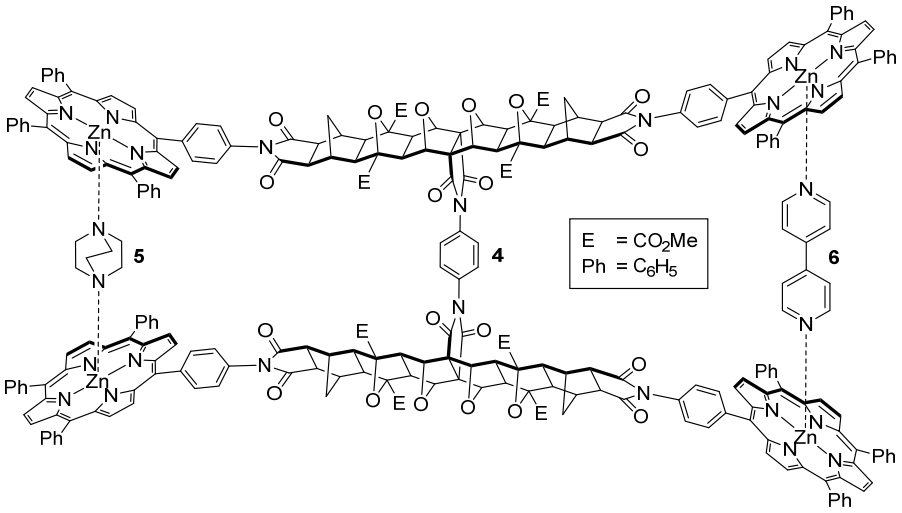

Figure 7.6 - Can tetra-porphyrin **4** simultaneously complex DABCO **5** and bipy **6**?

7.3 Next Generation Tweezers

The modular design of the tweezer architecture allows for maximum synthetic variability, and several next generation tweezers are now planned. These are discussed in the following examples.

7.3.1 Water Soluble Tweezers for Biological Substrates

Perhaps the most exciting future direction of this work is towards water soluble tweezers for biological substrates. The tweezer architectures all contain a number of methyl ester substituents (eight for the tetra-porphyrin system **4**), an artefact of the ACE reaction linking the receptors to the linker scaffold. Hydrolysis of these esters in the linker **48** to the carboxylic acid **65**, or esterification with water solubilising groups, could enable the complexation of biological substrates in aqueous media, for example amino acids and DNA bases (examples Figure 7.7). Furthermore, a tin (IV) porphyrin metal centre would allow for guests with carboxylic acid functionality to be complexed [96], while magnesium (II) is suitable for complexing to oxygen atoms [11], and could be combined with the zinc (II) porphyrin metal centre suitable for amines. Such a tweezer would be with a view towards potential candidates for enzyme mimics or targeted drug delivery and controlled release.

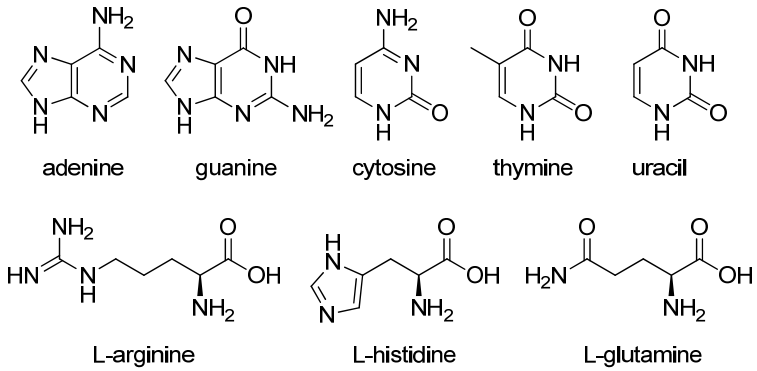

Figure 7.7 - Selected examples of biological diamino/carboxylic acid substrates.

There is literature precedent for the base-catalysed ester hydrolysis of polycyclic cyclobutene diesters [211], cyclobutane diester epoxides [104] and oxa- bridged diester ACE adducts [104] to give the corresponding carboxylic acids, which are able to be converted to the acid chloride and coupled with alcohols or amines to yield alternative esters and amides. Alternatively, the esters can be reduced to primary alcohols using lithium aluminium hydride [104]. Alternatively, Mitsudo reactions could be undertaken with di-*tert*-butylacetylenedicarboxylate and the tert-butyl esters cleaved to give the carboxylic acid [212]. The proposed new target, octa-carboxylic acid tetra-porphyrin tweezer **66**, is shown in Figure 7.8.

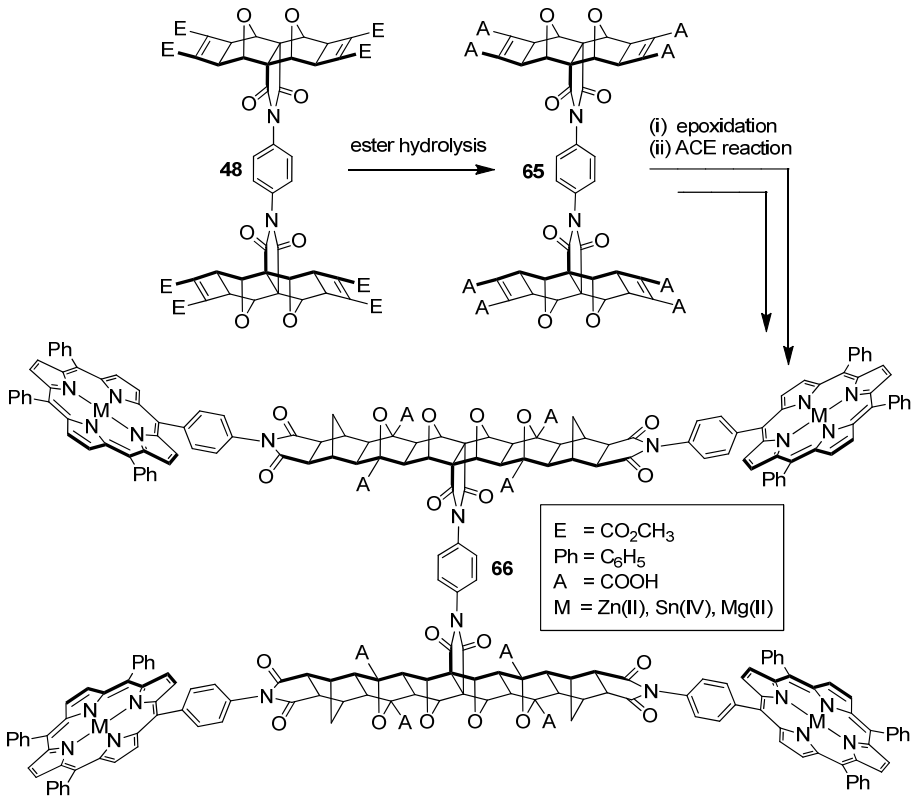

Figure 7.8 - Synthesis of the proposed octa-carboxylic acid tetra-porphyrin tweezer **65**.

7.3.2 Tetra-porphyrin Tweezer with Restricted Rotation

The effect of restricted rotation on the tetra-porphyrin system remains unexplored, and could reveal intriguing host-guest behaviour. Restricted rotation could be achieved similarly to the *syn*- **2** and *anti*- **3** restricted systems, by introducing a 2,3,5,6-tetramethylphenyl diimide core. The target restricted rotation tetra-porphyrin system **69** is shown in Figure 7.9, along with the precursor reagent 2,3,5,6-tetramethylbenzene-1,4-diboronic acid **67** [213] and 2,3,5,6-tetramethylphenyl diimide core **68**.

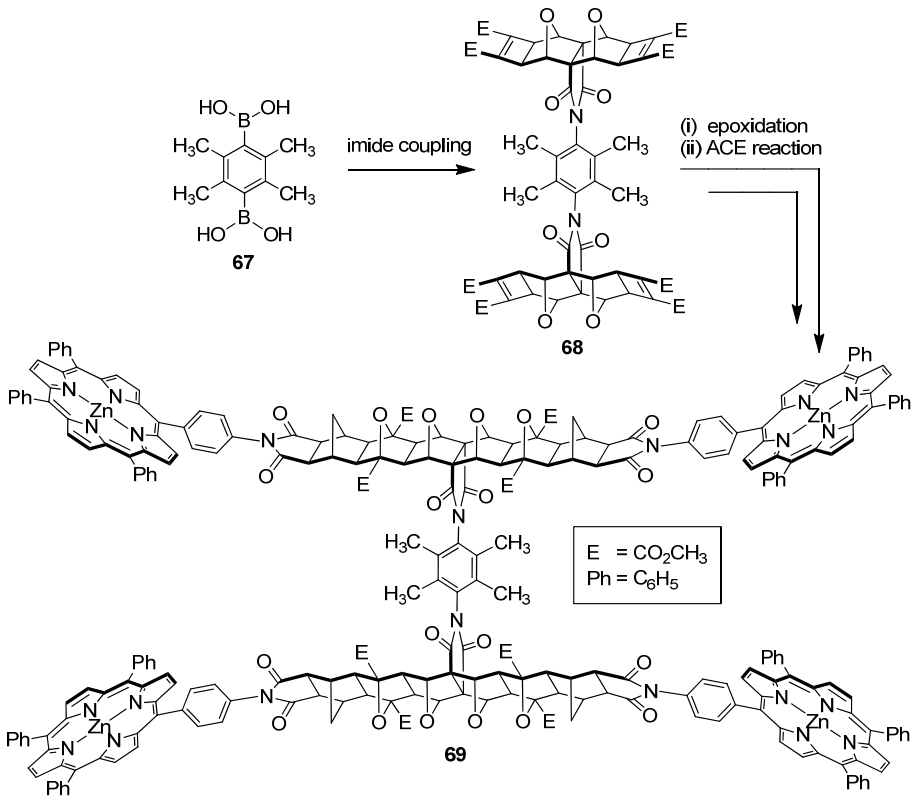

Figure 7.9 - Synthesis of the proposed restricted rotation tetra-porphyrin system **69** from 2,3,5,6-tetramethylbenzene-1,4-diboronic acid **67**.

In addition, the work in this thesis has only focussed on restricting phenyl diimide core rotation, and has so far neglected the role of porphyrin receptor rotation in complexation. Porphyrin *meso*-phenyl rotation with respect to the porphyrin β-pyrrole is well known [137-139], while the *exo*- imide phenyl rotation is similar to *endo*- phenyl imide **11**. Porphyrins with substituted *meso*-phenyl groups have been reported to display restricted rotation with respect to the porphyrin β-pyrrole [138, 139]. It is envisaged that a 2,3,5,6-tetramethyl phenyl group in-line between the porphyrin β-pyrrole and *exo*- imide would restrict porphyrin rotation, similarly to the 2,3,5,6-tetramethyl phenyl diimide compounds in Chapter 4. The proposed restricted rotation porphyrin receptor **73** is shown in Figure 7.10.

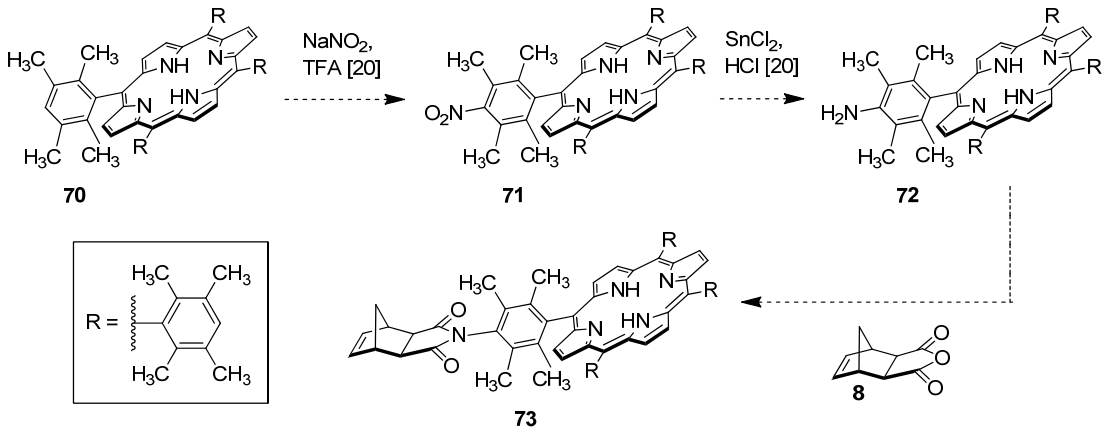

Figure 7.10 - Synthesis of the proposed restricted rotation porphyrin receptor **70**.

The porphyrin **70** has previously been reported in the literature [214], from the condensation of 2,3,5,6-tetramethylbenzaldehyde and pyrrole. However, *para*-phenyl nitration of this porphyrin in a single quadrant to **71** and reduction to the amine **72** by the known method [144] has not been attempted on compound **70**. Thus an alternative porphyrin synthesis could be necessary to generate the restricted rotation porphyrin receptor **73**.

7.3.3 Mixed Receptor Cooperative Tweezer

In order to experimentally measure interannular cooperativity in the tetra-porphyrin system, and not rely on indirect statistical methods, a heterotropic architecture must be designed such that different spectral responses occur on the binding of each guest, which can be measured independently of each other. This could be achieved by incorporating mixed receptors into the system, and is shown schematically in Figure 7.11, with receptors labelled A and B, which complex ligands C (●) and D (□) respectively. It is envisaged that mixed receptor systems could be accessed from a convergent synthesis via a mixed ACE reaction as described in Chapter 5. In this way, cooperativity could be determined by titrating species tweezer:● with ligand □ and comparing $K_{\bullet only}$ with $K_{\bullet with \square}$, and likewise tweezer:□ with ligand ● and comparing $K_{\square only}$ with $K_{\square with \bullet}$.

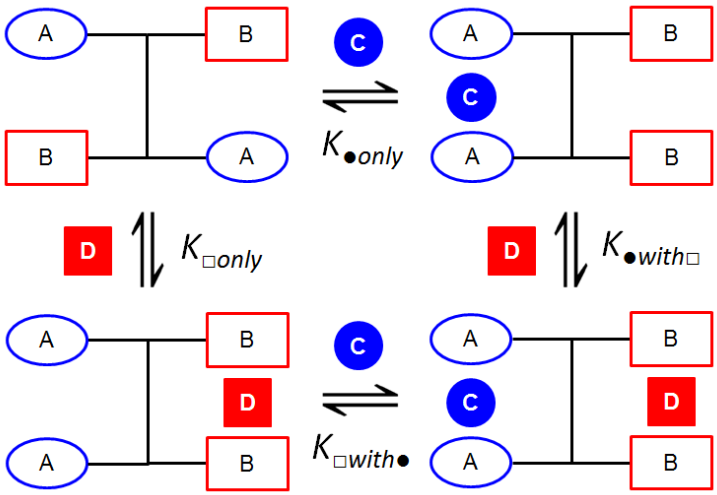

Figure 7.11 – Interannular cooperative tweezer with mixed receptors A and B, suitable for bidentate ligands C (●) and D (□) respectively.

7.4 Investigation of Linker as an Organogelator

Gels are a trending area of research resulting in the development of new materials that are stimuli-responsive [215], porous [216], and tuneable for different physical properties [217]. As such, gels find a range of applications from molecular recognition and sensing [218], targeted drug delivery and controlled release [217], molecular wires [219], simulating the extra-cellular matrix [220, 221], and stimulating cell growth [222].

The freely rotating Mitsudo linker **13** (Figure 7.12) was found to immobilise a significant volume of solvent during recrystallisation from chloroform (soluble) and hexane (insoluble). However, the viscous opaque mixture was slightly fluid, and it was difficult to ascertain by visual inspection whether the mixture was forming a suspension or undergoing partial gelation.

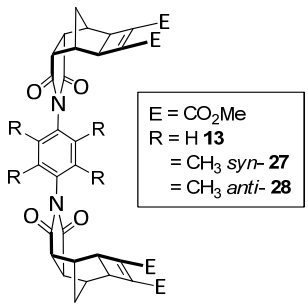

Figure 7.12 - Mitsudo linker under investigation as organogelator.

An SEM image of this material (not shown) was obtained (Jared Castle, William Gibbs, Flinders University), however, unfortunately the fibres appear to be linear

discrete entities, rather than a continuous woven structure. Structural analogues of this linker, including the restricted rotation *syn*- **27** and *anti*- **28** linkers from Chapter 4 (Figure 7.12), as well as structures with different ester substituents, E, are currently under further investigation as potential organogelators in our laboratory.

8. Experimental

8.1 Molecular Modelling

Molecular modelling was undertaken using the Wavefunction Spartan '10 software package [145]. Equilibrium geometry was calculated using a semi-empirical AM1 model. Rotational energy profiles were calculated according to the Tutorial and User's Manual, using a Hartree-Fock 6-31G* model for each conformation about the bond specified by the dihedral angle constraint, with the energy of each conformation recalculated using a B3LYP/6-31G* Density Functional model to improve the fitting function.

8.2 Instrumentation

NMR spectra were recorded on a Bruker UltraShield Avance III 400 MHz or 600 MHz NMR Spectrometer running the TopSpin 2.1 software package at 299 K and 293 K respectively. Spectra were calibrated to the residual solvent signal according to [223, 224]. $CDCl_3$ was deacidified by passing through a passage of neutral activated aluminium oxide (Scharlau, activity degree 1, 70-290 mesh, grain size 0.05-0.2 mm) and stored under a nitrogen atmosphere over silver foil/molecular sieves in a brown glass bottle.

UV-Vis spectra were recorded on a Cary 50 instrument at 20 °C in a Starna Type 21 SX 1 cm^2 quartz cuvette with the following parameters: average time 0.05 s, data interval 0.15 nm, scan rate 180 nm/min, wavelength range 300-700 nm, baseline correction to blank solvent. Dry $CHCl_3$ for recording spectra was prepared under a nitrogen atmosphere first by reflux over P_2O_5 then distillation [225], and deacidified and stored the same as above for $CDCl_3$.

High resolution mass spectrometry was conducted by Dr Daniel Jardine (Flinders Analytical, Flinders University) and Dr Sally Duck (Monash University). Calculated mass and/or theoretical spectra were generated from software available to the mass spectrometry operator, or from the mMass software package [226].

X-Ray crystallography was conducted by Prof Jonathon White (The University of Melbourne, measurement and solving), Assoc Prof Chris Sumby (The University of Adelaide, measurement), and Ms Rebecca Norman (Flinders University, solving). X-Ray crystallographic data will be uploaded to The Cambridge Crystallographic Data

Centre (CCDC) in the near future, accessible via www.ccdc.cam.ac.uk/data_request/cif. Figures were produced using the Mercury software package [227], or from software available to the crystallographer.

Melting points were measured using a Barloworld Scientific SMP10 melting point apparatus.

8.3 Method for Host-Guest Titrations

All samples for host-guest titrations were weighed using a five decimal point balance (Shimadzu AUW220D or AandD GR-202). Volumetric glassware (class A) was used for volumes > 1 mL. Gas tight microlitre syringes (SGE, Hamilton) were used for volumes ≤ 1 mL. UV-Vis host-guest titrations were carried out at constant host concentrations of 10^{-6}-10^{-7} M in $CHCl_3$. Association constants and speciation diagrams were calculated from the UV-Vis titration data using the HypSpec and HySS2009 software packages (Protonic software) [166] over 400-450 nm. A more detailed discussion of fitting and binding models can be found in Appendix 2. NMR host-guest titrations were carried out in $CDCl_3$ at non-constant host concentration, starting at 10^{-3}-10^{-4} M, and gradually diluted by aliquots of guest solution (usually 5-10 μL per 0.1 equivalents of guest).

8.4 Reagents

Where necessary, solvents and reagents for synthesis were purified according to the methods published in [225]. Dry THF was freshly distilled from sodium/benzophenone, dry CH_2Cl_2 freshly distilled from CaH_2, and dry DMF and DMSO were distilled under reduced pressure onto fresh molecular sieves after stirring on molecular sieves overnight. The following chemicals were purified by sublimation under high vacuum at 0.17 mmHg at the following temperatures, then stored under a nitrogen atmosphere, protected from light, and in a desiccator at room temperature unless otherwise specified: potassium *tert*-butoxide at 160 °C, *p*-phenylenediamine at 100 °C, 4,4'-bipyridyl twice at 90 °C, DABCO twice at 75 °C and stored at -20 °C. Benzene-1,4-diboronic acid (Sigma-Aldrich) was recrystallised from THF/H_2O and dried *in vacuo* at 50 °C for 3 hours.

Silica gel (Davisil, 60 Å, 40-63 μm, Grace Davison Discovery Sciences) was used for column chromatography. Kieselgel silica gel 60 F254 aluminium sheets (Merck)

was used for TLC. Colourless compounds were visualised using a UV lamp or permanganate dip stain.

8.5 General Procedure for Microwave-Accelerated Alkene plus Cyclobutane Epoxide (ACE) Reactions

Microwave reactions were performed in a CEM Discover S-Class microwave in 10mL reaction vessels loaded with 0.25 g combined starting materials suspended in no more than 2-3 mL of solvent (less than one third total volume of flask) using the following conditions:

ACE reaction conditions are based on those prescribed in [160] using dry THF as the solvent. The microwave was operated in variable power (dynamic) mode with the following parameters: temperature 170-180 °C, power 300 W, stirring high, compressed air cooling (PowerMAX) off. The time required to reach the temperature set point was approximately 10-30 minutes, with the pressure reaching between 8-16.5 bar (maximum pressure cut-off 20 bar). The sample was held at the set temperature for a further 1-2 hours, with the microwave power automatically modulated between 80-220 W. The pressure reported by the software was observed to slowly decrease during the course of the reaction.

8.6 General Procedure for Sealed Tube Alkene plus Cyclobutane Epoxide (ACE) Reactions

During periods of microwave maintenance/service, the ACE reaction was carried out in a sealed tube. An 80 mL sealed tube (BSG Glassware, Tasmania, screw thread stopper with upper and lower Viton O-rings) was fitted with a stirrer bar and loaded with 0.8 g combined starting suspended in no more than 20 mL of solvent (less than one quarter total volume of flask). The tube was wrapped in alfoil, immersed in an oil bath relative to the solvent level, and heated to 160 °C with stirring for 24 hours behind a blast shield. O-rings (Viton) were replaced for each reaction.

8.7 General Procedure for Porphyrin Zn(II) Metallation

Using standard porphyrin Zn(II) metallation conditions [159], a solution of $Zn(OAc)_2.2H_2O$ (excess, usually 5-10 eq. per porphyrin) in MeOH was added dropwise down the condenser to a refluxing solution of porphyrin in $CHCl_3$ (or CH_2Cl_2)/MeOH (4:1), such that the combined volume was $CHCl_3 \geq$ MeOH. The

solution was refluxed for 1-2 hours, with further $CHCl_3$ added during this time as necessary to prevent evaporation to dryness. The mixture was cooled, diluted with $CHCl_3$, washed with H_2O, dried with Na_2SO_4, filtered, and the solvent removed *in vacuo*. The material was purified by column chromatography (silica) and recrystallised from $CDCl_3$/MeOH to afford purple crystals.

8.8 Synthesis of Compounds and Characterisation Data

Abbreviations

E = CO_2CH_3

Ph = C_6H_5

8.8.1 Mono-porphyrin Receptor

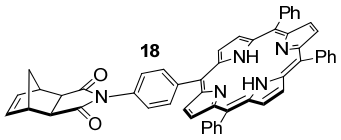

***exo*-imide porphyrin receptor, 18** [157]: A solution of *cis*-5-norbornene-*exo*-2,3-dicarboxylic anhydride **8** [143] (168 mg, 1.02 mmol) and 5-(4'-aminophenyl)-10,15,20-triphenylporphyrin **10** [144] (646 mg, 1.03 mmol) in degassed $CHCl_3$ (10 mL) was refluxed overnight under an argon atmosphere, forming a precipitate. The solvent was removed *in vacuo*, the residue redissolved in Ac_2O (10 mL), NaOAc (280 mg, 2.06 mmol) added, and the solution heated at 80 °C overnight, after which the Ac_2O was removed by distillation under reduced pressure. The mixture was redissolved in $CHCl_3$ (100 mL), washed with H_2O (2x 100 mL), NaOH (2 M, 3x 100 mL), H_2O (100 mL), dried with Na_2SO_4, filtered, and the solvent removed *in vacuo*. The crude material was purified by column chromatography (silica, 5 % THF/$CHCl_3$), and the solvent removed in vacuo to afford a purple solid (570 mg, 72 %, m.p. > 300 °C). ^{1}H NMR (400 MHz, $CDCl_3$, 26 ˚C, $CHCl_3$): 8.90-8.82 (m, 8H), 8.32 (d, J = 8.3 Hz, 2H), 8.22 (dd, J = 1.6, 7.6 Hz, 6H), 7.82-7.73 (m, 9H), 7.71 (d, J = 8.3 Hz, 2H), 6.45 (m, 2H), 3.56 (s, 2H), 3.04 (s, 2H), 1.76 (d, J = 10 Hz, 1H), 1.71 (d, J = 10 Hz, 1H), -2.8 (s, 2H). HRMS (ESI-TOF-MS) for $C_{53}H_{38}N_5O_2^+$ $[M+H]^+$: Calc: 776.3026. Found: 776.3044. UV-Vis ($CHCl_3$): λ_{max} (nm) = 418.9, 515.3, 550.5, 589.0, 644.5.

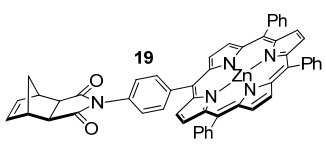

Zn(II) *exo*-imide porphyrin receptor, 19: $Zn(OAc)_2.2H_2O$ in MeOH was refluxed with *exo*-imide porphyrin receptor **18** in $CHCl_3$/MeOH according to the procedure in section 8.7, during which a precipitate formed. The precipitate was filtered and washed with $CHCl_3$, EtOAc, and MeOH (insoluble) to afford purple

crystals. ^{1}H NMR (600 MHz, DMSO-d_6, 20 ˚C, DMSO): 8.81-8.77 (m, 8H), 8.29 (d, J = 8.37 Hz, 2H), 8.21-8.16 (m, 6H), 7.84-7.77 (m, 9H), 7.72 (d, J = 8.37 Hz, 2H), 6.46 (m, 2H), 3.18-3.15 (m, 2H), 3.04-3.02 (m, 2H), 1.65 (d, J = 10.08 Hz, 1H), 1.59 (d, J = 10.08 Hz, 1H). HRMS (ESI-TOF-MS) for $C_{53}H_{35}N_5O_2{}^{(64)}ZnNa^+$ $[M+Na]^+$: Calc: 860.1980. Found: 860.2021. UV-Vis ($CHCl_3$): insoluble.

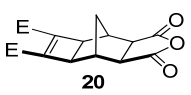

20

***exo*-cyclobutene diester anhydride, 20**: Using a modified procedure [151, 152], a solution of *cis*-5-norbornene-*exo*-2,3-dicarboxylic anhydride **8** [143] (8.0 g, 48.7 mmol), DMAD [149, 150] (13.9 g, 2 eq., 97.5 mmol), and $[RuH_2(CO)(PPh_3)_3]$ [148] (2.24 g, 2.4 mmol, 5 mol-%) in toluene (100 mL) was heated at 100 °C for 3 days under a nitrogen atmosphere and protected from light, forming a precipitate. If precipitation did not occur, the mixture was cooled and hexane added until precipitation occurred. The mixture was filtered, and the precipitate washed with hexane to afford a brown powder (10.0 g, 67 %), used for subsequent synthesis without further purification. A sample was recrystallised from $CHCl_3$/hexane to afford a beige powder for MS and melting point analysis. m.p. 190-193 °C. ^{1}H NMR (600 MHz, $CDCl_3$, 20 ˚C, $CHCl_3$): 3.80 (s, 6H), 2.92 (s, 2H), 2.90 (d, J = 1.4 Hz, 2H), 2.89 (s, 2H), 1.59 (d, J = 12.8 Hz, 1H), 1.19 (d, J = 12.8 Hz, 1H). ^{13}C NMR (150 MHz, $CDCl_3$): 171.89, 160.72, 141.88, 52.40, 47.89, 45.19, 38.70, 27.02. HRMS (ESI-TOF-MS) for $C_{15}H_{14}O_7Na^+$ $[M+Na]^+$: Calc: 329.0637. Found: 329.0643.

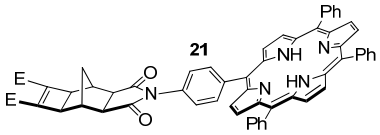

21

porphyrin (*exo*-cyclobutene diester imide), 21: A solution of *exo*-cyclobutene diester anhydride **20** (40 mg, 0.13 mmol) and 5-(4'-aminophenyl)-10,15,20-triphenylporphyrin **10** (82 mg, 0.13 mmol) in degassed $CHCl_3$ (5 mL) was refluxed overnight under an argon atmosphere, forming a precipitate. The solvent was removed *in vacuo*, and the solids redissolved in Ac_2O (10 mL), NaOAc (100 mg, 0.7 mmol) added, and the solution heated at 80 °C overnight, after which the Ac_2O was removed by distillation under reduced pressure. The mixture was redissolved in $CHCl_3$ (100 mL), washed with H_2O (2x 100 mL), NaOH (2 M, 3x 100 mL), H_2O (100 mL), dried with Na_2SO_4, filtered, and the solvent removed in vacuo. The crude material was purified by column chromatography (silica, 10 % THF/$CHCl_3$), the solvent removed in vacuo, and recrystallised from $CDCl_3$/MeOH to afford purple crystals (100 mg, 84 %, m.p. (solvent of crystallisation loss 240-245 °C), 262-269 °C. ^{1}H NMR (600 MHz, $CDCl_3$, 20 ˚C, $CHCl_3$, approximately 1 mM): 8.91-8.81 (m,

8H), 8.33 (d, J = 8.1 Hz, 2H), 8.22 (d, J = 7.2 Hz, 6H), 7.81-7.73 (m, 9H), 7.70 (d, J = 8.1 Hz, 2H), 3.86 (s, 6H), 3.08 (s, 2H), 3.04 (s, 2H), 2.95 (s, 2H), 1.66 (d, J = 12.9 Hz, 1H), 1.44 (d, J = 12.9 Hz, 1H), -2.80 (s, 2H). HRMS (ESI-TOF-MS) for $C_{59}H_{44}N_5O_6^+$ $[M+H]^+$: Calc: 918.3292. Found: 918.3313. UV-Vis ($CHCl_3$): λ_{max} (nm) = 418.7 (shoulder around 400), 515.3, 550.7, 589.4, 646.0.

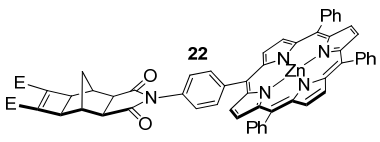

Zn (II) porphyrin (*exo*-cyclobutene diester imide), 22: $Zn(OAc)_2.2H_2O$ (190 mg, 0.87 mmol) in MeOH (3 mL) was refluxed with porphyrin (*exo*-cyclobutene diester imide) **21** (80 mg, 0.087 mmol) in $CHCl_3$/MeOH (4+1 = 5 mL), and worked up according to the procedure in section 8.7. The product was purified by column chromatography (silica, 10 % THF/$CHCl_3$), collecting the strong porphyrin band. The solvent was removed *in vacuo* and the purple powder (81 mg, 95 %) was recrystallised from $CDCl_3$/MeOH to afford bright purple crystals for host-guest titrations. m.p. (solvent of crystallisation loss 254-255 °C), 272-278 °C. ^{1}H NMR (600 MHz, $CDCl_3$, 20 ˚C, $CHCl_3$, approximately 5 mM): 8.99-8.93 (m, 8H), 8.28 (d, J = 8.2 Hz, 2H), 8.24 (d, J = 6.5 Hz, 6H), 7.82-7.72 (m, 9H), 7.48 (d, J = 8.2 Hz, 2H), 3.84 (s, 6H), 2.96 (s, 2H), 2.89 (s, 2H), 2.72 (s, 2H), 1.57 (d, J = 12.8 Hz, 1H), 1.31 (d, J = 12.8 Hz, 1H). HRMS (ESI-TOF-MS) for $C_{59}H_{41}N_5O_6{}^{(64)}ZnNa^+$ $[M+Na]^+$: Calc: 1002.2246. Found: 1002.2280. UV-Vis ($CHCl_3$): λ_{max} (nm) = 399.0 (shoulder), 419.3, 547.5, 585.0, $\varepsilon = 6.47 \times 10^5$ $Lmol^{-1}cm^{-1}$.

8.8.2 Freely Rotating Tweezer

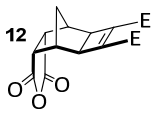

***endo*-cyclobutene diester anhydride, 12**: Using a modified procedure [151, 152], a solution of *cis*-5-norbornene-*endo*-2,3-dicarboxylic anhydride **7** [142] (8.0 g, 48.7 mmol), DMAD [149, 150] (13.9 g, 2 eq., 97.5 mmol), and $[RuH_2(CO)(PPh_3)_3]$ [148] (2.24 g, 2.4 mmol, 5 mol-%) in toluene (100 mL) was heated at 100 °C for 3 days under a nitrogen atmosphere and protected from light, forming a precipitate. If precipitation did not occur, the mixture was cooled and hexane added until precipitation occurred. The mixture was filtered, and the precipitate washed with hexane to afford a brown powder (11.6 g, 77 %), and used for subsequent synthesis without further purification. A sample was recrystallised from $CHCl_3$/hexane to afford a white powder for MS and melting point analysis. m.p. 165-167 °C. ^{1}H NMR (600 MHz, $CDCl_3$, 20 ˚C, $CHCl_3$): 3.79 (s, 6H), 3.57-3.52 (m, 2H), 2.99 (s, 2H), 2.95-2.89 (m, 2H), 1.82 (d, J = 11.6 Hz, 1H), 1.52

(dt, J = 11.6, 1.3 Hz, 1H). ^{13}C NMR (100 MHz, $CDCl_3$): 170.78, 160.59, 141.20, 52.33, 48.63, 42.40, 37.36, 34.55. HRMS (ESI-TOF-MS) for $C_{15}H_{14}O_7Na^+$ $[M+Na]^+$: Calc: 329.0637. Found: 329.0641.

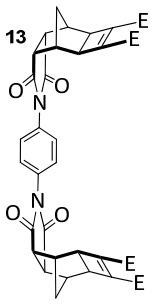

freely rotating *endo*- Mitsudo linker, 13: A solution of *endo*-cyclobutene diester anhydride **12** (4.92 g, 16.1 mmol) and sublimed *p*-phenylenediamine **9** (0.869 g, 8.0 mmol) in dry DMF (80 mL) was heated at 80 °C under an argon atmosphere for 3 days, after which the solution had turned black. The DMF was removed by distillation under reduced pressure, the mixture redissolved in Ac_2O (80 mL), NaOAc (8.75 g, 64.3 mmol) added, and the solution heated at 80 °C under a nitrogen atmosphere for a further 3 days, after which a precipitate could sometimes be observed. The Ac_2O was removed by distillation under reduced pressure, the mixture redissolved in $CHCl_3$ (200 mL), washed with H_2O (2x 200 mL), NaOH (2 M, 3x 200 mL, or until aqueous phase was no longer black), HCl (2 M, 1x 100 mL), H_2O (1x 100 mL), dried with Na_2SO_4, and the solvent removed *in vacuo* to afford off-white flakes (1.38 g, 25 %), used for subsequent synthesis without further purification. A sample was recrystallised from $CHCl_3$/hexane to afford a white powder for MS and melting point analysis. m.p. > 300 °C. ^{1}H NMR (600 MHz, $CDCl_3$, 20 ˚C, $CHCl_3$): 7.39 (s, 4H), 3.78 (s, 12H), 3.43-3.38 (m, 4H), 2.98 (s, 4H), 2.97-2.94 (m, 4H), 1.82 (d, J = 11.4 Hz, 2H), 1.56 (d, J = 11.4 Hz, 2H). ^{13}C NMR (150 MHz, $CDCl_3$): 175.63, 160.73, 141.28, 131.69, 127.22, 52.26, 47.61, 42.62, 36.89, 34.41. HRMS (ESI-TOF-MS) for $C_{36}H_{32}N_2O_{12}Na^+$ $[M+Na]^+$: Calc: 707.1853. Found: 707.1832.

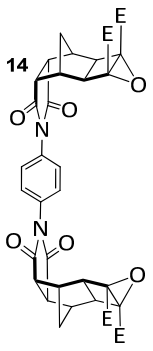

freely rotating *endo*- bis-epoxide linker, 14: freely rotating *endo*-Mitsudo linker **13** (600 mg, 0.88 mmol) was dissolved in dry CH_2Cl_2 (50 mL) under a nitrogen atmosphere and cooled to 0 °C. Anhydrous *tert*-butyl hydroperoxide in toluene [153] (3.3 M, 664 µL, 2.2 mmol, 2.5 eq.) was added and stirred for a further 10 mins at 0 °C, after which sublimed potassium *tert*-butoxide (98 mg, 0.88 mmol, 1 eq.) was added. The mixture was allowed to warm to room temperature over 30 minutes, during which a white precipitate formed. After stirring at room temperature for a further 3 hours, the mixture was diluted with CH_2Cl_2 (50 mL) and sodium sulfite (10 % aqueous solution, 10 mL) added with vigorous stirring for 15 minutes. The mixture was further diluted with $CHCl_3$ (1 L), washed with brine (500 mL), dried with Na_2SO_4, filtered, and the solvent removed *in vacuo*, to afford a white

powder (237 mg, 28 %, 3:1 mixture of bis-epoxide to starting material based on relative NMR integration). Limited solubility in a range of solvents made further purification difficult, and the bis-epoxide was characterised as a mixture with starting material. ^{1}H NMR (400 MHz, $CDCl_3$, 26 ˚C, $CHCl_3$): as a mixture with starting material, 7.33 (s, 4H), 3.82 (s, 12H), 3.44 (s, 4H), 3.37 (s, 4H), 2.56 (s, 4H), 2.2 (d, J = 12 Hz, 2H), 1.81 (d, J = 12 Hz, 2H).

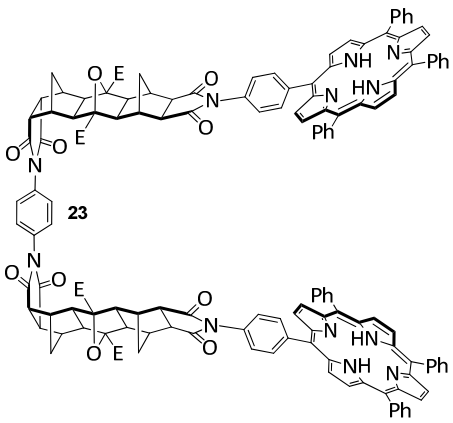

free base freely rotating tweezer, 23: A suspension of unpurified freely rotating *endo*-bis-epoxide linker **14** (0.10 g of a 3:1 mixture of **14**:**13**, approximately 75 mg/0.11 mmol bis-epoxide) and *exo*-imide porphyrin receptor **18** (0.16 g, 0.21 mmol, 2 eq. based on **14**) in dry THF (2 mL) was subjected to microwave irradiation under the conditions specified in section 8.5. The solvent was removed *in vacuo* and the material purified by column chromatography (silica, 10 % THF/CH_2Cl_2), recovering *exo*-imide porphyrin receptor in the first major porphyrin band, with the tweezer (88 mg, 38 %) eluted as the second major porphyrin band. The tweezer was recrystallised from $CHCl_3$/MeOH to afford purple crystals. m.p. > 300 ˚C. ^{1}H NMR (600 MHz, $CDCl_3$, 20 ˚C, $CHCl_3$): 8.84 (s, 16H), 8.30 (d, J = 8.2 Hz, 4H), 8.23-8.16 (m, 12H), 7.81-7.70 (m, 18H), 7.65 (d, 4H, J = 8.2 Hz), 7.60 (s, 4H), 3.98 (s, 12H), 3.27 (s, 4H), 2.97 (s, 4H), 2.89 (s, 4H), 2.84 (s, 4H), 2.75 (d, J = 11.1 Hz, 2H), 2.55 (d, J = 11.9 Hz, 2H), 2.41 (s, 4H), 2.34 (s, 4H), 1.38 (d, J = 11.1 Hz, 2H), 1.22 (d, J = 11.9 Hz, 2H), -2.81 (s, 4H). HRMS (ESI-TOF-MS) for $C_{142}H_{107}N_{12}O_{18}^+$ $[M+H]^+$: Calc: 2267.7813. Found: 2267.7854. UV-Vis ($CHCl_3$): λ_{max} (nm) = 419.0, 514.9, 551.1, 590.0, 645.9.

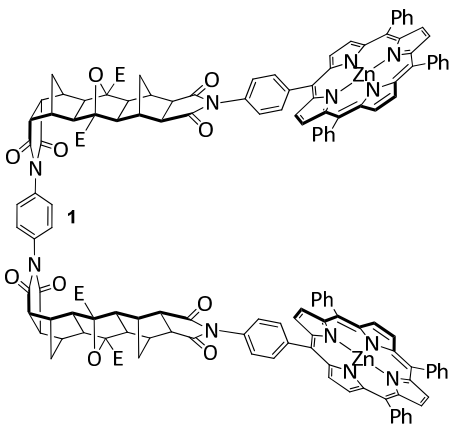

Zn (II) freely rotating tweezer, 1: $Zn(OAc)_2.2H_2O$ (100 mg, 0.456 mmol) in MeOH (2 mL) was refluxed with free base freely rotating tweezer **23** (94 mg, 0.041 mmol) in $CHCl_3$/MeOH (4+1 = 5 mL), and worked up according to the procedure in section 8.7. The product was purified by column chromatography (silica, 10 % THF/$CHCl_3$ to remove minor components at the solvent front, followed by 30 % THF/$CHCl_3$),

collecting the strong porphyrin band. The solvent was removed *in vacuo* to afford a purple powder (94 mg, 95 %), which was recrystallised from $CHCl_3$/MeOH to afford bright purple crystals for host-guest titrations. m.p. > 300 °C. ^{1}H NMR (600 MHz, $CDCl_3$, 20 ˚C, $CHCl_3$): 8.96-8.92 (m, 16H), 8.31 (d, J = 8.3 Hz, 4H), 8.23-8.18 (m, 12H), 7.80-7.70 (m, 18H), 7.66 (d, J = 8.3 Hz, 4H), 7.60 (m, 4H), 3.98 (s, 12H), 3.28 (m, 4H), 2.97 (s, 4H), 2.89 (s, 4H), 2.84 (m, 4H), 2.76 (d, J = 11 Hz, 2H), 2.55 (d, J = 12.1 Hz, 2H), 2.41 (s, 4H), 2.34 (s, 4H), 1.39 (d, J = 11 Hz, 2H), 1.23 (d, J = 12.1 Hz, 2H). HRMS (ESI-TOF-MS) for $C_{142}H_{107}N_{12}O_{18}Zn_2^+$ $[M+H]^+$: Calc: 2391.6094. Found: 2391.6044. UV-Vis ($CHCl_3$): λ_{max} (nm) = 419.5, 547.7, 583.9, $\varepsilon_{single\ porphyrin}$ = 5.44 x 10^5 $Lmol^{-1}cm^{-1}$.

8.8.3 Restricted Rotation Tweezer (*syn-* + *anti-*)

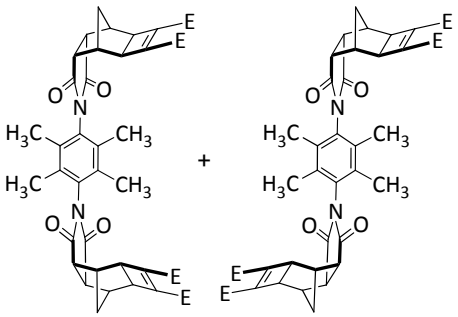

syn- **27** *anti-* **28**

restricted rotation *endo-* Mitsudo linker (mixture of *syn-* 27 + *anti-* 28): A solution of *endo*-cyclobutene diester anhydride **12** (3.73 g, 12.2 mmol) and 2,3,5,6-tetramethyl-*p*-phenylenediamine **26** (1.0 g, 6.1 mmol, 0.5 eq.) in degassed DMSO (60 mL) was heated at 80 °C under an argon atmosphere for 1 day. The DMSO was removed by distillation under reduced pressure, the mixture redissolved in Ac_2O (80 mL), NaOAc (7.2 g, 53 mmol) added, and the solution heated at 80 °C under a nitrogen atmosphere for a further 1 day, after which a precipitate was observed. Preliminary ^{1}H NMR of the reaction mixture suggested two isomers in an approximately 60:40 ratio (although may be due to different solubility), distinguished by outer and inner pairs of non-equivalent CH_3 phenyl substituent resonances. The precipitate was removed by filtration and the solids redissolved in $CHCl_3$ (200 mL), washed with H_2O (2x 200 mL), aqueous NaOH solution (2 M, 3x 200 mL), aqueous HCl solution (2 M, 1x 100 mL), H_2O (1x 100 mL), dried (Na_2SO_4), and the solvent removed *in vacuo* to afford a white powder (3.25 g, 72 %, m.p > 300 °C). The linker was used as a mixture due to difficulty in separation of the isomers.

A small sample was separated by column chromatography, using either of the following methods or a combination of both. Method A: silica (10 % THF/$CHCl_3$) to partially resolve isomers, if bands co-elute then silica (5 % MeOH/$CHCl_3$), followed by recrystallisation from $CHCl_3$/MeOH, wash solids with MeOH. Method B: silica

plug (EtOAc), then silica (load $CHCl_3$, elute 50 % EtOAc/$CHCl_3$, poor solubility and precipitation on column). Unfortunately the assignment of each isomer as either *syn*- or *anti*- could not be achieved by ^1H NOE spectroscopy, and so are referred to by the inner and outer CH_3 isomer nomenclature established above.

Inner CH_3 isomer: ^1H NMR (600 MHz, $CDCl_3$, 20 ˚C, $CHCl_3$): 3.80 (s, 12H), 3.50-3.47 (m, 4H), 3.11 (s, 4H), 2.98-2.95 (m, 4H), 2.07 (b) (s, 6H), 1.95 (b) (s, 6H), 1.86 (d, J = 11.61 Hz, 2H), 1.59 (d, J = 11.61 Hz, 2H). ^{13}C NMR (150 MHz, $CDCl_3$): 175.72, 160.80, 141.45, 133.16, 132.62, 132.04, 52.27, 48.16, 43.15, 36.53, 34.83, 16.18, 15.51. HRMS (ESI-TOF-MS) for $C_{40}H_{40}N_2O_{12}Na^+$ $[M+Na]^+$: Calc: 763.2479. Found: 763.2494.

Outer CH_3 isomer: ^1H NMR (600 MHz, $CDCl_3$, 20 ˚C, $CHCl_3$): 3.80 (s, 12H), 3.50-3.46 (m, 4H), 3.12 (s, 4H), 2.98-2.96 (m, 4H), 2.09 (s, 6H), 1.94 (s, 6H), 1.86 (d, J = 11.49 Hz, 2H), 1.59 (d, J = 11.49 Hz, 2H). ^{13}C NMR (150 MHz, $CDCl_3$): 175.74, 160.79, 141.45, 133.11, 132.71, 132.03, 52.27, 48.18, 43.15, 36.55, 34.84, 16.17, 15.58. HRMS (ESI-TOF-MS) for $C_{40}H_{40}N_2O_{12}Na^+$ $[M+Na]^+$: Calc: 763.2479. Found: 763.2494.

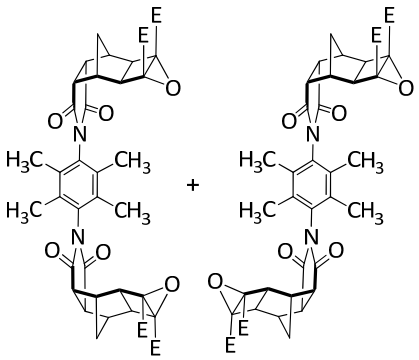

syn- + *anti-* **29**

restricted rotation *endo*- bis-epoxide linker, *syn*- + *anti*- mixture 29: restricted rotation *endo*-Mitsudo linker (mixture of **27** + **28**) (1.50 g, 2.0 mmol) was dissolved in dry CH_2Cl_2 (75 mL) under a nitrogen atmosphere and cooled to 0 °C. Anhydrous *tert*-butyl hydroperoxide in toluene [153] (3.3 M, 1.53 mL, 5.1 mmol, 2.5 eq.) was added and stirred for a further 10 mins at 0 °C, after which sublimed potassium *tert*-butoxide (0.23 g, 2.0 mmol, 1 eq.) was added. The mixture was allowed to warm to room temperature over 30 minutes, and after stirring at room temperature for a further 3 hours, the mixture was diluted with CH_2Cl_2 (50 mL) and sodium sulfite (10 % aqueous solution, 10 mL) added with vigorous stirring for 15 minutes. The mixture was further diluted with $CHCl_3$ (1 L), washed with brine (500 mL), dried with Na_2SO_4, filtered, and the solvent removed *in vacuo*. NMR of the reaction mixture indicated approximately 50 % remaining starting material, and so the reaction was repeated on this mixture using the same quantities of epoxidation reagents (for later repeats of this reaction, double the

epoxidation reagent quantity was used from the beginning). This afforded a white powder (0.80 g, 51 %), used in subsequent reactions without further purification and as a mixture of isomers. A sample was recrystallised from $CHCl_3$/hexane for MS and melting point analysis (mixture of isomers). m.p. > 250-300 °C (decomposition). ^{1}H NMR (600 MHz, $CDCl_3$, 20 ˚C, $CHCl_3$): as mixture of isomers 3.82 (s, 12H), 3.46-3.41 (m, 8H), 2.74-2.70 (m, 4H), 2.24 (d, J = 11.2 Hz, 2H), 2.03 (a) + 2.00 (b) (both singlets, combined integration 6H), 1.92 (b) + 1.89 (a) (both singlets, combined integration 6H), 1.84 (d, J = 11.2 Hz, 2H). HRMS (ESI-TOF-MS) for $C_{40}H_{40}N_2O_{14}Na^+$ $[M+Na]^+$: Calc: 795.2377. Found: 795.2393.

free base restricted rotation tweezer (mixture of *syn*- 34 + *anti*- 35):

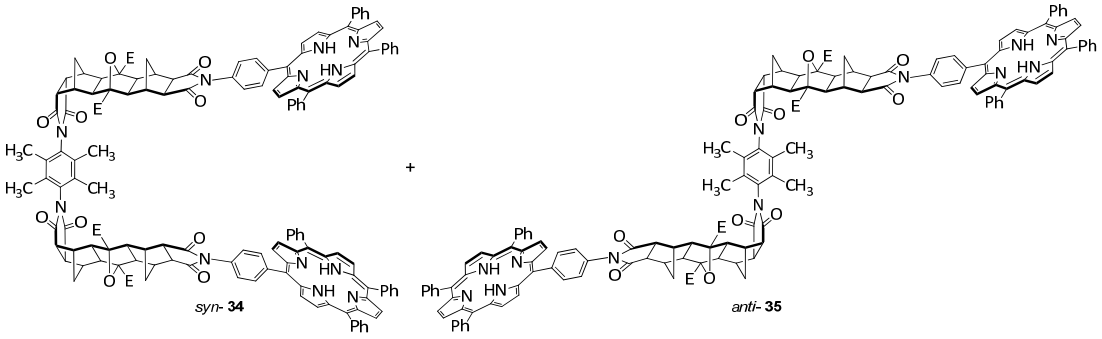

A suspension of restricted rotation *endo*- bis-epoxide linker mixture **29** (0.2 g, 0.26 mmol) and *exo*-imide porphyrin receptor **18** (0.4 g, 0.52 mmol, 2 eq.) in dry THF (10 mL) was heated in a sealed tube at 160 °C for 20-24 hours using the procedure specified in section 8.6. This procedure was repeated several times on a similar scale until 1.0 g epoxide had been reacted. The material from each reaction was combined. The solvent was removed *in vacuo* and the material purified by column chromatography (silica, 10 % THF/CH_2Cl_2), recovering *exo*- imide porphyrin receptor in the first major porphyrin band. The subsequent two closely eluting porphyrin bands each contained a majority of each isomer, and each isomer was resubjected to column chromatography to further improve separation. Isomers could be speculated as *syn*- and *anti*- on the basis of desymmetrisation of the porphyrin aromatic resonances (significant for *syn*-) and quantified by the difference in relative integrations of the inner pyridyl resonances. This afforded a purple powder (combined isomer mass 0.68 g, 23 % = 10 % *syn*- + 13 % *anti*-). The *anti*- isomer was isolated completely free of *syn*-, while the *syn*- isomer contained ~25 % residual *anti*-. Each isomer was crudely recrystallised from $CDCl_3$/MeOH, however, further

purification (particularly removal of the *anti*- **35** isomer from the *syn*- **34** sample) was carried out post- Zn(II) metalation in an effort to conserve product.

Anti- **35**: ^{1}H NMR (600 MHz, $CDCl_3$, 20 ˚C, $CHCl_3$): 8.85 (s, 16H), 8.30 (d, J = 8.16 Hz, 4H), 8.25-8.18 (m, 12H), 7.82-7.73 (m, 18H), 7.62 (d, J = 8.1 Hz, 4H), 3.98 (s, 12H), 3.34-3.30 (m, 4H), 2.92 (s, 4H), 2.90 (s, 4H), 2.85-2.82 (m, 4H), 2.76 (d, J = 10.92 Hz, 2H), 2.58-2.51 (m, 6H), 2.32 (s, 4H), 2.28 (s, 6H), 2.04 (s, 6H), 1.41 (d, J = 10.92 Hz, 2H), 1.22 (d, J = 11.88 Hz, 2H), -2.80 (s, 4H).

Syn- **34**: characterised as the Zn(II) derivative.

HRMS (ESI-TOF-MS) for two samples containing different ratios of *syn*-/*anti*-. $[C_{146}H_{116}N_{12}O_{18}]^{2+}$ $[M+2H]^{2+}$: Calc: 1162.4260. Found: 1162.4267.
$[C_{146}H_{114}N_{12}O_{18}Na_2]^{2+}$ $[M+2Na]^{2+}$: Calc: 1184.4079. Found: 1184.4110.

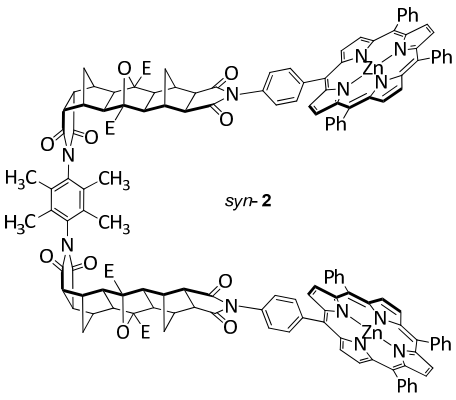

***syn*- Zn(II) restricted rotation tweezer, 2**: $Zn(OAc)_2.2H_2O$ (1.0 g, 4.55 mmol) in MeOH (10 mL) was refluxed with *syn*- **34** (mixture with 25 % *anti*- **35**, 0.37 g, 0.16 mmol) in CH_2Cl_2 (20 mL), during which the solution developed a green/blue hue, and was worked up according to the procedure in section 8.7. The product was purified by column chromatography to remove the green/blue impurity (silica, 10 % THF/$CHCl_3$) collecting the strong porphyrin band. The solvent was removed *in vacuo* to afford a purple powder (0.31 g, 79 %), in which remained 33 % *anti*- isomer (determined by relative NMR integration). This material was recrystallised repeatedly from $CHCl_3$/MeOH until free of the *anti*- isomer (approximately three to four times), to afford bright purple crystals for host-guest titrations. ^{1}H NMR (600 MHz, $CDCl_3$, 20 ˚C, approx. 1 mM, concentration dependent): 8.93-8.84 (m, 16H), 8.23-8.16 (m, 8H), 8.14-8.09 (m, 8H), 7.78-7.70 (m, 6H), 7.66-7.60 (m, 12H), 7.48-7.38 (bs, 4H), 3.98 (s, 12H), 3.33 (m, 4H), 2.88-2.83 (m, 8H), 2.81 (s, 4H), 2.77 (d, J = 11.07 Hz, 2H), 2.56 (s, 4H), 2.49 (d, J = 11.85 Hz, 2H), 2.33 (s, 4H), 2.31 (s, 6H), 2.00 (s, 6H), 1.43 (d, J = 11.07 Hz, 2H), 1.13 (d, J = 11.85 Hz, 2H). UV-Vis ($CHCl_3$): λ_{max} (nm) = 418.4 (shoulder around 400), 547.3, 583.9, $\varepsilon_{\text{single porphyrin}} = 4.9 \times 10^5$ $Lmol^{-1}cm^{-1}$.

***anti*- Zn(II) restricted rotation tweezer, 3**:

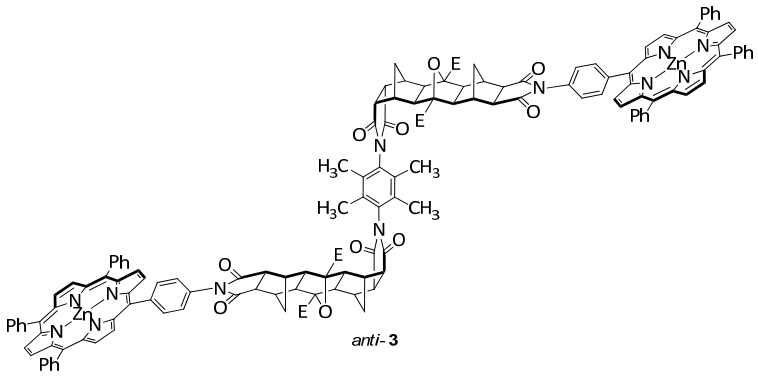

$Zn(OAc)_2.2H_2O$ (1.0 g, 4.55 mmol) in MeOH (10 mL) was refluxed with free base *anti*- restricted rotation tweezer **35** (0.31 g, 0.13 mmol) in CH_2Cl_2 (20 mL) and worked up according to the procedure in section 8.7. The product was purified by column chromatography (silica, 10 % THF/$CHCl_3$) collecting the strong porphyrin band. The solvent was removed *in vacuo* to afford a purple powder (0.29 g, 89 %), which was recrystallised from $CHCl_3$/MeOH to afford bright purple crystals (free from *syn*- isomer) for host-guest titrations. ^{1}H NMR (600 MHz, $CDCl_3$, 20 ˚C, approx. 0.85 mM): 8.97-8.94 (m, 16H), 8.31 (d, J = 8.22 Hz, 4H), 8.24-8.20 (m, 12 H), 7.81-7.73 (m, 18 H), 7.61 (d, J = 8.22 Hz, 4H), 3.98 (s, 12H), 3.33 (m, 4H), 2.91 (s, 4H), 2.89 (s, 4H), 2.84 (m, 4H), 2.77 (d, J = 10.75 Hz, 2H), 2.58-2.50 (m, 6H), 2.32 (s, 4H), 2.28 (s, 6H), 2.04 (s, 6H), 1.42 (d, J = 10.75 Hz, 2H), 1.22 (d, J = 12.24 Hz, 2H). UV-Vis ($CHCl_3$): λ_{max} (nm) = 399.2 (shoulder), 419.3, 547.4, 585.8, $\varepsilon_{single\ porphyrin}$ = 5.80 x 10^5 $Lmol^{-1}cm^{-1}$.

8.8.4 Tetra-porphyrin Tweezer

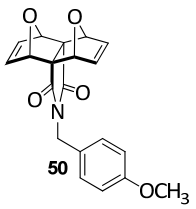

PMB protected T-piece, 50: Using a modified procedure [106, 189], T-piece anhydride **37** [188][31] (21 g, 0.090 mol) was dissolved in $CHCl_3$ (300 mL, deacidified) under a nitrogen atmosphere. 4-methoxybenzylamine (2 eq., 25 g/23.6 mL, 0.18 mol, Sigma-Aldrich) was added and the solution stirred at 50 °C overnight under a nitrogen atmosphere, during which a white precipitate formed. The mixture was cooled, filtered, and the precipitate washed with $CHCl_3$ (3x 100 mL). The precipitate was dissolved in Ac_2O (350 mL), NaOAc (2 eq., 24.6 g, 0.181 mol) added, and the mixture stirred overnight at 50 °C under a nitrogen atmosphere, after which the Ac_2O was removed by distillation under reduced pressure at 50 °C. The solids were

[31] anhydride [188] from bis-carboxylic acid [185, 186].

redissolved into $CHCl_3$ (300 mL), washed with H_2O (2x 200 mL), HCl (2 M, 200 mL), NaOH (2 M, 5x 200 mL)[32], H_2O (200 mL), dried with Na_2SO_4, filtered, and the solvent removed *in vacuo*. The solid was washed with hexane (2x 100 mL), Et_2O (2x 100 mL), and EtOH (5x 100 mL, to remove significant brown byproduct) to afford a white powder (16.5 g, 52 %). A sample was recrystallised from $CHCl_3$/hexane for MS and melting point analysis. m.p. 231-233 °C. Single crystals for X-ray analysis were grown from CH_3CN by slow evaporation. ^{1}H NMR (600 MHz, $CDCl_3$, 20 ˚C, $CHCl_3$): 7.15 (d, J = 8.76 Hz, 2H), 6.79 (d, 8.76 Hz, 2H), 6.37 (m, 4H), 5.20 (m, 4H), 4.28 (s, 2H), 3.77 (s, 3H). ^{13}C NMR (150 MHz, $CDCl_3$): 173.86, 159.31, 138.90, 130.51, 127.28, 113.74, 81.39, 69.21, 55.30, 41.79. HRMS (ESI-TOF-MS) for $C_{20}H_{17}NO_5Na^+$ $[M+Na]^+$: Calc: 374.1004. Found: 374.1000. X-Ray crystallographic data will be uploaded to The Cambridge Crystallographic Data Centre (CCDC) in the near future. A summary is provided in Appendix 4.

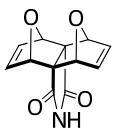

51

T-piece imide, 51: Using a modified procedure [106, 189-192], PMB protected T-piece **50** (16 g, 0.046 mol) was slowly dissolved in a mixture of 9:1 CH_3CN/H_2O (1 L) at 40 °C for 1 hr. Ammonium cerium(IV) nitrate (82 g, 3.3 eq.) was added in two portions; 2.3 eq. for 90 mins, followed by 1 eq. for a further 30 minutes; with reaction progress monitored by NMR. The volume of the solution was reduced by approximately two thirds *in vacuo* at 50 °C, or until a precipitate formed. The precipitate was filtered and put aside to later be combined with additional product. The filtrate volume was then further reduced *in vacuo* at 50 °C until only H_2O remained. The mixture was diluted with further H_2O, extracted with EtOAc (10x 200 mL), and the EtOAc extracts combined. The volume of EtOAc was reduced *in vacuo* at 50 °C until a precipitate formed. The precipitate was filtered, and combined with the first crop of product. The filtrate volume was further reduced, and the precipitate collection cycle repeated until only an orange/brown oily sludge remained (p-anisaldehyde byproduct). The combined precipitate was washed with H_2O (2x 100 mL) and EtOH (10x 100 mL) to afford a white powder (7.64 g, 73 %). m.p. partial decomposition (darkens) > 200 ˚C, violent decomposition (boiling) at 293-295 ˚C. Single crystals for X-ray analysis were grown from CH_3CN/DMSO by slow evaporation. ^{1}H NMR (600 MHz, DMSO-d_6, 20 ˚C, DMSO): 10.79 (s, 1H), 6.71 (s, 4H), 5.24 (s, 4H). 13C NMR (150 MHz, DMSO-

[32] Caution: NaOH reacts exothermically with residual Ac_2O, temperature should remain below 50 °C for optimum product stability.

d_6): 175.34, 139.36, 80.39, 70.03. HRMS (ESI-TOF-MS) for $C_{12}H_8NO_4^-$ [M-H]$^-$: Calc: 230.0453. Found: 230.0457. X-Ray crystallographic data will be uploaded to The Cambridge Crystallographic Data Centre (CCDC) in the near future. A summary is provided in Appendix 4.

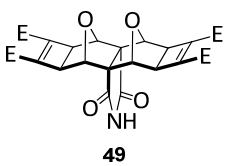

49

Mitsudo T-piece imide, 49: A solution of T-piece imide **51** (5.0 g, 0.022 mol), DMAD [149, 150] (12.3 g, 4 eq., 0.087 mol), and [$RuH_2(CO)(PPh_3)_3$] [148] (7.2 g, 2.4 mmol, 36 mol-%) in dry DMF (150 mL) was stirred at 60 °C under a nitrogen atmosphere for 1 day. The black solution was cooled, and the DMF removed by distillation under reduced pressure. The remaining sludge was purified by several rounds of column chromatography using different solvents to elute the product as follows: (1) (silica, plug, 20 % THF/$CHCl_3$), collecting several large plug length fractions, NMR to determine fractions which contained product, (2) these fractions recolumned (silica, 5 % THF/$CHCl_3$), collecting the middle band, (3) and this fraction recolumned (silica, EtOAc). The solvent was removed *in vacuo*, and the product recrystallised from EtOAc/hexane or $CHCl_3$/hexane to afford a white to pale yellow powder (3.81 g, 34 %). m.p. (solvent of crystallisation loss 282-302 °C), 303-307 ˚C (decomposition). Single crystals for X-ray analysis were grown from CH_3CN by slow evaporation. ^{1}H NMR (600 MHz, $CDCl_3$, 20 ˚C, $CHCl_3$): 7.80 (s, 1H), 4.75 (s, 4H), 3.79 (s, 12H), 3.24 (s, 4H). ^{13}C NMR (150 MHz, $CDCl_3$): 172.12, 160.25, 140.19, 77.11, 71.57, 52.43, 44.82. HRMS (ESI-TOF-MS) for $C_{24}H_{20}NO_{12}^-$ [M-H]$^-$: Calc: 514.0986. Found: 514.0982. X-Ray crystallographic data will be uploaded to The Cambridge Crystallographic Data Centre (CCDC) in the near future. A summary is provided in Appendix 4.

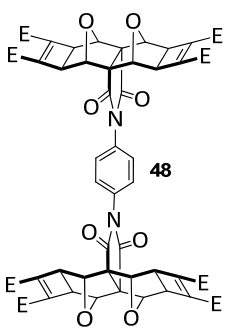

48

Mitsudo I-piece linker, 48: Using a modified procedure developed for coupling imidazole with phenyl boronic acid [197], Mitsudo T-piece imide **49** (380 mg, 0.74 mmol) was suspended in MeOH (25 mL), and compressed air was bubbled through a large gauge needle into the reaction mixture at flow rate of 3-4 bubbles per second. Benzene-1,4-diboronic acid (61 mg, 0.37 mmol, Sigma-Aldrich) was added, quickly followed by $Cu(OAc)_2.H_2O$ (7.5 mg, 0.038 mmol, no more than 2.5-5 mol-% per boronic acid). The mixture was refluxed for 12 hours during which a white precipitate formed. The volume of MeOH was monitored for evaporation and the level maintained. The air bubbler needle was

changed every 1 hour to prevent clogging of the tip, while the air flow rate was varied as necessary to maintain the blue/green colour of the solution (greater air flow required if the solution was brown), yet without causing cooling the mixture below reflux. The reaction produced two compounds, the I-piece linker (precipitate), and a solvent-dependent side product (filtrate). The side product in the filtrate (**60**, **61**) was characterised without further purification. The desired product (precipitate) was purified using the following method:

The mixture was cooled, the precipitate removed by filtration, and the solids washed with MeOH (100 mL). The solid was dissolved in CH_2Cl_2 (100 mL), washed with H_2O (100 mL), dried with Na_2SO_4, the solvent removed *in vacuo*, and the solids washed again with MeOH (100 mL) and hexane (100 mL) to afford a white powder (150 mg, 37 %). This procedure was repeated several times on a similar scale to generate additional material. A sample was recrystallised from $CHCl_3$/hexane for MS and melting point analysis. m.p. > 300 °C (partial decomposition). ^{1}H NMR (600 MHz, $CDCl_3$, 20 ˚C, $CHCl_3$): 7.38 (s, 4H), 4.87 (s, 8H), 3.80 (s, 24H), 3.23 (s, 8H). ^{13}C NMR (150 MHz, $CDCl_3$): 171.50, 160.17, 140.11, 131.21, 127.03, 77.61, 70.37, 52.49, 44.82. HRMS (ESI-TOF-MS) for $C_{54}H_{44}N_2O_{24}Na^+$ $[M+Na]^+$: Calc: 1127.2182. Found: 1127.2166.

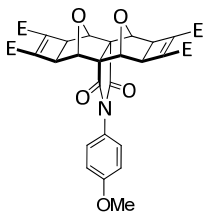

60

side product with solvent MeOH, **60**: ^{1}H NMR (600 MHz, $CDCl_3$, 20 ˚C, $CHCl_3$): 7.08 (d, 2H, J = 9.00 Hz), 6.99 (d, 2H, J = 9.00 Hz), 4.86 (s, 4H), 3.84 (s, 3H), 3.80 (s, 12H), 3.26 (s, 4H). HRMS (ESI-TOF-MS) for $C_{31}H_{27}NO_{13}Na^+$ $[M+Na]^+$: Calc. 644.1380. Found. 644.1362.

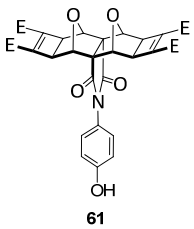

61

side product with solvent 9:1 THF/H_2O, **61**: ^{1}H NMR (600 MHz, $CDCl_3$, 20 ˚C, $CHCl_3$): 7.04 (d, 2H, J = 8.88 Hz), 6.93 (d, 2H, J = 8.88 Hz), 5.31 (s, 1H), 4.86 (s, 4H), 3.80 (s, 12H), 3.25 (s, 4H). HRMS (ESI-TOF-MS) for $C_{30}H_{25}NO_{13}Na^+$ $[M+Na]^+$: Calc. 630.1224. Found. 630.1203.

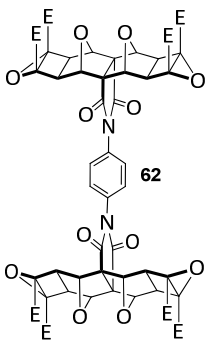

quad-epoxide I-piece linker, 62: Mitsudo I-piece linker **48** (300 mg, 0.27 mmol) was dissolved in dry CH_2Cl_2 (100 mL) under a nitrogen atmosphere and cooled to 0 °C. Anhydrous *tert*-butyl hydroperoxide in toluene [153] (3.3 M, 0.55 mL, 1.82 mmol, at least 5 eq.) was added and stirred for a further 10 mins at 0 °C, after which sublimed potassium *tert*-butoxide (70 mg, 0.62 mol, approx. 2 eq.) was added. The mixture was allowed to warm to room temperature over 30 minutes, and after stirring at room temperature for a further 3 hours, the mixture was diluted with CH_2Cl_2 (50 mL) and sodium sulfite (10 % aqueous solution, 10 mL) added with vigorous stirring for 15 minutes. The mixture was further diluted with CH_2Cl_2 (200 mL), washed with brine (200 mL), dried with Na_2SO_4, filtered, and the solvent removed *in vacuo*. This afforded a white powder (160 mg, 50 %), used in subsequent reactions without further purification. A sample was recrystallised from CH_2Cl_2/hexane for MS and melting point analysis. m.p. > 300 °C (partial decomposition 200 °C). ^{1}H NMR (600 MHz, CD_2Cl_2, 20 ˚C, CH_2Cl_2): 7.26 (s, 4H), 5.60 (s, 8H), 3.81 (s, 24H), 2.87 (s, 8H). ^{13}C NMR (150 MHz, CD_2Cl_2): 171.30, 163.63, 131.30, 127.36, 80.95, 70.86, 63.03, 53.35, 49.15. HRMS (ESI-TOF-MS) for $C_{54}H_{44}N_2O_{28}Na^+$ $[M+Na]^+$: Calc: 1191.1978. Found (two different samples): 1191.1984, 1191.2006.

free base tetra-porphyrin tweezer, 63:

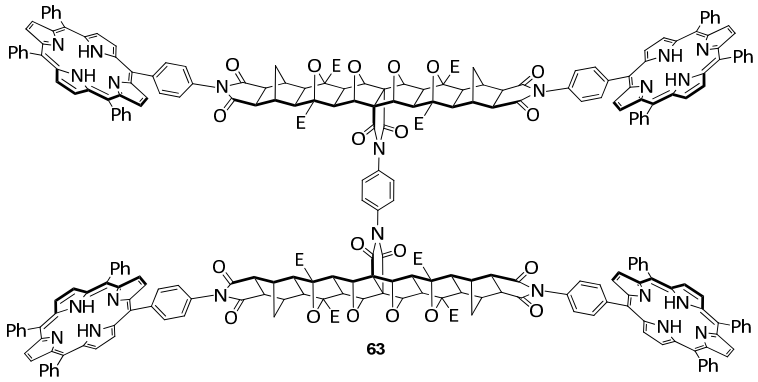

A suspension of quad-epoxide I-piece linker **62** (55 mg, 0.047 mmol) and *exo*-imide porphyrin receptor **18** (180 mg, 0.23 mmol, 4.9 eq.) in dry THF (3 mL) was subjected to microwave irradiation under the conditions specified in section 8.5. This procedure was repeated several times on a similar scale until 150 mg (0.128 mmol) epoxide had been reacted. The material from each reaction was combined, the solvent removed *in vacuo*, and the material purified by column chromatography

(silica, $CHCl_3$) to recover unreacted *exo*-imide porphyrin receptor **18**, after which the mobile phase was changed to 10 % THF/$CHCl_3$ and the strong porphyrin band collected. ^{1}H NMR of this material suggested the band contained a majority of the desired tetra-porphyrin adduct with small amounts of other porphyrin stoichiometries. The material was recrystallised twice from $CHCl_3$/MeOH to afford purple crystals of the pure tetra-porphyrin tweezer (88 mg, 16 %). ^{1}H NMR (600 MHz, $CHCl_3$, 20 ˚C, $CHCl_3$, approximately 0.8 mM): 8.83 (s, 32H), 8.30 (bs, 8H), 8.23-8.13 (m, 24H), 7.80 (s, 4H), 7.79-7.69 (m, 36H, 7.65 (bs, 8H), 4.94 (s, 8H), 4.02 (s, 24H), 2.96 (bs, 8H), 2.91 (s, 8H), 2.67 (s, 8H), 2.63 (d, 11.67 Hz, 4H), 2.36 (s, 8H), 1.28 (d, 11.67 Hz, 4H), -2.81 (s, 8H). HRMS (ESI-TOF-MS) for: $C_{266}H_{196}N_{22}O_{36}^{4+}$ $[M+4H]^{4+}$: Calc: 1068.3540. Found 1068.3566. $C_{266}H_{195}N_{22}O_{36}^{3+}$ $[M+3H]^{3+}$: Calc: 1424.1363. Found 1424.1392. $C_{266}H_{194}N_{22}O_{36}^{2+}$ $[M+2H]^{2+}$: Calc: 2135.7008. Found 2135.7022. UV-Vis ($CHCl_3$): λ_{max} (nm) = 419.0 (shoulder around 400), 515.2, 550.8, 590.0, 644.6.

Zn(II) tetra-porphyrin tweezer, 4:

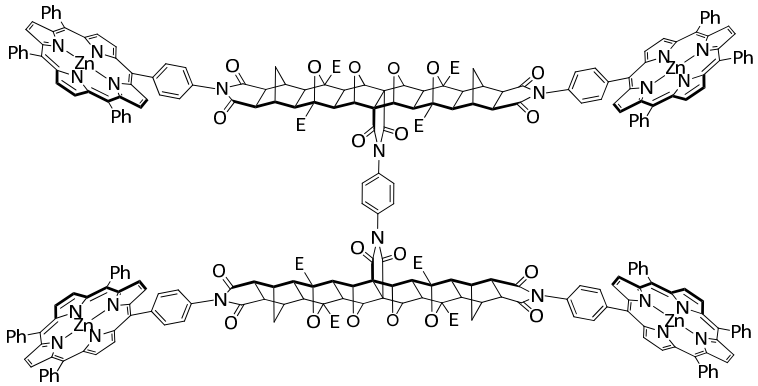

$Zn(OAc)_2.2H_2O$ (100 mg, 0.46 mol) in MeOH (10 mL) was refluxed with free base tetra-porphyrin tweezer **63** (88 mg, 0.021 mmol) in $CHCl_3$/MeOH (8+2 = 10 mL) for 2 hours, and worked up according to the procedure in section 8.7. The product was purified by column chromatography (silica, 10 % THF/$CHCl_3$), collecting the strong porphyrin band, and the solvent removed *in vacuo* to afford a purple powder (78 mg, 84 %). The material was recrystallised from $CDCl_3$/MeOH to afford purple crystals (65 mg, 70 %) for host-guest titrations. ^{1}H NMR (600 MHz, $CHCl_3$, 20 ˚C, $CHCl_3$, approximately 0.4 mM, concentration dependent): 8.93 (s, 32H), 8.31 (bs, 8H), 8.25-8.13 (m, 24H), 7.82-7.69 (m, 40H), 7.65 (bs, 8H), 4.94 (s, 8H), 4.02 (s, 24H), 2.96 (bs, 8H), 2.90 (bs, 8H), 2.67 (s, 8H), 2.62 (d, broad and low signal to noise, 4H), 2.36 (s, 8H), 1.27 (low signal to noise with overlapping impurity, 4H). UV-Vis ($CHCl_3$):

λ_{max} (nm) = 419.5 (shoulder around 400), 546.8, 585.3, $\varepsilon_{single\ porphyrin}$ = 5.65 x 10^5 $Lmol^{-1}cm^{-1}$.

8.8.5 Miscellaneous

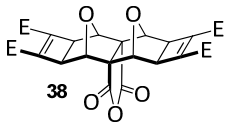

Mitsudo T-piece anhydride, 38 [157]: Using a similar method to [228], a solution of T-piece anhydride **37** [188][33] (1.0 g, 4.31 mmol), DMAD [149, 150] (1.3 g, approx. 2 eq., 9.15 mmol), and $[RuH_2(CO)(PPh_3)_3]$ [148] (0.2 g, 0.22 mmol, 5 mol-%) in toluene (20 mL) was heated at 80 °C for 4 days under a nitrogen atmosphere and protected from light, forming a white precipitate. The mixture was cooled, filtered, and the precipitate washed with EtOAc to afford a white powder (1.92 g, 86 %), used for subsequent synthesis without further purification. m.p. (decomposition) 272-276 °C. ^{1}H NMR (400 MHz, $CHCl_3$, 26 ˚C, $CHCl_3$): 4.83 (s, 4H), 3.81 (s, 12H), 3.27 (s, 4H). ^{13}C NMR (100 MHz, $CHCl_3$): 166.69, 160.04, 140.00, 77.74, 72.87, 52.48, 44.57. HRMS (ESI-TOF-MS) for $C_{24}H_{20}O_{13}Na^+$ $[M+Na]^+$: Calc: 539.0802. Found: 539.0801.

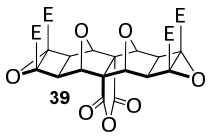

bis-epoxide T-piece anhydride, 39: Mitsudo T-piece anhydride **38** (1.0 g, 1.94 mmol) was dissolved in dry CH_2Cl_2 (100 mL) under a nitrogen atmosphere and cooled to 0 °C. Anhydrous *tert*-butyl hydroperoxide in toluene [153] (3.3 M, 1.47 mL, 4.85 mmol, 2.5 eq.) was added and stirred for a further 10 mins at 0 °C, after which sublimed potassium *tert*-butoxide (0.21 g, 1.87 mmol, ~1 eq.) was added. The mixture was allowed to warm to room temperature over 30 minutes, during which a white precipitate formed. After stirring at room temperature for a further 3 hours, sodium sulfite (10 % aqueous solution, 10 mL) was added with vigorous stirring for 15 minutes. The mixture was diluted with $CHCl_3$ (100 mL), washed with brine (200 mL), HCl (2M, 100 mL), NaOH (2M, 100 mL), H_2O (100 mL), dried with Na_2SO_4, filtered, and the solvent removed *in vacuo* to afford an off-white powder (0.52 g, 49 %). The material was purified by passage through a plug (silica, CH_2Cl_2), followed by column chromatography (silica, CH_2Cl_2 to remove impurity, followed by elution of product with THF). This afforded white and pale yellow flakes used for subsequent reactions. A sample was recrystallised from $CHCl_3$/toluene (white powder precipitates during rotatory evaporation) for MS and melting point analysis. m.p. (solvent of crystallisation loss 180-185 °C, then

[33] anhydride [188] from bis-carboxylic acid [185, 186].

partial decomposition) > 300 °C. ^{1}H NMR (400 MHz, $CDCl_3$, 26 ˚C, $CHCl_3$): 5.57 (s, 4H), 3.84 (s, 12H), 2.94 (s, 4H). ^{13}C NMR (150 MHz, $CDCl_3$): 165.98, 163.31, 80.84, 73.16, 62.68, 53.33, 48.57. HRMS (ESI-TOF-MS) for $C_{24}H_{20}O_{15}Na$ $[M+Na]^+$: Calc. 571.0700. Found. 571.0688.

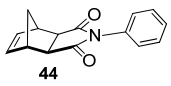
44

***exo*-imide phenyl, 44**: A solution of aniline (3.47 g, 37.3 mmol) in $CHCl_3$ (10 mL) was added dropwise to a solution of *cis*-5-norbornene-*exo*-2,3-dicarboxylic anhydride **8** [143] (3.05 g, 18.6 mmol) in $CHCl_3$ (30 mL) at 0 °C. The mixture was refluxed for 3 days under a nitrogen atmosphere and the solvent was removed *in vacuo*. The residue was redissolved in Ac_2O (50 mL), NaOAc (5.08 g, 37.3 mmol) added, and the mixture heated at 60 °C for 3 days under a nitrogen atmosphere, after which the Ac_2O was removed by distillation under reduced pressure. The mixture was redissolved in $CHCl_3$ (100 mL), washed with H_2O (2x 100 mL), HCl (2 M, 3x 100 mL), NaOH (2 M, 3x 100 mL), H_2O (100 mL), dried with Na_2SO_4, filtered, the solvent removed *in vacuo*, and recrystallised from EtOAc/hexane to afford beige crystals (3.17 g, 71 %). ^{1}H NMR (400 MHz, $CDCl_3$, 26 ˚C, $CHCl_3$): 7.49-7.42 (m, 2H), 7.41-7.35 (m, 1H), 7.28-7.22 (m, 2H), 6.34 (m, 2H), 3.39 (m, 2H), 2.85 (m, 2H), 1.61 (d, 1H, J = 9.92 Hz), 1.48 (d, 1H, J = 9.92 Hz). HRMS (ESI-TOF-MS) for $C_{15}H_{14}NO_2^+$ $[M+H]^+$: Calc. 240.1025. Found. 240.1030.

phenyl T-piece anhydride: A suspension of bis-epoxide T-piece anhydride **39** (50 mg, 0.091 mmol) and *exo*-imide phenyl **44** (44 mg, 0.18 mmol, 2 eq.) in dry THF (2 mL) was subjected to microwave irradiation under the conditions specified in section 8.5 (two different samples, 180 °C/2 hrs, and 140 °C/50 minutes).

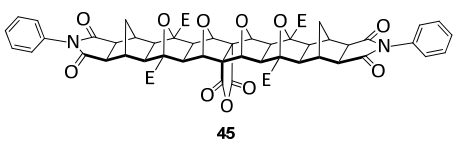
45

bis-phenyl T-piece anhydride, **45**: For the 180 °C/2 hrs sample, the solvent was removed *in vacuo* and the solid suspended in $CHCl_3$ (50 mL) and stirred for 10 minutes. The solid was filtered and washed with $CHCl_3$ (3x 50 mL), and the solid purified by passage through a plug (silica, loaded as a suspension in $CHCl_3$ to remove impurity, followed by THF [partially soluble] to elute the product as an opaque solution). A white powder was recovered after removal of the solvent *in vacuo*, and was identified as the bis-phenyl adduct by ^{1}H NMR (soluble DMSO-d_6). ^{1}H NMR (600 MHz, DMSO-d_6, 20 ˚C, DMSO): 7.47-7.42 (m, 4H), 7.42-7.37 (m, 2H), 7.22-7.17 (m, 4H), 5.01 (s, 4H), 3.86 (s, 12H), 2.77 (s, 4H), 2.65 (s, 4H), 2.53 (s, 4H), 2.33 (s, 4H), 2.12 (d, 2H, J = 11.1 Hz), 0.91 (d, 2H, J = 11.1 Hz).

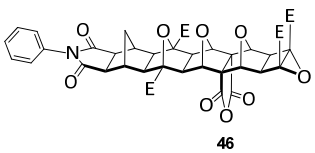

mono-phenyl T-piece epoxide anhydride[34] **46**: For the 140 °C/50 minutes sample, the solvent was removed *in vacuo* and the solid suspended in $CHCl_3$ (50 mL) and stirred for 10 minutes. The solid was filtered and washed with $CHCl_3$ (3x 50 mL), and the filtrate purified by column chromatography (silica, 5 % THF/$CHCl_3$) to recover a white powder, identified as the mono-phenyl adduct by ^{1}H NMR (soluble DMSO-d_6 or $CDCl_3$). ^{1}H NMR (600 MHz, DMSO-d_6, 20 ˚C): 7.50-7.42 (m, 2H), 7.42-7.37 (m, 1H), 7.22-7.17 (m, 2H), 5.57 (s, 2H), 5.21 (s, 2H), 3.87 (s, 6H), 3.72 (s, 6H), 2.87 (s, 2H), 2.77 (s, 2H), 2.65 (s, 2H), 2.54 (s, 2H), 2.33 (s, 2H), 2.14 (d, 1H, J = 10.95 Hz), 0.91 (d, 1H, J = 10.95 Hz).

bis-porphyrin T-piece anhydride, 40:

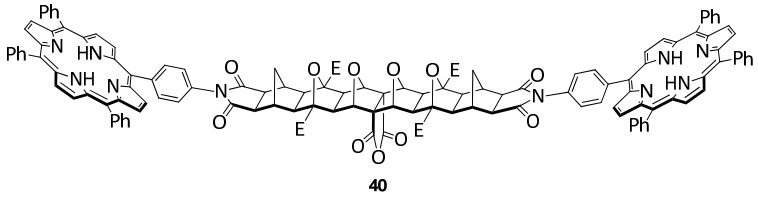

A suspension of bis-epoxide T-piece anhydride **39** (50 mg, 0.09 mmol) and *exo*-imide porphyrin receptor **18** (166 mg, 0.21 mmol, ~2 eq.) in dry THF (3 mL) was subjected to microwave irradiation under the conditions specified in section 8.5, forming a purple precipitate. The precipitate was filtered, and washed with THF, $CHCl_3$, CH_3CN, toluene, EtOAc, MeOH, and hexane to afford a purple solid (130 mg, 68 %), which exhibited extremely poor solubility in many solvents ($CHCl_3$, CH_3CN, EtOAc, THF, acetone, DMSO, toluene, pyridine) with the exception of acids (TFA, H_2SO_4). No NMR or UV-Vis data obtained (insoluble). m.p. > 300 °C. HRMS (ESI-TOF-MS) for $C_{130}H_{96}N_{10}O_{19}^{2+}$ $[M+2H]^{2+}$: Calc: 1050.3421. Found 1050.3432.

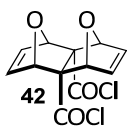

T-piece bis-oxa bis-acid chloride, 42: Using a modified procedure [67, 187], bis-oxa bis-carboxylic acid **36** (7.0 g, 28 mmol, crystals ground to fine powder) was suspended in dry $CHCl_3$ (700 mL, does not dissolve) in a two-necked flask and degassed with argon for 30 minutes. PCl_5 (11.65 g, 56 mol, 2 eq.) was added and stirred at room temperature for 6-12 hours under a continual flow of argon to remove HCl generated as the reaction proceeded (via thick walled tubing

[34] structure not confirmed, however mono-epoxide functionality has been previously observed to be conserved in a mono-ACE reaction on a diepoxide substrate (accurate mass spectrometry) [78].

from the second neck of the flask into a beaker of H_2O, tubing inspected regularly for deterioration and replaced as necessary). The mixture became soluble during the reaction, changing from a white opaque mixture to a pale yellow/orange semi-transparent solution. Reaction progress was monitored by NMR, and if necessary, was continued overnight, after installing new tubing and switching to nitrogen gas. The reaction mixture was filtered to remove any solids, and the pale yellow/orange filtrate was reduced in volume by rotary evaporation below 50 °C until a beige precipitate formed (hexane added to aid precipitation if necessary). This precipitate was filtered and temporarily stored under vacuum or inert atmosphere. The filtrate was further reduced in volume to precipitate further product, and this process repeated until product was no longer precipitated as a homogenous powder. The precipitate was combined, washed with hexane (3x 100 mL), and dried *in vacuo* to afford a beige powder (4.3 g, 54 %), and stored under a nitrogen atmosphere[35]. IR (KI): ~1808 cm^{-1}. ^1H NMR (400 MHz, $CDCl_3$, 20 ˚C, $CHCl_3$): 6.81 (m, 4H), 5.35 (m, 4H). ^1H NMR (400 MHz, acetone-d_6, 20 ˚C): 6.90 (m, 4H), 5.46 (m, 4H). ^{13}C NMR (100 MHz, acetone-d_6)[36]: 168.40, 141.28, 85.55, one of either 83.03 or 82.13.

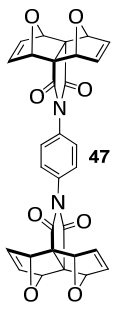

freely rotating non-Mitsudo I-piece, 47: Using an alternative method to [118], *p*-phenylenediamine **9** (0.188 g, 1.74 mmol) was dissolved in dry degassed THF (50 mL) under an argon atmosphere. LiHMDS[37] (900 µL, 0.9 mmol, <<1 eq., 1 M in THF, Sigma-Aldrich) was added dropwise from a syringe with stirring over 10-15 seconds, giving a pale yellow solution. After 30 minutes, T-piece bis-acid chloride **42** [67, 187] (1.0 g, 3.48 mmol, 2 eq.) was added in portions as a solid, immediately forming a precipitate. Although no change was observed after 1 hour, the mixture was allowed to stir overnight for good measure, and the precipitate filtered and washed with Et_2O to afford a red/brown powder (0.46 g, 0.78 mmol, 86 %, NMR consistent with amic acid). The powder was subjected to ring closing conditions as per [67] using the following procedure. The powder was suspended in dry THF (50 mL) under an argon

[35] The product darkened during storage (brown/black within weeks), and could be purified by the following method: dissolve in $CHCl_3$, filter to remove solids, hexane added to filtrate until a black precipitate formed, filter, product remains in the yellow/orange filtrate).

[36] Differences in ^{13}C NMR resonance assignment compared to [187].

[37] Personal communication with either Louis Barriault or P. Andrew Evans [193].

atmosphere, and HOBt (at least 0.32 g, 2.33 mmol, at least 3 eq.) was added with stirring. After 5 minutes, DCC (at least 0.48 g, 2.33 mmol, at least 3 eq.[38]) and Et_3N (1.1 mL, 7.8 mmol, ~10 eq.) were added in quick succession and the mixture stirred at room temperature for 4 days (ring closing halfway), then at 50 °C for a further 2 days. The mixture was cooled and filtered, and the solids washed with hexane (100 mL), acetone (100 mL), CH_3CN (100 mL), EtOH (100 mL), and hexane (100 mL) to remove impurity (product sparingly soluble). The remaining solid was dissolved in CH_2Cl_2 (200 mL) and washed with HCl (2 M, 100 mL) NaOH (2 M, 100 mL), H_2O (100 mL), dried with Na_2SO_4, filtered, and the solvent removed *in vacuo* to afford a beige powder. m.p. > 300°C. ^{1}H NMR (600 MHz, $CDCl_3$, 20 ˚C, $CHCl_3$): 7.12 (s, 4H), 6.73 (s, 8H), 5.35 (s, 8H). ^{13}C NMR (150 MHz, $CHCl_3$): 172.91, 139.37, 131.28, 126.69, 81.73, 69.35. HRMS (ESI-TOF-MS) for $C_{30}H_{20}N_2O_8Na^+$ $[M+Na]^+$: Calc: 559.1117. Found: 559.1123. Single crystal grown from DMSO by slow evaporation for X-ray diffraction. X-Ray crystallographic data will be uploaded to The Cambridge Crystallographic Data Centre (CCDC) in the near future. A summary is provided in Appendix 4.

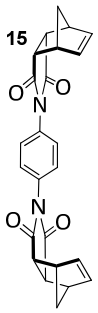

freely rotating *endo*- non-Mitsudo linker, 15: A solution of *cis*-5-norbornene-*endo*-2,3-dicarboxylic anhydride **7** [142] (0.97 g, 5.9 mmol) and sublimed *p*-phenylenediamine **9** (0.32 g, 2.96 mmol) in $CHCl_3$ (50 mL) was refluxed under an nitrogen atmosphere for 3 days. The $CHCl_3$ was removed *in vacuo*, the mixture redissolved in Ac_2O (25 mL), NaOAc (1.60 g, 11.76 mmol) added, and the solution heated at 60 °C under a nitrogen atmosphere for a further 5 days. The mixture was cooled, poured on ice/water (100 mL), extracted in $CHCl_3$ (3x 100 mL), washed with H_2O (2x 100 mL), and dried with Na_2SO_4. The $CHCl_3$ was removed *in vacuo*, and the product precipitated from residual Ac_2O with hexane. The precipitate was filtered, washed with hexane, and recrystallised from EtOAc/hexane to afford a white powder (0.60 g, 51 %). m.p > 300 °C (partial decomposition). ^{1}H NMR (600 MHz, $CHCl_3$, 20 ˚C, $CHCl_3$): 7.23 (s, 4H), 6.23 (s, 4H), 3.49 (s, 4H), 3.42 (s, 4H), 1.78 (d, 2H , J = 8.58 Hz), 1.60 (d, 2H, J = 8.58 Hz). ^{13}C NMR (150 MHz, $CHCl_3$): 176.55, 134.74, 131.72, 127.10, 52.38, 45.89, 45.68. HRMS (ESI-TOF-MS) for $C_{24}H_{20}N_2O_4Na^+$ $[M+Na]^+$: Calc. 423.1321. Found. 423.1318.

[38] An excess of warm DCC was added as a liquid.

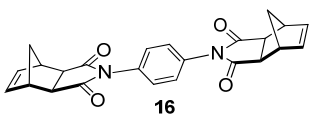

16

freely rotating *exo*- non-Mitsudo linker, 16: Using a modified method [154, 155], a solution of *cis*-5-norbornene-*exo*-2,3-dicarboxylic anhydride **8** [143] (0.97 g, 5.9 mmol) and sublimed *p*-phenylenediamine **9** (0.32 g, 2.96 mmol) in $CHCl_3$ (50 mL) was refluxed under an nitrogen atmosphere for 3 days. The $CHCl_3$ was removed *in vacuo*, the mixture redissolved in Ac_2O (25 mL), NaOAc (1.60 g, 11.76 mmol) added, and the solution heated at 60 °C under a nitrogen atmosphere for a further 5 days. The mixture was cooled, poured on ice/water (100 mL), extracted in $CHCl_3$ (3x 100 mL), washed with H_2O (2x 100 mL), and dried with Na_2SO_4. The $CHCl_3$ was removed *in vacuo*, and the product precipitated from residual Ac_2O with hexane. The precipitate was filtered, washed with hexane, and recrystallised from EtOAc/hexane to afford a white powder (0.65 g, 55 %). m.p > 300 °C. ^{1}H NMR (600 MHz, $CDCl_3$, 20 ˚C, $CHCl_3$): 7.42 (s, 4H), 6.35 (m, 4H), 3.41 (m, 4H), 2.86 (m, 4H), 1.62 (d, 2H, J = 9.96 Hz), 1.45 (d, 2H, J = 9.96 Hz). ^{13}C NMR (150 MHz, $CHCl_3$): 176.79, 138.15, 131.83, 126.98, 47.98, 46.01, 43.14. HRMS (ESI-TOF-MS) for $C_{24}H_{20}N_2O_4Na^+$ $[M+Na]^+$: Calc. 423.1321. Found. 423.1308.

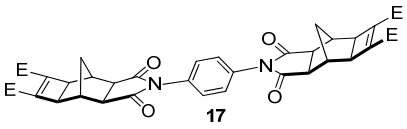

17

freely rotating *exo*- Mitsudo linker, 17: A solution of *exo*-cyclobutene diester anhydride **20** (4.00 g, 13.1 mmol) and sublimed *p*-phenylenediamine **9** (0.706 g, 6.53 mmol) in dry DMF (50 mL) was heated at 80 °C under an nitrogen atmosphere for 5 days, during which a grey precipitate formed. The precipitate was filtered, washed with $CHCl_3$, redissolved in Ac_2O (250 mL), NaOAc (7.11 g, 52.2 mmol) added, and the solution heated at 120 °C under a nitrogen atmosphere for a further 5 days, during which a precipitate formed. The precipitate was filtered, redissolved in $CHCl_3$ (200 mL), washed with H_2O (2x 200 mL), dried with Na_2SO_4, filtered, and the solvent removed *in vacuo*. The solid was redissolved in CH_2Cl_2 (100 mL), filtered through a pad of cotton wool, and the solvent removed *in vacuo* to afford a solid (1.54 g, 34 %), used for subsequent synthesis without further purification. m.p. > 300 °C (partial decomposition 250 °C). ^{1}H NMR (400 MHz, $CDCl_3$, 26 ˚C, $CHCl_3$): 7.42 (s, 4H), 3.81 (s, 12H), 2.94 (s, 4H), 2.93 (s, 4H), 2.79 (s, 4H), 1.54 (d, 2H, J = 12.60 Hz), 1.19 (d, 2H, J = 12.60 Hz). HRMS (ESI-TOF-MS) for $C_{36}H_{32}N_2O_{12}Na^+$ $[M+Na]^+$: Calc: 707.1853. Found: 707.1845.

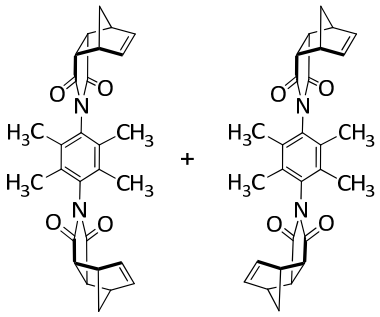

syn- + *anti-* **30**

restricted rotation *endo*- non-Mitsudo linker, 30 (*syn*- + *anti*- mixture): A solution of *cis*-5-norbornene-*endo*-2,3-dicarboxylic anhydride **7** [142] (3.0 g, 18.3 mmol) and 2,3,5,6-tetramethyl-*p*-phenylenediamine **26** (1.5 g, 9.1 mmol, 0.5 eq., Sigma-Aldrich, used as purchased) in degassed dry DMF (50 mL) was heated at 80 °C under an argon atmosphere for 3 days. The DMF was removed by distillation under reduced pressure, and the remaining solids washed with hexane. The resulting white powder was redissolved in Ac_2O (50 mL), NaOAc (5.0 g, 36.7 mmol) added, and the mixture heated at 80 °C under a nitrogen atmosphere for a further 3 days. Any precipitate was filtered, and the precipitate and Ac_2O filtrate separately purified. The precipitate was washed with hexane (2x 100 mL), redissolved in $CHCl_3$ (100 mL), washed with H_2O (2x 100 mL), dried with Na_2SO_4, and the solvent removed *in vacuo* to afford a solid product. For the Ac_2O filtrate, the Ac_2O was removed by distillation under reduced pressure, the solid washed with hexane (2x 100 mL), redissolved in $CHCl_3$ (100 mL), washed with H_2O (2x 100 mL), dried with Na_2SO_4, and the solvent removed *in vacuo* to afford a solid. Although the *syn*- and *anti*- isomers could not be distinguished by their ^1H NMR (near identical resonances for the CH_3 pairs), the ^{13}C NMR phenyl and CH_3 substituent resonances for the precipitate and filtrate show that each contains a majority of the opposite isomer. *Precipitate*: ^1H NMR (600 MHz, $CDCl_3$, 20 ˚C, $CHCl_3$): 6.31 (m, 4H), 3.51 (m, 8H), 1.95 (s, 6H), 1.91 (s, 6H), 1.81 (d, 2H, J = 8.76 Hz), 1.64 (d, 2H, J = 8.76 Hz). ^{13}C NMR (150 MHz, $CHCl_3$): 176.35, 135.77, 133.21, 132.41, 131.68, 53.07, 46.92, 45.29, 16.22 (CH_3), 15.46 (CH_3). *Filtrate*: ^1H NMR (600 MHz, $CDCl_3$, 20 ˚C, $CHCl_3$): 6.31 (m, 4H), 3.50 (m, 8H), 1.94 (s, 6H), 1.91 (s, 6H), 1.81 (d, 2H, J = 8.79 Hz), 1.63 (d, 2H, J = 8.79 Hz). ^{13}C NMR (150 MHz, $CHCl_3$): 176.32, 135.75, 133.31, 132.26, 131.65, 53.05, 46.90, 45.27, 16.13 (CH_3), 15.54 (CH_3). A sample of the isomer dissolved in the filtrate was crystallised by slow evaporation from CH_3CN for melting point and MS analysis. m.p. > 300 °C (possible loss of solvent of crystallisation loss, partial decomposition). HRMS (ESI-TOF-MS) for $C_{28}H_{28}N_2O_4Na^+$ $[M+Na]^+$: Calc: 479.1947. Found: 479.1954.

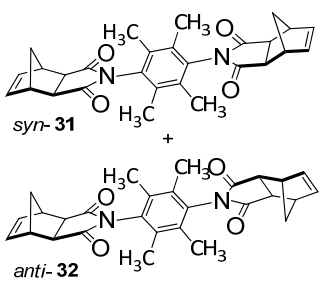

restricted rotation *exo*- non-Mitsudo linker, *syn*- 31 + *anti*- 32: A solution of *cis*-5-norbornene-*exo*-2,3-dicarboxylic anhydride **8** [143] (3.0 g, 18.3 mmol) and 2,3,5,6-tetramethyl-*p*-phenylenediamine **26** (1.5 g, 9.1 mmol, 0.5 eq., Sigma-Aldrich, used as purchased) in degassed dry DMF (50 mL) was heated at 80 °C under an argon atmosphere for 3 days, during which a white precipitate formed. The mixture was filtered, washed with hexane, the solid redissolved in Ac_2O (50 mL), NaOAc (5.0 g, 36.7 mmol) added, and the mixture heated at 80 °C under a nitrogen atmosphere for a further 3 days. Any precipitate was filtered, and the precipitate and Ac_2O filtrate separately purified. The precipitate was washed with hexane (2x 100 mL), redissolved in $CHCl_3$ (100 mL), washed with H_2O (2x 100 mL), dried with Na_2SO_4, and the solvent removed *in vacuo* to afford a solid. For the Ac_2O filtrate, the Ac_2O was removed by distillation under reduced pressure, the solid washed with hexane (2x 100 mL), redissolved in $CHCl_3$ (100 mL), washed with H_2O (2x 100 mL), dried with Na_2SO_4, and the solvent removed *in vacuo* to afford a solid. ^{1}H NMR of the filtrate and precipitate show that each contains a majority of the opposite isomer, *syn*- and *anti*-, distinguished by outer and inner pairs of non-equivalent CH_3 phenyl substituent resonances. Additionally, XRD of single crystals of both the filtrate and precipitate isomers allowed their assignment as *syn*- and *anti*- respectively.

syn- (filtrate, outer CH_3) **31**: m.p. > 300 °C (crystals crack, partial decomposition). ^{1}H NMR (600 MHz, $CDCl_3$, 20 ˚C, $CHCl_3$): 6.34 (m, 4H), 3.42 (m, 4H), 2.91 (s, 4H), 2.051 (s, 6H), 1.967 (s, 6H), 1.68 (m, 4H). ^{13}C NMR (150 MHz, $CHCl_3$): 176.72, 138.03, 133.08, 132.67, 131.86, 48.47, 45.29, 43.80, 15.90, 15.63. HRMS (ESI-TOF-MS) for $C_{28}H_{28}N_2O_4Na^+$ $[M+Na]^+$: Calc: 479.1947. Found: 479.1957. Single crystal grown from CH_3CN by slow evaporation for X-ray diffraction. X-Ray crystallographic data will be uploaded to The Cambridge Crystallographic Data Centre (CCDC) in the near future. A summary is provided in Appendix 4.

anti- **32** *(precipitate, inner CH_3)*: m.p. > 300 °C (crystals transition from clear to white 195-205 °C, partial decomposition by 300 °C). ^{1}H NMR (600 MHz, $CDCl_3$, 20 ˚C, $CHCl_3$): 6.34 (m, 4H), 3.42 (m, 4H), 2.91 (s, 4H), 2.039 (s, 6H), 1.973 (s, 6H), 1.67 m, 4H). ^{13}C NMR (150 MHz, $CHCl_3$): 176.70, 138.01, 133.14, 132.58, 131.84, 48.46, 45.28, 43.78, 15.99, 15.50. HRMS (ESI-TOF-MS) for $C_{28}H_{28}N_2O_4Na^+$

$[M+Na]^+$: Calc: 479.1947. Found: 479.1949. Single crystal grown from CH_3CN by slow evaporation for X-ray diffraction, co-crystallised with ~6% epoxide. X-Ray crystallographic data will be uploaded to The Cambridge Crystallographic Data Centre (CCDC) in the near future. A summary is provided in Appendix 4.

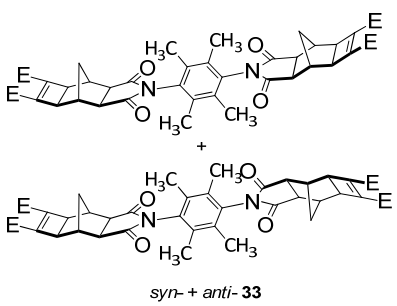

syn- + *anti-* **33**

restricted rotation *exo*- Mitsudo linker, 33 (*syn*- + *anti*- mixture): A solution of *exo*-cyclobutene diester anhydride **20** (1.0 g, 3.27 mmol) and 2,3,5,6-tetramethyl-*p*-phenylenediamine **26** (0.27 g, 1.64 mmol, 0.5 eq., Sigma-Aldrich, used as purchased) in degassed DMSO (15 mL) was heated at 80 °C under an argon atmosphere for 3 days. The mixture was cooled, and EtOAc added to cause precipitation. If this did not cause precipitation, the DMSO was removed by distillation under reduced pressure. The mixture was redissolved in Ac_2O (50 mL), NaOAc (1.0 g, 7.35 mmol) added, and the solution heated at 80 °C under a nitrogen atmosphere for a further 3 days, during which a precipitate formed. Preliminary ^1H NMR of the reaction mixture suggested two isomers, *syn*- and *anti*-, distinguished by outer (a) and inner (b) pairs of non-equivalent CH_3 phenyl substituent resonances. The precipitate was filtered, washed with hexane (100 mL), redissolved in $CHCl_3$ (100 mL), washed with H_2O (2x 100 mL), dried with Na_2SO_4, and the solvent removed *in vacuo* to afford a solid. m.p. > 300 °C (crystal movement at 175 and 200 °C, partial decomposition 250-300 °C). ^1H NMR (600 MHz, $CDCl_3$, 20 ˚C, $CHCl_3$): as a mixture of isomers 3.80 (s, 12H), 2.95 (s, 4H), 2.93 (s, 4H), 2.84 (s, 4H), 2.04 (a) + 2.02 (b) (both singlets, combined integration 6H), 1.96 (b) + 1.94 (a) (both singlets, combined integration 6H), 1.59 (d, 2H, J = 8.22 Hz), 1.40 (d, 2H, J = 8.22 Hz). ^{13}C NMR (150 MHz, $CHCl_3$): 176.54, 160.86, 142.19, 133.19 (b) 133.14 (a), 132.58 (a) 132.52 (b), 131.85, 52.25, 47.98, 46.00, 37.48, one of either 26.73 or 26.43 (other is impurity), 16.06 (b) 16.00 (a), 15.52 (a), 15.47 (b). HRMS (ESI-TOF-MS) for $C_{40}H_{40}N_2O_{12}Na^+$ $[M+Na]^+$: Calc: 763.2479. Found: 763.2456.

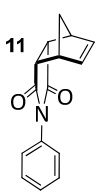

***endo*- non-Mitsudo imide phenyl, 11**: Using a different procedure to [152, 229], a solution of aniline (8.0 g, 85.9 mmol) in $CHCl_3$ (25 mL) was added dropwise to a solution of *cis*-5-norbornene-*endo*-2,3-dicarboxylic anhydride **7** [143] (7.05 g, 42.9 mmol) in $CHCl_3$ (75 mL) at 0 °C. The mixture was refluxed for 3 days under a nitrogen atmosphere and the solvent was removed *in vacuo*. The residue was redissolved in Ac_2O (50 mL), NaOAc (11.7 g, 86 mmol)

added, and the mixture heated at 60 °C for 3 days under a nitrogen atmosphere, after which the Ac_2O was removed by distillation under reduced pressure. The mixture was redissolved in $CHCl_3$ (100 mL), washed with H_2O (2x 100 mL), HCl (2 M, 3x 100 mL), NaOH (2 M, 3x 100 mL), H_2O (100 mL), dried with Na_2SO_4, filtered, the solvent removed *in vacuo*, and recrystallised from EtOAc/hexane to afford a white crystalline powder (8.92 g, 87 %). ^{1}H NMR (400 MHz, $CDCl_3$, 26 ˚C, $CHCl_3$): 7.45-7.38 (m, 2H), 7.38-7.31 (m, 1H), 7.16-7.09 (m, 2H), 6.25 (m, 2H), 3.48 (m, 2H), 3.43-3.37 (m, 2H), 1.76 (d, 1H, J = 8.8 Hz), 1.58 (d, 1H, J = 8.8 Hz). HRMS (ESI-TOF-MS) for $C_{15}H_{14}NO_2^+$ $[M+H]^+$: Calc. 240.1025. Found. 240.1027.

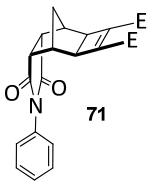

71

***endo*- Mitsudo imide phenyl, 71**: A solution of *endo*- non-Mitsudo imide phenyl **11** (4.0 g, 16.7 mmol), DMAD [149, 150] (4.74 g, 2 eq., 33.4 mmol), and $[RuH_2(CO)(PPh_3)_3]$ [148] (0.76 g, 0.83 mmol, 5 mol-%) in toluene (100 mL) was heated at 100 °C for 10 days[39] under a nitrogen atmosphere and protected from light, forming a precipitate. The mixture was cooled, filtered, and the precipitate washed with hexane to afford an off-white powder (3.77 g, 59 %). ^{1}H NMR (400 MHz, $CDCl_3$, 26 ˚C, $CHCl_3$): 7.50-7.44 (m, 2H), 7.43-7.37 (m, 1H), 7.24-7.20 (m, 2H), 3.78 (s, 6H), 3.41-3.38 (m, 2H), 3.01 (s, 2H), 2.98-2.94 (m, 2H), 1.82 (d, 1H, J = 11.50 Hz), 1.56 (d, 1H, J = 11.50 Hz). ^{13}C NMR (100 MHz, $CHCl_3$): 176.00, 160.78, 141.30, 131.73, 129.42, 129.01, 126.69, 52.21, 47.66, 42.70, 36.86, one of either 34.41 or 48.89 (weak signals). HRMS (ESI-TOF-MS) for $C_{21}H_{19}NO_6Na^+$ $[M+Na]^+$: Calc. 404.1110. Found. 404.1113.

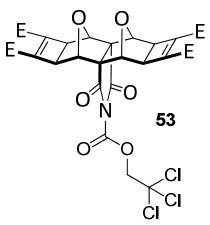

53

troc-protected Mitsudo T-piece, 53: Using a modified procedure [106, 230], Mitsudo T-piece imide **49** (400 mg, 0.78 mmol) was dissolved in dry DMF (15 mL), NaH (80 mg, 2 mmol, 2-3 eq.) added, and stirred for 10 minutes under a nitrogen atmosphere. 2,2,2-trichloroethoxycarbonyl chloride (300 μL, 2.18 mmol, 2-3 eq.) was added dropwise over 15 seconds, during which a precipitate quickly formed. The mixture was stirred for 4 hours under nitrogen atmosphere at room temperature, after which it was cautiously poured onto H_2O (100 mL). The mixture was extracted with $CHCl_3$ (2x 100 mL), dried with Na_2SO_4, and the $CHCl_3$ removed *in vacuo*, with residual DMF remaining. The solution was diluted with $CHCl_3$ (10 mL), and hexane added dropwise until a brown precipitate formed. The precipitate was filtered and

[39] 3-5 days most likely to be sufficient.

purified by column chromatography (silica, 20 % THF/$CHCl_3$), collecting the band at the solvent front. The solvent was removed *in vacuo*, redissolved in $CHCl_3$ (1 mL), and hexane added dropwise to precipitate the product as a solid, impure with 20 % Mitsudo T-piece imide starting material **49** by ^{1}H NMR. HRMS (ESI-TOF-MS) for $C_{27}H_{22}NO_{14}Cl_3Na^+$ $[M+Na]^+$: Calc. 712.0004. Found. 711.9997.

Mitsudo T-piece phenyl imide, 56:

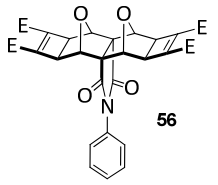

56

Method A - microwave/aryl halide/Cu(0): Using a modified procedure (N-aryl imides from succinimide/phthalimide and mono-halo aryl) [196], Mitsudo T-piece imide **49** (100 mg, 0.19 mmol), activated elemental copper [231][40] (100 mg, 1.57 mmol, at least 5 eq.), and iodobenzene **55** (500 μL, 0.44 mmol, solvent/excess) were suspended in a 10 mL microwave vessel. The microwave was operated in variable power (dynamic) mode with the following parameters: temperature 150 °C, power 300 W (automatically modulated around the set temperature), stirring high, compressed air cooling (PowerMAX) on. The sample was held at this temperature for 10 minutes, and this repeated for 3-4 cycles, removing the sample in between runs to check the vessel integrity, ensure thorough mixing, and recharge with additional iodobenzene (500 μL) as necessary if the contents had thickened to a paste or solidified. The mixture was diluted with EtOAc (100 mL), filtered to remove Cu(0), and any solids washed with $CHCl_3$ (100 mL). The combined EtOAc/$CHCl_3$ filtrate was washed with KOH (2 M, 2x 100 mL), H_2O (2x 100 mL), dried with Na_2SO_4, and the solvents removed *in vacuo*. The residual iodobenzene was diluted with hexane to precipitate the product, which was filtered and washed with hexane to afford a white powder. ^{1}H NMR (600 MHz, $CDCl_3$, 20 ˚C, $CHCl_3$): 7.53-7.48 (m, 2H), 7.48-7.44 (m, 1H), 7.20-7.16 (m, 2H), 4.87 (s, 4H), 3.80 (s, 12H), 3.28 (s, 4H). ^{13}C NMR (150 MHz, $CHCl_3$): 171.92, 160.17, 140.23, 130.70, 130.30, 129.73,

[40] prior to precipitation of copper, the zinc dust was pre-treated with 2 % hydrochloric acid according to [225] to ensure it met the oxide-free requirements of [231]. Freshly precipitated elemental copper was dried *in vacuo*, and not at 100 °C as per [231]. The solid appeared as a brown powder, and was not particularly metallic/lustrous.

126.22, 77.56, 70.36, 52.42, 44.89. HRMS (ESI-TOF-MS) for $C_{30}H_{25}NO_{12}Na^+$ $[M+Na]^+$: Calc. 614.1274. Found. 614.1279.

Method B - phenylboronic acid/Cu(II)/air: Using the method developed from [197] for the Mitsudo I-piece linker **48** described previously, the reaction was undertaken on Mitsudo T-piece imide **49** using phenylboronic acid. The crude sample mixture contained the same ^{1}H NMR resonances assigned to product from Method A.

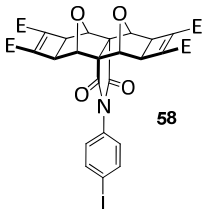

58

Mitsudo T-piece 4-iodophenyl imide, 58: Using a modified procedure [196], Mitsudo T-piece imide **49** (100 mg, 0.19 mmol), activated elemental copper [231] (100 mg, 1.57 mmol), and 1,4-diiodobenzene **57** (500 mg, 1.52 mmol, excess) were suspended in solvent (EtOAc, 1 mL) in a 10 mL microwave vessel. The microwave was operated in variable power (dynamic) mode with the following parameters: temperature 120-150 °C, power 300 W (automatically modulated around the set temperature), stirring high, compressed air cooling (PowerMAX) on. The mixture was microwaved at 120 °C for 1 hr, after which further activated copper (100 mg, 1.57 mmol) was added, and microwaved for an additional 1.5 hrs (total 2.5 hrs). The mixture was charged with toluene (1 mL), and microwaved at 150 °C for an additional 1 hr (total 3.5 hrs). NMR after 3.5 hrs total reaction time indicated 30 % conversion to the coupled adduct. Microwaving was continued for a total of 12 hrs, after which NMR indicated approximately 66 % conversion to the coupled adduct. The yellow/brown liquid was filtered, the solids washed with toluene (50 mL), EtOAc (50 mL), $CHCl_3$ (50 mL), the solvent removed from the filtrate *in vacuo*, and the material purified by column chromatography (silica, 20 % EtOAc/$CHCl_3$) to afford a white powder (20 mg, 14 %). ^{1}H NMR (600 MHz, $CDCl_3$, 20 ˚C, $CHCl_3$): 7.83 (d, 2H, J = 8.61 Hz), 6.95 (d, 2H, J = 8.61 Hz), 4.86 (s, 4H), 3.79 (s, 12H), 3.22 (s, 4H). HRMS (ESI-TOF-MS) for $C_{30}H_{24}NO_{12}INa^+$ $[M+Na]^+$: Calc. 740.0241. Found. 740.0251.

9. Appendix 1 - Tweezer Characterisation Data

Accurate Mass spectrometry was conducted by Dr Daniel Jardine (Flinders Analytical) and Dr Sally Duck (Monash University).

NMR annotations

S = solvent

I = impurity

G = grease

W = H_2O

A = acetone

SM = starting material

C = $CDCl_3$

D = DMSO-d_6

M = CD_2Cl_2

9.1 Freebase Freely Rotating Tweezer **23**

9.1.1 ^{1}H NMR

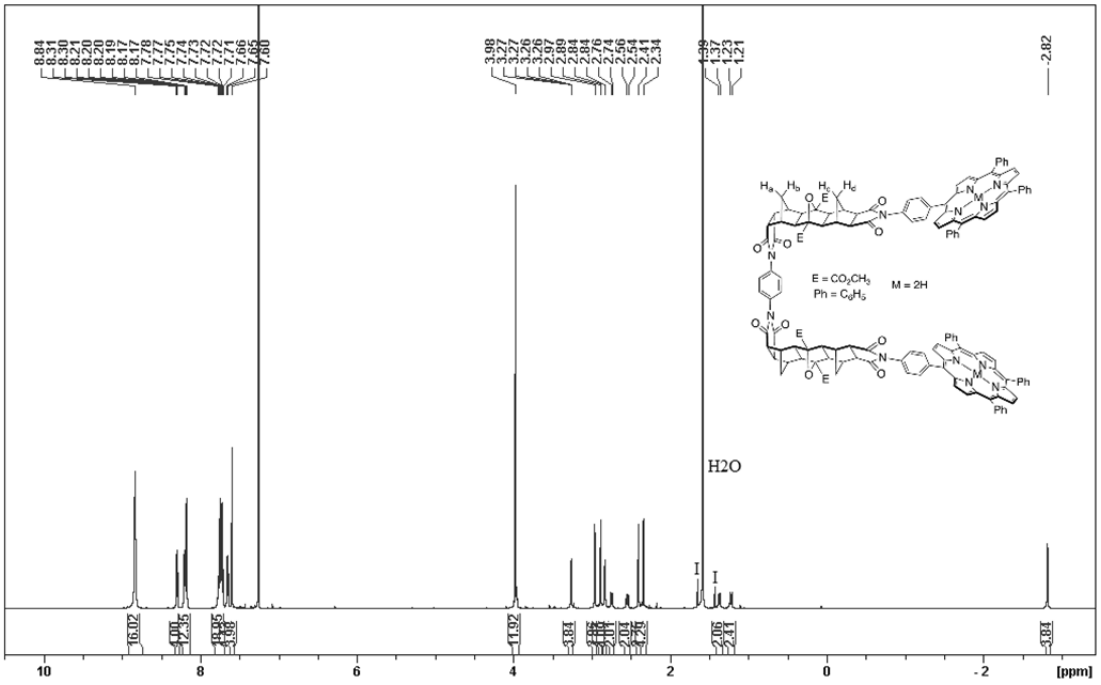

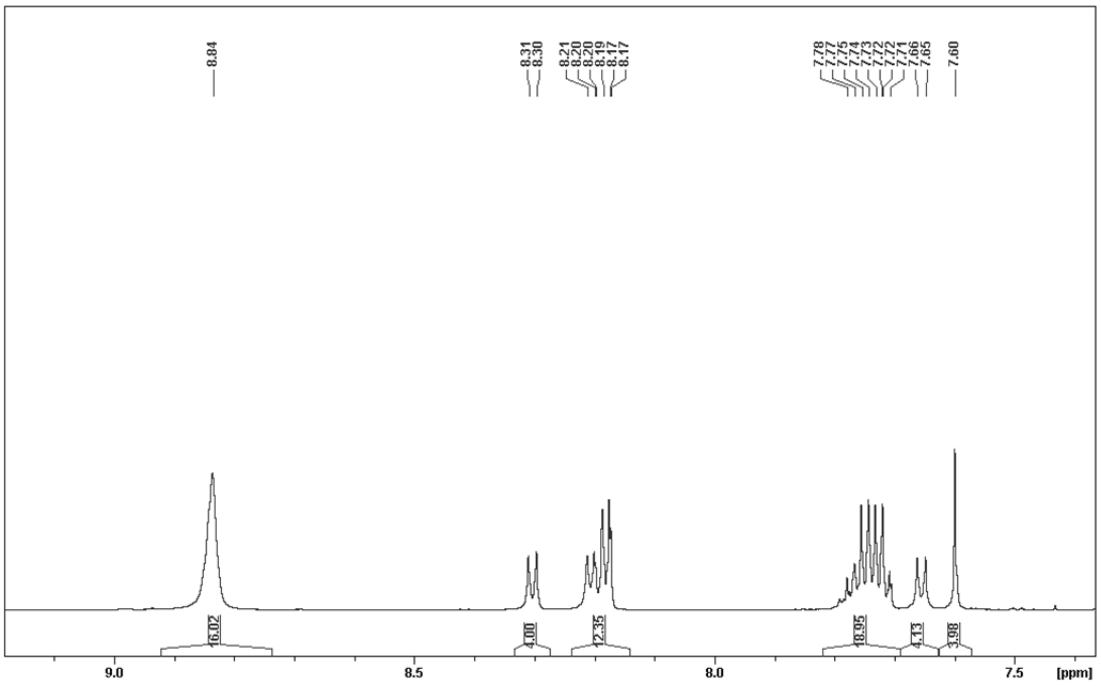

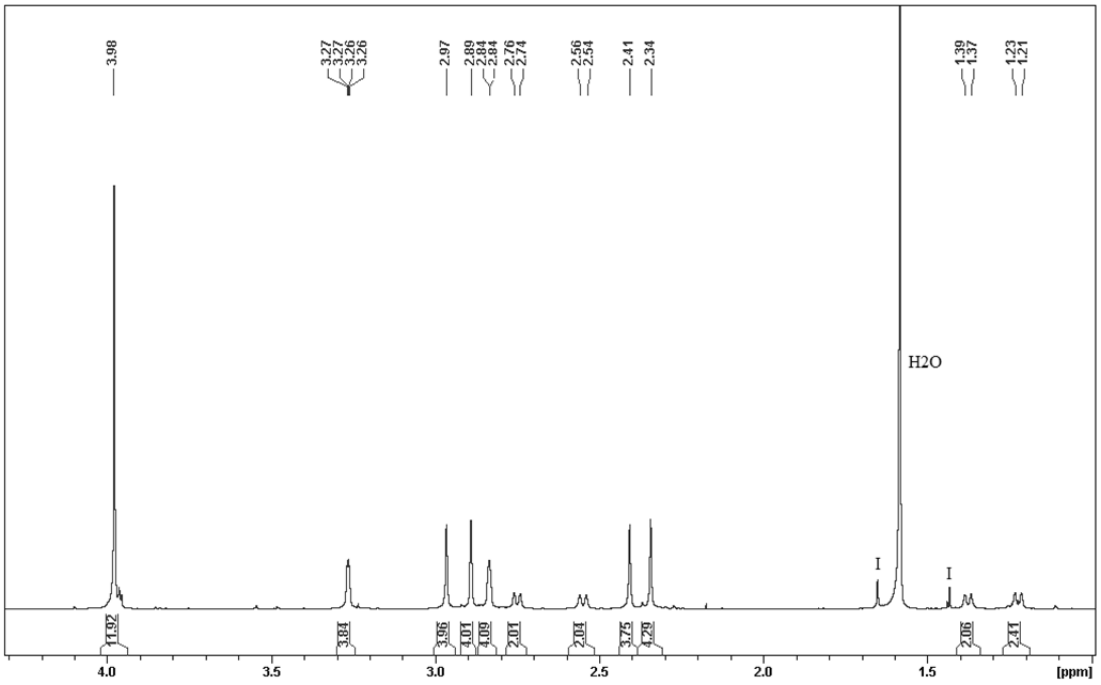
3.98
3.27
3.27
3.26
3.26
2.97
2.89
2.84
2.84
2.76
2.74
2.56
2.54
2.41
2.34
1.39
1.37
1.23
1.21
H2O
I
I
11.92
3.84
3.96
4.01
4.09
2.01
2.04
3.75
4.29
2.06
2.11
4.0
3.5
3.0
2.5
2.0
1.5
[ppm]

9.1.2 UV-Vis

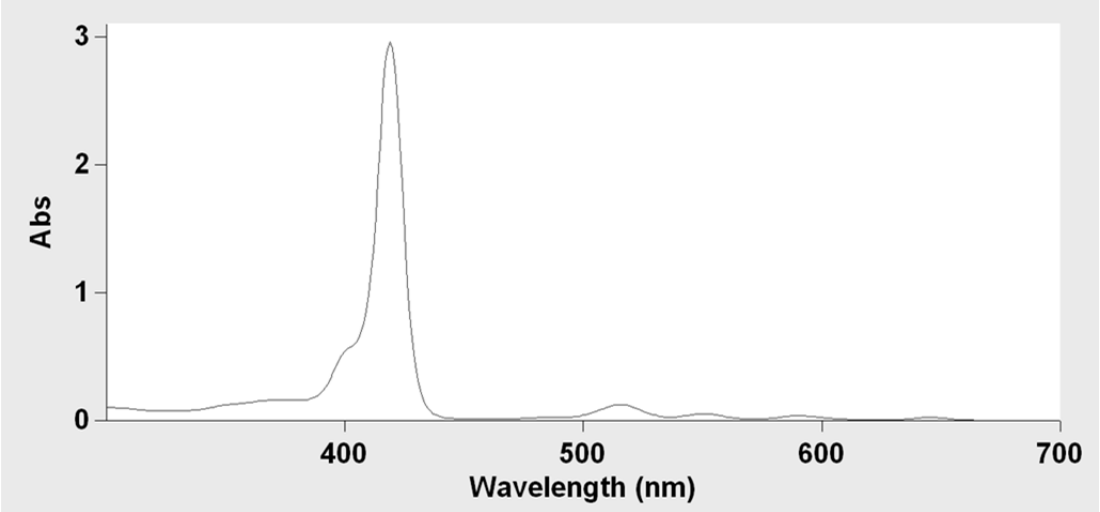
Abs
3
2
1
0
400
500
600
700
Wavelength (nm)

9.1.3 MS

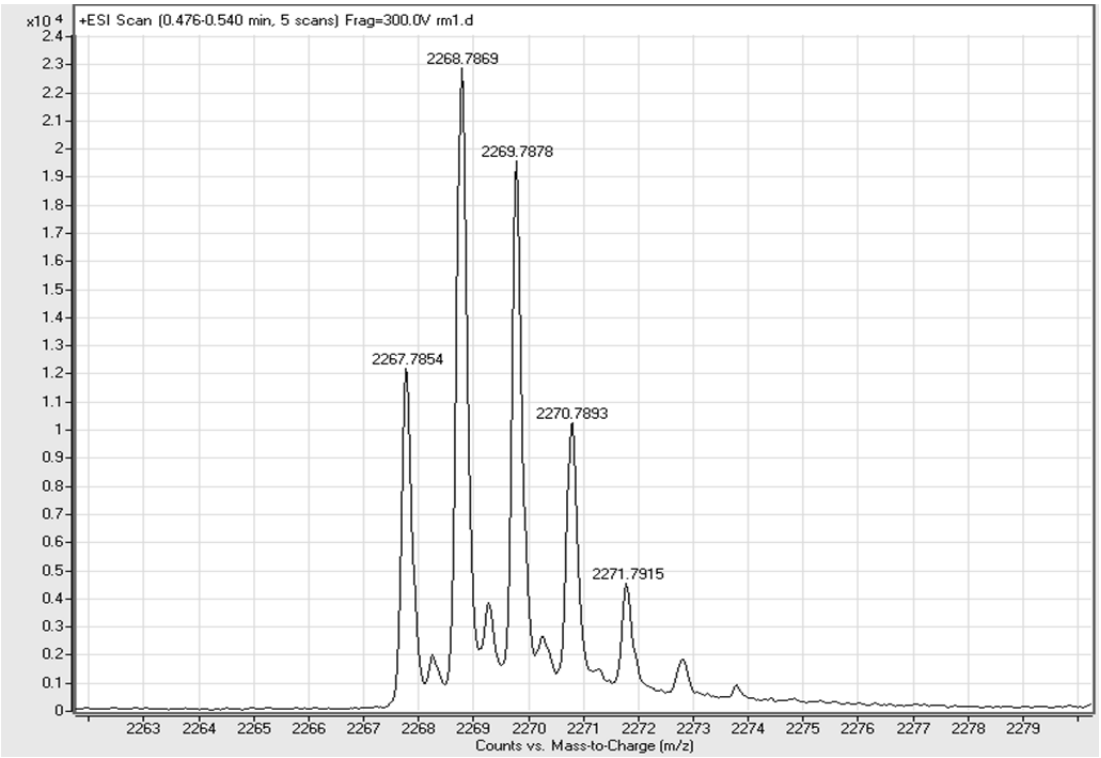

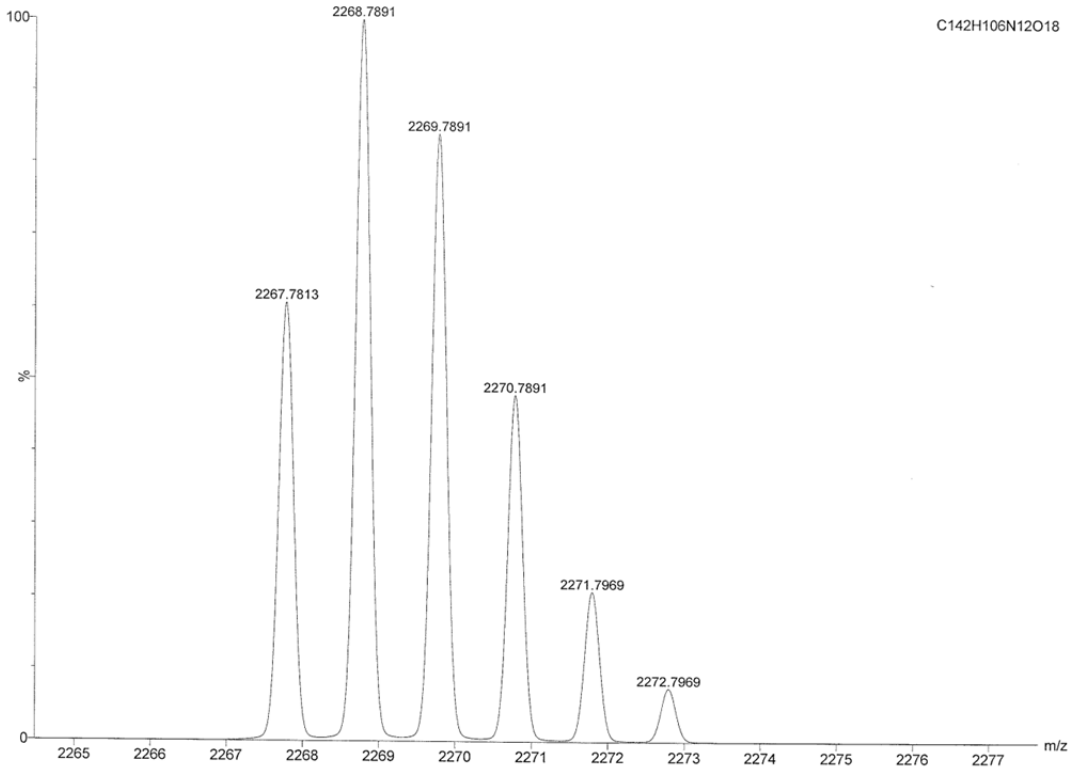

ESI-TOF of $C_{142}H_{107}N_{12}O_{18}^{+}$ $[M+H]^{+}$: Calc: 2267.7813. Found: 2267.7854.

9.2 Zn(II) Freely Rotating Tweezer **1**

9.2.1 ^{1}H NMR

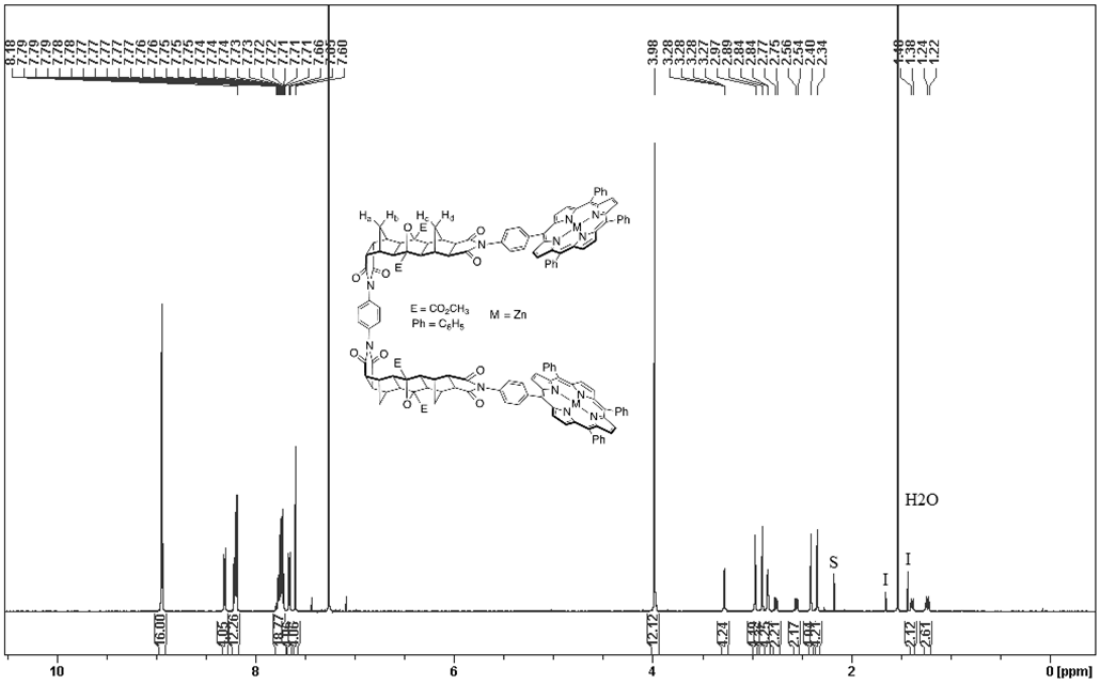

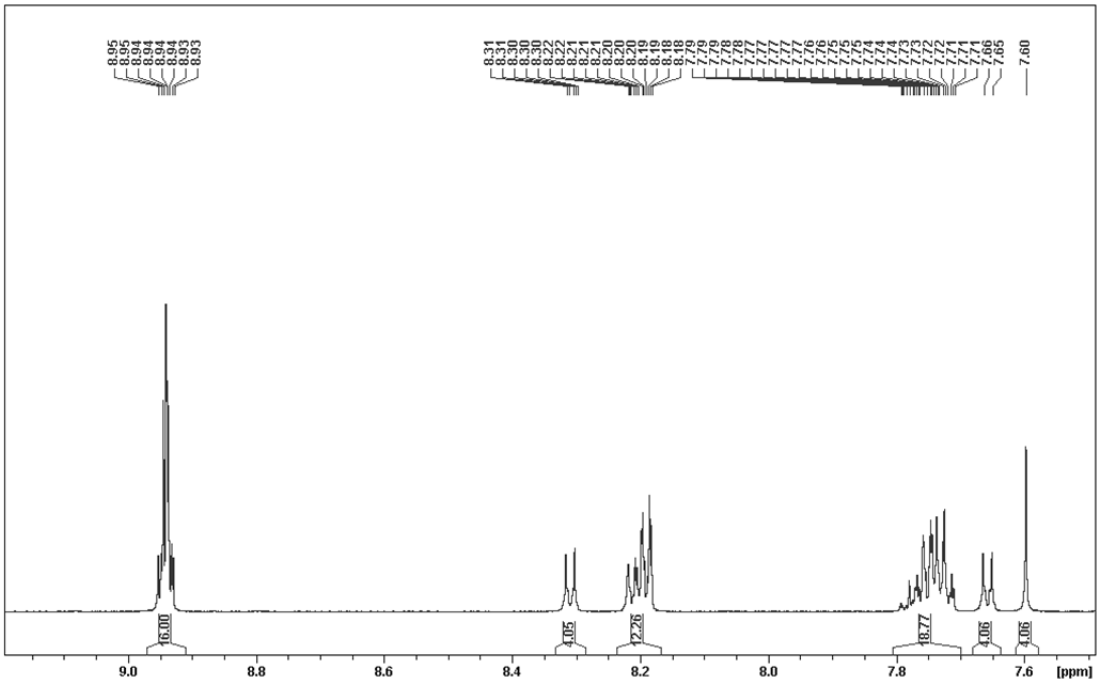

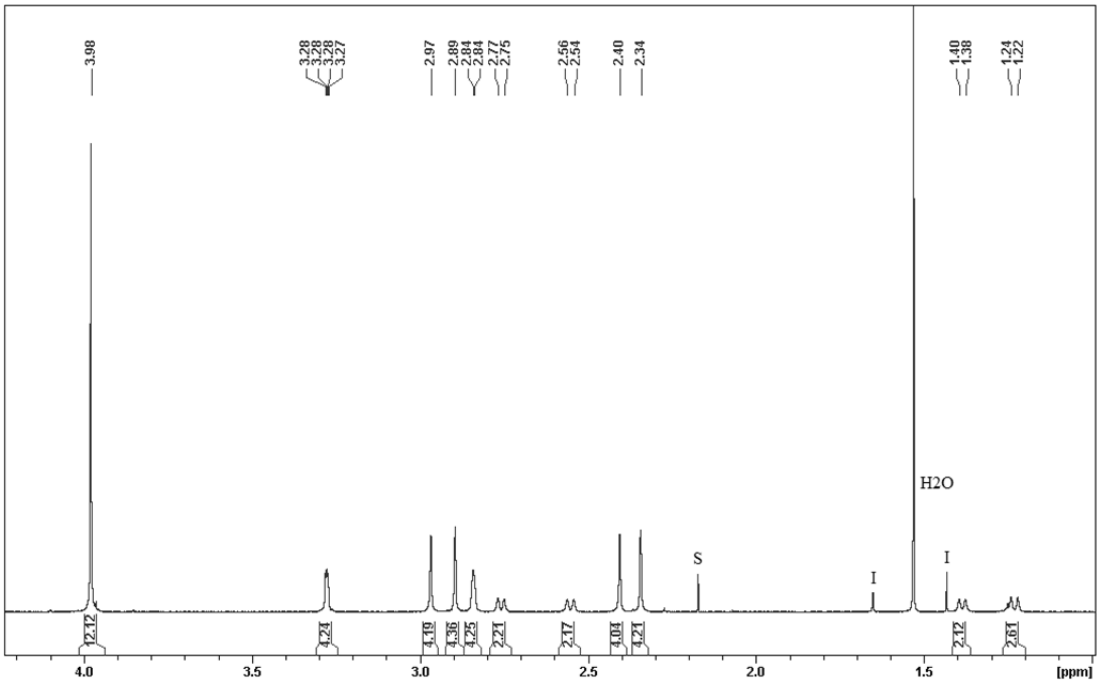
3.98
3.28
3.28
3.28
3.27
2.97
2.89
2.84
2.84
2.77
2.75
2.56
2.54
2.40
2.34
1.40
1.38
1.24
1.22
H2O
S
I
I
12.12
4.24
4.19
4.36
4.25
2.21
2.17
4.04
4.21
2.12
2.61
4.0
3.5
3.0
2.5
2.0
1.5
[ppm]

9.2.2 UV-Vis

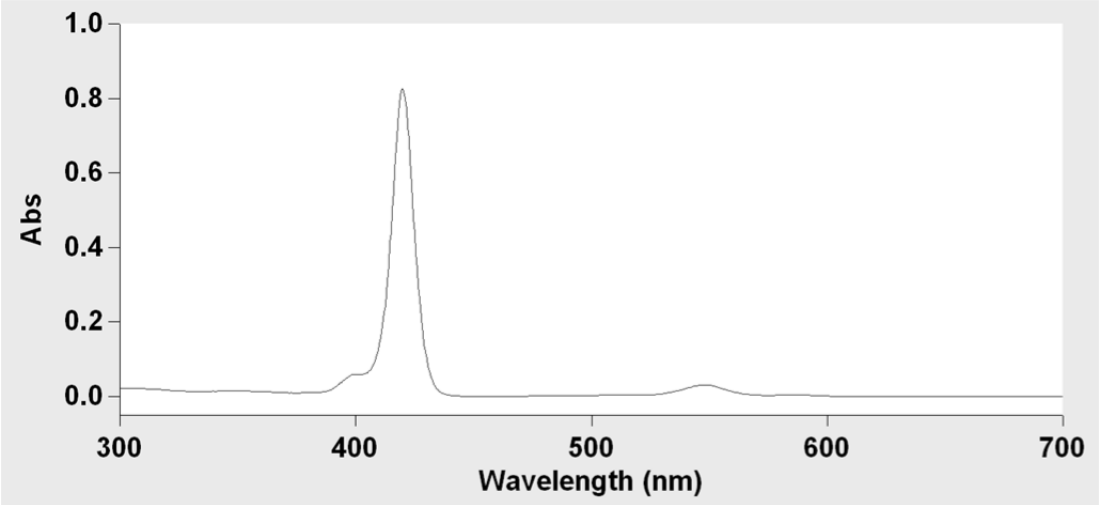
1.0
0.8
0.6
0.4
0.2
0.0
Abs
300
400
500
600
700
Wavelength (nm)

9.2.3 MS

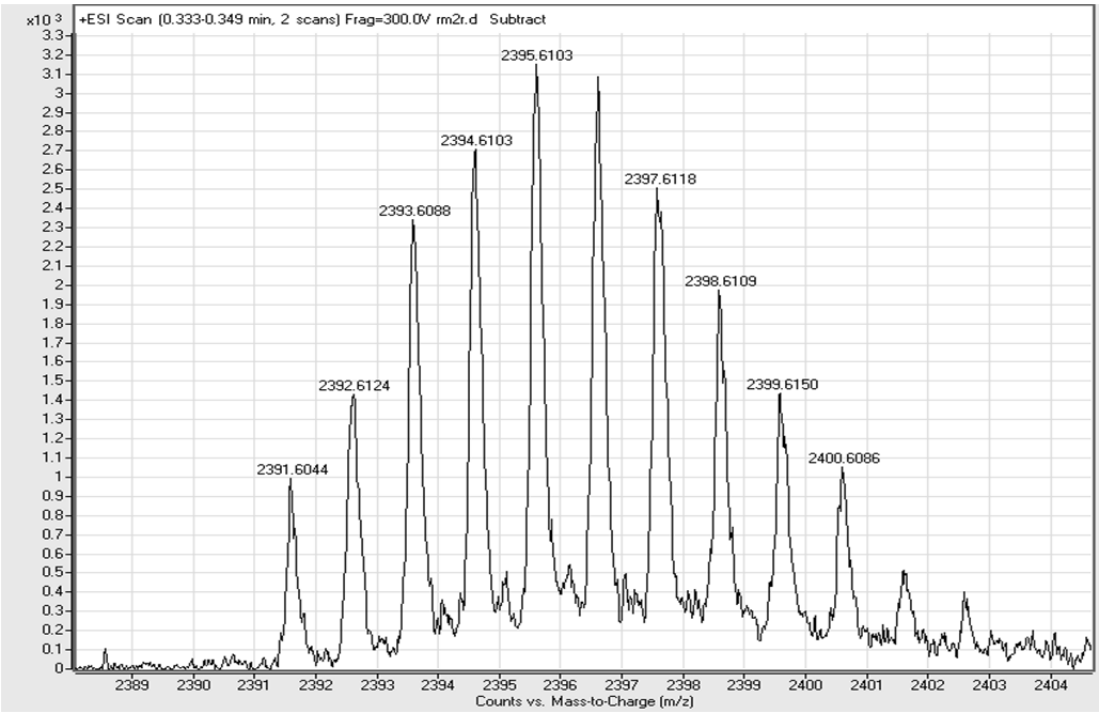

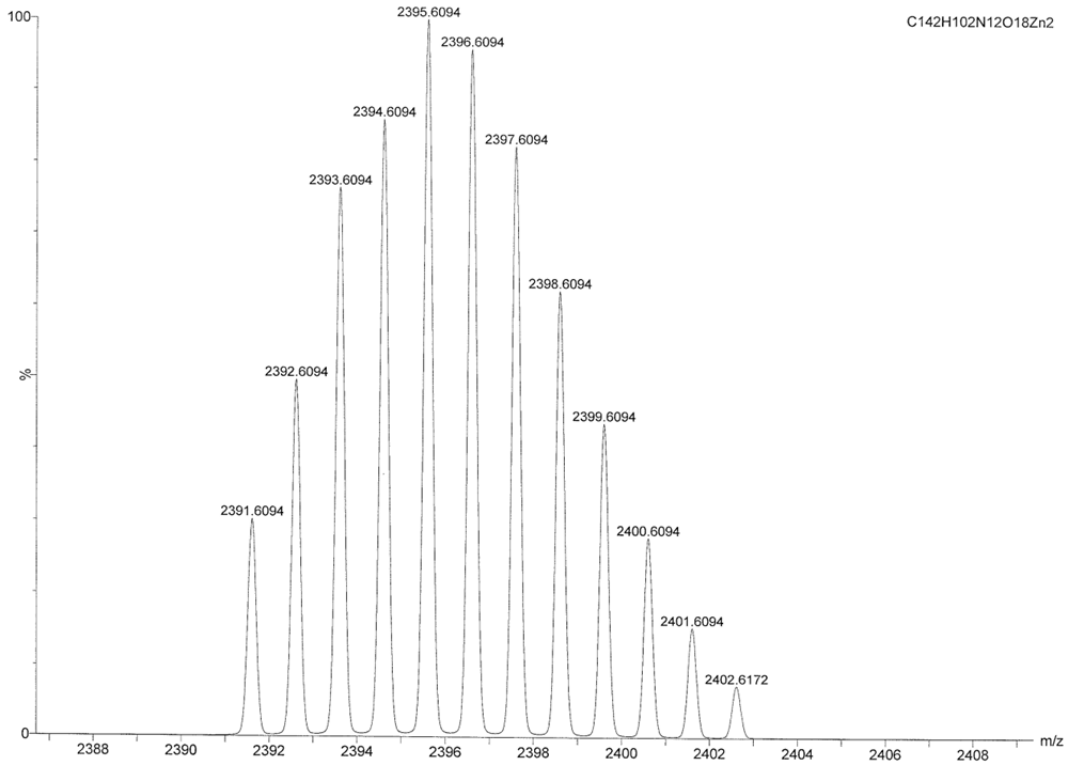

ESI-TOF of $C_{142}H_{107}N_{12}O_{18}Zn_2^+$ $[M+H]^+$: Calc: 2391.6094. Found: 2391.6044.

9.3 Freebase *Anti*- Restricted Rotation Tweezer **35**

9.3.1 ^{1}H NMR

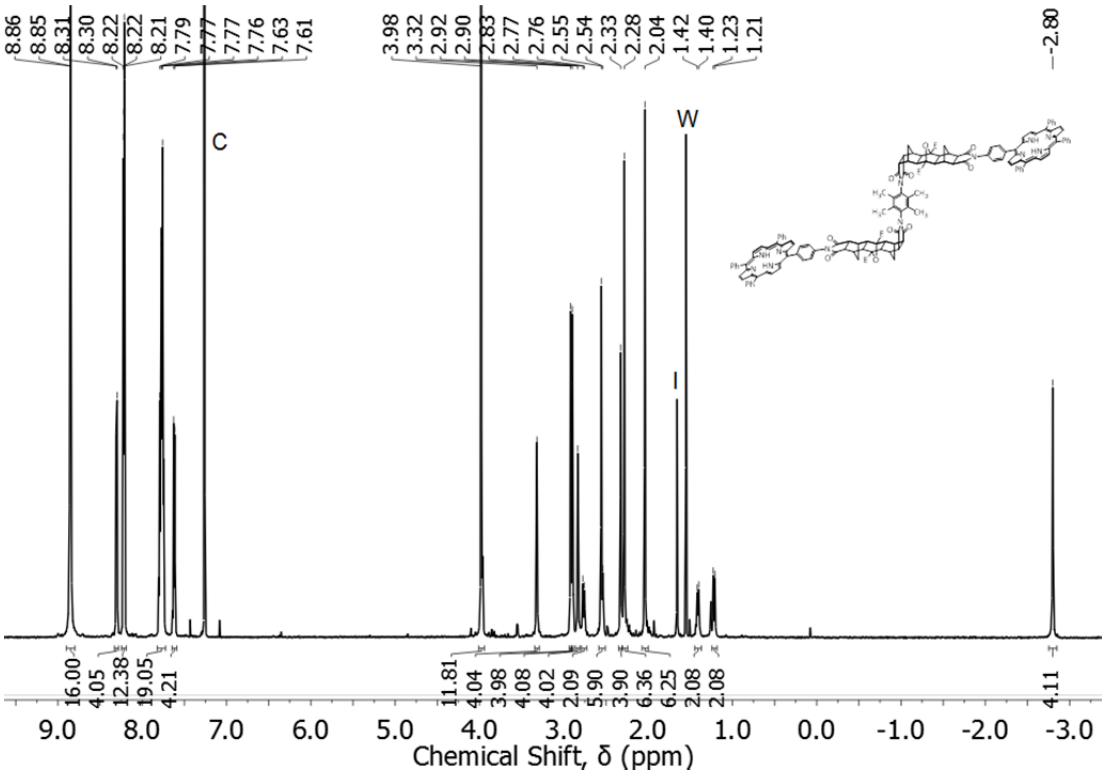

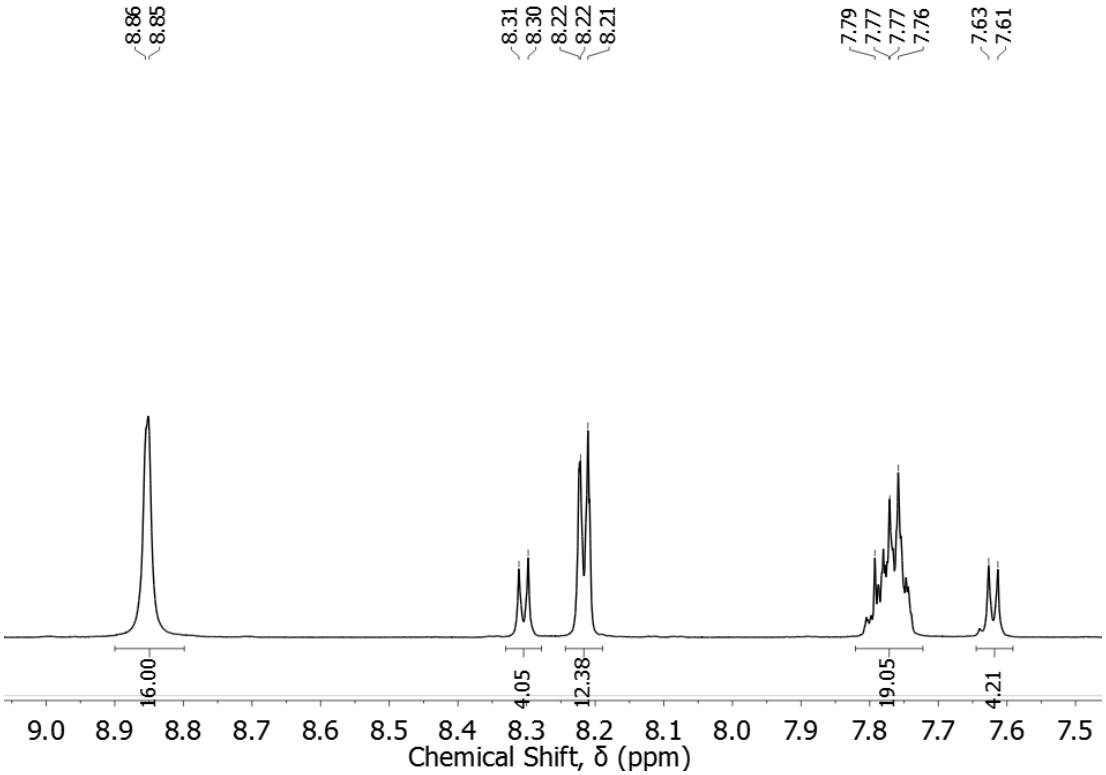

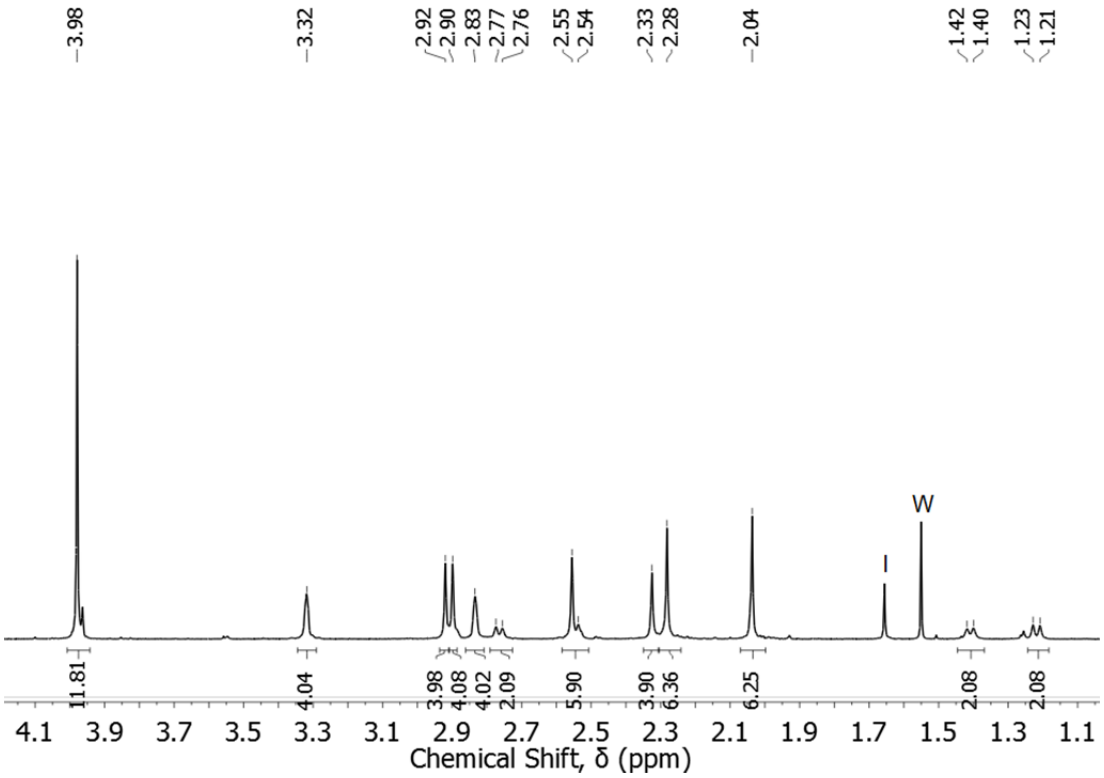

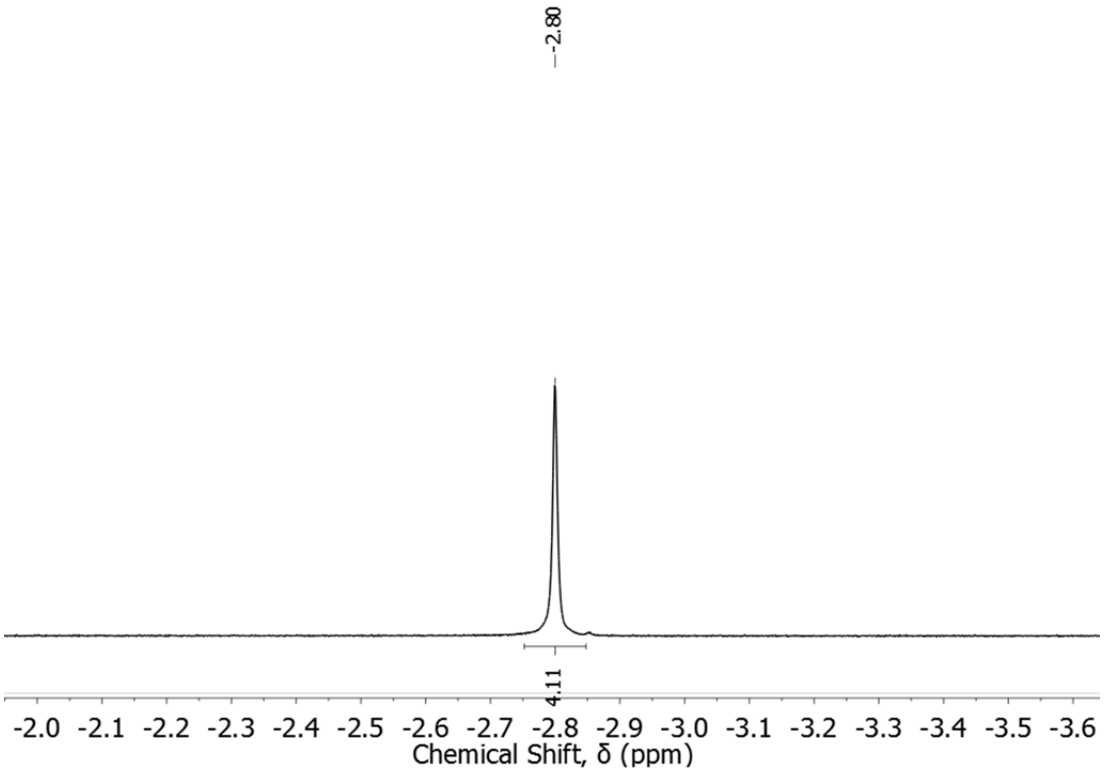

* Note: Freebase *syn*- **34** was characterised as the Zn(II) derivative.

9.3.2 MS

Two samples containing different ratios of *syn*- **34** and *anti*- **35**.

Sample 1.

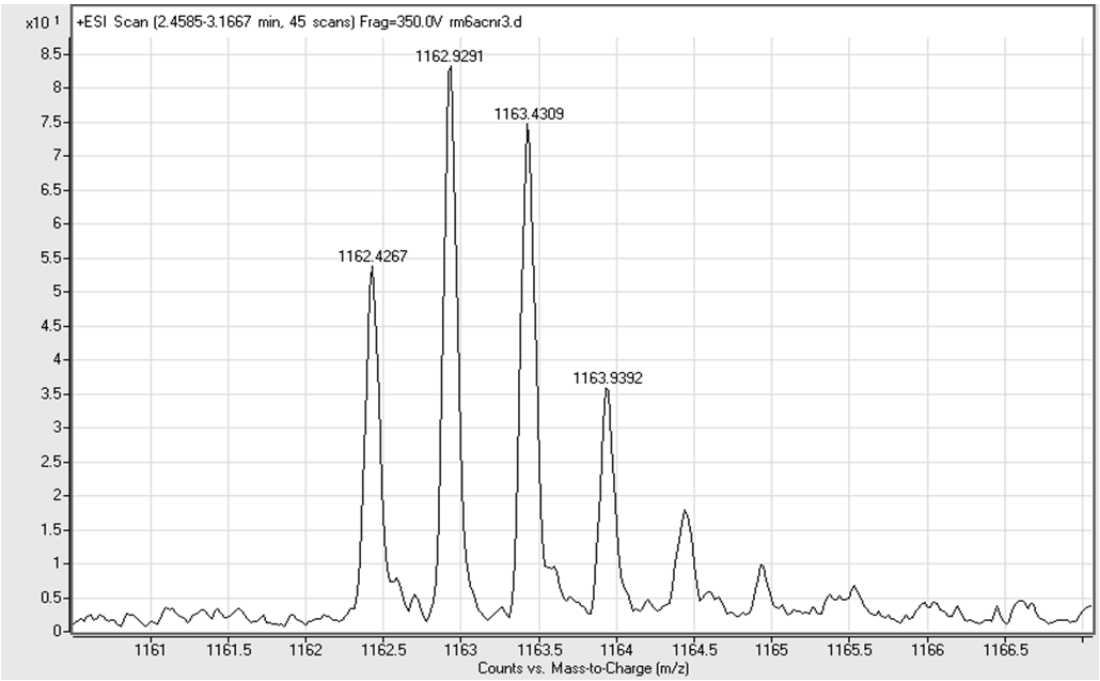

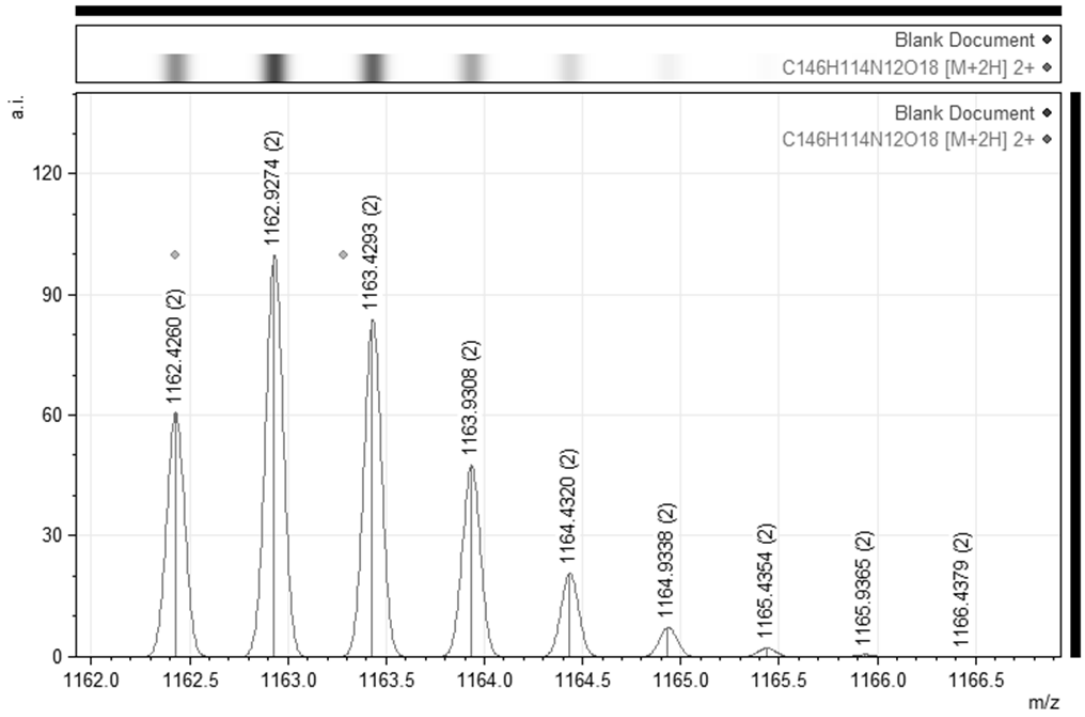

ESI-TOF for $[C_{146}H_{116}N_{12}O_{18}]^{2+}$ $[M+2H]^{2+}$: Calc: 1162.4260. Found: 1162.4267.

Sample 2.

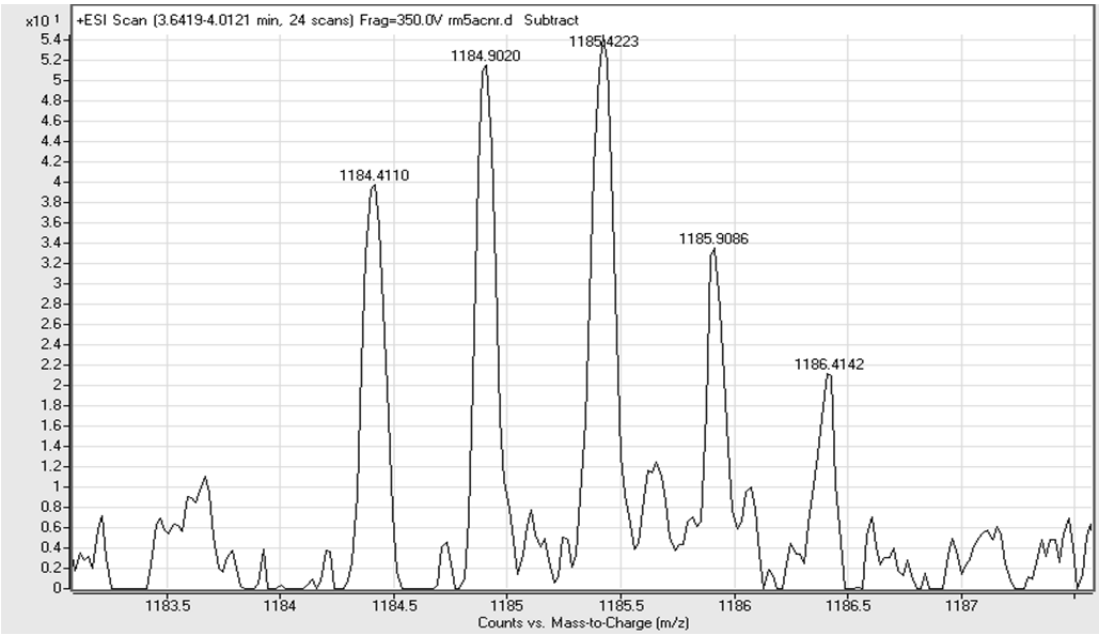

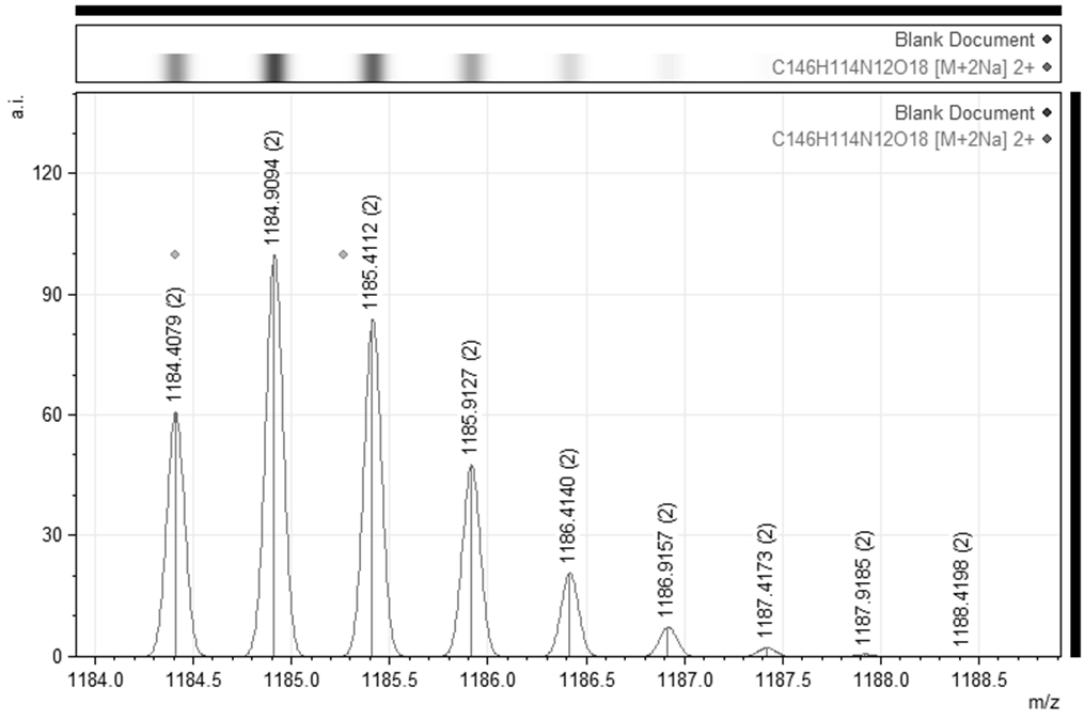

ESI-TOF for $[C_{146}H_{114}N_{12}O_{18}Na_2]^{2+}$ $[M+2Na]^{2+}$: Calc: 1184.4079. Found: 1184.4110.

9.4 Zn(II) *Syn*- Restricted Rotation Tweezer **2**

9.4.1 ^{1}H NMR

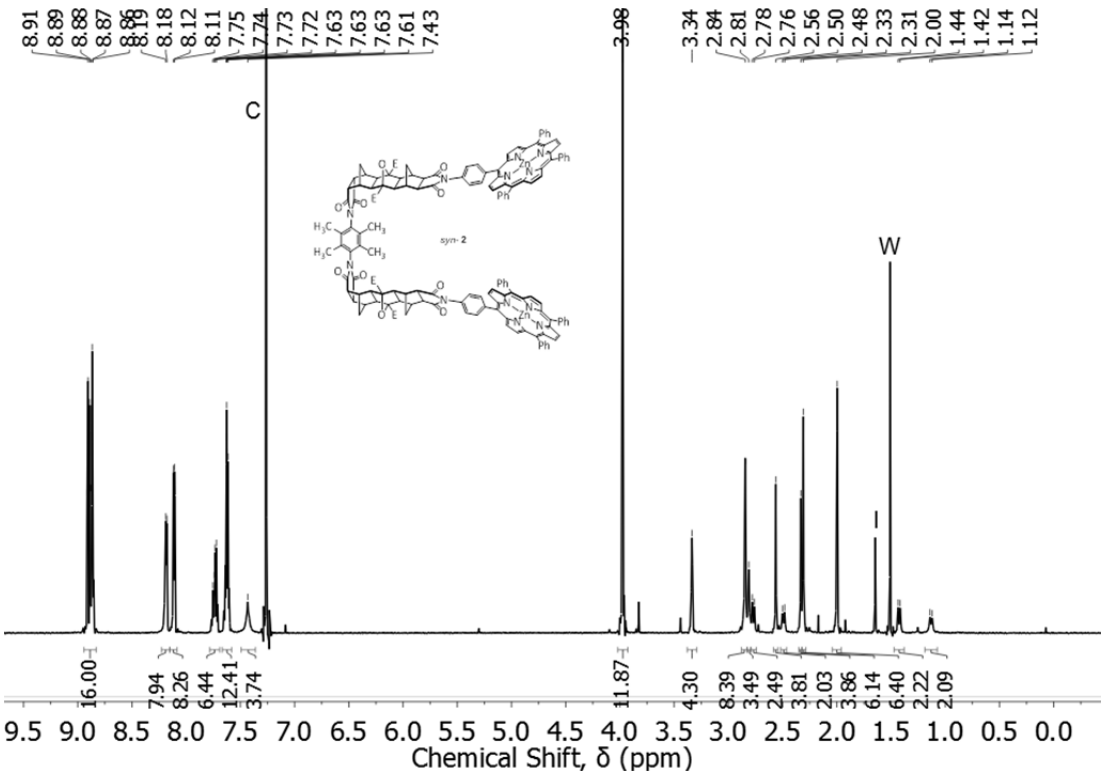

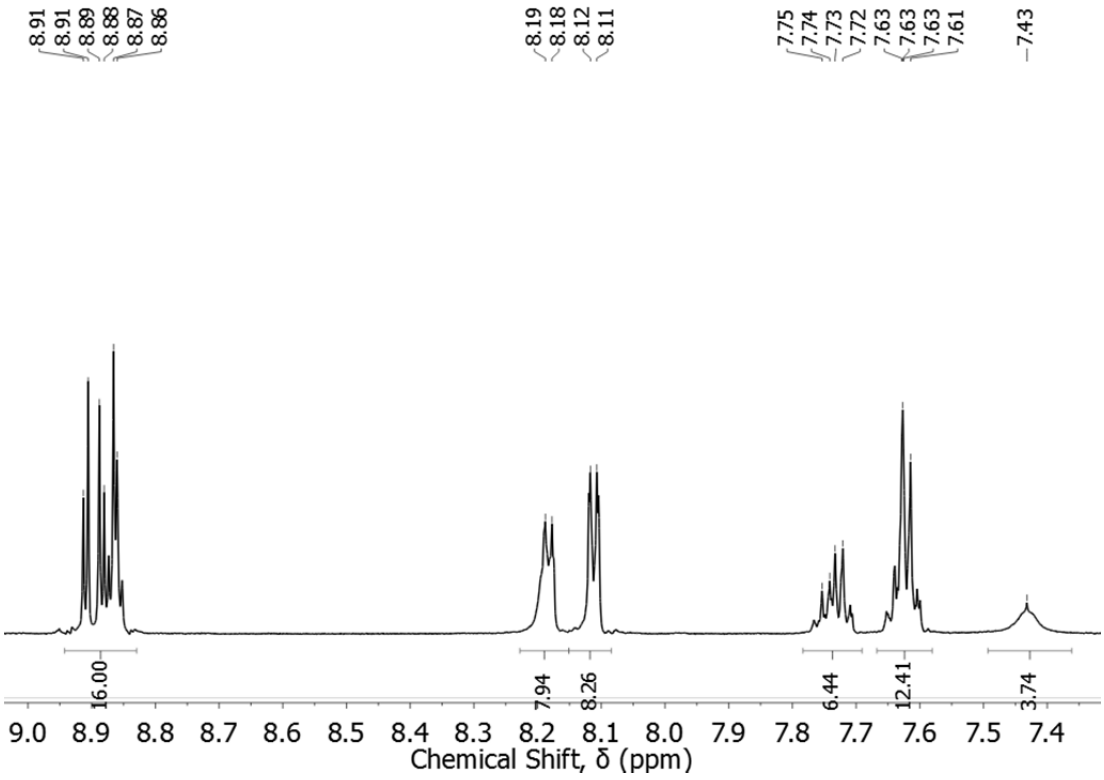

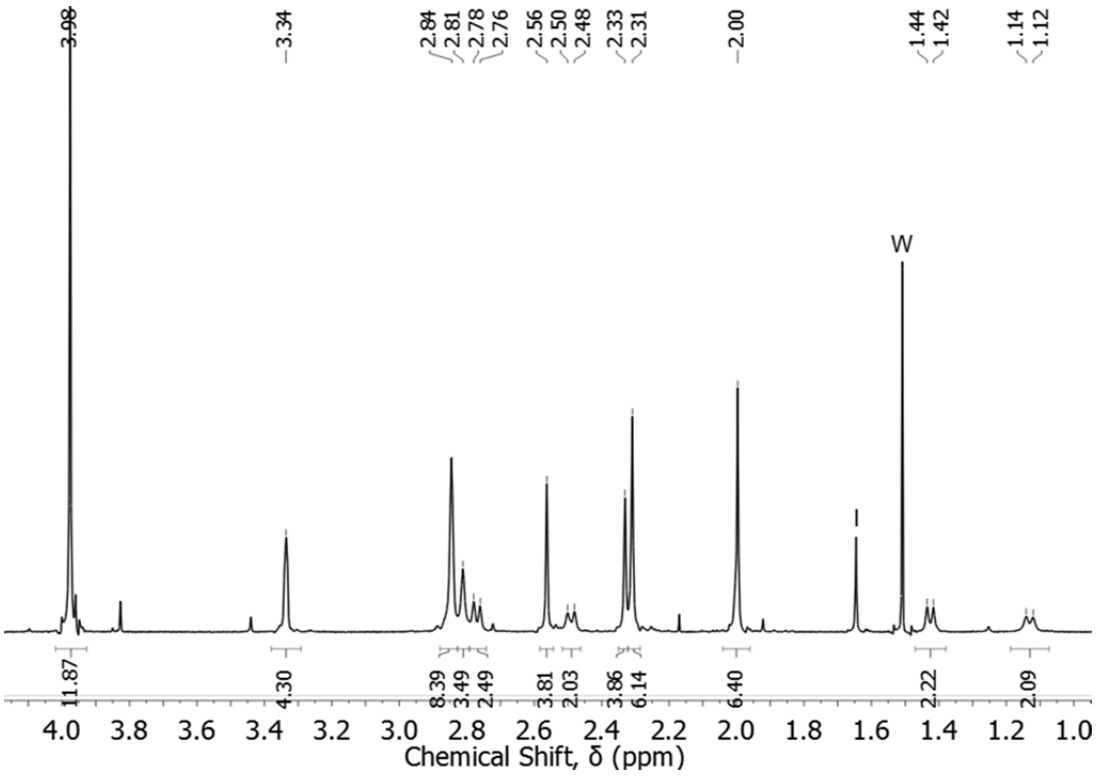
3.98
3.34
2.84
2.81
2.78
2.76
2.56
2.50
2.48
2.33
2.31
2.00
1.44
1.42
1.14
1.12
W
I
11.87
4.30
8.39
3.49
2.49
3.81
2.03
3.86
6.14
6.40
2.22
2.09
4.0 3.8 3.6 3.4 3.2 3.0 2.8 2.6 2.4 2.2 2.0 1.8 1.6 1.4 1.2 1.0
Chemical Shift, δ (ppm)

9.4.2 UV-Vis

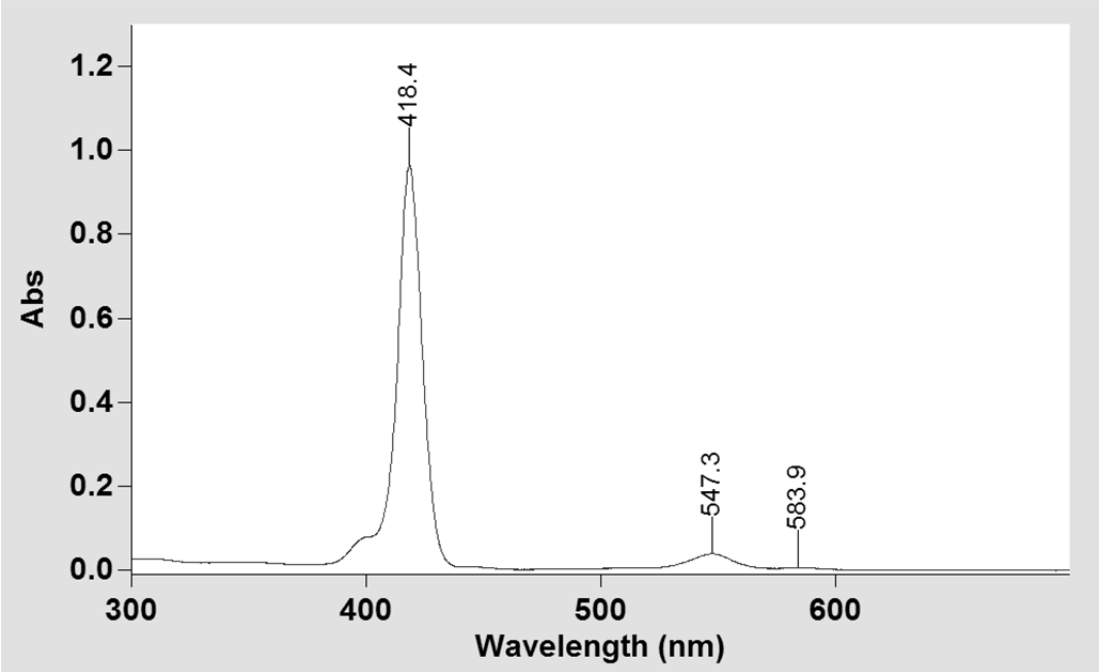
418.4
547.3
583.9
Abs
1.2
1.0
0.8
0.6
0.4
0.2
0.0
300
400
500
600
Wavelength (nm)

9.5 Zn(II) *Anti*- Restricted Rotation Tweezer **3**

9.5.1 ^{1}H NMR

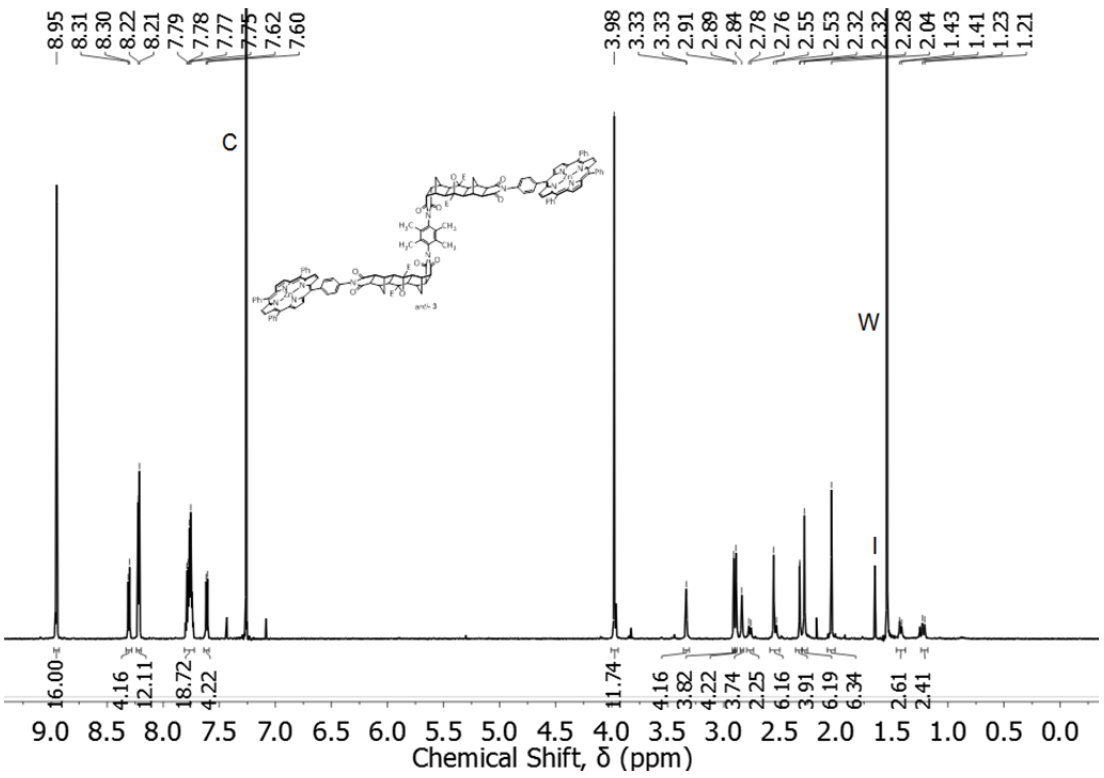

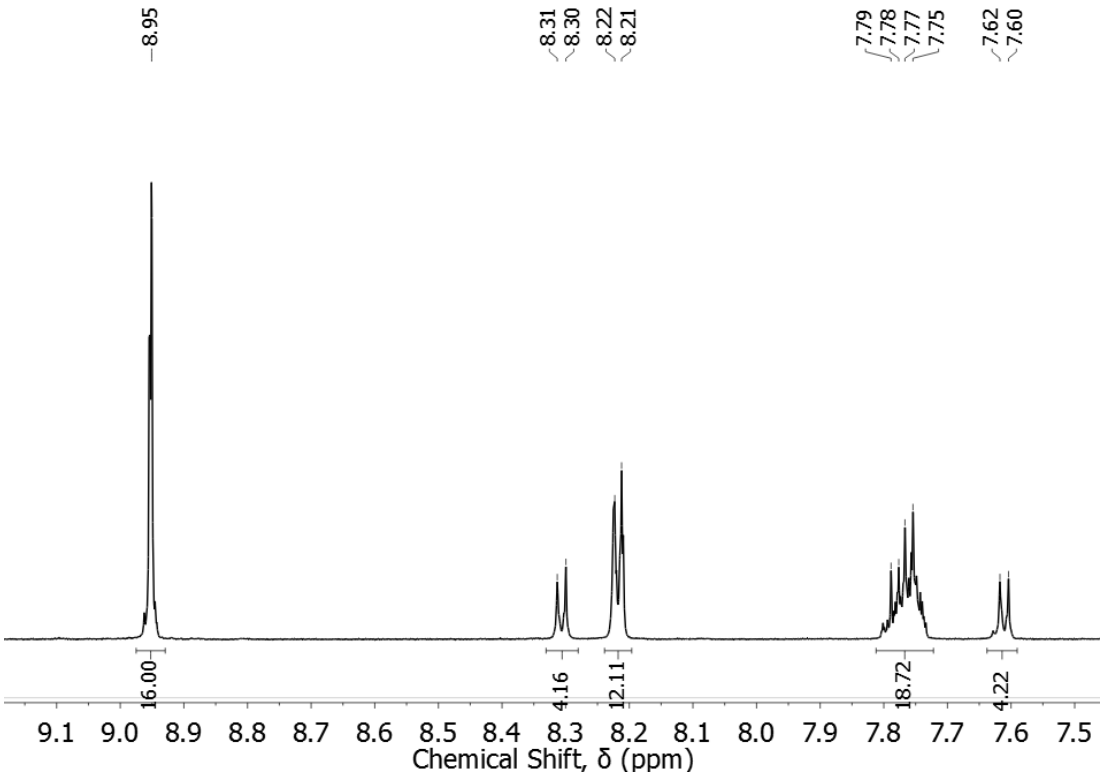

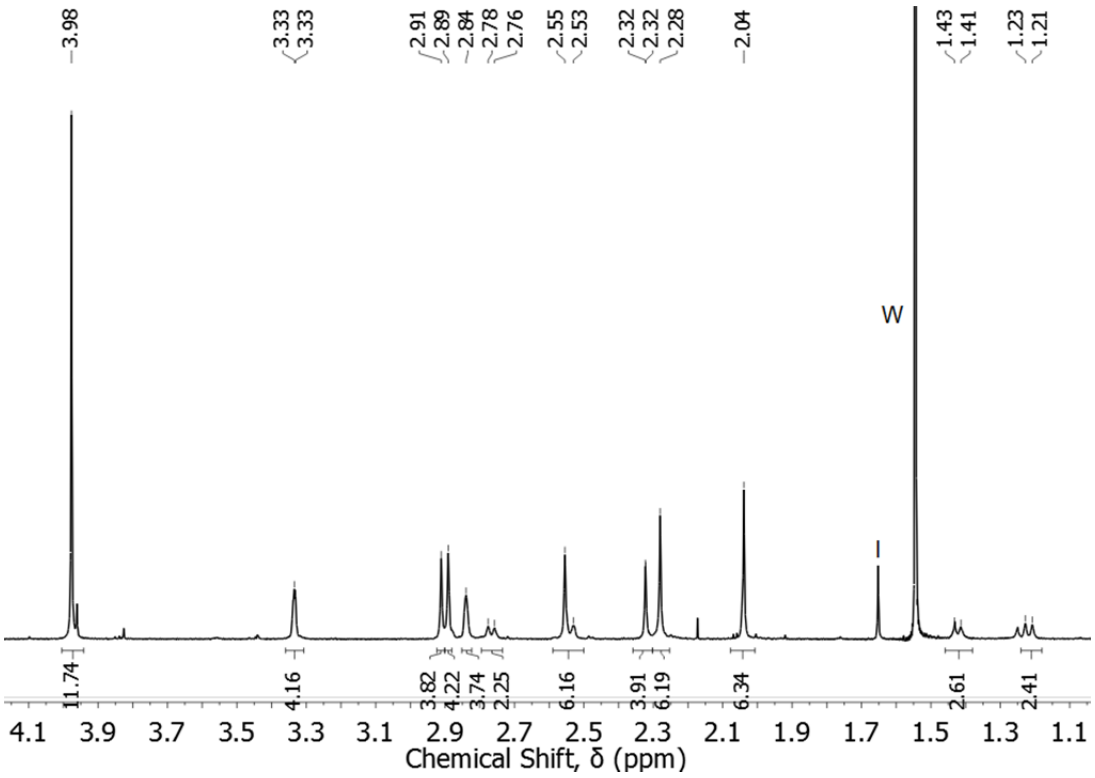
3.98
3.33
3.33
2.91
2.89
2.84
2.78
2.76
2.55
2.53
2.32
2.32
2.28
2.04
1.43
1.41
1.23
1.21
W
11.74
4.16
3.82
4.22
3.74
2.25
6.16
3.91
6.19
6.34
2.61
2.41
4.1 3.9 3.7 3.5 3.3 3.1 2.9 2.7 2.5 2.3 2.1 1.9 1.7 1.5 1.3 1.1
Chemical Shift, δ (ppm)

9.5.2 UV-Vis

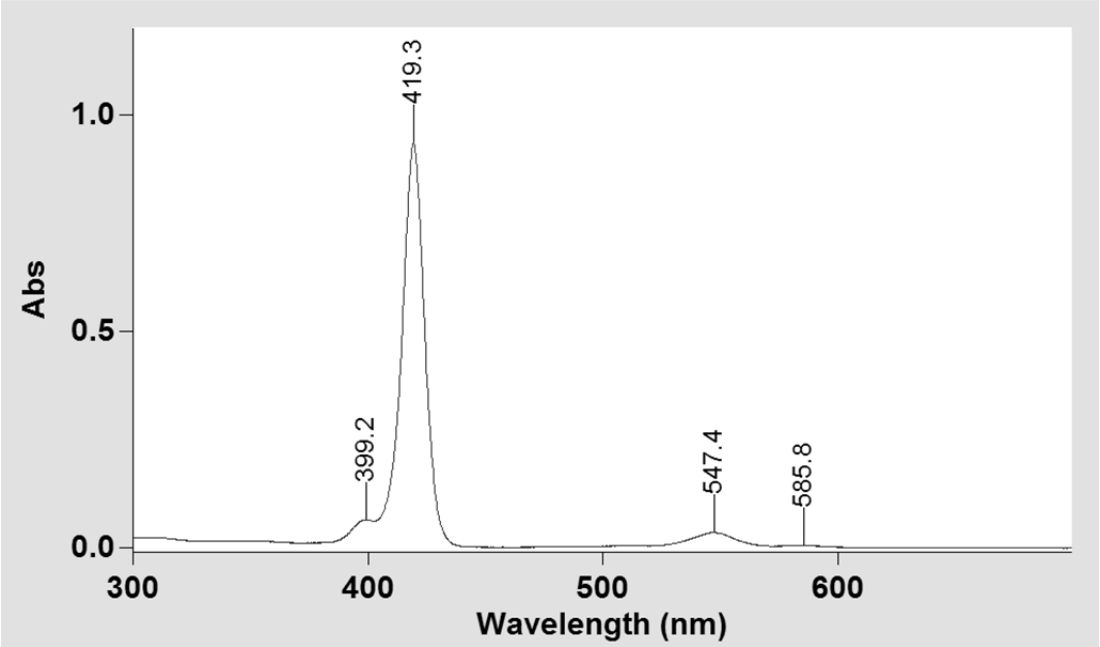
419.3
399.2
547.4
585.8
1.0
0.5
0.0
Abs
300
400
500
600
Wavelength (nm)

9.6 Freebase Tetra-porphyrin Tweezer **63**

9.6.1 ^{1}H NMR

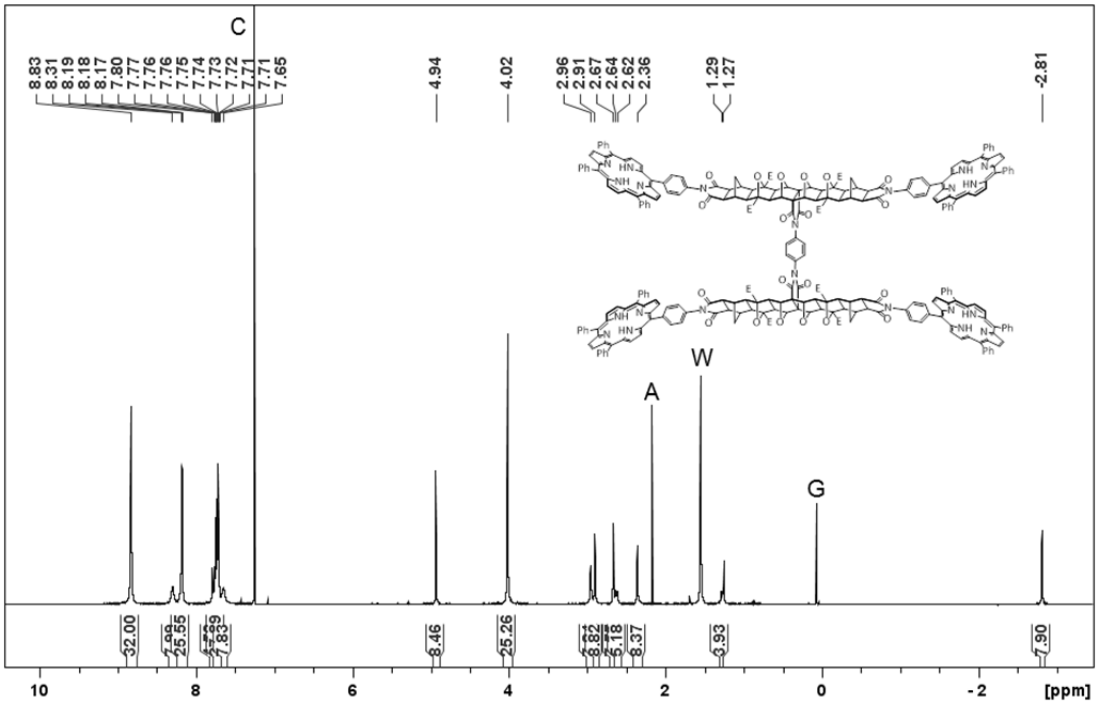

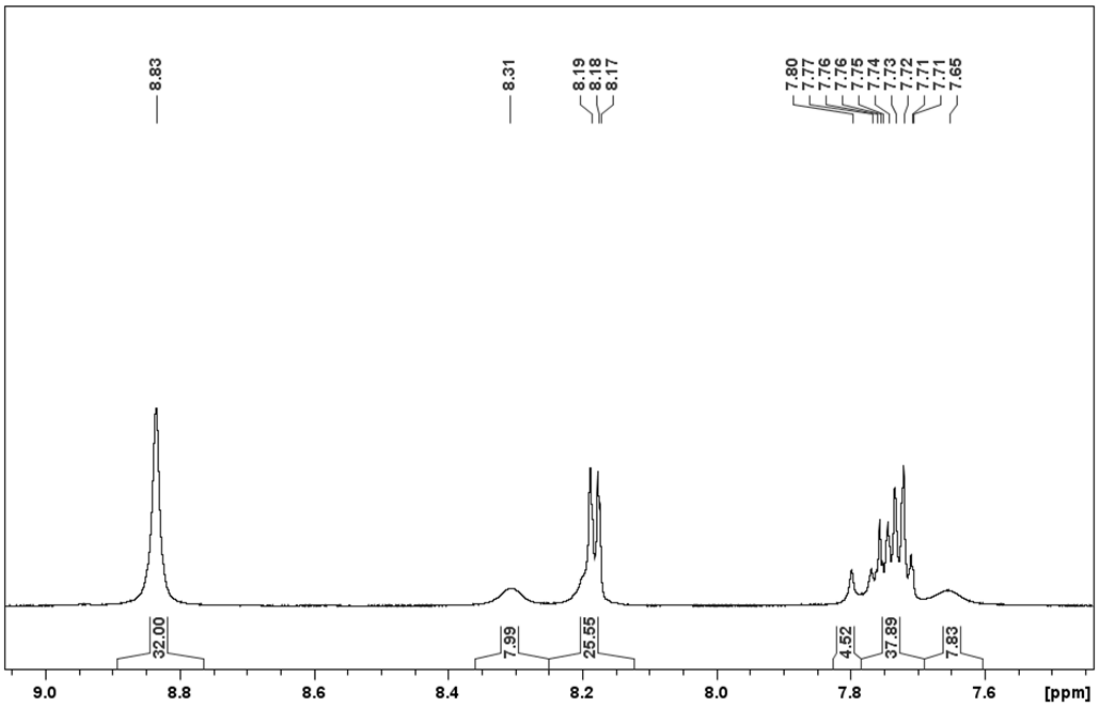

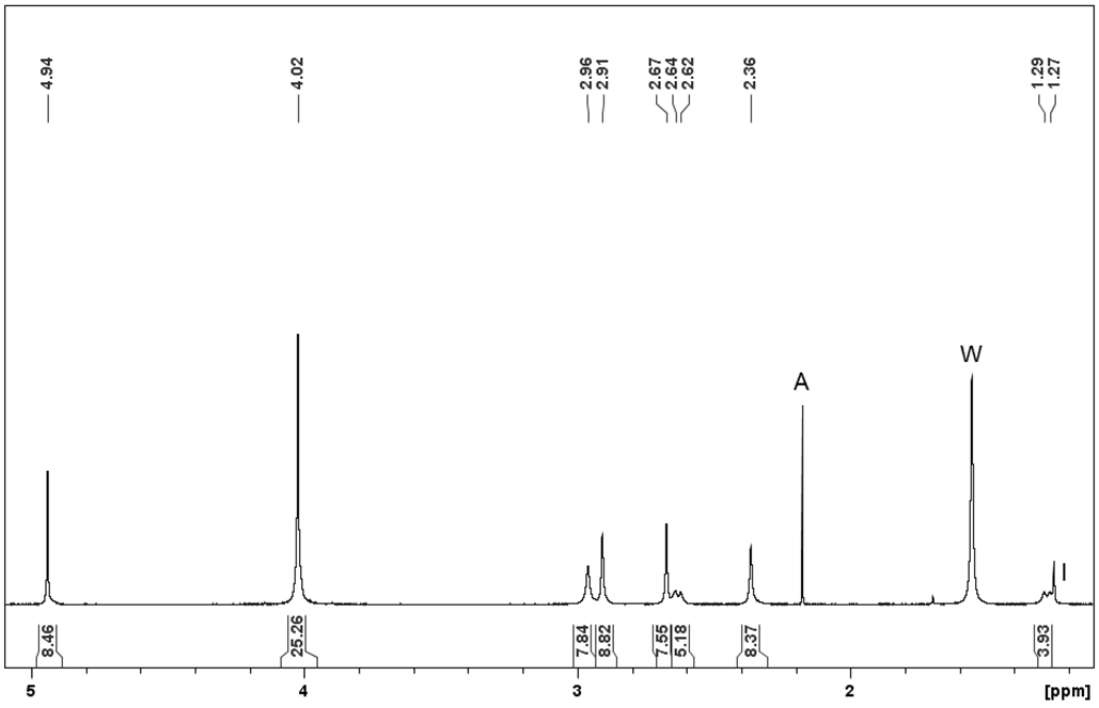
4.94
4.02
2.96
2.91
2.67
2.64
2.62
2.36
1.29
1.27
A
W
I
8.46
25.26
7.84
8.82
7.55
5.18
8.37
3.93
5
4
3
2
[ppm]

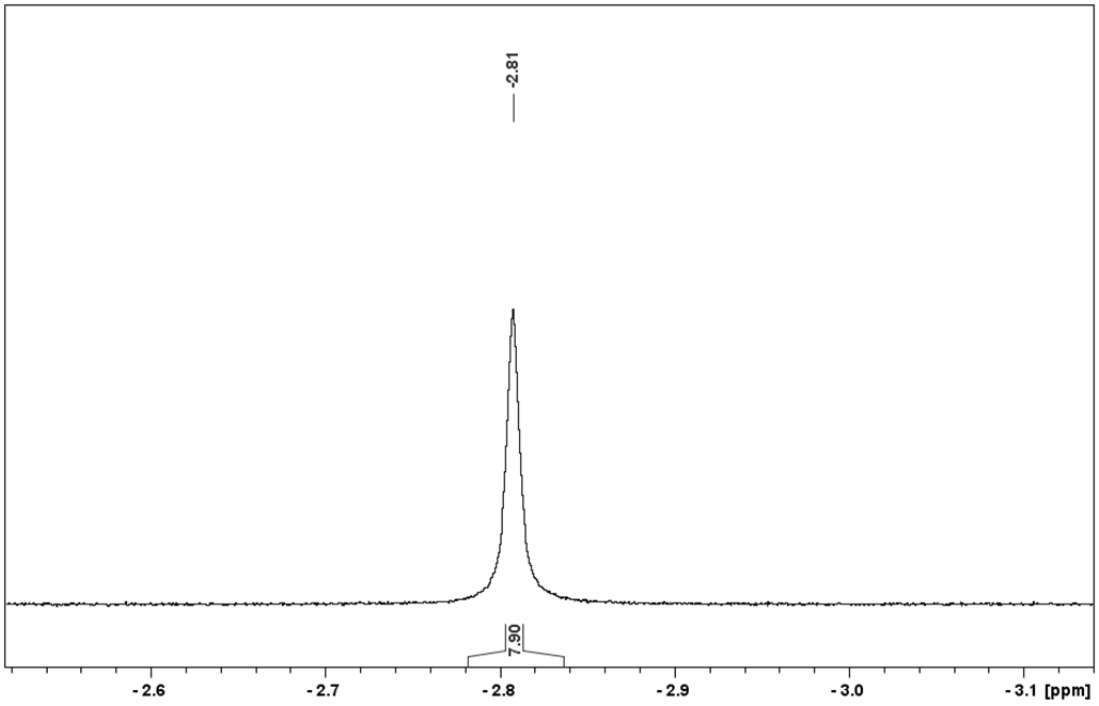
-2.81
7.90
-2.6
-2.7
-2.8
-2.9
-3.0
-3.1 [ppm]

9.6.2 UV-Vis

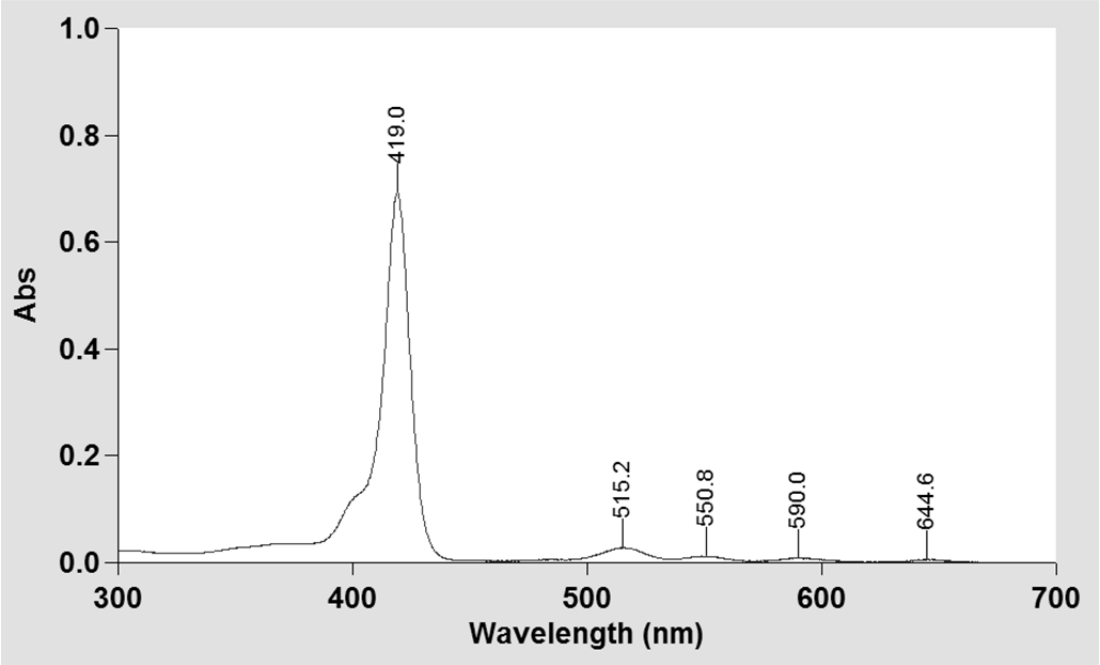
1.0
0.8
0.6
0.4
0.2
0.0
Abs
419.0
515.2
550.8
590.0
644.6
300
400
500
600
700
Wavelength (nm)

9.6.3 MS

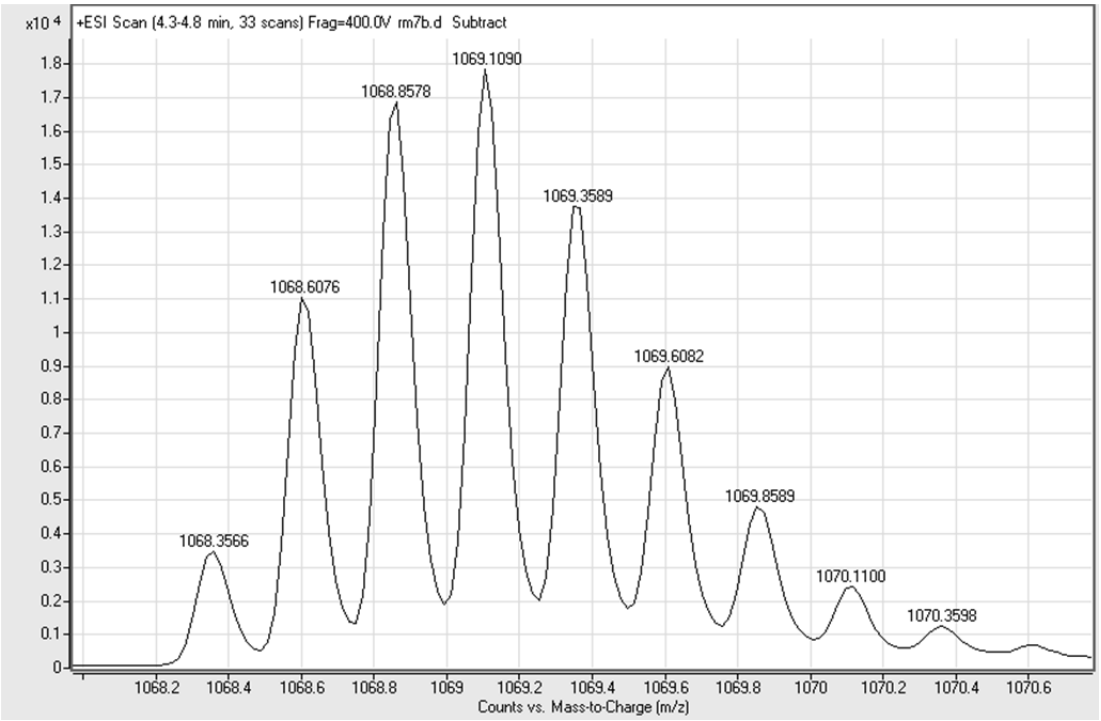

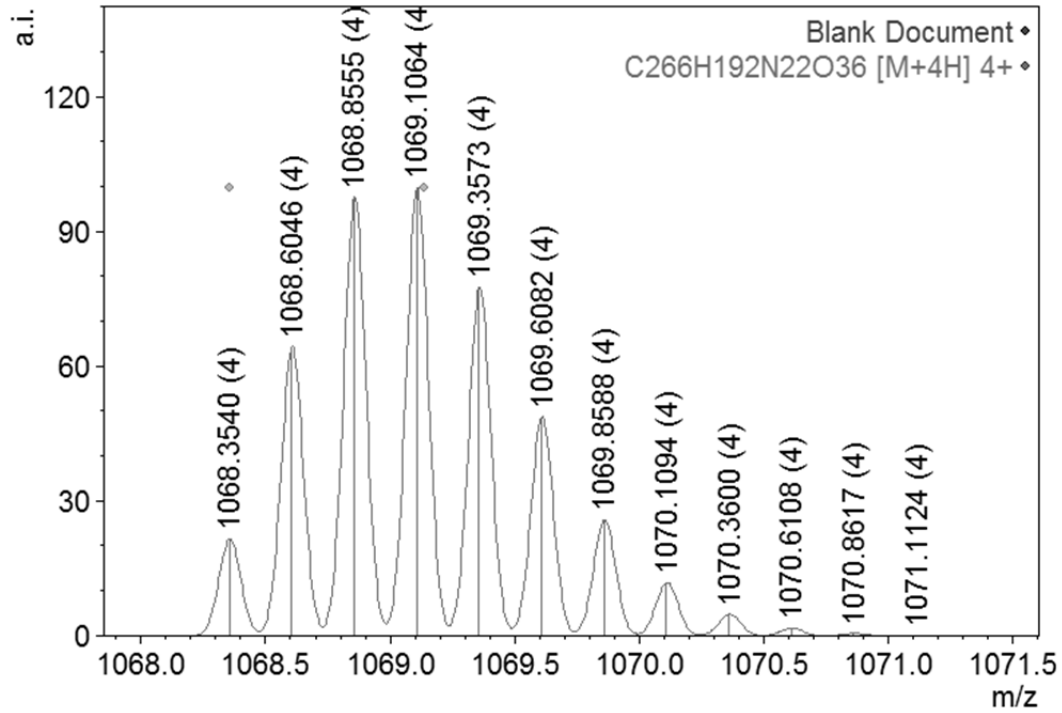

ESI-TOF of $C_{266}H_{196}N_{22}O_{36}^{4+}$ $[M+4H]^{4+}$: Calc: 1068.3540. Found 1068.3566.

9.7 Zn(II) Tetra-porphyrin Tweezer **4**

9.7.1 ^{1}H NMR

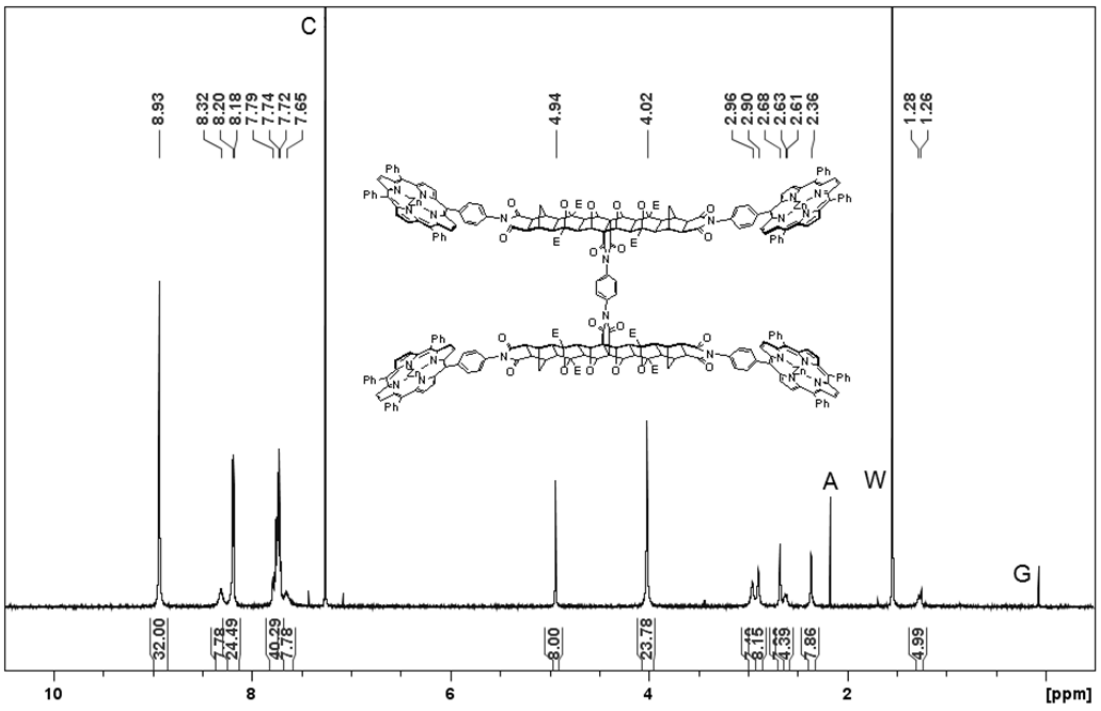

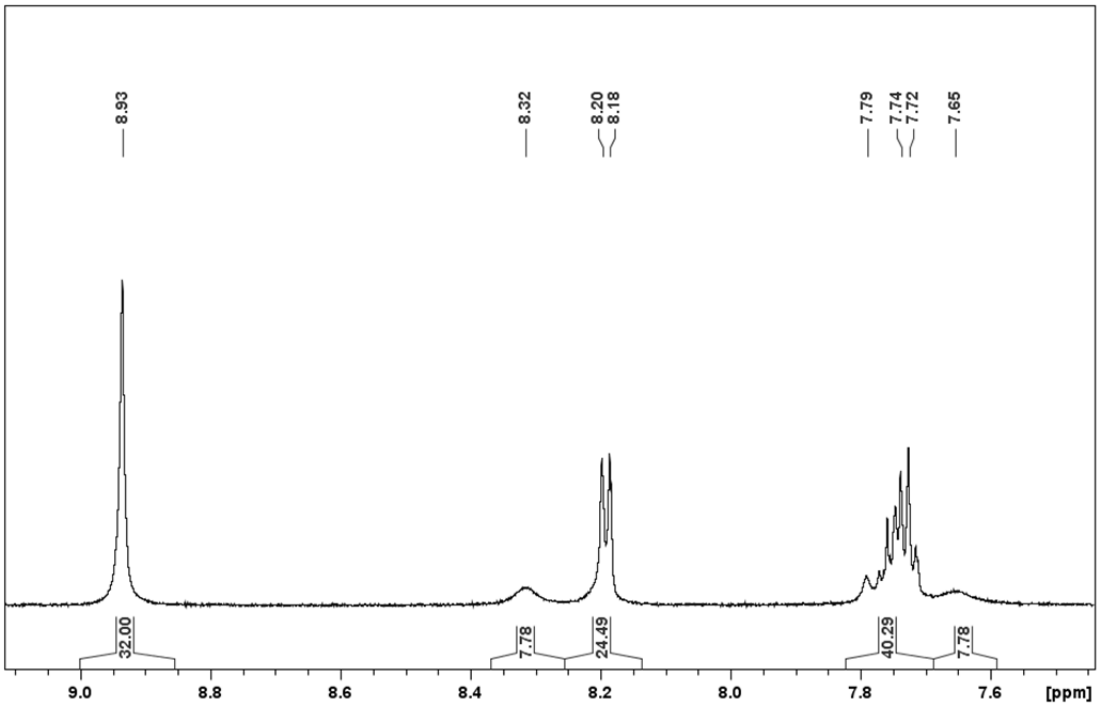

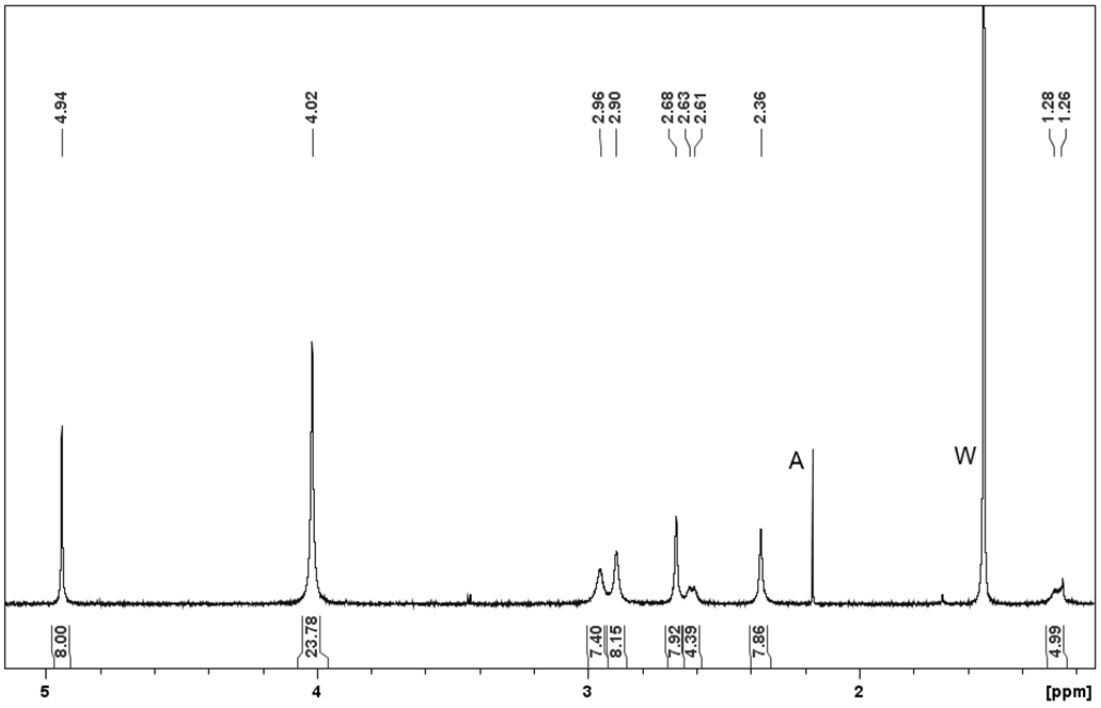
4.94
4.02
2.96
2.90
2.68
2.63
2.61
2.36
1.28
1.26
A
W
8.00
23.78
7.40
8.15
7.92
4.39
7.86
4.99
5
4
3
2
[ppm]

9.7.2 UV-Vis

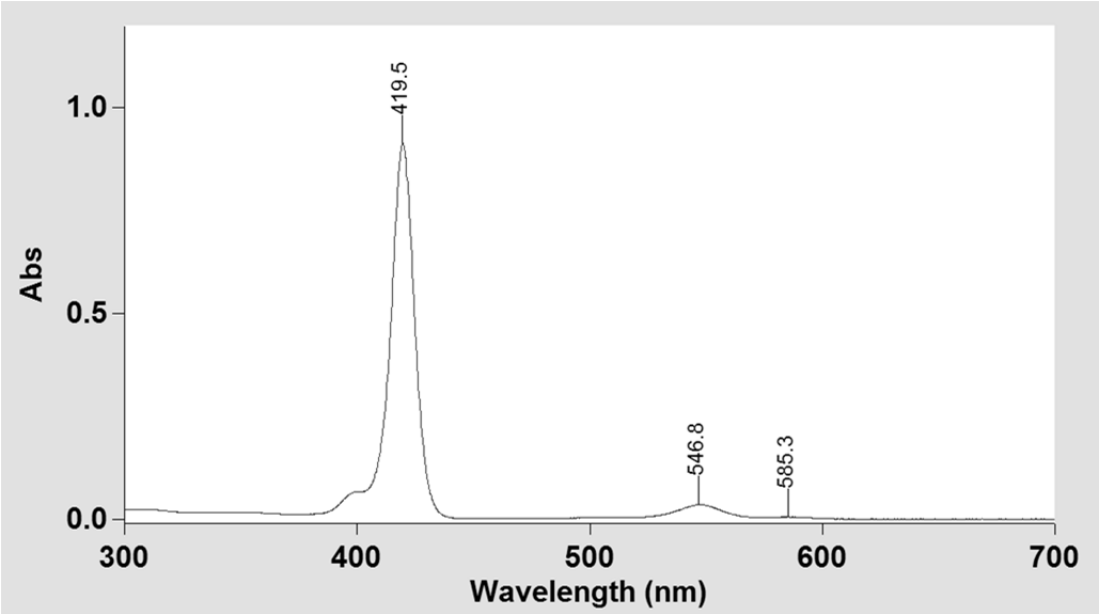
419.5
546.8
585.3
1.0
0.5
0.0
Abs
300
400
500
600
700
Wavelength (nm)

9.8 Freebase *Exo*- Mono-porphyrin Receptor (Soluble for Titrations) **21**

9.8.1 ^{1}H NMR

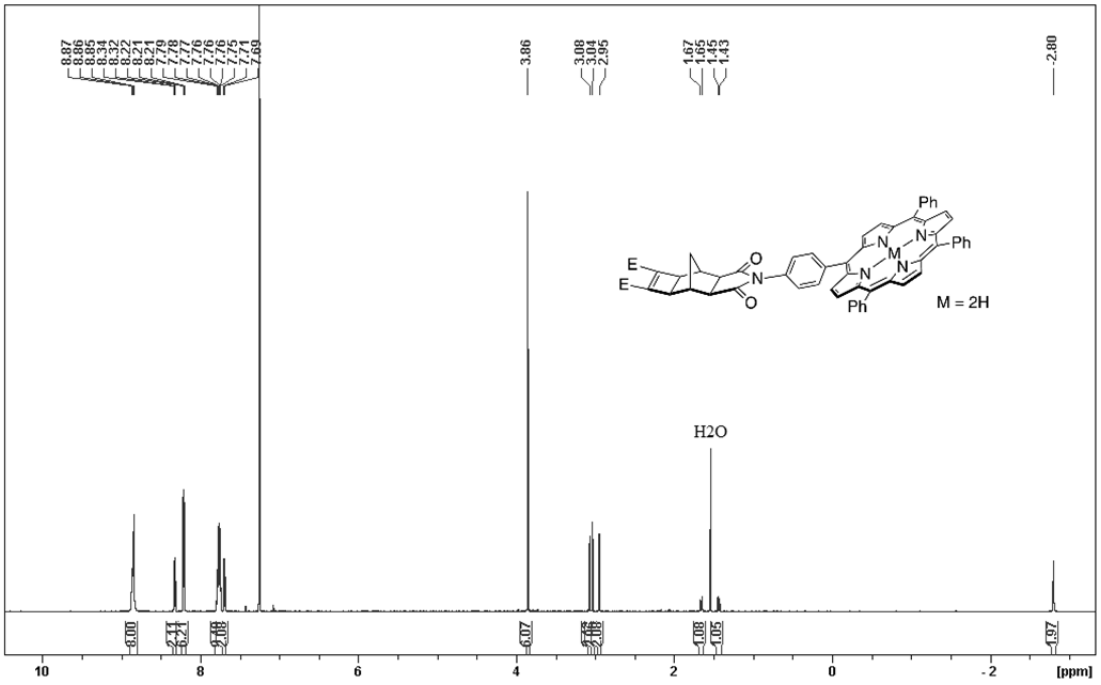

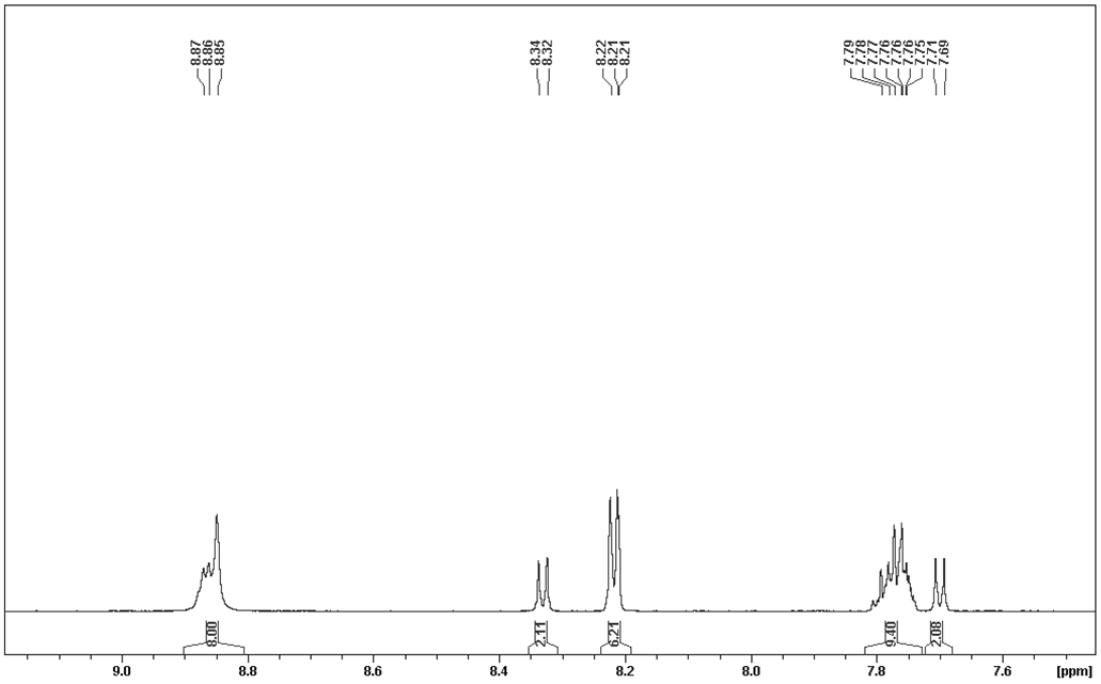

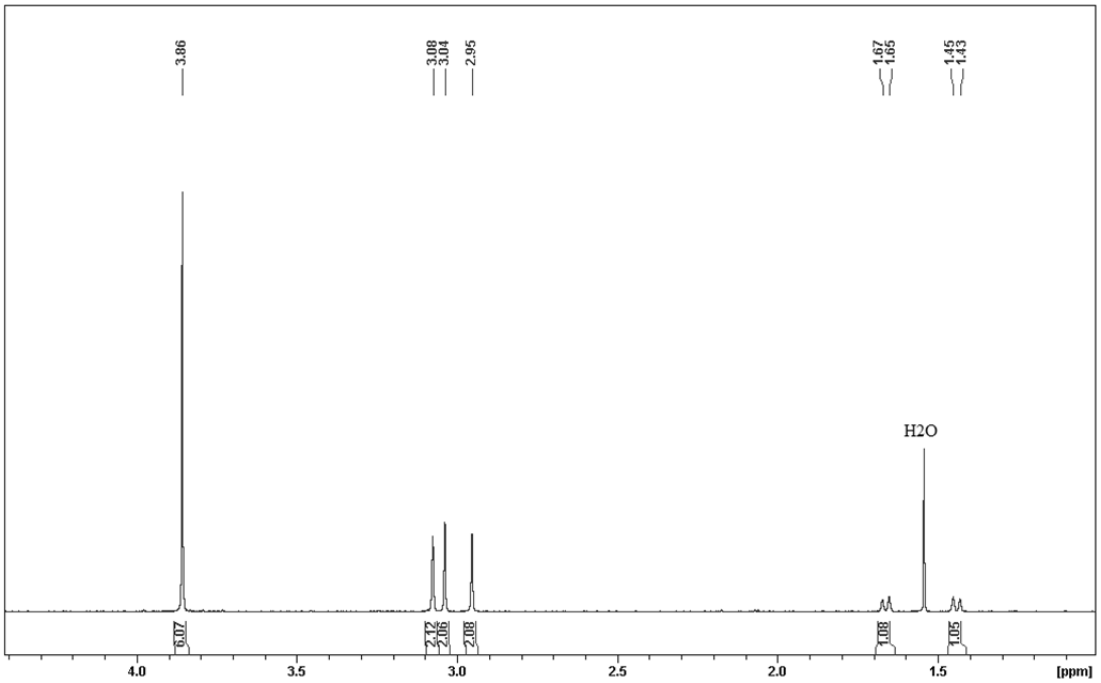
3.86
3.08
3.04
2.95
1.67
1.65
1.45
1.43
H2O
6.07
2.12
2.06
2.08
1.08
1.05
4.0
3.5
3.0
2.5
2.0
1.5
[ppm]

9.8.2 UV-Vis

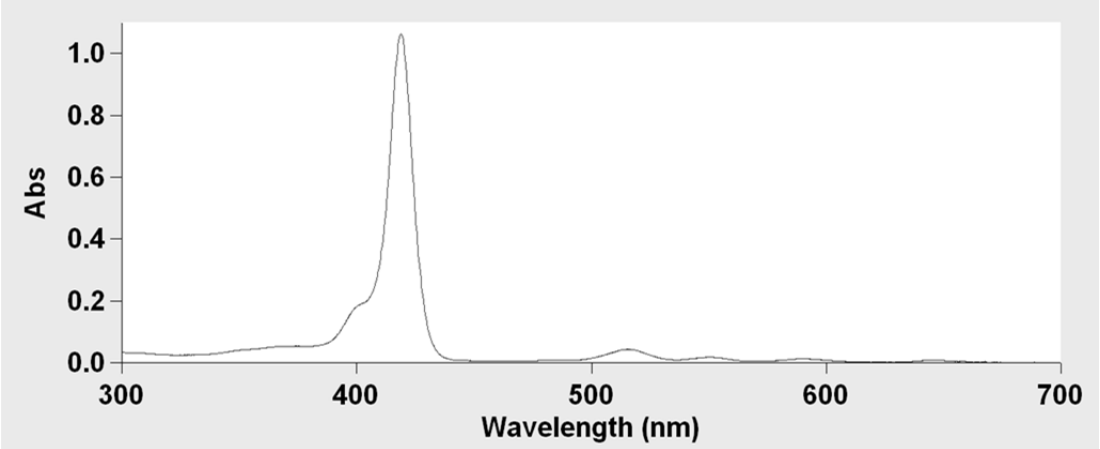
Abs
1.0
0.8
0.6
0.4
0.2
0.0
300
400
500
600
700
Wavelength (nm)

9.9 Zn(II) *Exo*- Mono-porphyrin Receptor (Soluble for Titrations) **22**

9.9.1 ^{1}H NMR

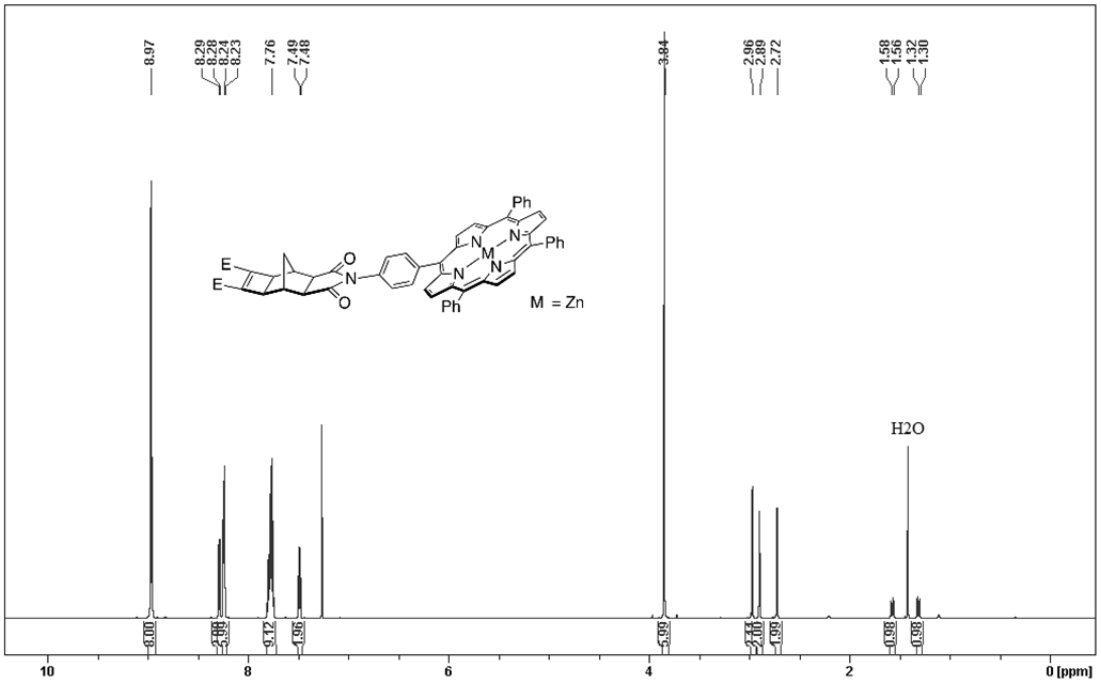

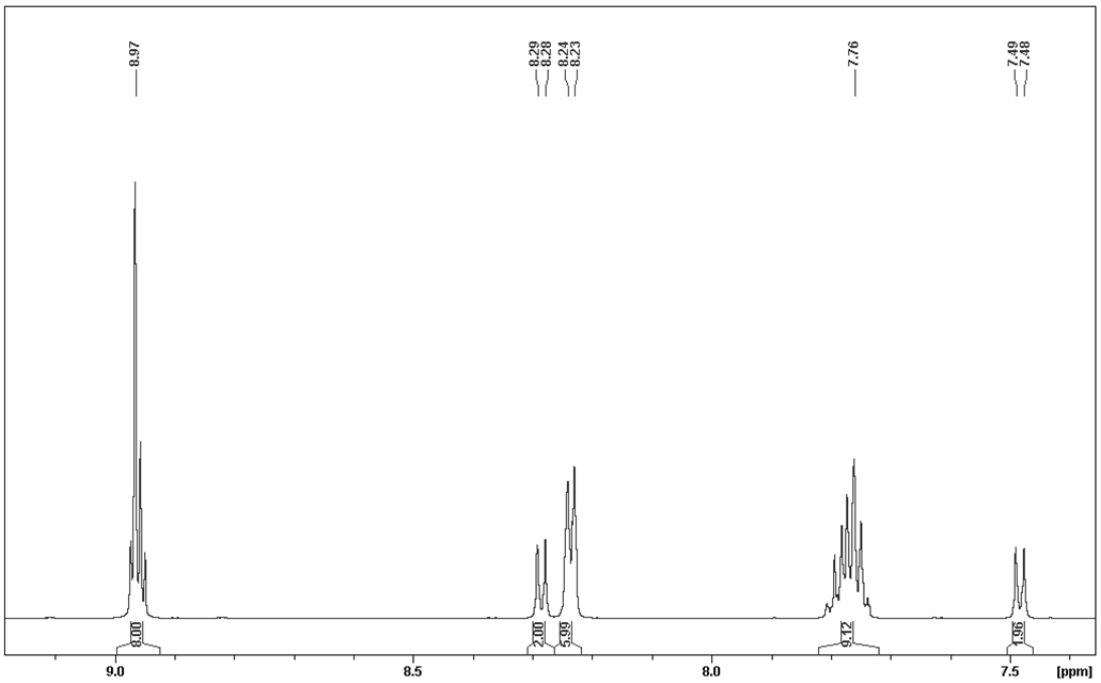

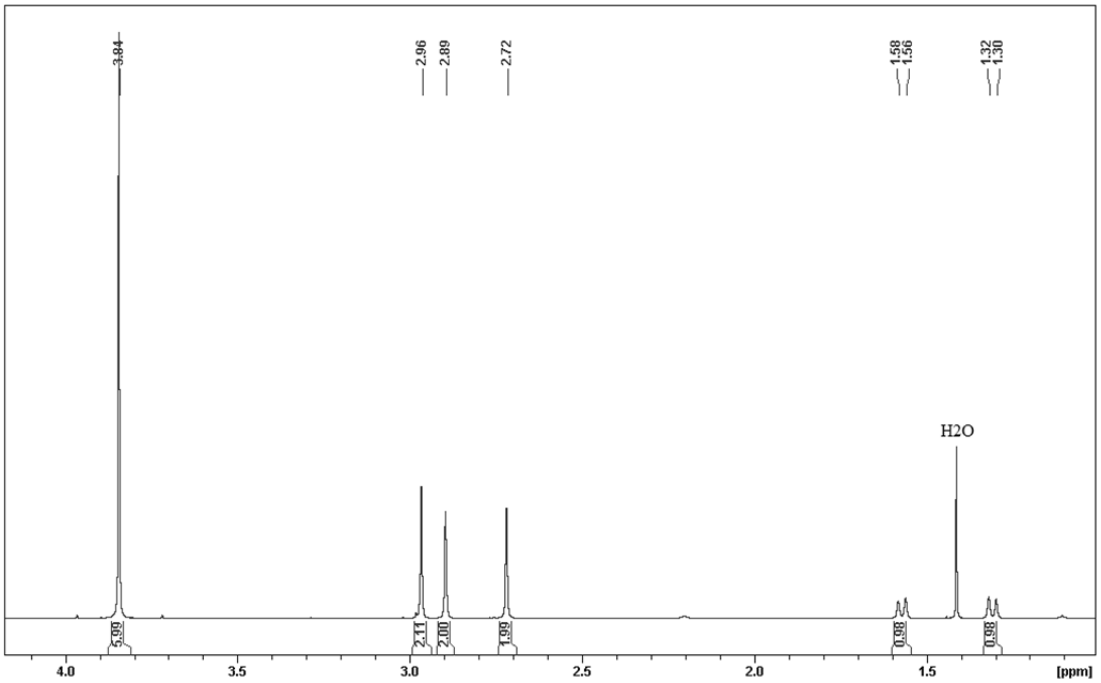
3.84
2.96
2.89
2.72
1.58
1.56
1.32
1.30
H2O
5.00
2.11
2.00
1.99
0.98
0.98
4.0
3.5
3.0
2.5
2.0
1.5
[ppm]

9.9.2 UV-Vis

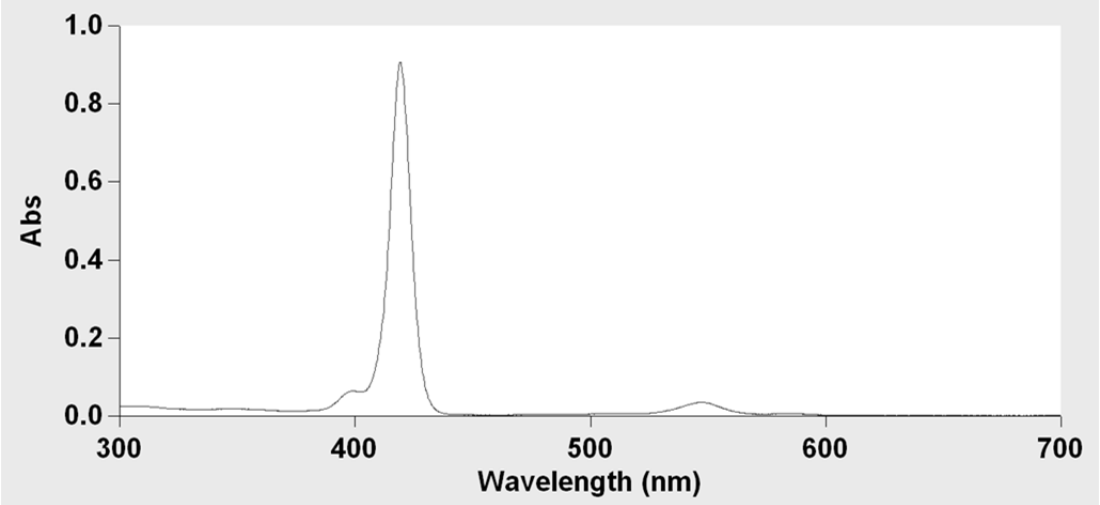
1.0
0.8
0.6
0.4
0.2
0.0
Abs
300
400
500
600
700
Wavelength (nm)

10. Appendix 2 - Methodology for the Determination of Binding Models, Speciation, and Cooperativity

10.1 Multivariate Global Spectral Analysis (curve fitting)

HypSpec [166] is a commerically available multivariate global spectral analysis computer program, which enables UV-Vis spectrophotometric titration data to be fitted (nonlinear least-squares) to a binding model to determine association constants. The freely available HySS program enables speciation diagrams to be generated. Multivariate global spectral analysis is employed by many supramolecular research groups [32, 66, 82, 165, 232] as the best method for determining binding models in supramolecular systems.

In the case of HypSpec, the user inputs a spreadsheet containing concentrations of host and guest for the titration, along with the range of wavelengths and corresponding absorbances. Within the program, a binding model in the format $(host)_x$:$(guest)_y$ is entered based on the suspected behaviour of the supramolecular system and the data is analysed in terms of the number of different coloured species in solution (the program caters for the formation of multiple simultaneous species).

To begin with, the data is manually fitted by providing an initial approximation of the association constant(s) for the species. The association constants for the species are then refined by the HypSpec program, which converges on the association constants for the entered binding model.

The output must then be cautiously analysed to determine if the fit is valid (or in circumstances where multiple binding models can be fitted, which is the best fit). In deciding whether the fit is valid, several considerations are important; (a) visual inspection of the fit; (b) the standard deviation of the association constant(s), and the difference between calculated and observed data points (the residuals); (c) the physical ability of the system to form the species being fitted; (d) whether the calculated UV-Vis spectrum resembles the experimental spectrum (intensity profile), and whether the calculated species assigned to a particular wavelength is experimentally reasonable based on the ratio of components and their known experimental values (e.g. the wavelengths of different porphyrin states [free/uncomplexed, sandwich, and mono-complexed] are all experimentally known).

However, the goodness of the data fitting alone is not always sufficient to decide the correct binding model [30]. In some cases, UV-Vis titration data can be equally fitted to two different binding models, where the intermediate sandwich species has the same empirical stoichiometry (e.g. intramolecular 1:1 or intermolecular 2:2) and are indistinguishable at a single concentration (UV-Vis is micromolar). This is addressed by comparison with the results of the NMR titration (millimolar concentration), and is explained in the next paragraph.

10.2 Predicting NMR behaviour based on the results of UV-Vis

To test the validity of the fitted binding model, and to assign the correct binding model when the UV-Vis suggests to equally suitable candidates, several research groups apply the association constants determined from the UV-Vis titration data to predict the behaviour of the system during NMR titrations [28, 30, 31, 58]. This is achieved by calculating a simulated NMR speciation diagram and comparing it to the experimental NMR titration data [28, 30, 31]. This can be applied to the example of intramolecular 1:1 or intermolecular 2:2 in the previous paragraph because the 2:2 assembly is dependent on porphyrin concentration, and so its stability is increased at higher concentrations, allowing it to be distinguished from the intramolecular 1:1 species, which is independent of porphyrin concentration [30].

However, this technique cannot be applied in circumstances where intermolecular species are not observed at UV-Vis concentrations (typically micromolar), but are observed at NMR concentrations (typically millimolar). An example of this was discussed for mono-porphyrin/DABCO in chapter 3, and the work in this thesis has presented additional examples where the UV-Vis results cannot be translated to the NMR results.

10.2.1 Experimental Speciation from NMR Titration Data

When a system is in slow exchange between two species, free and complex A, the relative integration of the complexed resonance to the total host resonance (free plus complexed) can be used to determine the population of the species [28, 30, 31] (Equation 1).

$$\%\ speciation = \left(\frac{\int_{complexed\ resonance\ only}}{\int_{total\ host\ resonance\ (free+complexed)}}\right) \times 100 \quad \text{..... Equation 1}$$

Subsequently, when a system moves into fast exchange between two different species, A and B, the average chemical shift can be used to determine the population of the species [28, 30, 31], by considering the position of the averaged chemical shift along a continuum between the two extremes of each pure species A and B, provided these chemical shifts are both known (Equation 2).

$$\%\ speciation\ =\ abs\left(\frac{\delta_{average}-\delta_{species\ A}}{\delta_{species\ B}-\delta_{species\ A}}\right)\times 100$$ …… Equation 2 [30]

Equations 1 and 2 assume that each stage (slow and fast exchange respectively) only involve two species each; that free host is wholly converted to complex A by a given point, after which species B begins to form from complex A.

10.3 Determination of Interannular Cooperativity by Statistical Analysis

In a series of publications by Ercolani [88, 93, 199], a method is presented for the statistical analysis of associations constants using symmetry numbers, and in which inter- and intra- molecular processes are considered as two fundamentally different types of interactions. This method is founded on Ercolani's notion that "*to assess cooperativity, only virtually identical processes described by equilibrium constants having the same dimensions should be compared*", and as such, intermolecular processes (units M^{-1}) must be considered independently of intramolecular processes (dimensionless). This concept explained in further detail in the original method [93, 199]. Most recently, Ercolani has defined interannular cooperativity as cooperativity which arises from the interplay between two or more intramolecular binding interactions [88].

Prior to analysing the experimentally determined association constants for cooperativity, the statistical symmetry factor for the supramolecular event, K_σ, must be calculated from the symmetry factors for each species, $\sigma_{species}$ (products and reactants, see Equations 3 and 4). This constant accounts for the contribution of degenerate bound states to the magnitude of the association constant, and an excellent summary of this is provided in [93, 199].

$$xX + yY \overset{K}{\rightleftharpoons} zZ$$ …… Equation 3 [88, 93]

$$K_\sigma = \frac{\sigma_{reactants}}{\sigma_{products}} = \frac{{\sigma_X}^x {\sigma_Y}^y}{{\sigma_Z}^z}$$ …… Equation 4 [88, 93]

$\sigma_{species} = \sigma_{ext}\sigma_{int}$ ..... Equation 5 [93]

$\sigma_{species}$ is the product of the external symmetry number, σ_{ext} and the internal symmetry number, σ_{int} (Equation 5) [93]. σ_{ext} is the number of different but indistinguishable atomic arrangements obtained by rotating the molecule as a whole, calculated by multiplying the order of the independent simple rotational axes of the molecule's point group point [93] (Table 10.1, partially reproduced from [93]). σ_{int} is the number indistinguishable rotations about single bonds within the molecule. Assessment of σ_{int} depends on the statistician's existing knowledge of the ability of single bonds to freely rotate in a given molecule, and is not always known. In deciding whether to include or discount a rotation, it is important to remain consistent in the approach for all subsequent manipulations. The calculation of symmetry numbers is further explained in [93, 199] and references within.

Table 10.1 - Selected External Symmetry Numbers, σ_{ext}, for Various Point Groups (partially reproduced from [93]).

Point Group	**σ_{ext}**
C_s	1
C_{nv}, C_{nh}	n
D_{nh}	2n

To undertake Ercolani's method of assessing interannular cooperativity [88], the following parameters must be derived from the experimental data:

(1) The reference microscopic intermolecular association constant, K_{inter}, is derived from the experimentally determined association constant for monodentate receptor with monodentate ligand, along with K_σ for this system.

(2) The reference microscopic effective molarity, EM,[41] is derived from the experimentally determined association constant for bidentate receptor with bidentate ligand, along with K_σ for this system, using K_{inter} determined from step (1).

(3) The product of the effective molarity for the interannular system with bidentate ligand in which cooperativity is being assessed, EM_1EM_2 (for two binding

[41] Microscopic EM is defined as the ratio K_{intra}/K_{inter} (units $molL^{-1}$) [93]. The non-microscopic EM is the product of microscopic EM and the cyclisation statistical factor [88, 92]. EM is a measure of the stabilisation resulting from the chelate effect for related intermolecular and intramolecular interactions [30, 52, 58], and has been used extensively by both Hunter and Anderson [30, 31, 52, 53] to quantify host-guest complementarity [53].

sites), is derived from the experimentally determined association constant for this system, along with K_σ for this system, using K_{inter} determined from step (1).

Steps (1) to (3) can be achieved by substitution into the universal Equation 6 [88], where b is the number of binding interactions joining components, and c is the degree of cyclicity of the assembly, equal to $b - i + 1$, where i is the number of components.

$$K_{exp} = \alpha\gamma K_\sigma K_{inter}^{b} EM^{c} \quad \text{..... Equation 6 [88]}$$

The constants α and γ in Equation 6 refer to the allosteric and interannular cooperativity factors of the system respectively. It is important to ascertain that allosteric cooperativity is not present for the system, otherwise this can result in the incorrect determination of the reference EM value, leading to allosteric cooperativity being misinterpreted as interannular cooperativity [88]. This can be achieved by studying association of the bidentate receptor with monodentate ligand [88].

Most importantly, Equation 7 enables the interannular cooperativity factor, γ, to be quantified from the ratios of the reference EM to the interannular EM determined in steps (2) and (3).

$$\gamma = \frac{EM_1 EM_2}{EM^2} \text{..... Equation 7 [88]}$$

If EM is equal to EM_1 and equal to EM_2, the system is non-cooperative and γ = 1. If EM_1EM_2 is greater than EM^2, the system is positively interannularly cooperative and γ is greater than 1. If EM_1EM_2 is less than EM^2, the system is negatively interannularly cooperative and γ is less than 1.

A worked example of this method [88] applied to the tetra-porphyrin tweezer/DABCO system from Chapter 5 is provided in Appendix 5.

11. Appendix 3 - Mitsudo Reactivity

11.1 Summary

During the course of this work, difficulty was encountered with the Mitsudo [2+2] cycloaddition reaction for bis-norbornene phenyl diimide substrates **15** and **47** (Figure 11.1 (a), (b)). Very few substrates are identified in the literature that do not undergo the Mitsudo reaction [118, 233]. The substrates in this work have been partially investigated in our laboratory by designing several additional structurally related compounds, however further investigation is still required. A summary of work completed so far is provided in this Appendix, along with a discussion of various literature substrates both successful and unsuccessful for the Mitsudo reaction.

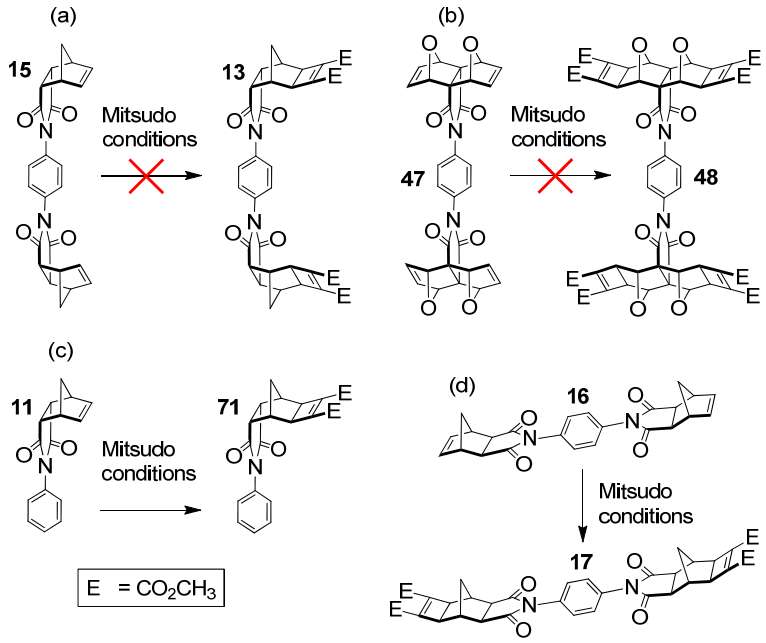

Figure 11.1 - bis-norbornene phenyl diimide substrates which do not (a), (b), and do (c), (d) undergo the Mitsudo reaction (conditions: 2 eq. DMAD per double bond, 5 mol-% $[RuH_2(CO)(PPh_3)_3]$ per double bond, solvent, Δ, up to several days).

Preliminary results suggest that the bis-*exo*- norbornene phenyl diimide **16**[42] (Figure 11.1 (d)) does undergo the Mitsudo reaction, as does the mono-*endo*- norbornene phenyl imide **11**[43] (Figure 11.1 (c)), contrary to reports in [152] about **11**. This indicated that the poor reactivity of **15** and **47** could be related to the orientation of the bis-norbornene in these compounds; two closely spaced *endo*- moieties could

[42] Compound **16** has been previously synthesised using a different method [154-156].

[43] Compound **11** has been previously synthesised using a different method [152, 229].

impede access to the alkene[44] by the sterically bulky catalyst $Ru[H_2CO(PPh_3)_3]$ in these freely rotating substrates.

Preliminary data for the *syn*- **27** and *anti*- **28** restricted rotation analogues (structures in Chapter 4) of freely rotating compound **15** suggests that only one of the two conformation successfully undergoes the Mitsudo reaction. However, this is very much a preliminary result, and requires further investigation before this can be confirmed. It remains unknown why the compound **15** does not react (Figure 11.1 (a)), as this can undergo free rotation between both the *syn*- and *anti*- conformations.

If conformational dependence on Mitsudo reactivity is established for the *syn*- **27** and *anti*- **28** restricted rotation analogues of freely rotating **15**, the Mitsudo reaction will be attempted on the problem substrates using the alternative and less sterically encumbered catalyst Ru[Cl(cod)(Cp*)] [147, 234] (cod = 1,5-cyclooctadiene, Cp* = pentamethylcyclopentadienyl).

11.2 Literature Examples

There are many literature examples of substrates where sterically congested *syn*- bis-norbornenes successfully undergo the Mitsudo reaction [103, 233, 235-239], as shown in Figure 11.2. Molecular modelling (not shown) comparing the substrates in Figure 11.2 and with compounds **15** and **47** (Figure 11.1 (a) and (b)) does show that the two alkenes in **15** and **47** are directed more inward towards each other (more sterically congested) than the compounds in Figure 11.2.

Substrates which do not undergo the Mitsudo reaction appear to be uncommon and are infrequently published. The most notable example published in the literature is shown in Figure 11.3 [233], which are oxygenated analogues of Figure 11.2 (a) and (b). Furthermore, poor reactivity for the substrates in Figure 11.3 was observed for cycloaddition with *s*-tetrazine derivatives, a reaction which is known to proceed by an inverse electron demand Diels-Alder reaction [240, 241]. The authors suggest that the ketone and alcohol substituents in Figure 11.3 modify the reactivity of the norbornene π bonds compared to the carbon analogues in Figure 11.2 (a) and (b) [233].

[44] The relative rate of the Mitsudo reaction on the *endo*- and *exo*- anhydrides **7** and **8** to derivatives **12** and **20** respectively (structures in Chapter 3) is reported to be slower for the *endo*- substrate [152], which [152] suggest could be related to additional steric factors in compound **7**.

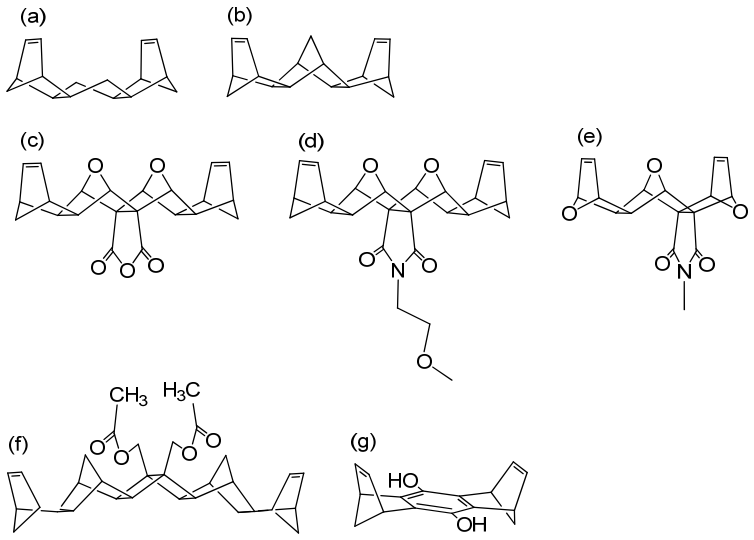

Figure 11.2 - Examples of closely spaced *syn*- bis-norbornenes which successfully undergo the Mitsudo reaction [103, 233, 235-239].

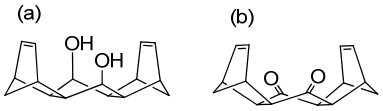

Figure 11.3 - Examples of closely spaced *syn*- bis-norbornenes which are inert to the Mitsudo reaction [233]; (a) does not undergo Mitsudo reaction or cycloadditions with *s*-tetrazine derivatives; (b) does not undergo the Mitsudo reaction, and cycloaddition with tetrazine derivatives occurs on a single side only.

In addition, imide substitution has been reported to significantly influence the yield of the Mitsudo reaction (Figure 11.4) [118]. Low yields are reported for ethylene glycol imides compared to phenyl imides (Figure 11.4 (a)), leading the authors to suggest that the cycloaddition catalyst could be involved in competitive binding with the ethylene glycol functionality [118]. For the phenyl imide (Figure 11.4 (b)), significantly higher yields for the Mitsudo reaction are reported on the ring closed imide compared to the precursor amic acid imide. While retro- Diels-Alder reactions are known to occur in these substrates, perhaps this process occurs at a higher rate in the amic acid than the imide.

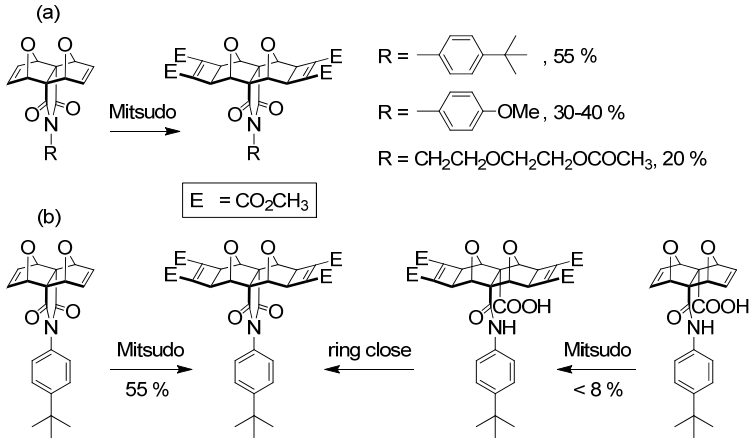

Figure 11.4 - Substrates with variable Mitsudo yields depending on imide substitution [118].

11.3 Concluding Remarks

In summary, there does not appear to be any defining structural feature to predict a substrate's suitability for the Mitsudo reaction. It is possible that the Mitsudo reaction is affected by both steric and electronic factors depending on the substrate and its substitution. Further investigations are underway in our laboratory.

12. Appendix 4 - X-Ray Crystallographic Data

X-Ray diffraction measurements and solving of X-ray crystal structures was conducted by Dr Rebecca Norman (Flinders University), Assoc Prof Christopher Sumby (The University of Adelaide), and Prof Jonathan White (The University of Melbourne). The following data was provided by these people.

12.1 PMB Protected T-piece **50**

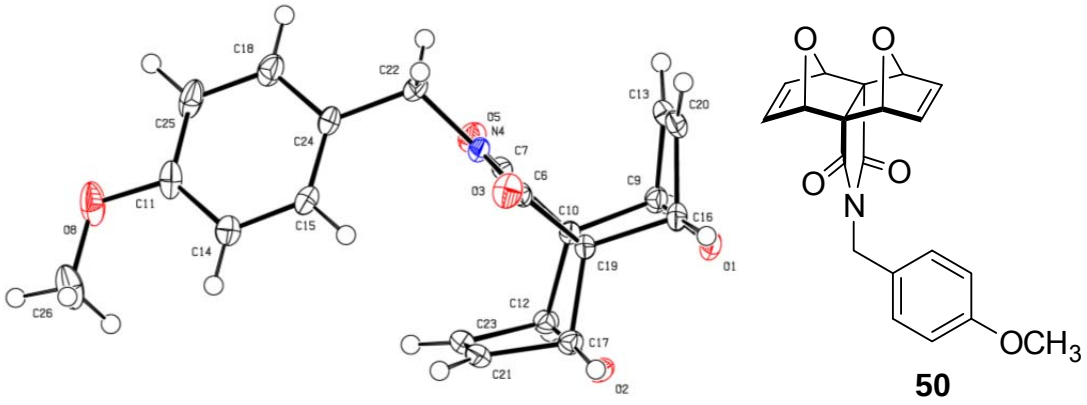

50

Table 12.1 - Crystal Data and Structure Refinement for PMB protected T-piece **50**.

Parameter	**PMB protected T-piece 50**
Empirical formula	C20 H17 N O5
Formula weight	351.35
Temperature (K)	150
Wavelength (Å)	0.71073
Crystal system	triclinic
Space group	'P 21/n'
Unit cell dimensions	a =7.4138(4) b=22.8374(10) c=9.5317(5)
Theta max	29.27
Reflections used	3830
Final R indices [I > 2σ(I)]	
R1	0.0439
wR2	0.1067
Data completeness	0.879

12.2 T-piece Imide **51**

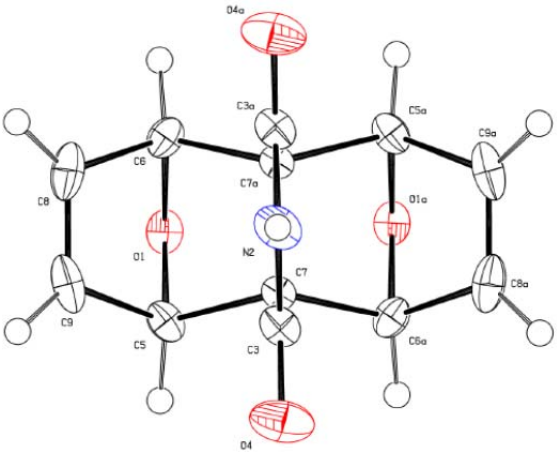

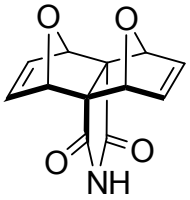

51

Table 12.2 - Crystal Data and Structure Refinement for T-piece Imide **51**.

Parameter	**T-piece Imide 51**
Empirical formula	C12 H9 N O4
Formula weight	231.2
Temperature (K)	150
Wavelength (Å)	0.71073
Crystal system	monoclinic
Space group	'C 1 2/c 1'
Unit cell dimensions	a=13.5746(16) b=6.6256(4) c=13.5089(16)
Theta max	29.2
Reflections used	944
Final R indices [I > 2σ(I)]	
R1	0.0445
wR2	0.1272
Data completeness	0.883

12.3 Mitsudo T-piece Imide **49**

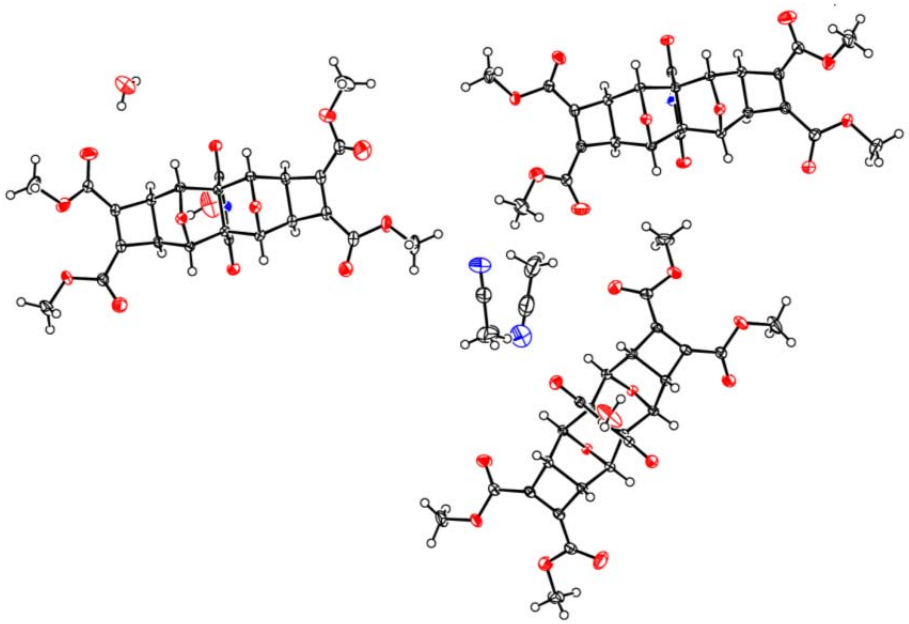

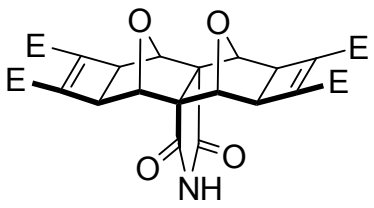

49

Table 12.3 - Crystal Data and Structure Refinement for Mitsudo T-piece Imide **49**.

Parameter	**Mitsudo T-piece Imide 49**
Empirical formula	3(C24 H21 N O12), 2(C2 H3 N), 3(H2 O)
Formula weight	1682.41
Temperature (K)	150
Wavelength (Å)	0.71073
Crystal system	monoclinic
Space group	'P 21/c'
Unit cell dimensions	a=9.0952(2) b=6.6256(6) c=24.0116(5)
Theta max	29.4
Reflections used	14596
Final R indices [I > 2σ(I)]	
R1	0.0569
wR2	0.1424
Data completeness	0.866

12.4 Freely Rotating non-Mitsudo I-piece **47**

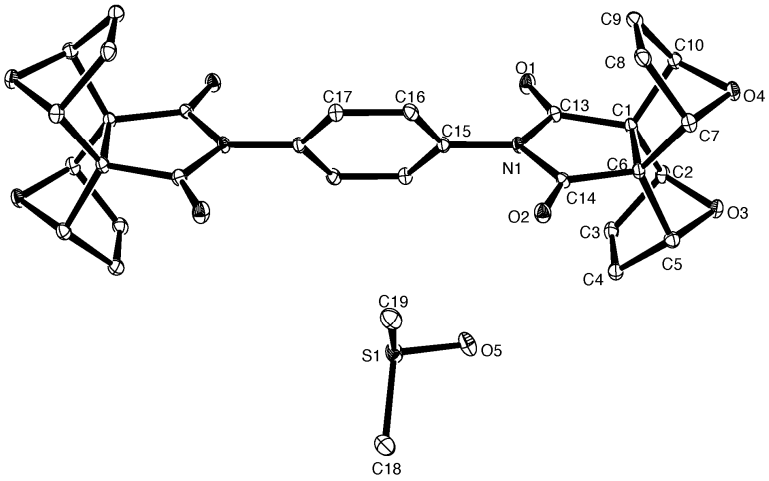

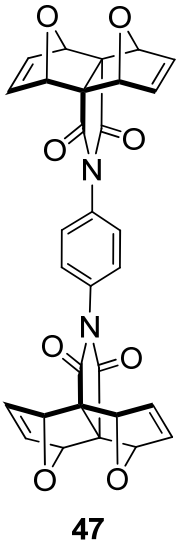

47

Table 12.4 - Crystal Data and Structure Refinement for Freely Rotating non-Mitsudo I-piece **47**.

Parameter	**Freely Rotating non-Mitsudo I-piece 47**
Empirical formula	C30 H20 N2 O8, 2(C2 H6 O S)
Formula weight	346.37
Temperature (K)	100.00
Wavelength (Å)	1.5418
Crystal system	Triclinic
Space group	'P-1'
Unit cell dimensions	a = 7.6974(5) b = 9.8515(7) c = 10.6292(9)
Theta max	76.766
Reflections used	3169
Final R indices [I > 2σ(I)]	
R1	0.0552
wR2	0.1413
Data completeness	0.941

12.5 *Syn*- Restricted Rotation *Exo*- non-Mitsudo Linker **31**

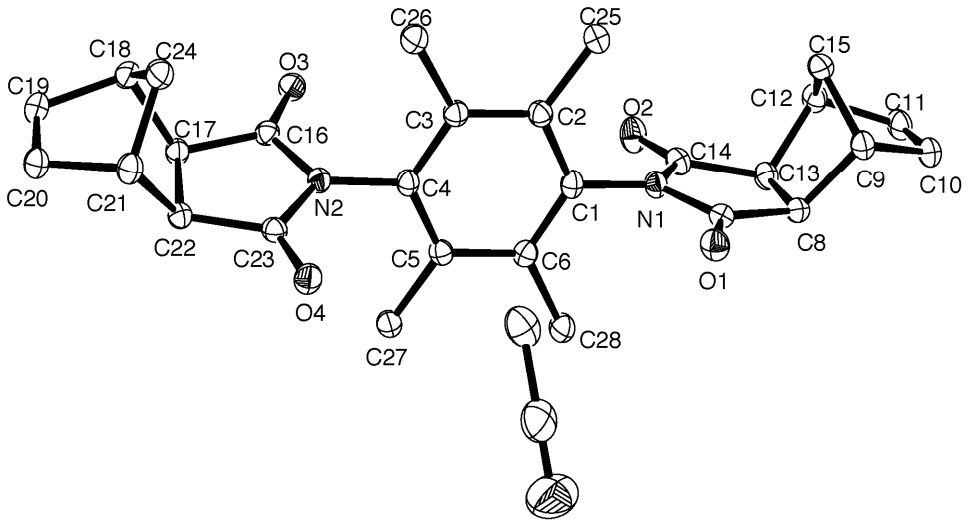

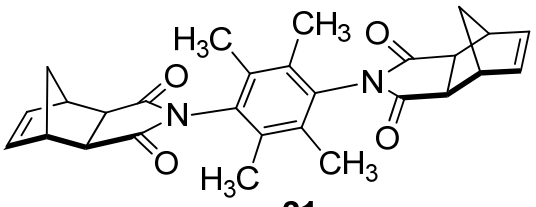

31

Table 12.5 - Crystal Data and Structure Refinement for *syn*- restricted rotation *exo*- non-Mitsudo linker **31**.

Parameter	***syn*- restricted rotation *exo*- non-Mitsudo linker 31**
Empirical formula	C28 H28 N2 O4, C2 H3 N
Formula weight	534.63
Temperature (K)	130.00
Wavelength (Å)	1.5418
Crystal system	Triclinic
Space group	'P-1'
Unit cell dimensions	a = 8.6452(5) b = 11.1356(5) c = 15.0205(6)
Theta max	76.683
Reflections used	5163
Final R indices [I > 2σ(I)]	
R1	0.0407
wR2	0.1054
Data completeness	0.973

12.6 *Anti*- Restricted Rotation *Exo*- non-Mitsudo Linker **32**

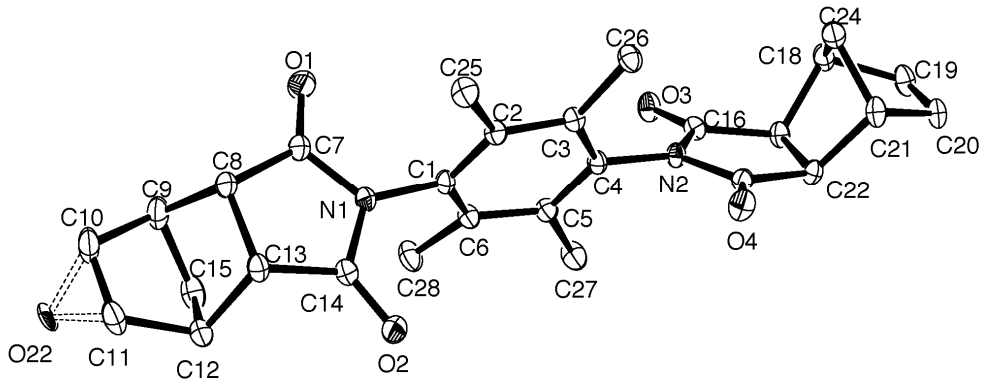

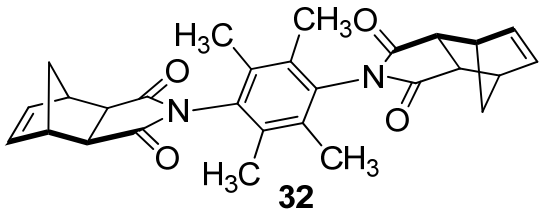

32

Table 12.6 - Crystal Data and Structure Refinement for *anti*- restricted rotation *exo*- non-Mitsudo linker **32**.

Parameter	***anti*- restricted rotation *exo*- non-Mitsudo linker 32**
Empirical formula	C28 H28 N2 O4.06
Formula weight	457.56
Temperature (K)	130.00
Wavelength (Å)	0.7107
Crystal system	Triclinic
Space group	'P-1'
Unit cell dimensions	a = 10.5365(13) b = 10.7150(9) c = 11.866(2)
Theta max	32.017
Reflections used	6270
Final R indices [I > 2σ(I)]	
R1	0.0486
wR2	0.1311
Data completeness	0.794

13. Appendix 5 - Statistical Analysis of Association Constants and Interannular Cooperativity

This appendix provides tables of parameters, diagrams, and formulae supporting the statistical analysis of interannular cooperativity presented in Chapter 5. In addition, a fully worked example of assessing interannular cooperativity of the tetra-porphyrin/DABCO system is provided, using Ercolani's method [88], previously summarised in Chapter 5 and Appendix 2.

13.1 Tables of Parameters

Table 13.1 - Summary of statistical parameters

Species	Point Group	σ_{ext}	σ_{int}	$\sigma_{species}$	K_σ
Quinuclidine **24**	C_{3v}	3	1	3	-
Pyridine **25**	C_{2v}	2	1	2	-
DABCO **5**	D_{3h}	6	1	6	-
Bipyridine **6**	D_{2h}	4	1	4	-
mono-porphyrin **22**	C_s	1	2	2	-
freely rotating host **1**	C_{2h}	2	4	8	-
tetra-porphyrin host **4**	D_{2h}	4	64	256	-
mono-por:quin **22**:**24**	C_s	1	3	3	2
mono-por:pyridine **22**:**25**	C_s	1	2	2	2
freely rotating:DABCO **1**:**5**	C_{2h}	2	3	6	8
freely rotating:bipy **1**:**6**	C_{2h}	2	2	4	8
tetra-porphyrin:$(DABCO)_2$ **4**:$(\mathbf{5})_2$	D_{2h}	4	9	36	256
tetra-porphyrin:$(bipy)_2$ **4**:$(\mathbf{6})_2$	D_{2h}	4	4	16	256

Table 13.2 - Summary of experimental association constants, calculated K_{inter}, EM, EM_1EM_2, and γ

Species	K_{exp}	K_{inter}	EM[#]	EM_1EM_2	γ[#]
mono-por:quin **22**:**24**	2.53×10^5 M^{-1}	1.265×10^5 M^{-1}	-	-	-
mono-por:pyridine **22**:**25**	2×10^3 M^{-1} *	1×10^3 M^{-1}	-	-	-
freely rotating:DABCO **1**:**5**	8.1×10^7 M^{-1}	-	6.28×10^{-4} M	-	-
freely rotating:bipy **1**:**6**	4.97-5.27 $\times 10^5$ M^{-1} †	-	6.21 - 6.59 $\times 10^{-2}$ M †	-	-
tetra-porphyrin:$(DABCO)_2$ **4**:$(\mathbf{5})_2$	6.32×10^{13} M^{-2}	-	-	9.5×10^{-10} M^2	2.41×10^{-3}
tetra-porphyrin:$(bipy)_2$ **4**:$(\mathbf{6})_2$	5.17×10^{12} M^{-2}	-	-	2.02×10^{-2} M^2	4.65 - 5.24 †

* literature reports association constants of the order of 10^3 M^{-1} [27, 53, 55, 58, 78, 97, 98, 165]. † quoted as a range due to uncertainty in the stock tweezer concentration for this titration, affecting the association constant, EM, and γ. [#] assuming the absence of allosteric cooperativity ($\alpha = 1$).

13.2 Worked Example

Calculating Reference K_{inter}

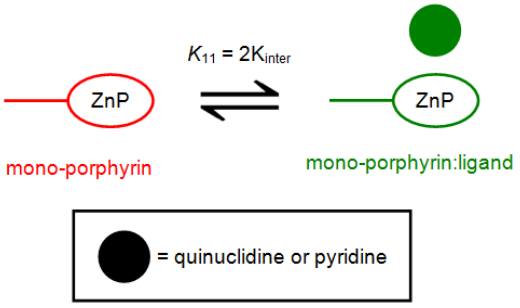

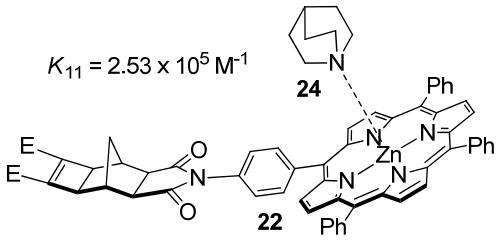

$$K_\sigma = \frac{\sigma_{quin}{}^1 \sigma_{mono-por}{}^1}{\sigma_{mono-por:quin}{}^1} = \frac{3\times2}{3} = 2$$

$K_{exp} = \alpha\gamma K_\sigma K_{inter}^b EM^c$ [88] ; α = 1 (none), γ = 1 (none), K_σ = 2, b = 1, c = 0

$$K_{11} = 2K_{inter} = 2.53 \times 10^5\ M^{-1}$$

$$K_{inter} = \frac{K_{11}}{2} = \frac{2.53 \times 10^5\ M^{-1}}{2} = 1.265 \times 10^5\ M^{-1}$$

Calculating Reference EM

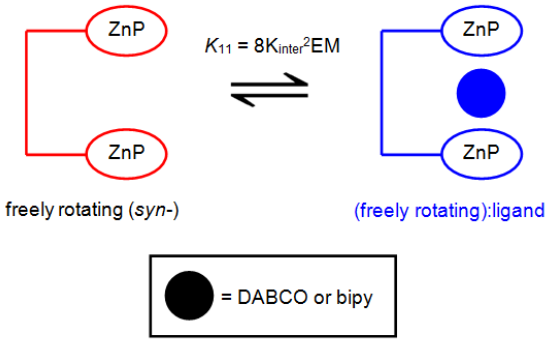

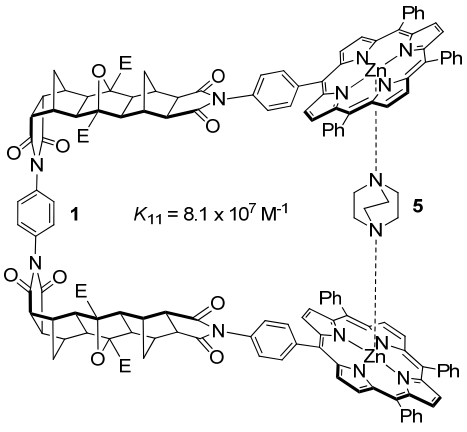

$$K_\sigma = \frac{\sigma_{DABCO}{}^1 \sigma_{freely\ rotating\ tweezer}{}^1}{\sigma_{freely\ rotating\ tweezer:DABCO}{}^1} = \frac{6\times8}{6} = 8$$

$K_{exp} = \alpha\gamma K_\sigma K_{inter}^b EM^c$ [88] ; α = 1 (assumed), γ = 1 (none), K_σ = 8, b = 2, c = 1

$K_{11} = 8K_{inter}^2 EM = 8.1 \times 10^7\ M^{-1}$; K_{inter} = 1.265 x 10^5 M^{-1}

$$EM = \frac{K_{11}}{8K_{inter}^2} = \frac{8.1 \times 10^7\ M^{-1}}{8(1.265 \times 10^5\ M^{-1})^2} = 6.33 \times 10^{-4}\ M$$

Calculating EM_1EM_2

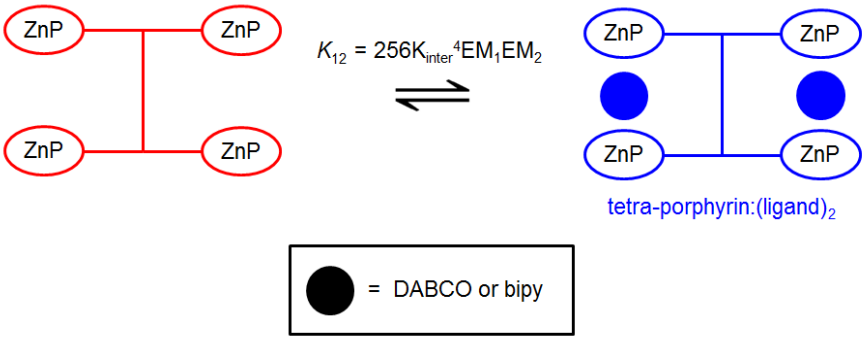

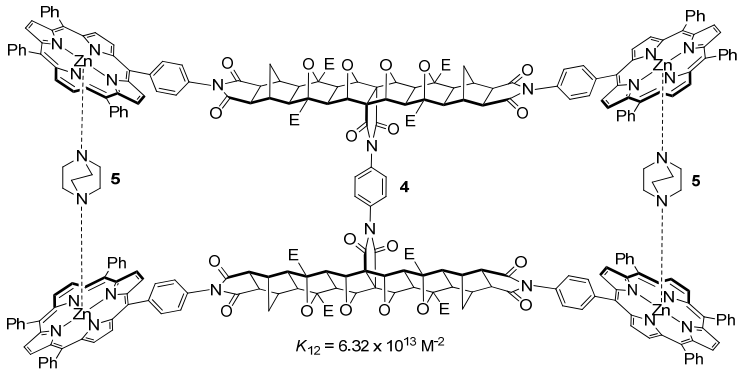

$$K_\sigma = \frac{\sigma_{DABCO}{}^2 \sigma_{tetra-porphyrin\ tweezer}{}^1}{\sigma_{tetra-porphyrin\ tweezer:(DABCO)_2}{}^1} = \frac{6^2 \times 256}{36} = 256$$

$K_{exp} = \alpha\gamma K_\sigma K_{inter}^b EM^c$ [88] ; α = 1 (assume), K_σ = 256, b = 4, c = 2 = EM$_1$EM$_2$

$K_{12} = 256K_{inter}^4 EM_1\ EM_2 = 6.32 \times 10^{13}\ M^{-2}$; K_{inter} = 1.265 x 10^5 M^{-1}

$$EM_1\ EM_2 = \frac{K_{12}}{256K_{inter}^4} = \frac{6.32 \times 10^{13}\ M^{-2}}{256(1.265 \times 10^5\ M^{-1})^4} = 9.64 \times 10^{-10}\ M^2$$

Calculating Interannular Cooperativity Factor, γ

$\gamma = \frac{EM_1EM_2}{EM^2}$; EM = 6.28 x 10^{-4} M, EM$_1$EM$_2$ = 9.5 x 10^{-10} M^2

$$\gamma = \frac{9.64 \times 10^{-10}\ M^2}{(6.33 \times 10^{-4}\ M)^2}$$

$\gamma = 2.4 \times 10^{-3}$; γ < 1

∴ negative interannular cooperativity.

References

1. Murphy, R.B., et al., *Molecular Tweezers with Freely Rotating Linker and Porphyrin Moieties.* Eur. J. Org. Chem., 2013. **2013**(15): p. 2985-2993.
2. Murphy, R.B., et al., *Tetra-Porphyrin Molecular Tweezers with Two Binding Sites Linked via a Polycyclic Rotatable Phenyl Diimide Core.* drafted, 2015.
3. Lehn, J.-M. *Nobel Lecture, Supramolecular Chemistry - Scope and Perspectives, Molecules - Supermolecules - Molecular Devices,* http://nobelprize.org/nobel_prizes/chemistry/laureates/1987/lehn-lecture.html. 1987.
4. Steed, J.W. and J.L. Atwood, *Supramolecular Chemistry*. first ed. 2000: John Wiley & Sons, Ltd.
5. Balzani, V., C. Credi, and M. Venturi, *Light Powered Molecular Machines.* Chem. Soc. Rev., 2009. **38**: p. 1542-1550.
6. Lee, C.-H., H. Yoon, and W.-D. Jang, *Biindole-Bridged Porphyrin Dimer as Allosteric Molecular Tweezers.* Chem. - Eur. J., 2009. **15**: p. 9972-9976.
7. Hardouin-Lerouge, M., P. Hudhomme, and M. Sallé, *Molecular clips and tweezers hosting neutral guests.* Chem. Soc. Rev., 2011. **40**: p. 30-43.
8. Harvey, P.D., et al., *The photophysics and photochemistry of cofacial free base and metallated bisporphyrins held together by covalent architectures.* Coord. Chem. Rev., 2007. **251**: p. 401-428.
9. Leblond, J. and A. Petitjean, *Molecular Tweezers: Concepts and Applications.* ChemPhysChem, 2011. **12**(6): p. 1043-1051.
10. Beletskaya, I., et al., *Supramolecular Chemistry of Metalloporphyrins.* Chem. Rev., 2009. **109**(5): p. 1659-1713.
11. Valderrey, V., G. Aragay, and P. Ballester, *Porphyrin tweezer receptors: Binding studies, conformational properties and applications.* Coord. Chem. Rev., 2014. **258-259**: p. 137-156.
12. Durot, S., J. Taesch, and V. Heitz, *Multiporphyrinic Cages: Architectures and Functions.* Chem. Rev., 2014. **114**(17): p. 8542-8578.
13. Chen, C.-W. and H.W. Whitlock, Jr., *Molecular Tweezers: A Simple Model of Bifunctional Intercalcation.* J. Am. Chem. Soc., 1978. **100**(15): p. 4921-4922.
14. Zimmerman, S.C. and C.M. VanZyl, *Rigid Molecular Tweezers: Synthesis, Characterization and Complexation Chemistry of a Dacridine.* J. Am. Chem. Soc., 1987. **109**: p. 7894-7896.

15. Leblond, J., et al., *pH-Responsive Molecular Tweezers.* J. Am. Chem. Soc., 2010. **132**: p. 8544-8545.
16. Rebek, J., Jr., et al., *Allosteric Effects in Organic Chemistry. Site-Specific Binding.* J. Am. Chem. Soc., 1979. **101**(15): p. 4333-4337.
17. Rebek, J., Jr. and R.V. Wattley, *Allosteric Effects. Remote Control of Ion Transport Selectivity.* J. Am. Chem. Soc., 1980. **102**(14): p. 4853-4854.
18. Rebek, J., Jr. and L. Marshall, *Allosteric Effects: An On-Off Switch.* J. Am. Chem. Soc., 1983. **105**(22): p. 6668-6670.
19. Weinig, H.-G., et al., *Molecular Signal Transduction by Conformational Transmission: Use of Tetrasubstituted Perhydroanthracenes as Transducers.* Chem. - Eur. J., 2001. **7**(10): p. 2075-2088.
20. Yuasa, H., et al., *A tong-like fluorescence sensor for metal ions: perfect conformational switch of hinge sugar by pyrene stacking.* Org. Biomol. Chem., 2004. **2**: p. 3548-3556.
21. Ayabe, M., et al., *A novel [60]fullerene receptor with a Pd(II)-switched bisporphyrin cleft.* Chem. Commun., 2002: p. 1032-1033.
22. Sun, D., et al., *Porphyrin−Fullerene Host−Guest Chemistry.* J. Am. Chem. Soc., 2000. **122**(43): p. 10704-10705.
23. Tashiro, K., et al., *A Cyclic Dimer of Metalloporphyrin Forms a Highly Stable Inclusion Complex with C_{60}.* J. Am. Chem. Soc., 1999. **121**(40): p. 9477-9478.
24. Muraoka, T., K. Kinbara, and T. Aida, *Mechanical Twisting of a Guest by a Photoresponsive Host.* Nature, 2006. **440**: p. 512-515.
25. Reek, J.N.H., et al., *Templated assembly of a molecular capsule.* Chem. Commun., 1998(1): p. 11-12.
26. Allen, P.R., et al., *Resolution of a porphyrin analogue of Tröger's base by making use of ligand binding affinity differences of the enantiomers.* Tetrahedron: Asymmetry, 1997. **8**(8): p. 1161-1164.
27. Anderson, H.L., et al., *Thermodynamics of Induced-Fit Binding Inside Polymacrocyclic Porphyrin Hosts.* J. Am. Chem. Soc., 1990. **112**(15): p. 5780-5789.
28. Ballester, P., et al., *DABCO-Induced Self-Assembly of a Trisporphyrin Double-Decker Cage: Thermodynamic Chacterization and Guest Recognition.* J. Am. Chem. Soc., 2006. **128**: p. 5560-5569.

29. Hunter, C.A., M.N. Meah, and J.K.M. Sanders, *DABCO-Metalloporphyrin Binding: Ternary Complexes, Host-Guest Chemistry, and the Measurement of π-π Interactions.* J. Am. Chem. Soc., 1990. **112**: p. 5773-5780.
30. Ballester, P., et al., *DABCO-Directed Self-Assembly of Bisporphyrins (DABCO = 1,4-Diazabicyclo[2.2.2]octane).* Chem. - Eur. J., 2005. **11**(7): p. 2196-2206.
31. Baldini, L., et al., *Molecular Acrobatics: Self-Assembly of Calixarene-Porphyrin Cages.* J. Am. Chem. Soc., 2003. **125**(46): p. 14181-14189.
32. Etxebarria, J., A. Vidal-Ferran, and P. Ballester, *The effect of complex stoichiometry in supramolecular chirality transfer to zinc bisporphyrin systems.* Chem. Commun., 2008: p. 5939-5941.
33. Rein, R., M. Gross, and N. Solladié, *Adjustable cavity for host-guest recognition in cofacial bis-porphyrinic tweezer.* Chem. Commun., 2004: p. 1992-1993.
34. Solladié, N., et al., *Structure-reactivity correlations in extended multi-porphyrinic architectures.* J. Porphyrins Phthalocyanines, 2003. **7**: p. 270-281.
35. Solladié, N., et al., *Influence of the spacer in bis-porphyrinic tweeers on the association constant for host/guest complexes.* J. Porphyrins Phthalocyanines, 2005. **9**: p. 779-787.
36. Solladié, N., et al., *Bis-porphyrin tweezers: rigid or flexbile linkers for better adjustment of the cavity to bidentate bases of various size.* J. Porphyrins Phthalocyanines, 2008. **12**: p. 1250-1260.
37. Hunter, C.A., J.K.M. Sanders, and A.J. Stone, *Exciton coupling in porphyrin dimers.* Chem. Phys., 1989. **133**(3): p. 395-404.
38. Dudič, M., et al., *Calixarene-based metalloporphyrins: molecular tweezers for complexation of DABCO.* Tetrahedron, 2003. **59**(14): p. 2409-2415.
39. Voyer, N. and F. Maltais, *A novel supramolecular device with a tunable absorption spectrum.* Advanced Materials, 1993. **5**(7-8): p. 568-570.
40. Jokic, D., Z. Asfari, and J. Weiss, *The First Versatile Synthetic Approach to Cofacial Bis-Porphyrins with Calixarene Spacers.* Org. Lett., 2002. **4**(13): p. 2129-2132.
41. Jokic, D., et al., *Structural and Binding Features of Cofacial Bis-Porphyrins with Calixarene Spacers: Pac-Man Porphyrins That Can Chew.* Chem. - Eur. J., 2005. **11**(14): p. 4199-4209.

42. Gil, S., et al., *Molecular Tweezers for Enantiodiscrimination in NMR: Di-(R,R)-1-[10-(1-hydroxy-2,2,2-trifluoroethyl)-9-anthyrl]-2,2,2-trifluoroethyl Benzenedicarboxylates.* Chirality, 2010. **22**: p. 548-556.

43. Huang, X., et al., *Absolute Configurational Assignments of Secondary Amines by CD-Sensitive Dimeric Zinc Porphyrin Host.* J. Am. Chem. Soc., 2002. **124**: p. 10320-10335.

44. Bhyrappa, P., V.V. Borovkov, and Y. Inoue, *Supramolecular Chirogenesis in Bis-porphyrins: Interaction with Chiral Acids and Application for the Absolute Configuration Assignment.* Org. Lett., 2007. **9**(3): p. 433-435.

45. Borovkov, V. and Y. Inoue, *A Versatile Bisporphyrinoid Motif for Supramolecular Chirogenesis.* Eur. J. Org. Chem., 2009. **2009**(2): p. 189-197.

46. Monahan, C., J.T. Bien, and S. B.D., *Fluorescence sensing due to allosteric switching of pyrene functionalised cis-cyclohexane-1,3-dicarboxylate.* Chem. Commun., 1998(3): p. 431-432.

47. Milgrom, L.R., *The Colours of Life: An Introduction to the Chemistry of Porphyrins and Related Compounds*. 1997: Oxford University Press Inc., New York.

48. *The Porphyrin Handbook*, ed. K.M. Kadish, K.M. Smith, and R. Guilard. Vol. 1 Synthesis and Organic Chemistry; 3. Inorganic, Vol. 3 Organometallic and Coordination Chemistry. 2000-2003: Academic Press.

49. Thordarson, P., et al., *Epoxidation of polybutadiene by a topologically linked catalyst.* Nature, 2003. **424**: p. 915-918.

50. Fang, Z., K.Y. Pu, and B. Liu, *Asymmetric Fluorescence Quenching of Dual-Emissive Porphyrin-Containing Conjugated Polyelectrolytes for Naked-Eye Mercury Ion Detection.* Macromolecules, 2008. **41**(22): p. 8380-8387.

51. Schmitt, F., et al., *Combined arene ruthenium porphyrins as chemotherapeutics and photosensitizers for cancer therapy.* J. Biol. Inorg. Chem., 2009. **14**: p. 101-109.

52. Anderson, H.L., *Conjugated Porphyrin Ladders.* Inorg. Chem., 1994. **33**: p. 972-981.

53. Anderson, H.L., S. Anderson, and J.K.M. Sanders, *Ligand binding by butadiyne-linked porphyrin dimers, trimers and tetramers.* J. Chem. Soc. Perkin Trans. 1, 1995: p. 2231-2245.

54. Anderson, S., H.L. Anderson, and J.K.M. Sanders, *The role of templates in the syntheses of porphyrin oligomers.* J. Chem. Soc. Perkin Trans. 1, 1995: p. 2255-2267.

55. Ballester, P., et al., *Self-Assembly, Binding, and Dynamic Properties of Heterodimeric Porphyrin Macrocycles.* J. Org. Chem., 2005. **70**(17): p. 6616-6622.

56. Borovkov, V.V., et al., *Supramolecular Chirogenesis in Zinc Porphyrins: Interaction with Bidentate Ligands, Formation of Tweezer Structures, and the Origin of Enhanced Optical Activity.* J. Org. Chem., 2003. **68**(19): p. 7176-7192.

57. Borovkov, V., et al., *Supramolecular Chirogenesis in Weakly Interacting Hosts: Role of the Temperature, Structural, and Electronic Factors in Enhancement of Chiroptical Sensitivity.* Org. Lett., 2008. **10**(6): p. 1283-1286.

58. Mulholland, A.R., et al., *Porphyrin dyads linked by a rotatable 3,3[prime or minute]-biphenyl scaffold: a new binding motif for small ditopic molecules.* Org. Biomol. Chem., 2012. **10**(30): p. 6045-6053.

59. Gil-Ramírez, G., et al., *A Cyclic Porphyrin Trimer as a Receptor for Fullerenes.* Org. Lett., 2010. **12**(15): p. 3544-3547.

60. Sprafke, J.K., et al., *All-or-Nothing Cooperative Self-Assembly of an Annulene Sandwich.* Angew. Chem. Int. Ed., 2011. **50**(24): p. 5572-5575.

61. Kondratuk, D.V., et al., *Two Vernier-Templated Routes to a 24-Porphyrin Nanoring.* Angew. Chem. Int. Ed., 2012. **51**(27): p. 6696-6699.

62. Liu, S., et al., *Caterpillar Track Complexes in Template-Directed Synthesis and Correlated Molecular Motion.* Angew. Chem. Int. Ed., 2015. **54**(18): p. 5355-5359.

63. Neuhaus, P., et al., *A Molecular Nanotube with Three-Dimensional π-Conjugation.* Angew. Chem. Int. Ed., 2015. **54**(25): p. 7344-7348.

64. Durola, F., et al., *Cyclic [4]Rotaxanes Containing Two Parallel Porphyrinic Plates: Toward Switchable Molecular Receptors and Compressors.* Acc. Chem. Res., 2014. **47**(2): p. 633-645.

65. Collin, J.-P., et al., *Adjustable Receptor Based on a [3]Rotaxane Whose Two Threaded Rings Are Rigidly Attached to Two Porphyrinic Plates: Synthesis and Complexation Studies.* J. Am. Chem. Soc., 2009. **131**(15): p. 5609-5620.

66. Taylor, P.N. and H.L. Anderson, *Cooperative Self-Assembly of Double-Strand Conjugated Porphyrin Ladders.* J. Am. Chem. Soc., 1999. **121**(49): p. 11538-11545.

67. Gaynor, S.P., et al., *Probing the dimensions of semi-rigid inner functionalised U-shaped bis-porphyrin cavities.* Org. Biomol. Chem., 2006. **4**: p. 2253-2266.

68. Shephard, M.J. and M.N. Paddon-Row, *Electrostatically Driven Geometry Changes Accompanying Charge Sepration in Supposedly Rigid Bichromophoric Systems.* J. Phys. Chem. A, 2000. **104**: p. 11628-11635.

69. Shephard, M.J. and M.N. Paddon-Row, *Large Predicted Changes in Geometry Accompanying Charge Separation in Various "Rigid" Multichromophoric Systems in the Gas Phase: An ab Initio MO Study.* J. Phys. Chem. A, 1999. **103**(18): p. 3347-3350.

70. Johnston, M.R., M.J. Latter, and R.N. Warrener, *Bisporphyrin Cavities: from Guest Complexation to Molecular Capsule Formation.* Aust. J. Chem., 2001. **54**: p. 633-636.

71. Long, B.M. and F.M. Pfeffer, *The Influence of the Framework: An Anion-Binding Study Using Fused [n]Polynorbornanes.* Chem. - Asian J., 2014. **9**(4): p. 1091-1098.

72. Johnstone, M.D., et al., *Modular Synthesis of Linear Bis- and Tris-monodentate Fused [6]Polynorbornane-Based Ligands and their Assembly into Coordination Cages.* Chem. - Eur. J., 2015. **21**(10): p. 3948-3955.

73. Johnston, M.R. and D.M. Lyons, *Synthesis and Complexation Studies of a Convex Bis-poprhyrin Tweezer - A Molecular Capsule Precursor.* Supramol. Chem., 2005. **17**(7): p. 503-511.

74. Johnston, M.R., M.J. Gunter, and R.N. Warrener, *Templated formation of multi-porphyrin assemblies resembling a molecular universal joint.* Chem. Commun., 1998(24): p. 2739-2740.

75. Warrener, R.N., M.R. Johnston, and M.J. Gunter, *Preparation of New Porphyrin BLOCKs and their Application to the Synthesis of Spacer and Cavity Ribbon Structures.* Synlett, 1998(6): p. 593-595.

76. Johnston, M.R., M.J. Latter, and R.N. Warrener, *Porphyrin-Containing Molecular Capsules: Metal Mediated Dimerization of a Bis-Porphyrin Cavity.* Org. Lett., 2002. **4**(13): p. 2165-2168.

77. Flamigni, L., G. Marconi, and M.R. Johnston, *Bis-porphyrinic clamp for photo- and electro-active guests: a spectroscopic and photophysical study.* Phys. Chem. Chem. Phys., 2001. **3**: p. 4488-4494.

78. Lyons, D.M., *Porphyrin Containing Molecular Tweezers - From the Formation of Simple Complexes, to Porphyrin Nanoparticles*, in *School of Chemistry, Physics and Earth Sciences, Faculty of Science and Engineering*. PhD Thesis, 2007, Flinders University.

79. Otto, S., *Reinforced molecular recognition as an alternative to rigid receptors.* Dalton Trans., 2006(23): p. 2861-2864.

80. Nakash, M. and J.K.M. Sanders, *Structure−Activity Relationships in the Acceleration of a Hetero Diels−Alder Reaction by Metalloporphyrin Hosts.* J. Org. Chem., 2000. **65**(22): p. 7266-7271.

81. Rodriguez-Docampo, Z., et al., *Dynamic combinatorial development of a neutral synthetic receptor that binds sulfate with nanomolar affinity in aqueous solution.* Chem. Commun., 2011. **47**(35): p. 9798-9800.

82. Merkas, S., et al., *Pre-organized dinucleosides with pendant porphyrins for the formation of sandwich type complexes with DABCO with high association constants.* J. Porphyrins Phthalocyanines, 2015. **19**(01-03): p. 535-546.

83. Kim, D., et al., *A molecular-clip-based approach to cofacial zinc-porphyrin complexes.* J. Organomet. Chem., 2009. **695**(1): p. 111-119.

84. Kubo, Y., et al., *A new biphenyl-20-crown-6-derived zinc(II) porphyrin dimer with a potentially heterotropic allostery.* Tetrahedron Lett., 1999. **40**(33): p. 6019-6023.

85. Yagi, S., et al., *Diarylurea-Linked Zinc Porphyrin Dimer as a Dual-Mode Artificial Receptor: Supramolecular Control of Complexation-Facilitated Photoinduced Electron Transfer.* J. Am. Chem. Soc., 2003. **125**(14): p. 4068-4069.

86. Tong, L.H., et al., *Supramolecular Assemblies of Tripodal Porphyrin Hosts and C_{60}.* Chem. - Eur. J., 2008. **14**(10): p. 3035-3044.

87. Kovbasyuk, L. and R. Krämer, *Allosteric Supramolecular Receptors and Catalysts.* Chem. Rev., 2004. **104**: p. 3161-3187.

88. Ercolani, G. and L. Schiaffino, *Allosteric, Chelate, and Interannular Cooperativity: A Mise au Point.* Angew. Chem. Int. Ed., 2011. **50**(8): p. 1762-1768.

89. Kubo, Y., et al., *Chirality-Transfer Control Using a Heterotopic Zinc(II) Porphyrin Dimer.* J. Am. Chem. Soc., 2001. **123**(50): p. 12700-12701.

90. Sato, H., et al., *Positive Heterotropic Cooperativity for Selective Guest Binding via Electronic Communications through a Fused Zinc Porphyrin Array.* J. Am. Chem. Soc., 2005. **127**(38): p. 13086-13087.

91. Sato, H., et al., *Cyclic dimer of a fused porphyrin zinc complex as a novel host with two [small pi]-electronically coupled binding sites.* Chem. Commun., 2005(18): p. 2324-2326.

92. Hunter, C.A. and H.L. Anderson, *What is Cooperativity?* Angew. Chem. Int. Ed., 2009. **48**(41): p. 7488-7499.

93. Ercolani, G., et al., *Symmetry Numbers and Statistical Factors in Self-Assembly and Multivalency.* J. Phys. Chem. B, 2007. **111**(42): p. 12195-12203.

94. Radomski, J.L., *The Primary Aromatic Amines: Their Biological Properties and Structure-Activity Relationships.* Annu. Rev. Pharmacol. Toxicol., 1979. **19**(1): p. 129-157.

95. Kim, E.J., et al., *Theoretical Investigations into the Role of Aryl Nitrenium Ions' Stability on Their Mutagenic Potential.* Aust. J. Chem., 2011. **64**(7): p. 910-915.

96. Sanders, J.K.M., *The Coordination Chemistry of Oligoporphyrins, The Porphyrin Handbook*. The Porphyrin Handbook, ed. K.M. Kadish, K.M. Smith, and R. Guilard. Vol. 3, p. 347-368. 2000: Academic Press.

97. Hunter, C.A. and L.D. Sarson, *Self-Assembly of a Dimeric Porphyrin Host.* Angew. Chem. Int. Ed. Engl., 1994. **33**(22): p. 2313-2316.

98. Rudkevich, D.M., W. Verboom, and D.N. Reinhoudt, *Capped Biscalix[4]arene-Zn-Porphyrin: Metalloreceptor with a Rigid Cavity.* J. Org. Chem., 1995. **60**(20): p. 6585-6587.

99. Miller, J.R. and G.D. Dorough, *Pyridinate Complexes of Some Metallo-derivatives of Tetraphenylporphine and Tetraphenylchlorin.* J. Am. Chem. Soc., 1952. **74**: p. 3977-3981.

100. Warrener, R.N., et al., *The synthesis of polarofacial spacer molecules: a new twist in the coupling of ring strained olefins with oxadiazoles.* Tetrahedron Lett., 1991. **32**(16): p. 1889-1892.

101. Warrener, R.N., I.G. Pitt, and D.N. Butler, *The synthesis of new linear and angular systems useful as rigid rods and spacers in the design of molecules.* J. Chem. Soc., Chem. Commun., 1983(22): p. 1340-1342.

102. Warrener, R.N., et al., *A new building BLOCK technique based on cycloaddition chemistry for the regiospecific linking of alicyclic sub-units as a route to large, custom-functionalised substructures.* Chem. Commun., 1997(11): p. 1023-1024.

103. Warrener, R.N., S. Wang, and R.A. Russell, *The synthesis of U-shaped cavity molecules with "inner-surface" functionality.* Tetrahedron, 1997. **53**(11): p. 3975-3990.

104. Warrener, R.N., et al., *New and improved 'LEGO' BLOCK protocols for the direct synthesis of hydrophilic ribbon molecules with acid, ester, or peptide functionality.* Tetrahedron Lett., 2000. **41**: p. 4671-4675.

105. Napper, A.M., et al., *An Unequivocal Demonstration of the Importance of Nonbonded Contacts in the Electronic Coupling between Electron Donor and Acceptor Units of Donor−Bridge−Acceptor Molecules.* J. Am. Chem. Soc., 2000. **122**(21): p. 5220-5221.

106. Head, N.J., Oliver, A.M., Look, K., Lokan, N.R., Jones, G.A., Paddon-Row, M.N., *Novel U-Shaped Systems Containing an Imide-Functionalized Cleft for the Study of Solvent-Mediated Electron Transfer and Energy Transfer: Synthesis and Binding Studies.* Angew. Chem. Int. Ed., 1999. **38**(21): p. 3219-3222.

107. Golić, M., et al., *Use of a 9,10-Dihydrofulvalene Pincer Cycloadduct as a Cornerstone for Molecular Architecture.* Aust. J. Chem., 2006. **59**(12): p. 899-914.

108. Margetic, D., et al., *Synthesis and modelling of novel rigid rods derived from a simple pentacyclic bis-norbornene [1].* Tetrahedron Lett., 1998. **39**(29): p. 5277-5280.

109. Johnston, M., *Bis-Porphyrin Racks with Space-Separated Co-Planar Porphyrin Rings.* Molecules, 2001. **6**(4): p. 406-416.

110. Margetic, D., et al., *Computational study of supramolecular bis-porphyrin "molecular tweezers".* Theor. Chem. Acc., 2007. **117**(2): p. 239-245.

111. Lawson, J.M., et al., *Synthesis of a Variety of Bichromophoric "Ball-and-Chain" Systems Based on Buckminsterfullerene (C_{60}) for the Study of*

Intramolecular Electron and Energy Transfer Processes. J. Org. Chem., 1996. **61**: p. 5032-5054.

112. Bell, T.D.M., et al., *Remarkable Conformational Control of Photoinduced Charge Separation and Recombination in a Giant U-Shaped, Tetrad.* J. Am. Chem. Soc., 2000. **122**: p. 10661-10666.
113. Warrener, R.N., et al., *Incorporation of a Molecular Hinge into Molecular Tweezers by Using Tandem Cycloadditions onto 5,6-Dimethylenenorbornene.* Chem. - Eur. J., 2001. **7**(15): p. 3406-3414.
114. Gunter, M.J., H. Tang, and R.N. Warrener, *Establishing a library of porphyrin building blocks for superstructured assemblies: porphyrin dienes and dienophiles for cycloaddition reactions.* J. Porphyrins Phthalocyanines, 2002. **6**: p. 673-684.
115. Tang, H., et al., *Hinged bis-porphyrin scaffolds I. The synthesis of a new porphyrin diene and its role in constructing hinged porphyrin dyads and cavity systems.* Tetrahedron Lett., 2009. **50**(6): p. 667-670.
116. Napper, A.M., et al., *Use of U-shaped Donor-Bridge-Acceptor Molecules To Study Electron Tunneling through Nonbonded Contacts.* J. Am. Chem. Soc., 2002. **124**(34): p. 10171-10181.
117. Chou, T.-C., K.-C. Lin, and C.-A. Wu, *Quinoxaline-based U-shaped septuple-bridged [7,7]orthocyclophanes: synthesis, solid-state structure, and self-assembly.* Tetrahedron, 2009. **65**(49): p. 10243-10257.
118. Gaynor, S., *The Design, Synthesis and Geometric Analysis of Large Centrally Functionalised Porphyrin-Spacer-Porphyrins*. PhD Thesis, 2003, University of New England, Armidale, New South Wales.
119. Miller, C.W., et al., *Inter-Ring Torsions in N-Phenylmaleimide and Its o-Halo Derivatives: An Experimental and Computational Study.* J. Phys. Chem. A, 1999. **103**(32): p. 6406-6412.
120. Miller, C.W., et al., *Evaluation of N-Aromatic Maleimides as Free Radical Photoinitiators: A Photophysical and Photopolymerization Characterization.* J. Phys. Chem. B, 2001. **105**(14): p. 2707-2717.
121. Miller, C., et al., *N-Arylmaleimide derivatives.* J. Chem. Crystallogr., 2000. **30**(9): p. 563-571.
122. Langowski, B.A., R. Rothchild, and A.-M. Sapse, *Ab Initio Studies of Hindered Rotation of Some Aromatic Rings in N-2,6-difluorophenyl imides*

and Unsubstituted Bridgehead Phenyls. Spectrosc. Lett., 2001. **34**(2): p. 235-251.

123. Kondo, K., et al., *A new chiral axis due to N(open-chain imide)-Ar bond: Unexpected racemization effect of an acyl group.* Tetrahedron Lett., 1999. **40**(30): p. 5577-5580.
124. Mao, M., J. England, and S.R. Turner, *Alternating stilbene copolymers with negative birefringence.* Polymer, 2011. **52**(20): p. 4498-4502.
125. Yu, Y., et al., *Molecular containers with a dynamic orifice: open-cage fullerenes capable of encapsulating either H2O or H2 under mild conditions.* Chem. Sci., 2013. **4**(2): p. 814-818.
126. Verma, S. and N. Singh, *A study of conformation about the aryl C-N bonds in N-aryl imides by dynamic N.M.R. spectroscopy.* Aust. J. Chem., 1976. **29**(2): p. 295-300.
127. Curran, D.P., S. Geib, and N. DeMello, *Rotational features of carbon-nitrogen bonds in N-aryl maleimides. Atroposelective reactions of o-tert-butylphenylmaleimides.* Tetrahedron, 1999. **55**(18): p. 5681-5704.
128. Tanaka, K., et al., *Effect of methyl substituents on permeability and permselectivity of gases in polyimides prepared from methyl-substituted phenylenediamines.* J. Polym. Sci., Part B: Polym. Phys. , 1992. **30**(8): p. 907-914.
129. Zhang, Y., J.M. Lavin, and K.D. Shimizu, *Solvent Programmable Polymers Based on Restricted Rotation.* J. Am. Chem. Soc., 2009. **131**(34): p. 12062-12063.
130. Choi, D.-S., et al., *Molecules with Shape Memory Based on Restricted Rotation.* Org. Lett., 2001. **3**(23): p. 3757-3760.
131. Chen, Y., M.D. Smith, and K.D. Shimizu, *An axially chiral phosphine ligand based on restricted rotation in N-arylimides.* Tetrahedron Lett., 2001. **42**(41): p. 7185-7187.
132. Rasberry, R.D., et al., *A Small Molecule Diacid with Long-Term Chiral Memory.* Org. Lett., 2009. **11**(12): p. 2599-2602.
133. Degenhardt, C.F., et al., *Conformationally Imprinted Receptors: Atropisomers with "Write", "Save", and "Erase" Recognition Properties.* Org. Lett., 2005. **7**(19): p. 4079-4081.
134. Lavin, J.M. and K.D. Shimizu, *A supramolecular switch with molecular memory.* Chem. Commun., 2007(3): p. 228-230.

135. Carroll, W.R., P. Pellechia, and K.D. Shimizu, *A Rigid Molecular Balance for Measuring Face-to-Face Arene−Arene Interactions.* Org. Lett., 2008. **10**(16): p. 3547-3550.

136. Curran, D.P. and N.C. DeMello, *Origins of regioselectivity in radical reactions of axially twisted anilides.* J. Chem. Soc., Chem. Commun., 1993(17): p. 1314-1317.

137. Eaton, S.S.E., G.R., *Phenyl Ring Rotation in Metal Complexes of Tetraphenylporphyrin Derivatives.* J. Chem. Soc., Chem. Commun., 1974: p. 576-577.

138. Wagner, R.W., Johnson, T.E., Lindsey, J.S., *Soluble Synthetic Multiporphyrin Arrays. 1. Modular Design and Synthesis.* J. Am. Chem. Soc., 1996. **118**(45): p. 11166-11180.

139. Eaton, S.S.E., G.R., *Rotation of Phenyl Rings in Metal Complexes of Substituted Tetraphenylporphyrins.* J. Am. Chem. Soc., 1975. **97**(13): p. 3660-3666.

140. Misuraca, M.C., et al., *Relationship Between Conformational Flexibility and Chelate Cooperativity.* J. Org. Chem., 2011. **76**(8): p. 2723-2732.

141. Adams, H., et al., *Quantification of the Effect of Conformational Restriction on Supramolecular Effective Molarities.* J. Am. Chem. Soc., 2013. **135**(5): p. 1853-1863.

142. Diels, O. and K. Alder, *Synthesen in der hydroaromatischen Reihe.* Justus Liebigs Ann. Chem., 1928. **460**: p. 98-122.

143. Craig, D., *The Rearrangement of endo-3,6-Methylene-1,2,3,6-tetrahydro-cis-phthalic Anhydride.* J. Am. Chem. Soc., 1951. **73**: p. 4889-4892.

144. Luguya, R., et al., *Synthesis and reaction of meso-(p-nitrophenyl)porphyrins.* Tetrahedron, 2004. **60**: p. 2757-2763.

145. . Spartan '10 for Windows, Wavefunction, Inc., 18401 Von Karman Avenue, Suite 370, Irvine, CA 92612 USA, http://www.wavefun.com/index.html.

146. Mitsudo, T.-a., et al., *Ruthenium-Catalyzed [2 + 2] Cross-Addition of Norbornene Derivatives and Dimethyl Acetylenedicarboxylate.* J. Org. Chem., 1979. **44**(25): p. 4492-4496.

147. Mitsudo, T.-a., et al., *[2 + 2]Cycloaddition of Norbornenes with Alkynes Catalyzed by Ruthenium Complexes.* Angew. Chem. Int. Ed. Engl., 1994. **33**(5): p. 580-581.

148. Robinson, S.D., *B. Carbonyldihydridotris(triphenylphosphine)-ruthenium(II) (white isomer)*. Inorg. Synth., 1974. **15**: p. 48-50.

149. Huntress, E.H., T.E. Lesslie, and J. Bornstein, *Dimethyl Acetylenedicarboxylate.* Organic Syntheses, Coll., 1952. **32**: p. 55.

150. Huntress, E.H., T.E. Lesslie, and J. Bornstein, *Dimethyl Acetylenedicarboxylate.* Organic Syntheses, Coll., 1963. **4**: p. 329.

151. Shang, M., et al., *Synthesis of bis-peptides attached on poly[n]norbornene molecular scaffolds with well defined relative positions and distances.* Mol. Divers., 2011. **15**: p. 541-560.

152. Sealy, J., *The Synthesis of Binane Anhydrides*, in *Department of Chemistry*. 1995, York University, Ontario, Canada.

153. Hill, J.G., B.E. Rossiter, and K.B. Sharpless, *Anhydrous tert-Butyl Hydroperoxide in Toluene: The Preferred Regagent for Applications Requiring Dry TBHP.* J. Org. Chem., 1983. **48**: p. 3607-3608.

154. Lee, I.J., Choi, H.W., Nho, Y.C. & Suh, D.H., *Gamma-Ray Irradiation Effect of Polyethylene on Dimaleimides as a Class of New Multifunctional Monomers.* J. Appl. Polym. Sci., 2003. **88**: p. 2339-2345.

155. Heitz, W., et al., *Poly(norbornene imide)s: synthesis and simulations.* Macromol. Chem. Phys., 1999. **200**(2): p. 338-347.

156. Havens, J.R., Ishida, H. & Koenig, J.L., *High-Resolution Carbon-13 Nuclear Magnetic Resonance Study of Conjugation in Solid Polymers.* Macromolecules, 1981. **14**: p. 1327-1333.

157. Dennison, G., *unpublished results*. 2004.

158. Kruper, W.J., T.A. Chamberlin, and M. Kochanny, *Regiospecific Aryl Nitration of Meso-Substituted Tetraarylporphyrins: A Simple Route to Bifunctional Porphyrins.* J. Org. Chem., 1989. **54**: p. 2753-2756.

159. Fuhrhop, J.-H. and K.M. Smith, *Laboratory methods in porphyrin and metalloporphyrin research*. 1975.

160. Foitzik, R.C., A. Lowe, and F.M. Pfeffer, *Microwave-accelerated 1,3-dipolar cycloaddition for the formation of fused [n]polynorbornanes.* Tetrahedron Lett., 2009. **50**: p. 2583-2584.

161. Kasha, M., H.R. Rawls, and M.A. El-Bayoumi, *The exciton model in molecular spectroscopy.* Pure Appl. Chem., 1965. **11**(3-4): p. 371-392.

162. Osuka, A. and K. Maruyama, *Synthesis of Naphthalene-Bridged Porphyrin Dimers and Their Orientation-Dependent Exciton Coupling.* J. Am. Chem. Soc., 1988. **110**(13): p. 4454-4456.
163. Chang, C.K. and I. Abdalmuhdi, *Anthracene pillared cofacial diporphyrin.* J. Org. Chem., 1983. **48**(26): p. 5388-5390.
164. Staab, H.A. and T. Carell, *Synthesis and Properties of a Vertically Stacked Porphyrin(1)-Quinone(2)-Quinone Cyclophane.* Angew. Chem. Int. Ed. Engl., 1994. **33**(14): p. 1466-1468.
165. Camara-Campos, A., C.A. Hunter, and S. Tomas, *Cooperativity in the self-assembly of porphyrin ladders.* Proc. Natl. Acad. Sci. U.S.A., 2006. **103**(9): p. 3034-3038.
166. Protonic Software, T.A., Leeds, LS150HD, UK. (www.hyperquad.co.uk).
167. Olson, E.J. and P. Bühlmann, *Getting More out a Job Plot: Determination of Reactant to Product Stoichiometry in Cases of Displacement Reactions and n:n Complex Formation.* J. Org. Chem., 2011. **76**(20): p. 8406-8412.
168. Connors, K.A., *Binding Constants: The Measurement of Molecular Complex Stability*. 1987.
169. Kimura, M., et al., *Self-assembly of chiral-twisted porphyrin dimers.* New J. Chem., 2000. **24**(3): p. 113-114.
170. Hungerford, G., et al., *Intramolecular Energy Transfer in Bis-porphyrins Containing Diimine Chelates of Variable Geometry as Spacers.* Chem. - Eur. J., 1999. **5**(7): p. 2089-2100.
171. Beavington, R. and P.L. Burn, *Bis-porphyrin arrays. Part 3. The synthesis of model bis-porphyrin dimers and an electrochemical study.* J. Chem. Soc. Perkin Trans. 1, 2000: p. 1231-1240.
172. Mak, C.C., N. Bampos, and J.M.K. Sanders, *Metalloporphyrin Dendrimers with Folding Arms.* Angew. Chem. Int. Ed. Engl., 1998. **37**(21): p. 3020-3023.
173. Polam, J.R., et al., *Rates of axial ligand rotation in diamagnetic d^6 Co(III) and FE(II) porphyrinates.* Inorg. Chim. Acta, 1997. **263**(1-2): p. 109-117.
174. Medforth, C.J., et al., *NMR studies of nonplanar porphyrins. Part 1. Axial ligand orientation in highly nonplanar porphyrins.* J. Chem. Soc. Perkin Trans. 2, 1997(4): p. 833-837.
175. Hunter, C.A. and R.J. Shannon, *Photoinduced electron transfer on a supramolecular scaffold.* Chem. Commun., 1996(11): p. 1361-1362.

176. Hunter, C.A. and R.K. Hyde, *Photoinduced Energy and Electron Transfer in Supramolecular Porphyrin Assemblies.* Angew. Chem. Int. Ed. Engl., 1996. **35**(17): p. 1936-1939.

177. Mulholland, A.R., et al., *Supporting Information: Porphyrin dyads linked by a rotatable 3,3[prime or minute]-biphenyl scaffold: a new binding motif for small ditopic molecules.* Org. Biomol. Chem., 2012. **10**(30): p. 6045-6053.

178. Screen, T.E.O., et al., *Amplified Optical Nonlinearity in a Self-Assembled Double-Strand Conjugated Porphyrin Polymer Ladder.* J. Am. Chem. Soc., 2002. **124**(33): p. 9712-9713.

179. Drain, C.M., et al., *Porphyrin Tessellation by Design: Metal-Mediated Self-Assembly of Large Arrays and Tapes.* Angew. Chem. Int. Ed., 1998. **37**(17): p. 2344-2347.

180. Giancane, G., et al., *Conformational switching in bis(zinc porphyrin) Langmuir-Schaefer film as an effective tool for selectively sensing aromatic amines.* J. Colloid Interf. Sci., 2012. **385**(1): p. 282-284.

181. Borovkov, V.V., J.M. Lintuluoto, and Y. Inoue, *Temperature controlled syn-anti conformational switching in zinc containing porphyrin dimers via ligand assistance.* Tetrahedron Lett., 1999. **40**(27): p. 5051-5054.

182. Borovkov, V.V., J.M. Lintuluoto, and Y. Inoue, *Syn-Anti Conformational Changes in Zinc Porphyrin Dimers Induced by Temperature-Controlled Alcohol Ligation.* J. Phys. Chem. B, 1999. **103**(24): p. 5151-5156.

183. Borovkov, V.V., J.M. Lintuluoto, and Y. Inoue, *Supramolecular Chirogenesis in Zinc Porphyrins: Mechanism, Role of Guest Structure, and Application for the Absolute Configuration Determination.* J. Am. Chem. Soc., 2001. **123**(13): p. 2979-2989.

184. Bartlett, P.D., et al., *Reactivities of norbornene-type double bonds in propellane derivatives and their precursors; furan as a diene.* J. Am. Chem. Soc., 1982. **104**(11): p. 3131-3138.

185. Diels, O.A., K., *Synthesen in der Hydroaromatischen Reihe. XII. Mitteilung.* Justus Liebigs Ann. Chem., 1931. **490**(1): p. 243-257.

186. Kallos, J.D., P., *Configuration of Diels-Alder Adduct of Furan and Acetylene Dicarboxylic Acid*[I]. Can. J. Chem., 1966. **44**(11): p. 1239-1245.

187. Maier, G. and W.A. Jung, *Acetylendicarbonyldichlorid.* Chem. Ber., 1982. **115**(2): p. 804-807.

188. Margetic, D., Warrener, R.N., Sun, G., Butler, D.N., *The preparation of 7-substituted norbornadiene-2,3-dicarboxylic anhydrides and an experimental and theoretical study of their reactivity.* Tetrahedron, 2007. **63**: p. 4338-4346.

189. Mink, D., Deslongchamps, G., *A Novel Scaffold for the Modular Asseumbly of Receptor Models.* Tetrahedron Lett., 1996. **37**(39): p. 7035-7038.

190. Yamaura, M., Suzuki, T., Hashimoto, H., Yoshimura, J., Okamoto, T., *Oxidative Removal of N-(4-Methoxybenzyl) Group on 2,5-piperazinediones with Cerium(IV) Diammonium Nitrate.* Bull. Chem. Soc. Jpn., 1985. **58**: p. 1413-1420.

191. Yoshimura, J., Yamaura, M., Suzuki, T., Hashimoto, H., *Oxidative Removal of N-(p-methoxybenzyl) group on diketopiperazine skeleton with ceric ammonium nitrate.* Chem. Lett., 1983: p. 1001-1002.

192. Lonergan, D.G., *The Design and Synthesis of Clef and U-type Abiotic Receptors for Molecular Recognition Studies*, in *Graduate Academic Unit of Chemistry*. 1998, The University of New Brunswick.

193. Barriault, L., or, and P. Andrew Evans. 2011, Personal Communication while visiting Flinders University.

194. Murray, R.W. and M. Singh, *Synthesis of Epoxides using Dimethyldioxirane: trans-stilbene oxide.* Organic Syntheses, Coll., 1997. **74**: p. 91.

195. Murray, R.W. and M. Singh, *Synthesis of Epoxides using Dimethyldioxirane: trans-stilbene oxide.* Organic Syntheses, Coll., 1998. **9**: p. 288.

196. Yadav, L.D.S., B.S. Yadav, and V.K. Rai, *Active-Copper-Promoted Expeditious N-Arylations in Aqueous Media under Microwave Irradiation.* Synthesis, 2006. **2006**(11): p. 1868-1872.

197. Lan, J.-B., Chen, L., Yu, X.-Q., You, J.-S., Xie, R.-G., *A simple copper salt catalysed the coupling of imidazole with arylboronic acids in protic solvent†.* Chem. Commun., 2004: p. 188-189.

198. Emeritus Dr Malcolm Thompson. 2014, Personal Communication, Flinders University.

199. Ercolani, G., *Assessment of Cooperativity in Self-Assembly.* J. Am. Chem. Soc., 2003. **125**(51): p. 16097-16103.

200. Breuning, M., et al., *Enantioselective synthesis of tricyclic amino acid derivatives based on a rigid 4-azatricyclo[5.2.1.02,6]decane skeleton.* Beilstein J. Org. Chem., 2009. **5**: p. 81.

201. Schaefer, M., N. Hanik, and A.F.M. Kilbinger, *ROMP Copolymers for Orthogonal Click Functionalizations.* Macromolecules, 2012. **45**(17): p. 6807-6818.

202. Mansfeld, F.M., G. Feng, and S. Otto, *Photo-induced molecular-recognition-mediated adhesion of giant vesicles.* Org. Biomol. Chem., 2009. **7**(20): p. 4289-4295.

203. Crockett, G.C., et al., *A Preferred Method for Imide Preparation.* Synth. Commun., 1981. **11**(6): p. 447-454.

204. Flaih, N., Pham-Huy, C., Galons, H., *An Expeditious Synthesis of Cyclic Imides.* Tetrahedron Lett., 1999. **40**(1999): p. 3697-3698.

205. Roche, C., *Porphyrin-based [3]- and [4]Rotaxanes Towards an Adaptable Molecular Receptor*. 2012, Université de Strasbourg and The University of Sydney.

206. Nguyen, N.T., et al., *Binding ability of Zn-tetraarylporphyrins with two, four and eight 4-(4-(3,6-bis(t-butyl)carbazol-9-ylphenyl)-1,2,3-triazole end groups towards N-containing substrates of different nature.* Supramol. Chem., 2013. **25**(3): p. 180-188.

207. Eguia, L.P.H., *Supramolecular Chemistry of Bis-Porphyrins*. PhD Thesis, 2010, Rovira i Virgili University and Institute of Chemical Research of Catalonia.

208. Bélanger, S., et al., *Rapid derivatization of mesoporous thin-film materials based on Re(I) zinc-porphyrin 'molecular squares': selective modification of mesopore size and shape by binding of aromatic nitrogen donor ligands.* Coord. Chem. Rev., 1999. **190–192**: p. 29-45.

209. Aggarwal, V.K., I. Emme, and S.Y. Fulford, *Correlation between pKa and Reactivity of Quinuclidine-Based Catalysts in the Baylis−Hillman Reaction: Discovery of Quinuclidine as Optimum Catalyst Leading to Substantial Enhancement of Scope.* J. Org. Chem., 2003. **68**(3): p. 692-700.

210. Hine, J. and Y.J. Chen, *Basicity of, SN2 reactivity of, and basic catalysis by 1-azabicyclo[2.2.1]heptane.* J. Org. Chem., 1987. **52**(10): p. 2091-2094.

211. Hara, M., Y. Odaira, and S. Tsutsumi, *Photo-addition reactions of dimethyl maleate and dimethyl acetylene dicarboxylate with norbornene.* Tetrahedron, 1966. **22**(1): p. 95-100.

212. Pfeffer, F.M. and R.A. Russell, *Strategies and methods for the attachment of amino acids and peptides to chiral [n]polynorbornane templates.* Org. Biomol. Chem., 2003. **1**(11): p. 1845-1851.

213. Faury, T., et al., *Side functionalization of diboronic acid precursors for covalent organic frameworks.* CrystEngComm, 2013. **15**(11): p. 2067-2075.

214. Zheng, W.-Z., *Synthesis of Sterically Hindered Metalloporphyrins.* Hecheng Huaxue, 1995. **3**(1): p. 88-90.

215. Naota, T. and H. Koori, *Molecules That Assemble by Sound: An Application to the Instant Gelation of Stable Organic Fluids.* J. Am. Chem. Soc., 2005. **127**: p. 9324-9325.

216. Wei, Q. and S.L. James, *A metal-organic gel used as a template for a porous organic polymer.* Chem. Rev., 2005(12): p. 1555-1556.

217. Piepenbrock, M.-O.M., et al., *Metal- and Anion Binding Supramolecular Gels.* Chem. Rev., 2010. **110**(4): p. 1960-2004.

218. James, T.D., et al., *Cholesterol as a Versatile Platform for Chiral Recognition.* Tetrahedron, 1995. **51**(2): p. 555-566.

219. Puigmartí-Luis, J., et al., *Supramolecular Conducting Nanowires from Organogels.* Angew. Chem. Int. Ed. Engl., 2007. **46**: p. 238-241.

220. Tong, K.W.K., et al., *Pyromellitamide Gelators: Exponential Rate of Aggregation, Hierarchical Assembly, and Their Viscoelastic Response to Anions.* Langmuir, 2009. **21**(15): p. 8586-8592.

221. Webb, J.E.A., et al., *Pyromellitamide Aggregates and Their Response to Anion Stimuli.* J. Am. Chem. Soc., 2007. **129**: p. 7155-7162.

222. Silva, G.A., et al., *Selective Differentiation of Neural Progenitor Cells by High-Epitope Density Nanofibers.* Science, 2004. **303**: p. 1352-1355.

223. Gottlieb, H.E., V. Kotlyar, and A. Nudelman, *NMR Chemical Shifts of Common Laboratory Solvents as Trace Impurities.* J. Org. Chem., 1997. **62**(21): p. 7512-7515.

224. Fulmer, G.R., et al., *NMR Chemical Shifts of Trace Impurities: Common Laboratory Solvents, Organics, and Gases in Deuterated Solvents Relevant to the Organometallic Chemist.* Organometallics, 2010. **29**(9): p. 2176-2179.

225. Perrin, D.D., L. Armarego, and D.R. Perrin, *Purification of Laboratory Chemicals*. 1966, Oxford: Pergamon Press, Ltd.

226. . mMass 5.4.1, Martin Strohalm, 2012 http://www.mmass.org/.

227. Mercury 3.3, C., 2013, http://www.ccdc.cam.ac.uk/mercury/.

228. Johnston, M.R. Personal Communication.

229. Andrist, A.H. and M.J. Kovelan, *Ozonolysis of tetrahydrophthalimides (cyclohex-4-ene-1,2-dicarboximides): a sterically dependent unsymmetrical oxidative cleavage reaction.* J. Chem. Soc. Perkin Trans. 1, 1978(9): p. 918-923.

230. Windholz, T.B. and D.B.R. Johnston, *Trichloroethoxycarbonyl: a generally applicable protecting group.* Tetrahedron Lett., 1967. **8**(27): p. 2555-2557.

231. Gore, P.H., Hughes, G.K., *A Quantitative Ullmann Reaction.* J. Chem. Soc., 1959: p. 1615-1616.

232. Nguyen, H.-T., et al., *Complexation of Crystal Violet, Pyronine B, and Rhodamine B by Linked β-Cyclodextrin Trimers.* Aust. J. Chem., 2013. **66**(9): p. 1057-1064.

233. Warrener, R.N., et al., *Building BLOCK Strategies for the Synthesis of Molecular Clefts with Inside Functionality.* Org. Lett., 1999. **1**(2): p. 199-202.

234. Oshima, N., H. Suzuki, and Y. Moro-Oka, *Synthesis and Some Reactions of Dichloro(pentamethylcyclopentadienyl)ruthenium(III) Oligomer.* Chem. Lett., 1984. **13**(7): p. 1161-1164.

235. Warrener, R.N., et al., *Rigid molecular racks featuring the 1,10-phenanthroline ligand especially those co-functionalised with redox-active groups or other bidentate ligands.* Tetrahedron, 1997. **53**(11): p. 3991-4012.

236. Butler, D.N., et al., *Cavity-shaped molracs with inward-facing, direct line-of-sight functionality.* Tetrahedron Lett., 1995. **36**(34): p. 6145-6148.

237. Warrener, R.N., L. Maksimovic, and D.N. Butler, *The synthesis of internally functionalised cavity molecules using a cycloaddition strategy.* J. Chem. Soc., Chem. Commun., 1994(16): p. 1831-1832.

238. Warrener, R.N., et al., *New synthetic strategies for the production of rigid, internally functionalised cavity molecules.* Tetrahedron Lett., 1995. **36**(34): p. 6141-6144.

239. Butler, D.N., et al., *New synthetic routes to molrac spacer and platform systems which incorporate the 1,4-benzoquinone chromophore.* Tetrahedron Lett., 1996. **37**(13): p. 2157-2160.

240. *Advances in Strain in Organic Chemistry, A Personal Perspective on Norbornenes, Cyclobutenes, and Other Ring-Strained Dienophiles in Organic Synthesis by Ron N. Warrener* Vol. 6. 1997: JAI Press.

241. Warrener, R.N., *Isolation of isobenzofuran, a stable but highly reactive molecule.* J. Am. Chem. Soc., 1971. **93**(9): p. 2346-2348.